(e,2e) SPECTROSCOPIC INVESTIGATIONS OF THE SPECTRAL MOMENTUM DENSITIES OF THIN CARBON FILMS

by

John Robert Dennison

Dissertation submitted to the faculty of the
Virginia Polytechnic Institute and State University
in partial fulfillment of the requirements for the degree of
DOCTOR OF PHILOSOPHY
in
Physics

APPROVED:

A. L. Ritter, chairman

C. D. Williams

J. R. Long

T. K. Lee

R. Zallen

December, 1985

Blacksburg, Virginia

(e,2e) SPECTROSCOPIC INVESTIGATIONS OF THE SPECTRAL MOMENTUM DENSITIES OF THIN CARBON FILMS.

by

John Robert Dennison

Committee Chairman: A. L. Ritter

Physics

(ABSTRACT)

An (e,2e) electron scattering spectrometer has been constructed and used for the first time to investigate the spectral momentum density of the valence bands of a solid target. This technique provides fundamental information about the electronic structure of both crystalline and amorphous solids. The three fundamental quantities, the band structure, electron density of states, and electron momentum distribution can be simultaneously derived from the measured (e,2e) cross section.

A review of single electron and (e,2e) scattering theory is given with an emphasis on scattering from solids. The effects of multiple scattering are discussed and a method of deconvoluting those effects from the measured (e,2e) cross section is developed.

There is a detailed description of the spectrometer design and operation with particular attention given to the

electron optics and voltage distribution. The algorithms and software for computer aided data acquisition and analysis are also outlined, as is error analysis.

The techniques employed in the preparation and characterization of extremely thin film samples of a-C and single crystal graphite are described.

An analysis of the data taken for a-C samples is given. The data are compared with the results of complementary experiments and theory for graphite, diamond, and a-C which are given in a review of the literature. The existence of a definite dispersion relation $\mathcal{E}(q)$ in amorphous carbon is demonstrated. The a-C band structure appears to be more similar to that of graphite than to that of diamond, however it differs significantly from both in some respects. The measured spectral momentum density seems compatible with a model of a-C based on small, randomly-oriented islands of quasi-2D graphite-like continuous random network structures. However, no definitive interpretations can be made until higher resolution experiments are performed on both a-C and single crystal graphite.

ACKNOWLEDGMENTS

This dissertation presents the combined efforts of many people over the course of several years. It is impossible to acknowledge all those who have played a role, however I would like to recognize some of these people. The foremost of these is of course my advisor, Jimmy Ritter. The contributions that he has made are without measure, not the least of which was conceiving of the project in the first place and daring to take on the challenges that it posed.

was a major participant before his untimely death. A number of other graduate students made valuable contributions including the work on deconvolution by , initial work on the sample preparation chamber by , and Raman spectroscopy measurements by . , , , and were also involved in the project.

Invaluable technical assistance was provided by (computer programming), and (electronics), and , , , , and (machine shop). at Poly-scientific and at NRRFSS were of great help in preparation of graphite

samples. advice and EELS measurements are greatly appreciated.

On a personal note, I would like to thank my friends and family, and in particular my parents, for their support and encouragement over the years. Finally, and foremost, I acknowledge for all that she has done to make this dissertation possible.

TABLE OF CONTENTS

Appendices

LIST OF FIGURES

LIST OF TABLES

I. INTRODUCTION

This dissertation presents the design and application of an (e,2e) electron spectrometer for the investigation of the electronic properties of solids. Application of this technique is new to the field of solid state physics. It is able to provide fundamental information about both crystalline and amorphous solids by directly measuring the spectral momentum density of valence electrons. The spectral momentum density is the probability per unit energy and unit volume of momentum space of finding an electron in a system with an energy $\mathcal{E}$ and momentum q. This fundamental quantity can be shown to be directly related to the square of the momentum wave function of an electron bound in the solid by making some familiar approximations, namely the impulse, plane wave, and independent electron approximations. It is also closely related to three basic properties of solids, the band structure, density of states, and electron momentum density.

The concept of using (e,2e) scattering to investigate the spectral momentum density was first suggested in the early 1960's by nuclear theorists who saw a direct analogy with (p,2p) scattering in nuclear physics [10, 68, 102,

155]. The first (e,2e) spectra were observed by Amaldi et al in 1969 [3]. Several of the earliest (e,2e) experiments attempted to measure spectra from thin solid films [3, 30, 99, 100], however these efforts were not successful in resolving the valence bands in solids. The initial attempts at solid scattering were plagued by poor energy resolution and severe problems with target degradation. Several groups have recently begun new programs in this field [175, 185, 63], however the only successful experiments to date have been performed at VPI [144].

Studies of gaseous atomic and molecular systems have been much more successful. The technique has become well established and is now being extended to more complicated atomic and molecular systems. Active groups are in Australia [Weigold and McCarthy; 85, 109, 115, 177], Italy [Guidoni; 29, 30, 159], British Columbia [Brion], and the University of Maryland [Coplan and Moore; 117]. A particularly impressive experiment on atomic H recently found excellent agreement between the (e,2e) cross section and exact quantum mechanical calculations of the hydrogen momentum wave function [109]. Reviews of recent experiments and theory of (e,2e) gas scattering are given by Weigold and McCarthy [114, 175, 177]. These gas experiments provide a good example for the development of

(e,2e) solid scattering. Many of the theoretical concepts and experimental techniques described in this dissertation have come directly from such analogy.

Measurements of (e,2e) spectra of solids contain a wealth of information. Direct comparison can be made between theoretical calculations of the square of the momentum wave function $|\phi(\mathbf{q};\mathcal{E})|^2$ and the count rate $N(\mathcal{E},\mathbf{q})$ as a function of binding energy and momentum. In addition, comparisons can be made with three fundamental quantities that can be derived from the measured count rate. A projection of the $N(\mathcal{E},\mathbf{q})$ peaks onto the $(\mathcal{E},\mathbf{q})$ plane yields the dispersion curve $\mathcal{E}(\mathbf{q})$. Summation of the count rate over all momenta is directly related to the energy density of states $N(\mathcal{E})$. Summation over all binding energies can be directly related to the electron momentum density $J(\mathbf{q})$. Further, the simultaneous determination of the band structure allows the possibility of calculating $N(\mathcal{E})$ and $J(\mathbf{q})$ separately for each band. The prospect of simultaneously obtaining the band structure, density of states and momentum density from one sample is indeed exciting, however the most important contribution of (e,2e) spectroscopy may prove to be the comparison with theoretical calculations of the fundamental quantity $|\phi(\mathbf{q})|^2$.

Several techniques exist which measure various integrals of the spectral momentum density. These techniques provide important verification of (e,2e) measurements. Measurements of the electron binding energies through the density of states $N(\mathcal{E}) \sim \int N(\mathcal{E},\mathbf{q})\, d\mathbf{q}$ can be obtained, for example, by photoelectron spectroscopy (UPS and XPS). However, no momentum information is available. Angle-resolved photoelectron spectroscopy (ARPES) can in principle provide some momentum information. However, the theoretical understanding of this reaction is insufficient to quantitatively relate the intensity from the angle-resolved spectra to the spectral momentum density. Instead, the technique can be used to map the dispersion relation $\mathcal{E}(\mathbf{q})$. The electron momentum density $J(\mathbf{q}) \sim \int N(\mathcal{E},\mathbf{q})\, d\mathcal{E}$ can be studied by several techniques including positron annihilation, x ray and γ ray Compton scattering, and high energy inelastic electron scattering. In general, these techniques measure $J(\mathbf{q})$ integrated over one or two momentum directions. A more detailed review of these techniques and their relation to (e,2e) spectroscopy is given by McCarthy and Weigold [114].

An (e,2e) experiment can be defined as an electron ionization experiment in which the kinematics of all of the

electrons is fully determined. The mechanics of (e,2e) scattering is conceptually straightforward. The reaction can be viewed as a "billiard ball" experiment at the energies typical of our spectrometer. A high-energy electron of energy E_0 (typically 25 keV) and momentum P_0 incident on the sample scatters from an electron in the target and ejects this electron from the target. Those events in which the scattered and ejected electrons leave the target with equal energy are detected by coincidence techniques. The precollision binding energy $\mathcal{E} = E_0 - E_s - E_e$ and momentum $\hbar \mathbf{q} = \mathbf{P}_s + \mathbf{P}_e - \mathbf{P}_0$ of the target electron can be determined from the energies and momenta of the two scattered electrons E_s, P_s and E_e, P_e. This is illustrated schematically in Figure I.1.

Our spectrometer consists of an input arm and two output arms positioned at 45° with respect to the incident beam. The input arm contains an electron gun and electron optics to focus the beam onto a thin film target mounted in the target chamber. The two output (e,2e) arms (referred to as A and B) have complimentary electron optics which focus the scattered beam into a Wien filter energy analyzer. Momentum selection is accomplished by a set of limiting apertures and electrostatic deflectors which vary the beam angle on the target. Electrons with the proper

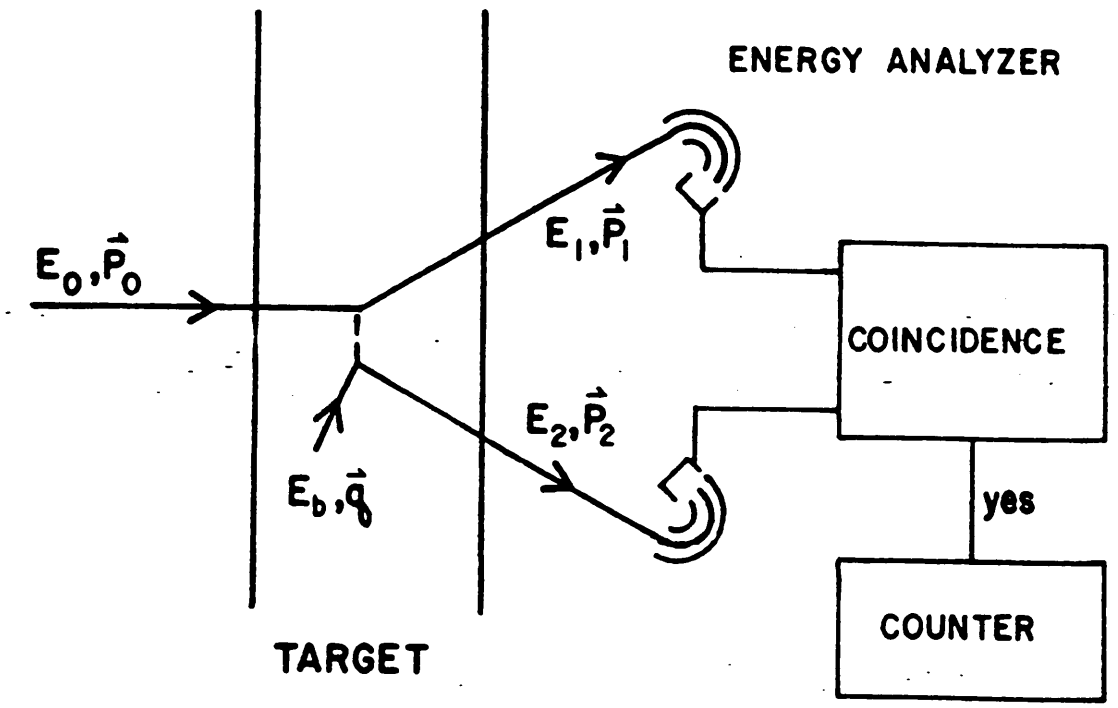

Figure I.1 Schematic representation of (e,2e) scattering.

energy and momentum are detected by electron multipliers and the signals are processed by counting and coincidence electronics.

The spectrometer operates in two modes referred to as the elastic and inelastic modes. Elastically scattered electrons are detected in the elastic mode by holding the (e,2e) arms at the same potential as the input arm. The (e,2e) arms are held at half the input potential in the inelastic mode, therefore the kinetic energy of the detected electrons is approximately half the energy of the incident beam. (e,2e) events are coincidence events measured in the inelastic mode.

Another feature of our spectrometer is a similar output beam arm which is collinear with the input beam arm that provides the capacity to study small-angle electron scattering. This arm is referred to as the (e,e') arm. The spectrometer can function as a high energy electron diffraction (HEED) instrument by measuring small-angle elastically scattered electrons over a range of angles with the (e,e') arm. Electron energy loss spectroscopy (EELS) can be performed by analyzing the energy loss of small-angle inelastically scattered electrons. These features provide important calibration of the spectrometer and can be used to quickly characterize a sample before attempting

the more difficult and time-consuming (e,2e) experiment.

This dissertation can be divided into three major topics. A review of single electron and (e,2e) scattering theory with an emphasis on scattering from solids is given in Section II. The effects of multiple scattering are discussed and a method of deconvoluting these effects from the measured (e,2e) cross section is developed. Next, there is a detailed description of our spectrometer design and operation with particular attention given to the electron optics and voltage distribution. The algorithms and software for computer aided data acquisition and analysis are also outlined, as is error analysis. The techniques employed in the preparation and characterization of extremely thin film samples of a-C and graphite are described. Finally, the data taken for a-C samples are shown and are compared with the results of complimentary experiments and theory for graphite, diamond, and a-C. Some conclusions are drawn regarding amorphous solids and a-C in particular.

II. THEORY OF (e,2e) SCATTERING

There are three important electron scattering processes that are pertinent to (e,2e) spectroscopy which are referred to as elastic, inelastic, and (e,2e) scattering. Inelastic scattering can actually be divided into two regimes, small-angle and large-angle inelastic scattering. The types of scattering are distinguished by the different physical phenomena that are responsible for them. Each of these cross sections can be determined independently by the spectrometer. (e,2e) scattering is actually an inelastic scattering reaction where the kinematics of both the incident and target electrons are fully determined. The measured (e,2e) count rate includes contributions from the true (e,2e) cross section and all other kinematically allowed multiple scattering events. Elastic and inelastic measurements are used to characterize the samples, to calibrate the machine, and in the correction for multiple scattering.

The theory section discusses the physical origins, kinematics, and cross sections of each of these processes and relates them to (e,2e) theory and the operation of our spectrometer. A detailed analysis of the (e,2e) cross section and the approximations involved in its derivation

follows. Some specific examples are used to illustrate the information available from the (e,2e) process. Finally, a theory of multiple scattering is derived and relates the measured cross section to the true (e,2e) cross section.

A. Summary of single electron scattering theory

Elastic scattering is characterized by no energy loss for an incident electron upon scattering. At small angles elastic scattering is primarily a result of coherent Bragg scattering. However, at large angles the diffraction cross section is almost featureless and incoherent scattering becomes dominant. The fundamental process involved in incoherent scattering is Rutherford scattering from the nuclei of the target.

The kinematics of elastic scattering is illustrated in Figure II.1. In incoherent scattering, an incident electron with high energy E_0 and momentum P_0 is scattered from a nucleus with final energy E_s and momentum P_s. A recoil momentum P_r and a small energy E_r are imparted to the nucleus. If the nuclei are considered stationary, approximating $M >> m_e$, then $E_r \approx 0$ and we are left with Rutherford scattering.

In the Born approximation the cross-section for

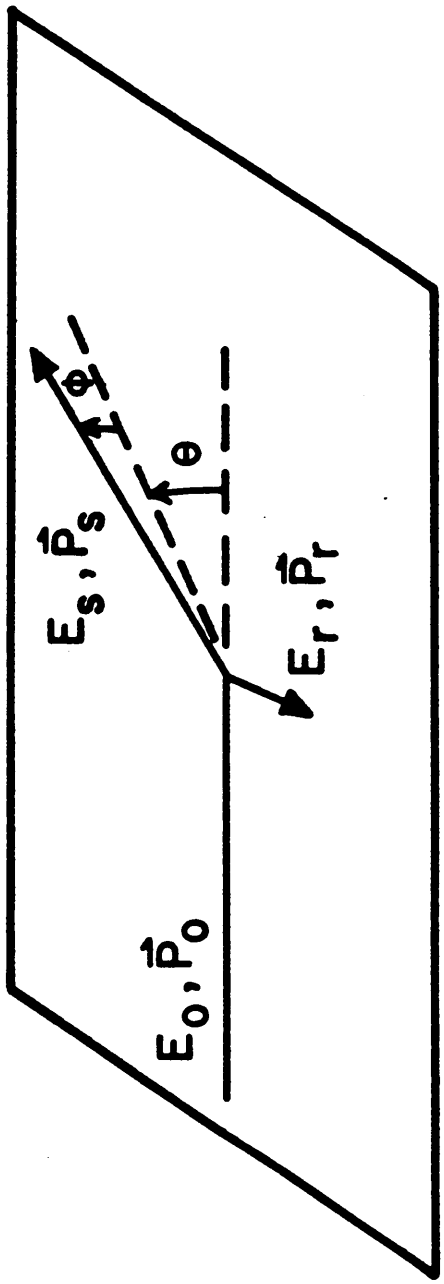

Figure II.1 Kinematics for single electron scattering

Rutherford scattering in the lab frame is given by

$$\left[\frac{d\sigma(\theta,\phi)}{d\Omega}\right]_R = \left(\frac{e^2 m_e Z}{2}\right)^2 \left[P_o \sin\left(\frac{\theta}{2}\right)\right]^{-4} = \left(\frac{e^2 Z}{4}\right)^2 \left[E_o \sin^2\left(\frac{\theta}{2}\right)\right]^{-2} \qquad \text{(II.1)}$$

where Z is the atomic number. In atomic units

$$\left[\frac{d\sigma(\Theta,\Phi)}{d\Omega}\right]_R = \left(\frac{Z}{2}\right)^2 \left[\frac{P_0}{\hbar} \sin\left(\frac{\theta}{2}\right)\right]^{-4} \qquad \text{(II.1a)}$$

measured in square Bohr radii.

The count rate is related to the cross-section by

$$[n]_e = I_o \left(\frac{\rho t A_o}{A}\right) \left[\frac{d\sigma}{d\Omega}\right]_R \Delta\Omega \qquad \text{(II.2)}$$

where I_0 is the incident charge current, ρ, t and A are the target mass density, thickness and atomic weight, A_0 is Avagadro's number, and $\Delta\Omega$ is the solid angle of the detector. For the 45^0 arms the solid angle can be related to the momentum resolution

$$\Delta\Omega \approx \frac{1}{2}\theta_p^2 \approx \left(\frac{\Delta P_o}{P_o}\right)^2 \qquad \text{(II.3)}$$

The elastic count rate then is proportional to the incident current and the target thickness and to the square of the momentum resolution divided by the sixth power of incident momentum. The count rate is independent of azimuthal angle ϕ and depends on the polar angle θ through the Rutherford cross section as illustrated in Figure II.2. For a typical

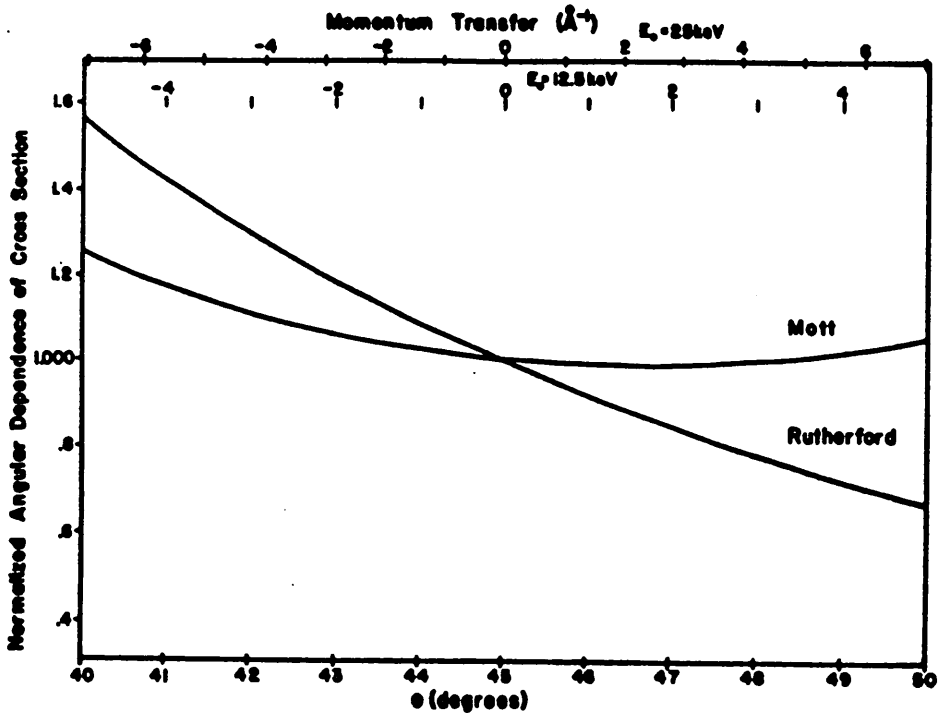

The angular dependence of the Rutherford cross section (curve R; Equation II.1) and the Mott cross section (curve M; Equation II.17) normalized to 1.0 at $\theta = 45^{\circ}$ are plotted versus angle. The alternate scales show momentum transfer at $E_0 = 25$ keV and $E_0 = 12.5$ keV.

Figure II.2 Angular dependence of Rutherford and Mott cross sections.

experiment with a 100 Å thick a-C film the count rate at in the 45^{o} arms is approximately 60 Mhz (see Table VII.1).

In small-angle inelastic scattering, a small momentum coupled with an energy loss is transferred to the target. The kinematics are identical to elastic scattering except that the energy loss is not necessarily zero. Potentially, there are numerous physical processes involved including bulk and surface plasmon creation, intra- and inter-band transitions, atomic excitations, ionizations, thermal diffuse scattering, and radiative losses which occur when the electron enters and leaves the sample. Detailed calculations of the total small-angle inelastic scattering cross section are beyond the scope of this synopsis; the reader is referred to papers by Ritchie [141] and Hattori and Yamada [74] and Sevier's review [151]. Only bulk plasmon creation and quasi-elastic phonon and imperfection scattering make significant direct contributions to the scattering considered here. This is the type of scattering that is measured by electron energy loss spectroscopy (EELS). The (e,e') arm in the elastic mode in our spectrometer acts as an EELS instrument and measures the combined cross sections of these effects. Reviews of the basic theory of EELS are given by Sevier [151] and Fields[59].

It is advantageous to separate small-angle inelastic scattering into elastic and inelastic components. Further, the cross-sections can be separated into products of independent functions of energy loss and momentum transfer. This factorization is reasonable, despite the direct connection between the energy and the component of momentum parallel to the beam axis, because the incident momentum in this direction is much larger than the momentum transfer. It suffices to fix the parallel momentum and consider only the momentum transfer perpendicular to the beam axis. This separation allows direct connection with existing theory and experiments and facilitates the multiple scattering deconvolution [59]. No attempt is made to estimate these absolute cross-sections because only the relative intensities are important to our analysis.

In small-angle elastic scattering momentum is transferred to the target without exciting the electrons. Typically, cross-sections such as Bragg scattering are broadened by quasi-elastic phonon scattering or from imperfections in the sample. The term thermal-diffuse scattering is used to describe multiple scattering background involving a combination of elastic and inelastic small-angle scattering.

The probability for small-angle elastic collisions can

be factored as

$$P_e(\mathcal{E},q) \cong F_e(q_\perp)\ \delta(\mathcal{E})\ \delta(q_\parallel) \qquad \text{(II.4)}$$

The delta-function in energy loss $\mathcal{E}$ results from considering elastic events and the delta-function in parallel momentum transfer $q_\parallel$ is a consequence of the high incident momentum and small scattering angle as discussed above.

The angular (momentum) dependence of small-angle elastic scattering can be described in analogy with the Rutherford cross-section for elastic scattering as

$$\left[\frac{d\sigma}{d\Omega}\right] = \left(\frac{me^2}{2}\right)^2 \left(\frac{1}{[P_o f(\theta)]^2}\right)^2 (Z - f_x)^2$$

$$f(\theta) = \tfrac{1}{2} \sin\left(\frac{\theta}{2}\right) \qquad \text{(II.5)}$$

This can be expressed approximately in the parameterized form

$$F_e(q_\perp) = \frac{G_e}{\left(q_\perp^2 + q_o^2\right)^2} \qquad \text{(II.6)}$$

Measurements of these parameters for a-C are given by Brünger and Menz [25] and for graphite and many other elements by Hartley [78]. Brünger and Menz also empirically determine the value of the small-angle elastic mean free path λ_e over a range of energies.

The probability for small-angle inelastic events can be factored as

$$P_u(\mathcal{E},q) \cong F_u(q_\perp)\, U(\mathcal{E})\, \delta(q_\parallel) \qquad \text{(II.7)}$$

The energy-loss function $U(\mathcal{E})$ for a-C has been studied by Burger and Misell [26] who describe the principle features as a weak lowered loss in the region ~7 eV, a strong, broad loss centered at ~25 eV (FWHM about 40 eV) and a broad loss centered at about 50 eV. The small lowered loss is associated with the π electron oscillations and no attempt is made to incorporate it into the theory used to fit our data. The dominant loss centered at ~25 eV is considered a volume plasma loss involving principally, if not exclusively, the σ-electrons. Burger and Misell state that there is no evidence for surface energy losses. They do cite, however, some limited evidence for such processes as atomic excitation, intra- and inter-band transitions and ionization; these effects are not significant below energy losses of about 200 eV and so no attempt is made to incorporate them into the theory either. This analysis is based on Bohm-Pines plasma oscillation theory [18].

The energy-loss function $U(\mathcal{E})$ is fit to an expression from the dielectric formulation of the total scattering cross-section per unit volume for single scattering of an electron of energy E_0 into scattering angles $0 < \theta < \theta_{max}$ with energy loss $\mathcal{E}$ [127]:

$$\left[\frac{d\sigma}{d\Omega}\right]_u = \frac{-1}{\pi a_o E_o} \ln\left(\frac{\theta_{max}}{\theta_E}\right) \mathrm{Im}\left(\frac{1}{\epsilon(\mathcal{E})}\right) \qquad \text{(II.8)}$$

An expression for $\mathrm{Im}(1/\epsilon(\mathcal{E}))$ from the Drude free-electron gas model of a metal [104] can be used to describe the main energy loss as

$$\left[\frac{d\sigma}{d\Omega}\right]_u \sim -\mathrm{Im}\left(\frac{1}{\epsilon(\mathcal{E})}\right) = \frac{\omega_p^2 \, \tau \, \omega}{(\omega_p^2 - \omega^2)^2 \, \tau^2 + \omega^2} \qquad \text{(II.9)}$$

where ω_p is the plasma frequency and τ is the half-life of the electron plasma excitation (plasmon). In paramaterized form this can be expressed as

$$U(\mathcal{E}) = \left\{ \begin{array}{ll} \dfrac{V_1 \, \mathcal{E}}{(\mathcal{E}^2 - V_2^2)^2 \, V_3 + \mathcal{E}^2} & ; \; \mathcal{E} > 0 \\ 0 & ; \; \mathcal{E} < 0 \end{array} \right\} \qquad \text{(II.10)}$$

There are no mechanisms for gaining energy, therefore $U(\mathcal{E})$ is zero for energy losses less than zero. Burger and Misell [26] fit extensive a-C data to evaluate these parameters which are in good agreement with theoretical values calculated using the Bohm-Pines plasma oscillation theory.

The angular dependence of the differential cross section for volume plasmons has been derived by Ferrell [57] as

$$\frac{d\sigma}{d\Omega} = \left\{ \begin{array}{ll} \dfrac{1}{2\pi a_o n} \dfrac{\theta_E}{\theta_E^2 + \theta^2} & ; \theta < \theta_c \\ 0 & ; \theta > \theta_c \end{array} \right\} \qquad \text{(II.11)}$$

where n is the free electron density, $\theta_E = \hbar \omega_p / 2 E_0$, and $\theta_C = \hbar \omega_p / E_F$. The

maximum scattering angle θ_c is related to the momentum just sufficient to cause an electron at the Fermi energy E_F to make a real transition, absorbing one plasma-quantum of energy $\hbar\omega_p$. As the scattering angle approaches the cut-off angle θ_c, damping effects, primarily due to the transfer of plasmon energy to individual electrons, cause the probability of excitation of a plasmon to fall to zero. In the vicinity of θ_c Equation II.11 must be multiplied by a correction factor to account for damping [58]. In parameterized form this can be expressed in terms of momentum as

$$F_u(q_\perp) = \frac{G_u}{(q_\perp^2 + q_E^2)(q_\perp^2 + q_c^2)} \quad ; q_\perp < q_c \qquad \text{(II.12)}$$

in the limit that $q_E^2 << q_C^2$, that is that $E_0 >> E_F$ [59].

The mean free path λ_i between small-angle inelastic collisions can be calculated by integrating Equation II.11 [57]. Its value is

$$\lambda_i = \frac{a_0}{\theta_E \ln(\theta_c/\theta_E)} \qquad \text{(II.13)}$$

This quantity is of importance in multiple scattering analysis and has been measured by Brünger and Menz [25] for a-C.

The total mean free path λ_t is given by

$$\frac{1}{\lambda_t} = \frac{1}{\lambda_e} + \frac{1}{\lambda_i} \qquad \text{(II.14)}$$

For (e,2e) geometries, the average path length of an electron through a target of thickness T is approximately

$$\bar{T} = \frac{\int_0^T d\tau \; [\tau + 2\sqrt{2}\,(T - \tau)]}{\int_0^T d\tau} = 1.91\ T \qquad \text{(II.15)}$$

and the effective mean free path for the entire target is

$$\bar{\lambda} = \frac{1}{T}\int_0^T d\tau \; [\tau\lambda_0 + 2\sqrt{2}\,(T - \tau)\,\lambda_i] = \frac{\left[\frac{\lambda_0}{2} + \sqrt{2}\,\lambda_i\right]}{1.91} \qquad \text{(II.16)}$$

where λ_0 and λ_i are the total mean free paths of an electron before and after the (e,2e) event respectively.

The elastic and small-angle inelastic count rates can be measured with our spectrometer in the elastic mode. The energy loss can be varied from 0 to ~80 eV by varying the band pass energy of the energy analyzer. In the non-coplanar geometry the spectra can be measured over a range of ϕ -- typically $\pm 5^\circ$ -- about $\phi = 0^\circ$ for $\theta = 0^\circ$ in the (e,e') arm and for $\theta = \pm 45^\circ$ in the (e,2e) arms. In the coplanar geometry the polar angle is fixed at $\phi = 0^\circ$ and measurement can be made over a range of θ about $\theta = 0^\circ$ in the (e,e') arm and about $\theta = 45^\circ$ in the (e,2e) arms. This is equivalent to a momentum range of ± 7 Å^{-1} for an incident energy of 12.5 keV.

Large-angle inelastic scattering has the same kinematics as elastic and small-angle inelastic scattering, but is distinguished from the latter by the much larger momentum transferred to the target. In standard operation of the inelastic mode of our spectrometer P_r is approximately equal to P_s and $E_r \approx E_s$ for electrons detected in the (e,2e) arms. For such high momentum transfer the collision must involve comparable masses, therefore the process involves the incident electron scattering off of a single electron in the target. At high energies where the plane-wave impulse approximation is valid the large-angle inelastic cross-section is the Mott cross-section given by

$$\left[\frac{d\sigma(\theta,\phi)}{d\Omega}\right]_M = \left[\frac{e^2}{4E_o}\right]^2 x$$

$$\left\{4\cos\theta \left[(\sin\theta)^{-4} - (\sin\theta\cos\theta)^{-2} + (\cos\theta)^{-4}\right]\right\} \qquad \text{(II.17)}$$

in the lab frame.

The count rate is related to the cross section by

$$[n]_M = I_o \left(\frac{\rho\ t\ A_o\ Z}{A}\right) \left[\frac{d\sigma}{d\Omega}\right]_M \Delta\Omega \qquad \text{(II.18)}$$

This has the same dependence on target properties, incident energy, and energy resolution as the elastic count rate, but differs with respect to the polar angle as shown in Figure II.2. For a typical experiment with a 100 Å thick a-C film, the Mott cross section at 45^o is

approximately 0.4 MHz, a factor of 150 less than the Rutherford scattering. This assumes that the target electron is stationary and has no binding energy; the cross section becomes almost uniformly spread over several keV when those effects are included and the large-angle inelastic count rate is then about 5000 times smaller than the elastic rate.

Multiple scattering has no significant net effect on the inelastic cross-section. Each electron which undergoes a large-angle inelastic scatter can have one or more quasi-elastic multiple scattering events occur before or after the large-angle event. This results in a convolution of the inelastic cross-section with a multiple scattering broadening. However, the inelastic cross-section is so nearly uniform in the region of $\theta = 45^{o}$ that the convolution hardly modifies the distribution.

Inelastic scattering produces a background of counts in the (e,2e) arms when the machine operates in the inelastic mode. These events satisfy the energy and momentum constraints of the analyzers, but are not coincidence events. It is possible to produce false coincidence events if an independent inelastic event occurs in each arm within a given time interval. The false coincidence background is subtracted from the measured coincidence rate using the coincidence electronics

described in Section IV. These inelastic counts provide an indispensable means of adjusting the tune conditions of the electron optics, since the measured coincidence rates are too low to provide feedback during tuning.

Inelastic scattering is measured with the spectrometer in the inelastic mode. The energy loss can be varied by two independent methods. The band pass energy of the energy analyzer can be varied over a range 0 to ~80 eV or the negative high voltage HV_ can be varied. The band pass energy can be varied manually or under computer control, while the negative high voltage must be adjusted by the operator. The two can operate together to cover a wide range; the negative high voltage provides a course adjustment to the energy loss and the band pass energy acts as a fine adjustment under control of the automated data acquisition system. The momentum transfer can be studied over a range of angle about the beam arm axes, just as in the elastic mode.

B. (e,2e) scattering theory

1. Kinematics

An (e,2e) scattering event can be defined as a single ionization event in which the kinematics of all of the electrons is fully determined. At the high electron kinetic energies involved it is valid to consider "billiard ball" kinematics to first order; such kinematics are shown in Figure II.3

An incident electron with energy E_0 and momentum $P_0(0,\phi)$ is incident on a target. This electron is inelastically scattered off of a target electron with final energy E_s and momentum $P_e(\theta_s,0)$. The ejected target electron has energy E_e and momentum $P_e(\theta_e,0)$. By convention, the z-axis is in the direction of the incident beam axis, the x-axis is in the scattering plane, and the y-axis is out of the scattering plane, throughout this work.

If the kinematics is fully determined then energy and momentum conservation lead to the equations

$$\mathcal{E} = E_0 - E_s - E_e - E_r \qquad \text{(II.19a)}$$

$$\hbar\vec{Q} = P_0 - P_s - P_e \qquad \text{(II.19b)}$$

The binding energy $\mathcal{E}$ is the energy difference between the initial target state and the final ionic state. The momentum transfer $\hbar\vec{Q}$ is the recoil momentum of

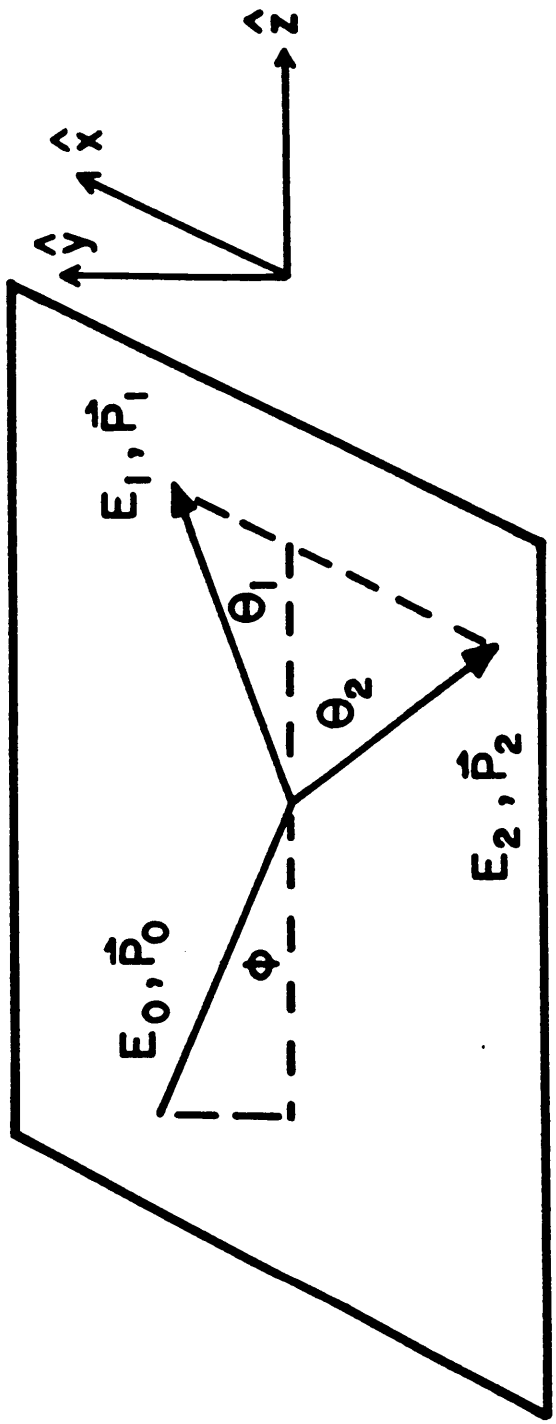

Figure II.3 Kinematics of (e,2e) scattering.

the ion and E_r is the recoil energy. If the incident electron energy is sufficiently high, i.e. $E_0 >> \mathcal{E}$, and the mass of the target is large in comparison with the electron mass, i.e. $M >> m_e$, then the recoil energy $E_r \approx 0$, and the momentum of the target electron prior to collision is given by $\mathbf{q} = -\vec{\mathcal{Q}}$.

There are two major kinematic divisions based on the geometry of the scattering, the symmetric geometry and the asymmetric geometry. The kinematic restrictions that $\theta_s = \theta_e \equiv \theta$ and that $E_s = E_e$ are applied to the symmetric case; these are not required in the asymmetric case. Our experiment and most standard (e,2e) gas experiments utilize the symmetric geometry. A brief review of some types of asymmetric experiments is given at the end of this section. The reader is referred to the review of McCarthy and Wiegold for further details [114].

Symmetric experimental arrangements have several advantages in experiments designed to probe the momentum-space wave function. The two outgoing electrons are indistinguishable, hence the subscripts s and e can be replaced by 1 and 2. The geometry maximizes the momentum transferred to the ejected electron, thus ensuring close electron-electron collisions. Further, if the incident energy is large, both outgoing electrons have high velocities so that the effect of the other electrons can be

largely neglected and the collisions regarded as one between two free electrons. In this geometry the target electron momentum can be expressed as

$$\hbar q_{\parallel} = 2\ P_1 \cos\theta - P_0 \cos\phi \qquad \text{(II.20a)}$$

$$\hbar q_{\perp} = P_0 \sin\phi \qquad \text{(II.20b)}$$

where $q_{\parallel}$ and $q_{\perp}$ are in the $\hat{z}$ and $\hat{y}$ directions respectively. There are two subdivisions within the symmetric geometry, coplanar and non-coplanar.

In the symmetric coplanar geometry all the trajectories lie within the scattering plane, that is $\phi = 0$. Only target electron momentum parallel to the incident beam axis is probed in this arrangement:

$$\hbar q_{\parallel} = 2\ P_1 \cos\theta - P_0 \qquad \text{(II.21a)}$$

Our spectrometer varies the angle θ only a few degrees on either side of 45^0, therefore in the small angle limit of small $\Delta\theta$,

$$\hbar q \approx -P_0\ \Delta\theta \qquad \text{(II.18b)}$$

where $\Delta\theta \equiv \theta - 45^0$ and $P_1 \approx P_0 / \sqrt{2}$.

The symmetric non-coplanar geometry has a variable angle ϕ while θ is kept fixed at $\theta = \theta_0$. The momentum relations for this geometry are

$$\hbar q_{\parallel} = 2\ P_1 \cos\theta_0 - P_0 \cos\phi \qquad \text{(II.22a)}$$

$$\hbar q_{\perp} = P_0 \sin\phi \qquad \text{(II.22b)}$$

In our spectrometer $\theta_0 = 45^0$ and ϕ is varied a few

degrees about 0^{o}. The parallel momentum transfer reduces to zero to first order in the small-angle limit and

$$\hbar q_{\perp} \approx P_0 \phi \qquad \text{(II.23)}$$

There is an advantage to the non-coplanar mode in that the (e,2e) cross section in this geometry depends on the scattering angles only through the square of the momentum-space wave function. In the coplanar mode, the value of the Mott cross-section contribution to the cross-section changes as a function of θ. This effect is illustrated in Figure II.2; it amounts to only a ±5% variation over a range of $\pm 4 \text{Å}^{-1}$ at $E_0 = 25$ keV. This is discussed further in the derivation of the cross section which follows.

All of the data taken to date with our spectrometer have been taken in the symmetric non-coplanar mode. The spectrometer is designed to take data also in the coplanar mode, however this option has not been utilized yet.

2. Cross section

A derivation of the (e,2e) cross-section is quite complex since it is at best a 3-body problem (hydrogen atom) and is a many-body problem for solid targets. There are two approaches taken in addressing the problem. In this section, a crude set of approximations is employed

which arrives at useful results in a straightforward manner. A much more detailed derivation of the (e,2e) scattering amplitude is given in Appendix A. This derivation is more general than is used in practice for (e,2e) calculations in solids, however it provides important insights into the concepts and approximations inherent in the cruder model.

The (e,2e) scattering amplitude M_{if} can be calculated using the plane-wave Born approximation neglecting exchange effects, and using the independent-electron approximation. The incident, scattered, and ejected wave functions are assumed to be plane waves and the orbital wave function of the electron in the target prior to the collision is $\Psi_n(r_2)$. The potential is just the Coulomb interaction between the two electrons. The scattering amplitude is

$$M_{if} = \frac{-\mu}{(2\pi)^4\hbar^2}\int\int d^3r_1\, d^3r_2\, e^{i\mathbf{k}_1\cdot\mathbf{r}_1}\, e^{i\mathbf{k}_2\cdot\mathbf{r}_2}\left(\frac{e^2}{|\mathbf{r}_1-\mathbf{r}_2|}\right) e^{-i\mathbf{k}_0\cdot\mathbf{r}_1}\,\Psi_n(r_2) \tag{II.24}$$

Introducing the expansion

$$\frac{1}{|\mathbf{r}_1-\mathbf{r}_2|} = \frac{1}{2\pi^2}\int\frac{d^3k}{k^2}\, e^{i\mathbf{k}\cdot(\mathbf{r}_1-\mathbf{r}_2)} \tag{II.25}$$

and rearranging terms, Equation II.24 becomes

$$M_{if} = \frac{-2\mu e^2}{(2\pi)^{3/2}\,\hbar^2}\left\{ \int \frac{d^3k}{k^2}\left[\frac{1}{(2\pi)^3}\int d^3r_1\; e^{i(\mathbf{k}+\mathbf{k}_1-\mathbf{k}_0)\cdot\mathbf{r}_1} \right] \right.$$

$$\left. \times \left[\frac{1}{(2\pi)^{3/2}}\int d^3r_2 e^{i(\mathbf{k}_2-\mathbf{k})\cdot\mathbf{r}_2}\,\Psi_n(\mathbf{r}_2) \right] \right\} \quad \text{(II.26)}$$

The separation of the integration in $\mathbf{r}_1$ and $\mathbf{r}_2$ is the equivalent of the factorization approximation, which is exact for the plane-wave approximation. The integral over $\mathbf{r}_1$ provides a delta-function and the subsequent integration over $\mathbf{k}$ yields

$$M_{if} = \left\{ \frac{-m_e e^2}{(2\pi)^{3/2}\hbar^2}\,\frac{1}{|\mathbf{k}_1 - \mathbf{k}_0|} \right\}\,\Phi_n(\mathbf{q})$$

$$\text{where } \mathbf{q} = \mathbf{k}_1 + \mathbf{k}_2 - \mathbf{k}_0 \quad \text{(II.27)}$$

The first term results in the Mott cross-section upon generalizing to include exchange effects. $\Phi_n(\mathbf{q})$ is the momentum wave function, that is the Fourier transform of $\Psi_n(\mathbf{r})$ as defined in Equation A.19. Equation II.27 should be compared with Equation A.21 in conjunction with Equations A.17 and A.19.

The approximations used in this derivation must be justified for solid targets. For clarity the approximations can be grouped in three main categories under the names impulse, plane-wave, and independent-electron approximations. The reader is referred to Appendix A for more details.

Perhaps the most compelling evidence for their verisimilitude is the spectacular agreement of many of the

(e,2e) gas experiments with theory. As an example, the agreement between measurements for atomic hydrogen and the exact calculations for its momentum-space wave functions is exact within small experimental errors [109]. The cross section was calculated in the plane-wave impulse approximation and measurements were taken with the non-coplanar symmetric technique at incident energies of 400 to 1200 eV. This provides strong evidence for the validity of the plane-wave approximation, especially at incident energies of tens of keV, but does not test the impulse and single-electron approximations appreciably. Camillon et al [29] have done a detailed study on the validity of the eikonal approximation and the distorted-wave impulse approximation as a function of E_0 and $\mathbf{q}$ for He. They conclude that in these experiments the eikonal approximation is valid for $E_0 \gtrsim 800$ eV and $\mathbf{q} < 1$ $Å^{-1}$ and suggest that there may be a limit to the impulse approximation for $\theta_1 + \theta_2 \lesssim 70^\circ$. Many other gas experiments on more complex atoms and molecules support the plane-wave and impulse approximations, particularly for $E_0 \gtrsim 1$ keV [114].

In addition to the three major approximations there are a few initial approximations which are rather easily justified. Relativistic effects are neglected; this has

its most important implications with regard to the treatment of electron spin effects. The highest velocities involved in this experiment (E_0 = 25 keV) are about .3 c; less than 4% error in the momentum results from neglect of relativistic effects. At energies above ~50 keV or for higher precision work, these effects may need to be considered. Assuming an infinite target mass is satisfied trivially for a solid target and is a very good approximation even for the lightest atoms. This is equivalent to neglecting the center-of-mass motion of the target atoms caused by the collision. We assume that the target is in the ground state which is equivalent to ignoring finite-temperature effects. The density of lattice vibrations and excited-state electrons is minimal at room temperature; the few electrons in perturbed states will produce an erroneous background which is well below detection limits since kT is much less than our energy resolution.

The impulse approximation is the most difficult approximation to characterize and justify. In simplistic terms, the impulse approximation hypothesizes that the electron collision happens in such a way that it is independent of all of the other electrons and atoms in the target. The collision must happen fast enough that the ion does not relax in response to the ionization before

both scattered electrons are out of effective range of its potential. The higher the electron velocities, the less time the electrons are in close proximity to the ion. The high incident energy, in our experiments typically at least 20 times that for gas experiments, reduces the time in proximity. The electrons must also collide at close range, which results in high momentum transfer. The symmetric geometry with $\theta \approx 45^{o}$ provides maximum momentum transfer; momentum transfer is typically $>50 \text{Å}^{-1}$ in our spectrometer.

A reasonable criterion may be that the impact parameter should be much less than the electron separation in the target state [13']. The separation distance of valence electrons is in general significantly larger than that of closely bound atomic orbitals. The extended electron states in a solid should provide a screening effect which limits the range of the ion potential. In addition, the response time of the ion should be inversely related to the energy imparted to the ion. Valence electron energies on the order of tens of eV, are comparable to H ionization energies rather than to those of more complex atoms studied [176] which have much larger binding energies. Taken together, the relatively long ion response time and the short time of proximity of the electrons seem ample justification for the impulse

approximation, in light of its validity in (e,2e) gas experiments.

The plane-wave approximation depends on the momenta of the electrons involved. Our kinematics is optimum for the highest scattered momenta in both arms. McCarthy and Weigold review this approximation for gases of both atoms and molecules [114]. They conclude that the plane-wave approximation is at least adequate for incident energies above 1200 eV for their examples. The energies we employ are significantly higher, so this approximation seems reasonable despite the uncertainties introduced by a solid target. The factorization employed is exact in the eikonal approximation, therefore its criteria are less demanding than the plane-wave approximation. Early work on (e,2e) in solids measured the angular correlations of oxygen 1s core electrons [30] and 1s [30,99] and unresolved n=2 [99] bands in carbon. Their results, over a limited region of q space and at low resolution, agreed with calculations based on the plane wave approximation. All of this work was done at incident energies below 10 keV.

The independent-electron approximation is a familiar one in solid state physics and has enjoyed widespread success. Successful application is most dependent on a careful choice of the basis state used in the expansion of

the target electron wave function. Kzasilnikova and Persiatseva's measurements on oxygen and carbon 1s orbitals in solids were in agreement with calculations based on either Slater determinants or Hartree-Fock orbitals [99]. Camillon et al found agreement with calculations based on both Roothaan and minimal-basis-set wave functions [30].

In practice, most solid state calculations are carried out using the plane-wave Born approximation. The requirements for this approximation are extensions of the impulse approximation and the eikonal approximation requiring large incident and exit speeds and large incident and exit kinetic energies. Glassgold and Ialongo [69] look at this for one- and two-electron atomic systems; Vriens [171] extends this discussion somewhat. The only certain test of this crude theory for solids will be comparison of data with theoretical calculations for a well understood system such as graphite.

The cross section is of course proportional to the square of M_{if} and is given by

$$\frac{d\sigma}{d\Omega_1 d\Omega_2 dE_1 dE_2} = \frac{mP_2}{\hbar^3}\left(\frac{d\sigma}{d\Omega_1}\right)_M \left|F_{if}(\mathbf{q}-\mathbf{k}_1+\mathbf{k}_2-\mathbf{k}_0)\right|^2 \delta(\mathcal{E}+E_1+E_2-E_0) \quad \text{(II.28)}$$

where use is made of Equation A.21. The delta function involving $\mathcal{E}$ determines the binding energy from the measured quantities E_0 and $E_1 + E_2$ rather than determining E_1 from E_2. This determines which bands

will be included in the sum over n' in Equation II.37. The cross section can be reduced by one degree of freedom by integrating over the energy shell for $E_2 = P_2/2m_e$: Levin et al [107] show that this results in

$$\frac{d\sigma}{d\Omega_1 d\Omega_2 dE_1} = \frac{mP_2}{\hbar^3}\left(\frac{d\sigma}{d\Omega}\right)_M \left|F_{if}(q)\right|^2 \left[\, 1 - \frac{\mathbf{k}_2 \cdot \vec{\nabla}_{\mathbf{k}} \mathcal{E}(\mathbf{k})}{2E_2} \,\right]^{-1} \qquad \text{(II.29)}$$

Here, $\mathbf{k} = \mathbf{k}_2 - \mathbf{q}$, the momentum transferred to the ejected electron. The count rate is given by

$$N(\mathcal{E},q) = \left[\, I_0 \left(\frac{\rho t A_0}{A}\right) n_v \,\right] \frac{d\sigma}{d\Omega_1 d\Omega_2 dE_1} \Delta\Omega_1 \, \Delta\Omega_2 \, \Delta E_1 \qquad \text{(II.30)}$$

where n_v is the number of electrons in an atom which participate, i.e. the number ofvalence electrons. A rough guide for the cross section dependence on important experimental quantities can be obtained by using the approximation that: 1) $E_0 \approx 2E_1 = 2E_2$; 2) $\Delta P_1 \approx \sqrt{2}\,\Delta P_0$; 3) the gradient term in Equation II.27 is negligible. The effective detector angle is then

$$\Delta\Omega_1 = \left(\frac{\Delta P_1}{P_1}\right)^2 = \frac{\frac{1}{3}\,\Delta q^2}{m\,E_0} \qquad \text{(II.31)}$$

where the total angular resolution (see Section III) is

$$\Delta q^2 = \Delta P_0^{\,2} + \Delta P_1^{\,2} + \Delta P_2^{\,2} = P_0^{\,2}(\theta_{p_0}^{\,2} + \theta_{p_1}^{\,2}) \qquad \text{(II.32)}$$

Recalling that the Mott cross section is inversely proportional to E_0^2, we arrive at the result

$$N \sim I_0 \left(\frac{\rho t}{A}\right) (\Delta q)^4 \, \frac{\Delta E}{E_0^{7/2}} \, \left|F_{1j}(q)\right|^2 \qquad \text{(II.33)}$$

3. *Specific examples*

As a qualitative illustration of what the (e,2e) cross section measures let us consider two simple cases, i.e. scattering from a free electron and from a simple atomic orbital.

For a simple atomic orbital the energy is a constant, E_a and the allowed momentum extends over a finite range. The form factor is simply equal to the momentum space wave function. The cross section then is non-zero only for $\mathcal{E} = E_a$ and its amplitude is modulated in the momentum direction by the square of the momentum wave function. Figure II.4 illustrates a typical distribution for a 1s orbital with a maximum at q = 0. The nth s orbital will have n maxima in **q**. The nth p orbital would have a minimum at q = 0 and have n maxima.

The form factor for a free electron with momentum $\mathbf{k}_e$ is

$$F_{\mathbf{k}_e}(\mathbf{q}) = (2\pi)^{3/2}\,\delta(\mathbf{k}_e-\mathbf{q}) \qquad \text{(II.34)}$$

Therefore, the cross section is a constant amplitude for all values **q** which satisfy the dispersion relation $\mathcal{E}(\mathbf{q}) = \hbar^2 q^2 / 2 m_e$ and will be zero for all other combinations of $\mathcal{E}$ and **k**. This produces a parabolic cross section of constant height as shown in Figure II.4. Of course the delta function distribution is

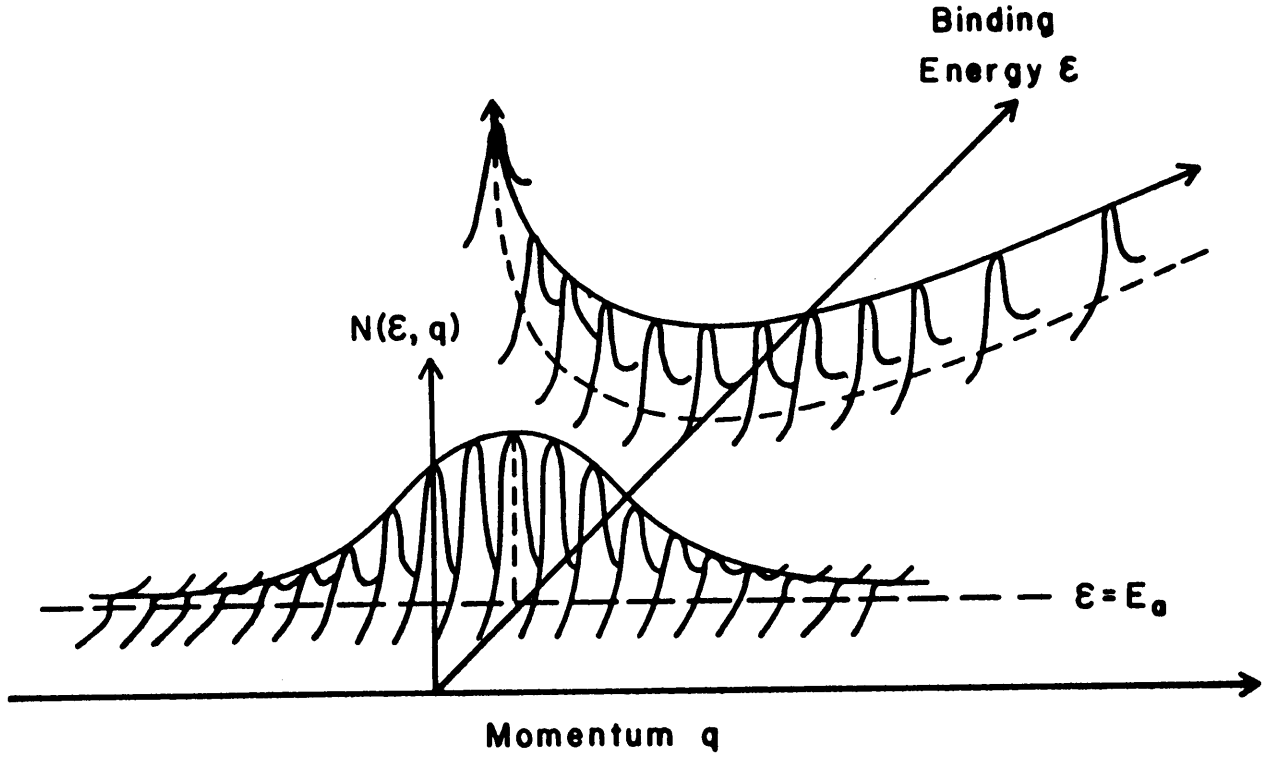

Figure II.4 Simple examples of the (e,2e) cross section.

The upper curve illustrates a free electron distribution while the lower curve illustrates a typical is atomic orbital distribution. The height of the curve is shown with solid lines, the projection on the E,q plane with dashed lines, and the instrumental width by the Gaussian curves.

broadened by instrumental effects.

Let us now turn to the calculations for the (e,2e) cross section of solids. There are two simple descriptions of electrons in solid which we can discuss, the nearly-free electron which models metallic valence electrons and the tight-binding description which models more tightly bound, atomic-like orbitals for core and some valence electrons. The fortuitous choice of the preceding two examples already allows qualitative understanding of the results.

Let us start with the tight binding case and begin by considering the problem of a single crystal target. The expansion for the single-particle tight-binding wave function (with crystal-momentum $\mathbf{k}$ in a band n) can be written in terms of a Bloch sum of atomic wave functions ψ_n as

$$\Psi_{n,\mathbf{k}}(\mathbf{r}) = \frac{1}{\sqrt{N}} \sum_{\mathbf{R}} e^{i\mathbf{k}\cdot\mathbf{R}} \psi_n(\mathbf{r}-\mathbf{R}) \qquad \text{(II.35)}$$

where N is the number of atoms in the crystal and the sum is over all the crystal-lattice sites. If we introduce this expansion for $\Psi_{n,\mathbf{k}}(\mathbf{r})$ into the equation for the form factor, Equation A.19 we get

$$F_{ij}(\mathbf{q}) \equiv F_{\mathbf{kn}}(\mathbf{q}) = \frac{1}{\sqrt{N}(2\pi)^{3/2}} \sum_{\mathbf{R}} \int d^3r_2 \; \psi_n(\mathbf{r}_2-\mathbf{R}) \; e^{i\mathbf{k}\cdot\mathbf{R}} \; e^{i\mathbf{q}\cdot(\mathbf{r}_2-\mathbf{R})} \qquad \text{(II.36)}$$

and the square of the form factor is

$$\left|F_{k,n}(q)\right|^2 = \sqrt{N} \sum_{G,n'} \delta_{q,k+G} \left|\Phi_{n',k}(k+G)\right|^2 \qquad \text{(II.37)}$$

The wave function $\Phi_{n',k}(k+G)$ is the Fourier transform of $\Psi_{n,k}(r)$ and G is a reciprocal lattice vector. It should be noted that we measure $\sum_{k} |F_{k,n}(q)|^2 \, \delta(\mathcal{E}-\mathcal{E}_n(k))$.

The summation over n' is over bands which are close to n where either there is a degeneracy at a point k in the first Brillouin zone or a near degeneracy where instrumental resolution allows mixing of the bands. The form factor $F_{k,n}(q)$ will be non-zero at a given binding energy $\mathcal{E}$ for some momenta q, provided that these q satisfy the dispersion relation

$$\mathcal{E} = \mathcal{E}_n(k) = \mathcal{E}_n(q-G) = E_0 - E_1 - E_2 \qquad \text{(II.38)}$$

Restricting measurement of q to within the first Brillouin zone (i.e., G=0), there will be at most one non-zero form factor for a given q within a single band. In essence, the form factor maps out the dispersion curve $\mathcal{E}_n(k)$ in the first Brillouin zone. Outside the first Brillouin zone $F_{k,n}(q)$ is non-zero for $G \neq 0$ as well. This analysis is very complex if q is not in the direction of one of the reciprocal lattice vectors, G_1. If q is along $\hat{G}_1$ then the form factor is non-zero for a series of equally spaced momenta

$$\mathbf{q} = \mathbf{k} + m\mathbf{G} \; ; \qquad m = 0,1,2... \tag{II.39}$$

at a given energy $\mathcal{E}_n(\mathbf{k})$. The magnitude of $F_{\mathbf{k},n}(\mathbf{q})$ depends on the magnitude of the momentum-space wave function $\Phi_{\mathbf{k},n}$. Since $\Phi_{\mathbf{k},n}$ rapidly goes to zero for large momentum, the form factor will vanish beyond only a few Brillouin zones. The amplitude of the form factor measures the probability of a given state with energy $\mathcal{E}$ and momentum q, therefore the count rate can be interpreted as related to a two-dimensional density of states $N(\mathcal{E}(\mathbf{k}),\mathbf{k})$ within the first Brillouin zone. Near the zone boundary there is a dip in form factor. At the zone boundary the wave function has the form

$$\phi = \frac{1}{\sqrt{2}} \left[|\mathbf{k}\rangle \pm |-\mathbf{k}\rangle \right] \tag{II.40}$$

Since the form factor is a function of momentum $\mathbf{q}$, not crystal-momentum, only one of these states contributes to the form factor which falls to half its value at the boundary. The width of the dip is dependent on the width of the region of mixing of states which is given by

$$\Delta k_n \approx \frac{V(G)}{E_n} k_n \tag{II.41}$$

where k_n and E_n are the momentum and energy at the zone boundary and V(G) is the matrix element which causes the mixing of the two states in Equation II.40.

For a polycrystalline sample the form factor is

averaged over all directions and therefore is approximately constant for **q** up to the Fermi momentum, i.e. the dips will be smoothed out. For highly anisotropic materials, however, the form factor should fall off more gradually and approach zero as **q** approaches its maximum value on the Fermi surface.

The case of nearly-free electrons is more nearly the same as its simple counterpart example. The form factor is given by

$$F_{\mathbf{k}}(\mathbf{q}) = \sqrt{\frac{(2\pi)^3}{NV}}\,\delta(\mathbf{q}-\mathbf{k}) \qquad \text{(II.42)}$$

where V is the crystal volume and the dispersion relation is

$$\epsilon(\mathbf{k}) = \epsilon(0) + \frac{(\hbar k)^2}{2m_{eff}} \qquad \text{(II.43)}$$

where m_{eff} is the effective mass. The gradient term in Equation II.29 is typically very small so the cross section reduces to

$$\frac{d\sigma}{d\Omega_1 d\Omega_2 dE_1} = \frac{mP_2}{\hbar^3}\left(\frac{d\sigma}{d\Omega_1}\right)_M 2\,n\,V\,\delta_{\mathbf{k},\mathbf{q}} \qquad \text{(II.44)}$$

where n is the number of valence electrons per unit volume of the crystal.

The distribution will extend up to the Fermi energy and will be zero above it. There will be dips in the distribution at the zone boundaries for the crystal case as described above.

There is an interesting discussion of the (e,2e) cross section for the hybrid s-d orbitals of Cu given by Levin et al [107]. They present the s-band electrons as nearly free electrons modeled by an orthogonalized plane-wave method and the d-band electrons modeled by the tight-binding scheme. A more simple example of hybridization for the N_2 molecule is discussed by Neudachin et al who also include some discussion for solid Al and the ionic crystal KCl [124].

Since the cross section depends on the momentum **q** of the electron in the target and not the crystal momentum **k** there is no reason why the spectral momentum density cannot be mapped out for amorphous solids as well. The only difficulty is interpretation of the results. There can be no measure of the dispersion curve $\mathcal{E}(\mathbf{k})$ for amorphous solids because **k** is not a good quantum number for them. The theory of band structure for crystalline solids rest firmly on the assumption of crystal translational symmetry, therefore there is no simple justification for the presence of band structure for amorphous solids. However, physical intuition would suggest that amorphous solids must retain at least some vestige of this fundamental property of crystalline solids, which they resemble in so many ways.

Ziman has proposed a model for the valence bands in an

amorphous material based on trial wave functions which are constructed out of linear combinations of bond orbitals (LCBO) [193]. The model is quite similar to the tight-binding crystal calculations based on linear combinations of atomic orbitals (LCAO) and has a similarly straightforward interpretation for the (e,2e) cross section. The expected nature of the band structure of amorphous materials will be taken up in Section VIII on the interpretation of our a-C spectrum.

4. Relation of measured cross section to (e,2e) cross section

The measured scattering cross section of the spectrometer is closely related to the (e,2e) cross sections, but it is broadened and distorted by several factors including inelastic background, instrumental broadening, and multiple scattering. Through data analysis, most of these effects can be deconvoluted and a reasonable estimate of the spectral momentum density can be extracted from the data. First we discuss the relation of the measured cross section to the (e,2e) cross section and the physical processes involved in the broadening. Then, a formalism is outlined and derivations of the general

formulas for deconvolution are given. Appendix B contains a derivation of the scattering function and relates the multiple scattering to the quasi-elastic functions discussed in Section II.A. The details of the numerical analysis technique used and an outline of the error analysis are outlined in Appendix F. Specific examples of applications of these techniques are found in Section VIII.

Much of the theory developed here is based on work by Fields on inelastic electron scattering [59]. The paper by Jones and Ritter develops this approach for (e,2e) scattering [90].

The corrections made to the measured cross section can be separated into three categories: inelastic background, instrumental broadening, and multiple scattering. The background analysis is fairly straightforward and can be accomplished by algebraic manipulations of the data. This is described in Section IV. Corrections for instrumental broadening and multiple scattering are much more complicated. The analysis of these two effects can be performed simultaneously using deconvolution techniques and Fourier analysis. Multiple scattering in (e,2e) scattering is caused by the processes referred to as quasi-elastic scattering in Section II.A.

The kinematics of an ideal (e,2e) event were discussed in Section III.B and are shown schematically in Figure

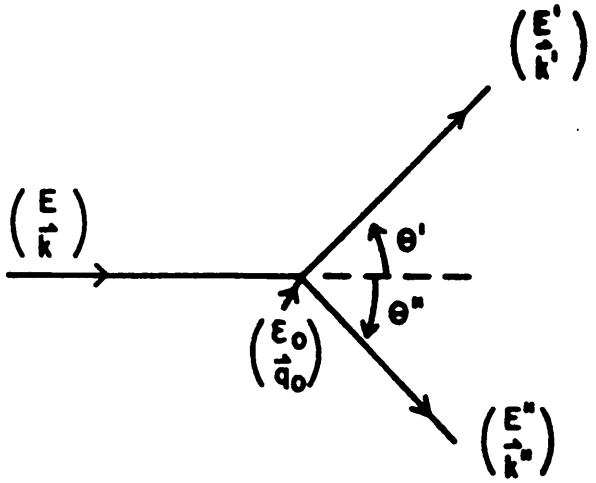

a. Kinematic diagram of an ideal (e,2e) event. An incident electron of energy E and momentum k, scatters with large energy-momentum transfer off an electron in the target whose energy and momentum prior to the interaction was ε_0 and q_0. The two electrons emerge with energies E', E", and momenta k', k".

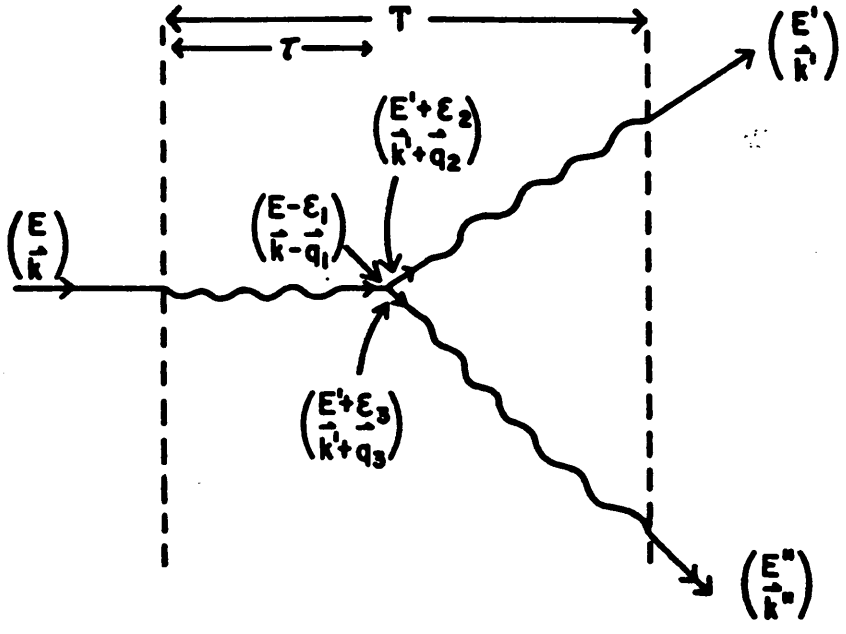

b. Diagram of (e,2e) scattering in a film of thickness T, which includes multiple scattering effects. The energy and momentum of each electron immediately before or after the (e,2e) event is shown in parentheses.

Figure II.5 Kinematics of (e,2e) Multiple Scattering.

II.5a. A more realistic picture of the scattering is illustrated in Figure II.5b. The incident electron enters a target of thickness T and travels a distance τ before the (e,2e) event. The electron loses an energy $\mathcal{E}_1$ and transfers a momentum $\mathbf{q}_1$ to the target in traversing this distance due to small energy-momentum transfer collisions with the target. At some infinitesimal distance before the (e,2e) event the incoming electron has an energy $E - \mathcal{E}_1$ and momentum $\mathbf{k} - \mathbf{q}_1$. This electron undergoes an ideal (e,2e) event and at an infinitesimal distance afterwards, the two outgoing electrons have energies $(E' + \mathcal{E}_2)$, $(E'' + \mathcal{E}_3)$ and momenta $(\mathbf{k}' + \mathbf{q}_2)$, $(\mathbf{k}'' + \mathbf{q}_3)$. The two electrons lose energies $\mathcal{E}_2, \mathcal{E}_3$, and transfer momenta $\mathbf{q}_2$, $\mathbf{q}_3$ respectively as they traverse the target and exit the target with energies E', E" and momenta $\mathbf{k}', \mathbf{k}''$. Furthermore, there is an uncertainty in the measured values E, $\mathbf{k}$, E', $\mathbf{k}'$, E", $\mathbf{k}''$ due to the non-ideal resolution of the beam source and the analyzers.

The measured cross section $\mathbf{R}'(E, \mathbf{k}, E', \mathbf{k}', E'', \mathbf{k}'')$ is related to the ideal (e,2e) cross section $\mathcal{R}'(E-\mathcal{E}_1, \mathbf{k}-\mathbf{q}_1, E'+\mathcal{E}_2, \mathbf{k}'+\mathbf{q}_2, E''+\mathcal{E}_3, \mathbf{k}''+\mathbf{q}_3)$ with a measure $dE'\ d^3k'\ dE''\ d^3k''\ d\tau$ by

$$\mathcal{R}'(E,\mathbf{k},E',\mathbf{k}',E'',\mathbf{k}'') = \int_0^T d\tau \int d^3q_1\, d^3q_2\, d^3q_3 \int d\epsilon_1\, d\epsilon_2\, d\epsilon_3$$

$$\times \left\{ \frac{d^4\vec{\mathcal{P}}}{d^3q_1\, d\epsilon_1}(\epsilon_1,q_1;E,\tau) \cdot \mathcal{R}'(E-\epsilon_1,\mathbf{k}-\mathbf{q}_1,E'+\epsilon_2,\mathbf{k}'+\mathbf{q}_2,E''+\epsilon_3,\mathbf{k}''+\mathbf{q}_3) \right.$$

$$\left. \times \frac{d^4\vec{\mathcal{P}}'}{d^3q_2\, d\epsilon_2}(\epsilon_2,q_2;E'+\epsilon_2,T') \frac{d^4\vec{\mathcal{P}}''}{d^3q_3\, d\epsilon_3}(\epsilon_3,q_3;E'+\epsilon_2,T'') \right\} \quad \text{(II.45)}$$

The effects on the incident beam of smearing due to multiple scattering and spectrometer resolution are contained in the function $\mathcal{P}$: the functions $\mathcal{P}'$ and $\mathcal{P}''$ are similar functions for the two scattered beams. T' and T" are the path lengths of the electrons after the (e,2e) collision, where

$$T' = \frac{T - \tau}{\hat{\mathbf{k}}' \cdot \hat{\mathbf{k}}} \qquad \text{(II.46)}$$

$$T'' = \frac{T - \tau}{\hat{\mathbf{k}}'' \cdot \hat{\mathbf{k}}}$$

These are approximate relations, since the path lengths are actually longer due to multiple scattering; this approximation will be discussed further below.

The kinematics of the (e,2e) collision and the geometry of the spectrometer actually limit these cross sections to functions of four variables. The input energy and momentum are independent variables. In terms of these variables the kinematic relations from Section II.B require that

$$E + \epsilon_0 = E' + E'' \qquad \text{(II.47a)}$$

$$\mathbf{k} + \mathbf{q}_0 = \mathbf{k}' + \mathbf{k}'' \qquad \text{(II.47b)}$$

and the spectrometer geometry requires that

$$E' = E'' \ (\Rightarrow |\mathbf{k}'| = |\mathbf{k}''|)$$

$$k_\theta' = -k_\theta''$$

$$k_\phi' = k_\phi'' \qquad \text{(II.48)}$$

since the arms are placed symmetrically about the spectrometer axis. Therefore, the cross sections may be written in terms of the variables $E_0 \equiv -\mathcal{E}_0$, and $\mathbf{k}_0 \equiv -\mathbf{q}_0$ as

$$R(E_0,\mathbf{k}_0) = R'\left[E,\mathbf{k},\frac{E-E_0}{2},\mathbf{k}',\frac{E-E_0}{2},\mathbf{k}''\right] \qquad \text{(II.49)}$$

There is an approximation in applying these conditions since the finite resolution of the spectrometer allows uncertainties in the measured quantities. These approximations are valid since the energies E, E', E'' are on the order of keV and the scattering angles are near 45°, while the uncertainties are much smaller, on the order of 5 eV and 0.2 milliradians.

The same approximations can also be used to simplify the $\mathcal{P}$ functions. The $\mathcal{P}$ functions vary slowly with electron energy, so the approximations

$$\epsilon_2 \ll E'$$

$$\epsilon_3 \ll E'' \qquad \text{(II.50)}$$

allow the substitution of E' for $E'+\mathcal{E}_2$ as an argument of $\mathcal{P}'$ in Equation II.45 (likewise for $\mathcal{P}''$). Further, the approximations

$$\epsilon_1 \ll E$$

$$\epsilon_0 \ll E, E', E''$$

$$\hat{k}' \cdot \hat{k} = \hat{k}'' \cdot \hat{k} \qquad \text{(II.51)}$$

allow E/2 to be substituted for E' and E" as arguments of $\mathcal{P}'$ and $\mathcal{P}''$, respectively.

The increase in the electron path length due to multiple scattering is negligible if the momentum transfer for each scattering is small and only a small number of multiple scatterings are considered in the analysis. The approximation in Equation II.51 implies that T' = T".

We can now rewrite Equation II.45 with the new functions $\mathbf{R}$ and $\mathfrak{R}$ including the approximations to the arguments of the $\mathcal{P}$-functions:

$$\mathbf{R}(\epsilon_o,\mathbf{k}_o) = \int_0^T d\tau \int d^3q_1\, d^3q_2\, d^3q_3 \int d\epsilon_1\, d\epsilon_2\, d\epsilon_3$$

$$\times \left\{ \frac{d^4\vec{\mathcal{P}}}{d^3q_1\, d\epsilon_1}(\epsilon_1,\mathbf{q}_1;E,\tau) \cdot \mathfrak{R}(E_o-\epsilon_1-\epsilon_2-\epsilon_3,\mathbf{k}_0-\mathbf{q}_1-\mathbf{q}_1-\mathbf{q}_3) \right.$$

$$\left. \times \frac{d^4\vec{\mathcal{P}}'}{d^3q_2\, d\epsilon_2}\left(\epsilon_2,\mathbf{q}_2;\frac{E}{2},T'\right) \frac{d^4\vec{\mathcal{P}}''}{d^3q_3\, d\epsilon_3}\left(\epsilon_3,\mathbf{q}_3;\frac{E}{2},T'\right) \right\} \qquad \text{(II.52)}$$

By a change of variables,

$$\epsilon \equiv \epsilon_1' = \epsilon_1 + \epsilon_2 + \epsilon_3 \qquad \mathbf{q} \equiv \mathbf{q}_1' = \mathbf{q}_1 + \mathbf{q}_2 + \mathbf{q}_3$$

$$\epsilon_2' = \epsilon_2 + \epsilon_3 \qquad \mathbf{q}_2' = \mathbf{q}_2 + \mathbf{q}_3$$

$$\epsilon_3' = \epsilon_3 \qquad \mathbf{q}_3' = \mathbf{q}_3 \qquad \text{(II.53)}$$

Equation II.52 takes the form of a convolution between $\mathfrak{R}$ and the $\mathcal{P}$ functions and can be written in terms of a

single smearing function $\mathcal{S}(\mathcal{E},\mathbf{q};E,T)$ as

$$R(E_0,\mathbf{k}_0) = \int d^3q \int d\epsilon \left\{ \mathcal{R}(E_0-\epsilon,\mathbf{k}_0-\mathbf{q})\ \mathcal{S}(\epsilon,\mathbf{q};E,T) \right\}$$

$$\text{where } \mathcal{S}(\epsilon,\mathbf{q};E,T) = \int_0^T d\tau \int d^3q_2' \ d^3q_3' \int d\epsilon_2' d\epsilon_3' \left\{ \frac{d^4\vec{\mathcal{P}}}{d^3q\ d\epsilon}(\epsilon-\epsilon_2',\mathbf{q}-\mathbf{q}_2') \right.$$

$$\left. \times \frac{d^4\vec{\mathcal{P}}'}{d^3q_2'\ d\epsilon_2'}(\epsilon_2'-\epsilon_3',\mathbf{q}_2'-\mathbf{q}_3') \ \frac{d^4\vec{\mathcal{P}}''}{d^3q_3' d\epsilon_3'}(\epsilon_3',\mathbf{q}_3') \right\} \quad \text{(II.54a)}$$

or in the more compact convolution notation

$$R(E_0,\mathbf{k}_0) = \mathcal{R} \otimes \mathcal{S}(\epsilon,\mathbf{q};E,T)$$

$$\text{where } \mathcal{S}(\epsilon,\mathbf{q};E,T) = \int_0^T d\tau \left\{ \frac{d^4\vec{\mathcal{P}}}{d^3q\ d\epsilon} \otimes \frac{d^4\vec{\mathcal{P}}'}{d^3q_2'\ d\epsilon_2'} \otimes \frac{d^4\vec{\mathcal{P}}''}{d^3q_3'\ d\epsilon_3'} \right\}$$

(II.54b)

Two problems remain in the deconvolution. Equation II.54 must be inverted so that $\mathcal{R}$ can be calculated from the measured cross section and the smearing function. First, however, the smearing function must be evaluated. This long, but very important calculation is performed in Appendix B based on the work by Jones and Ritter [90]. There, an analytic expression for the Fourier transform $\mathcal{T}$ of $\mathcal{S}$ is evaluated in terms of the quasi-elastic cross sections discussed in Section II.A and Gaussian instrumental broadening functions. The Fourier transform of the smearing function $\mathcal{T}$ can be evaluated in terms of eleven experimentally determined parameters: $a_{\mathcal{E}}$, a_x, a_y, $b_{\mathcal{E}}$, b_x, b_y, q_0, q_E, q_C, V_2 and V_3 by combining Equations B.6, B.7, and B.13. This can be

inverted using standard Fast Fourier Transform (FFT) numerical techniques to give an expression for the smearing function $\mathcal{S}$.

The whole purpose of this analysis is to extract the (e,2e) cross section from Equation II.54. There are many well established numerical techniques for performing this deconvolution (see for example Reference 31). Two approaches which we have used in the deconvolution of our data are discussed in Appendix F. Further details can be found in Jones and Ritter [90].

III. SPECTROMETER DESIGN

A. General Description

The spectrometer constructed at VPI is a prototype machine for the investigation of (e,2e) spectroscopy in solids. It has much in common with other electron spectrometers and incorporates many components used on such machines, in particular atomic and molecular (e,2e) spectrometers [3,30,114] and inelastic electron energy loss spectrometers [67,142]. In fact, almost all of the apparatus used are based on existing designs and were chosen to fit the specific needs of this experiment.

All electron spectrometers share four basic parts: an electron source, a detector, an analyzer, and an electron optics system to link these together.

Figure III.1 shows a block diagram of our spectrometer. The ultra-high vacuum chamber includes a target chamber and four beam arms which house these basic parts. The beam arms all lie in the scattering plane with the (e,e') arm colinear with the input arm and the two (e,2e) arms fixed at 45^{o} with respect to this axis. Table III.1 lists some of the operation parameters for our spectrometer and compares them to previous work by others in the field.

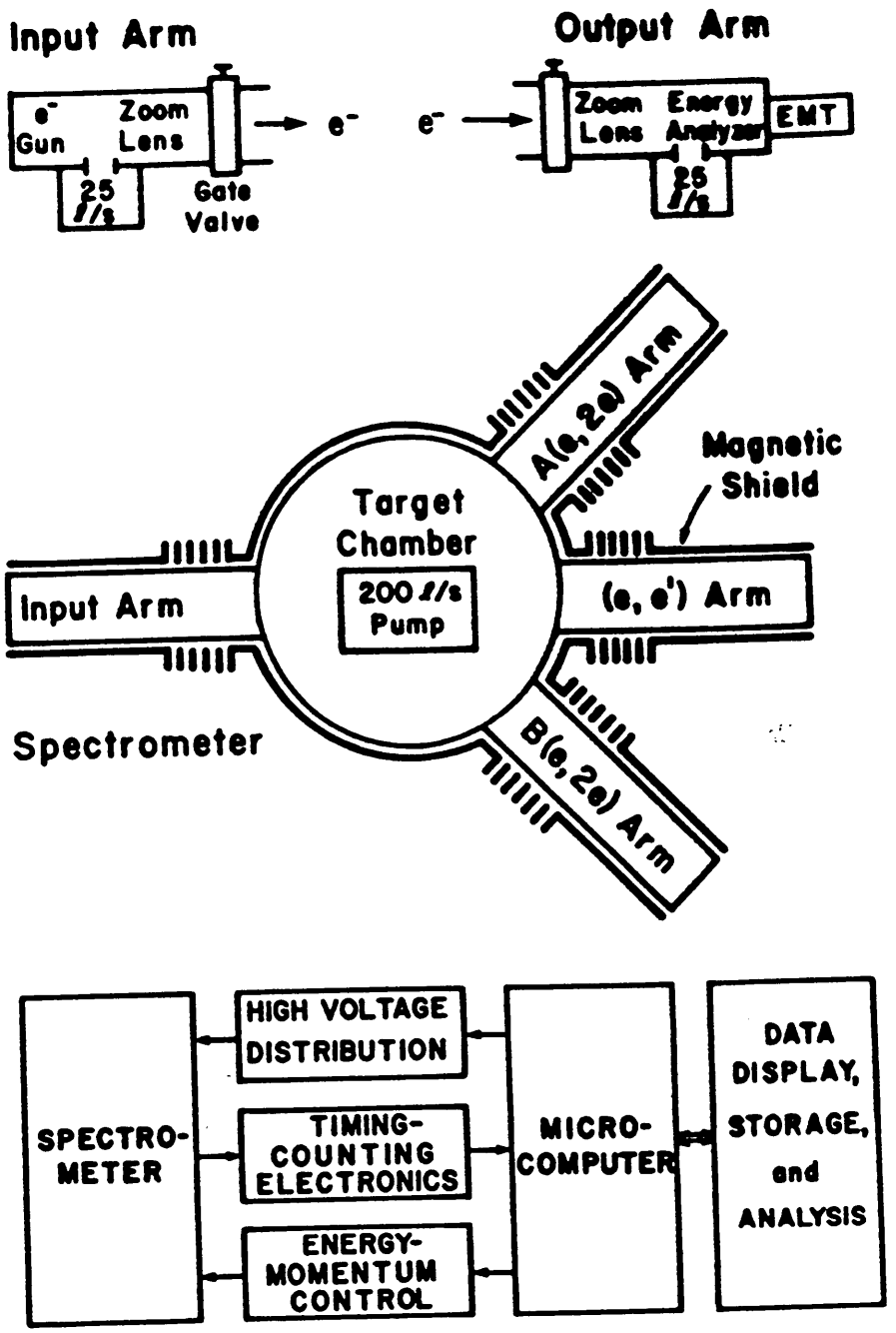

Figure III.1 Block diagram of (e,2e) Spectrometer

Table III.1 Design Parameters for (e,2e) Spectrometer

		VPI Spectrometer		Previous
		Measured	Design	Spectrometers[a]
Incident Current	I_0	~50μA	100μA	$\lesssim$0.1μA
Incident Energy	E_0	10-30keV	25keV	~10keV
Energy Resolution	ΔE	3-5eV	1eV	15-150eV
Energy Range	$\|E_b\|$	~100eV	<500eV	--
Momentum Resolution	Δq	0.2-1.1Å^{-1}	0.2-1.1Å^{-1}	1-2Å^{-1}
Momentum Range	q	4Å^{-1}	7Å^{-1}	--
Count Rate	N	0.1-0.2Hz	0.1-1.0Hz	0.01-1.0Hz
Stastical Count Error	ΔN	$\gtrsim$5%	5%	--
Target Vacuum	P	10^{-9}Torr	10^{-9}Torr	$\gtrsim 5\times10^{-7}$Torr

[a] Based on data collected by Amaldi et al (Reference 3); Camilloni et al (Reference 30); Krasilnikova and Persiatseva (References 100 and 101).

Important guidelines for design of this spectrometer are highlighted in the equation for (e,2e) count rate N(E,q) derived from Equation II.33.

$$N(E,q) \sim I_0 \left(\frac{\rho t}{A}\right) t \, |\Phi(q)|^2 \, (\Delta q)^4 \, \frac{\Delta E}{E_0^{7/2}} \qquad \text{(III.1)}$$

The inherent low count rates of coincidence experiments place paramount importance on maximizing N(E,q) which can be varied by adjusting the incident current I_0, target thickness t, momentum resolution Δq, energy resolution ΔE, and incident electron energy E_0. The count rate is particularly sensitive to the incident energy and momentum resolution.

The single most important constraint in choosing an electron source was the need to maximize count rate. Our spectrometer was designed to operate at an intensity of at least one thousand times that of previous machines. In addition to high intensity, our Pierce-type electron gun with a space-charge-limited diode electron source offers a well defined beam with reasonably low thermal energy spread.

A high gain electron multiplier tube (EMT) is used as a detector to meet the requirement of a low intensity, coincidence detection scheme, i.e., the ability to detect single electrons and the fast response time necessary for compatibility with coincidence electronics.

Both an energy analyzer and a momentum analyzer are required. For both of these systems, our choices were limited by the physics of the solids studied and further constrained by mechanical considerations in building the spectrometer. The dispersion curve for a typical valence band spans an energy of tens of electron volts with a Brillouin zone width of up to a few inverse angstroms. Based on these dimensions our spectrometer was designed to have an energy range of several hundred electron volts with a total energy resolution of 1 eV. The simplicity of the Wien filter and its straight-through geometry facilitated design of the other electron optics and such an analyzer is able to fulfill the modest energy resolution and angular acceptance we need. The desire for 1eV resolution is facilitated by utilizing a retarding field analyzer which requires only a modest resolving power from the energy analyzer. A momentum range of a few Brillouin zone widths and momentum resolution of $\sim$ 1/10 of the width of a typical Brillouin zone is necessary for useful study of momentum distributions. However the strong dependence of the (e,2e) count rate on the momentum resolution means that count rates are very low at this resolution. We opted to design a variable range momentum resolution from $0.2 \leq \Delta q \leq 1.0$ Å^{-1}, by using a variable magnification constant-focus zoom lens. Determination of

the momentum with a precision of $\Delta q = 0.2$ $Å^{-1}$ requires that the scattering angle be measured to better than 3 mrad. It would be prohibitively difficult to move the detectors mechanically and maintain this precision, therefore we chose to employ electrostatic deflection in our momentum selector with fixed beam arms.

The incident energy E_0 of the electrons striking the target is another major design parameter. Again, conflicting requirements act to narrow the range of useful energies. At lower energies multiple scattering becomes a serious problem even for very thin targets, so it is advantageous to use as high an incident energy as possible. However, the count rate decreases rapidly with increasing energy. A reasonable compromise is achieved at incident energies near 25 keV where the minimum thickness of self-supporting films is on the order of one mean free path.

Together, the requirements for high voltage incident electrons, a zoom lens, and compatibility with the electron gun, energy analyzer, and momentum analyzer provide more than ample guidelines for the electron optics system design.

Several auxiliary systems are necessary to complete the spectrometer. An ultra-high vacuum system is needed to minimize target degradation and magnetic shield is required

to reduce the effects of magnetic fields on the electron beam trajectory. These place further restrictions on the materials that can be used in construction of the machine. The long collection times necessitate that the spectrometer be interfaced with a computer to aid data acquisition.

B. Machine components

1. Overview of electron optics

The electron optics of the spectrometer form the nucleus of the machine. The following section describes the electron optics from a functional point of view, describing the trajectory of the electron beam and the operation of each of the components in order. The details of theory and dimensions are relegated to Appendix C, so that one can gain an appreciation for the overall system. The basic concepts and definitions of electron optics are also found in this appendix. Reference 143 offers a more concise description of our electron optics, reviewing the critical factors which have entered into the design of the spectrometer.

Figures III.2 and III.3 trace the beam profile through the lens columns. The images of the cathode (pupil) are labeled with arrows, while the window images are denoted by bars.

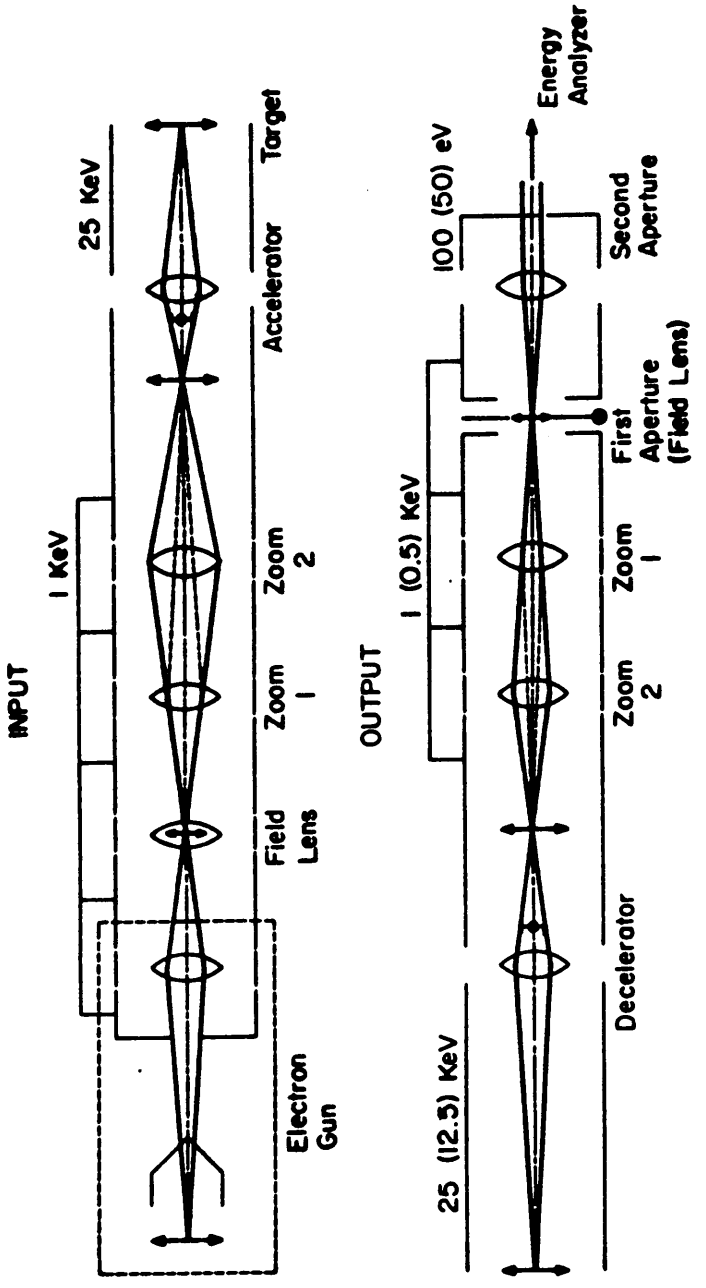

Figure III.2 Electron optics for the input and output beams.

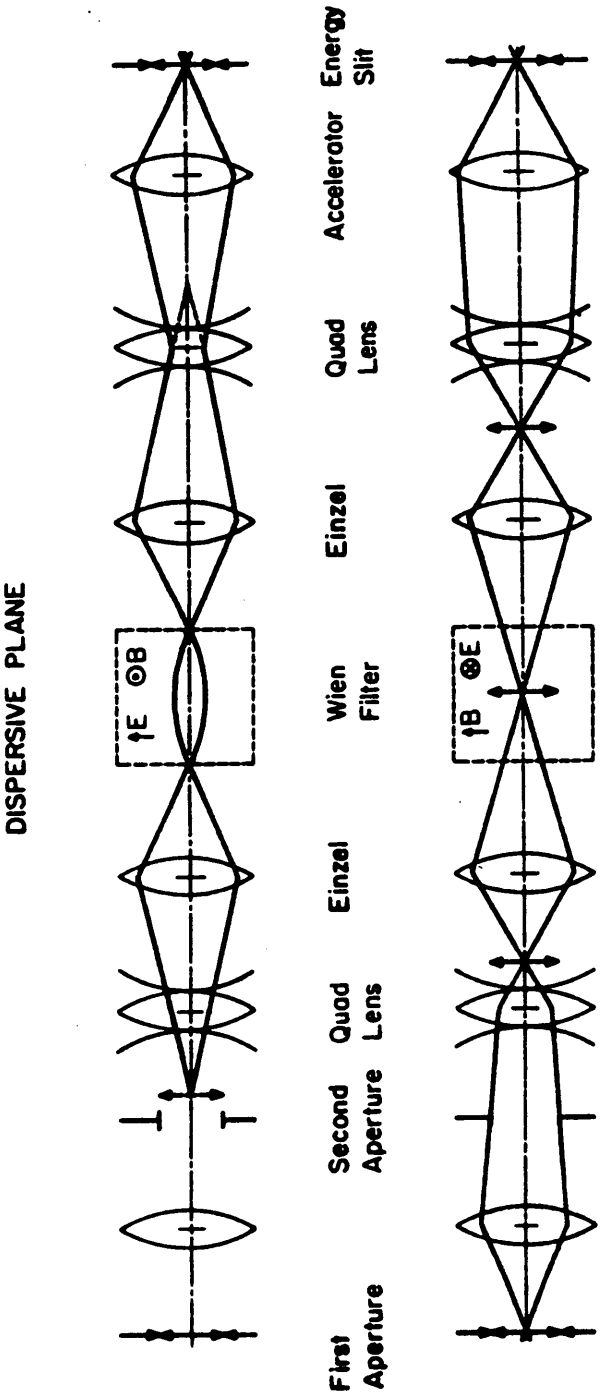

Figure III.3 Electron optics for the energy analyzer in two orthogonal planes.

The electron source employed in our spectrometer is a commercial electron gun (Cliftronics modified 3k/5U). It is a Pierce-type electron gun which employs a section of a space-charge-limited diode with a soft-cathode filament as its source. This type of gun was chosen over other more conventional types, e.g. triode guns, because it produces a beam of known current density and geometry and higher total currents.

Under normal operating conditions, the electron gun produces a virtual image of the cathode with an emittance (see Appendix C for definition) of 0.2 cm-mrad and a beam current of $\sim$10-100μA at an anode voltage of 1.0 keV. This image acts as the initial pupil image for the system and is located 1.1 cm before the anode aperture in the space-charge limit. The anode aperture, in general, acts as the initial window image. A summary of the properties of electron gun are shown in Table III.2 and a schematic diagram and an outline of the theory are found in Appendix C.3.

The Einzel lens in the electron gun assembly focuses the virtual pupil into the center of another Einzel lens, the Field lens. This lens is able to then adjust the location of the window (or equivalently, the pencil angle of the pupil) without affecting the location of the pupil. The location of the image of any object positioned on the

Table III.2 Properties of the Electron Gun under typical operating conditions

Anode Voltage	:	V_{AN} = 1000V
Thermal Voltage	:	$V_K \approx$ 0.1V (T≈1200K)
Cathode-Anode Separation	:	D = 3.68mm
Anode Aperture Radius	:	r_{AN} = 0.775 mm
Cathode Aperture Raduis	:	r_c = 0.394 mm

Property	Symbol	Units	Theory		Experiment
			Normal	Space Charge Limit	
Virtual Pupil Radius	r_p	mm	0.111	0.083	--
Pencil Angle	θ_p	mrad	7.5	7.5	--
Beam Angle	θ_b	mrad	53.	70.	--
Emzittance		cm-mrad	0.17	0.13	0.4 ± 0.2
Helmholtz-Lagrange Constant	HL	cm-mrad-$V^{1/2}$	5.3	3.9	13 ± 6
Perveance		$\mu A\text{-}V^{-3/2}$	--	0.32	
Emission Current	I_{AN}	mA	--	10	1-5
Beam Current		μA	--	--	
Current Density	J	$mA\text{-}cm^{-2}$	--	540	

first principle plane of a lens is unaffected by the focal properties of the lens and any lens employing this principle is called a field lens. The Field lens focuses the window so that its final image from the High Voltage lens is at infinity.

The next two Einzel lenses form a variable-magnification constant-focus "zoom" lens similar to that described by Gibbons et al [67] and Ritsko [142]. The pupil image in the Field lens is focused by the zoom lens to an intermediate image which, in turn, is projected by the High Voltage lens onto the target. By using different combinations of settings of the Zoom 1 and Zoom 2 lenses the size of the intermediate image can be varied without changing its position. Changing the size of the intermediate image results in a proportional change in the size of the image on the target. Since the emittance (the product of the radius times the pencil angle) is a constant for a given image, this amounts to being able to vary the angle of incidence of the electron beam on the target. Using only the Zoom 2 lens results in the largest angle of incidence (as shown by the solid line trajectory in Figure III.3), while using only the Zoom 1 lens results in smallest angle (broken line trajectory), with intermediate angles attainable by a suitable combination of both lenses.

Under normal operating conditions (1 kV anode voltage, 25 kV high voltage) the angle of incidence on the target is variable from 1.3 to 7.7 mrad with corresponding beam radii of 304 to 62 μm.

The angular divergence of the beam on the target is directly related to the momentum resolution Δq in the small angle approximation (see Equation II.32). The stated angular limits of the zoom lens correspond to a range $0.2 \leq \Delta q \leq 1.1$ Å^{-1}. The count rate for (e,2e) scattering is proportional to Δq^4, thus the zoom lens provides important flexibility in balancing the conflicting requirements of higher count rate and maximum momentum resolution. The factor of 6 in momentum resolution translates to an increase of over 1000 in the count rate.

The intermediate pupil image from the zoom lens is focused onto the target by a high voltage modified gap lens. The Field lens is adjusted so that a window image is placed on the low voltage focal point of the High Voltage lens; this projects the focal image of window to infinity, Therefore, the beam angle is zero and that the angle of incidence on the target is equal to the pencil angle. The high voltage lens operates in a range of 20 to 30 keV in the (e,2e) mode and half that in the elastic mode.

Within the target chamber there are several four-

quadrant cylindrical alignment deflectors that adjust the position of the beam on the target. There are two 1.3 cm long sets of deflectors at the entrance to the chamber and a set of 2.5 cm long deflectors at the exits for each output arm. Just to the target side of each of these sets of deflectors are 2.5 mm diameter alignment apertures. The size ($\gtrsim$ 1.5 times beam diameter) of these apertures is large enough to avoid vignetting, but is sufficiently small to aid in alignment of the beam. The momentum analyzer is also in the target chamber; it will be described at the end of this section.

The (e,e') beam arm High Voltage lens and Zoom lens are mirror images of the input arm. The beam spot on the target is imaged into the first aperture of the output arm by the High Voltage and Zoom lenses. The second aperture defines the accepted solid angle (window position) for electrons leaving the target. The initial output window which is focused into this aperture is at infinity (zero beam angle at target). The first aperture is also the Field lens which allows the necessary degree of freedom to focus the window into the second aperture. This field lens is a three-aperture lens. The filling factor in the Field lens is unity, since this lens itself acts as a limiting aperture. This is, in general, a bad design for electron

optics because of the resulting aberrations. This unorthodox approach is used because: (1) there is an image in the first aperture which reduces the aberrations associated with large filling factors; (2) it is possible to obtain short focal lengths with quite low voltages between the elements of an aperture lens due to the small diameter of the lens; (3) the total number of lenses necessary is reduced considerable by this approach. No significant effects of excessive aberration have been observed as a result of this technique.

There is a set of four-quadrant cylindrical alignment deflectors between the Zoom lens and the Field lens to position the beam in the center of the first aperture.

The function of the energy analyzer is to select a small range of the energy spectrum from the image of the target defined by the first and second apertures. The most fundamental component of our analyzer is the energy dispersing element, the **ExB** velocity analyzer of the Wien filter [183]. The characteristics of the Wien filter are what ultimately determine the properties of the energy analyzer. The analyzer also has a decelerating lens, accelerating lens, and other optics elements designed to adjust the images. A retarding field analyzer design is utilized, which greatly reduces the requirements for energy resolving power.

The Wien filter was chosen as the energy dispersing element of our system primarily because of its simple design and straight-through geometry which facilitated construction. The dispersion factor for the Wien filter is not as good as that of other analyzers that might have been chosen [73,98,150], i.e., hemispherical, cylindrical, or Möllenstedt analyzers. However, we require only modest energy resolution and limited angular acceptance. The low count rates involved require that the analyzer has a high transmission efficiency ; our analyzer is as good as or better than other types in this respect.

The Wien filter disperses the electron beam in the y-direction, that is in the direction of **E** out of the scattering plane. An image of the first aperture is formed at the entrance of the Wien filter in this dispersive direction. The analyzer is designed to focus this image on the exit plane of the filter. Chromatic aberration of the image results in an energy dispersed image. A virtual aperture at the exit plane determines the energy resolution of the spectrometer.

The Wien filter is configured to pass electrons with an energy eV_E with respect to the common point of the output arms. This common point is held at a voltage V_b above room ground, so varying V_b selects the energy (with

respect to room ground) of the electrons that pass through the filter.

The energy analyzer has several subunits in addition to the Wien filter as shown in Figure III.3. These additional elements are designed to focus the electron beam for optimum operation of the Wien filter. Electrons from the target are decelerated to a voltage V_{Z0}, typically 500 V, by the output High Voltage lens. They are further decelerated by a gap lens located between the first and second apertures to a voltage V_{E_1}, typically 100 V. This arrangement has the advantage that the actual analysis is carried out at low energy with a moderate resolving power ($eV_{E_1}/\Delta E \approx 200$) After leaving the Wien filter the electrons are accelerated back to the voltage V_{Z0} and are focused on the energy slit.

Quadruple lens are incorporated into the energy analyzer to compensate for the asymmetric focusing of the Wien filter. Quad lenses (see Appendix C.2 for a discussion of the geometries and focal properties of Quad lenses) act as converging lenses in the non-dispersive plane and as diverging lenses in the dispersive plane before the Wien filter and vice versa after the filter.

An einzel lens is added immediately before and after the Wien filter to allow the image of the first aperture to

be focused at the correct location. For optimum operation, as illustrated in Figure III.3, the decelerator, quad lens and input Einzel lens should combine to place an image of the first aperture at the entrance to the Wien filter in the dispersive plane. The Wien filter focuses this image at the exit of the filter and the output Einzel, quad lens and accelerator combine to focus a final image of the first aperture on the energy slit. In the non-dispersive plane, the decelerator and quad lens form an intermediate image which the input Einzel focuses at the center of the Wien filter. In this plane the Wien filter is transparent to the electron beam. This image is focused to an intermediate image by the output Einzel which is then projected on the energy slit by the quad lens and accelerator.

The width of the energy slit in the dispersive direction defines the energy resolution of the analyzer. The size of the virtual image of the energy slit produced by the accelerator, quad lens, and output Einzel at the exit of the Wien filter relates directly to the dispersion width y_D of the Wien filter (see Appendix C) in determining the energy resolution. The analyzer was designed to have a resolution of 1 eV (FWHM) and has a typical measured resolution of 3-5 eV (FWHM).

The resolution of the energy analyzer has been empirically determined from a scan of the count rate versus energy loss for quasi-elastic events in both the (e,e') and (e,2e) arms. The width of the zero energy loss peak is a good measure of the energy resolution of the spectrometer, including the energy analyzer and the thermal spread of the electron gun. The measured width of the elastic peak has been as small as 3 eV (FWHM) at beam current of 40 μA, however typical operation has a measured width of 5 to 7 eV (FWHM) (see Figure V.1).

Electrons which pass through the energy slit continue down a 10.7 cm long magnetically-shielded drift tube to the EMT. Another set of four-quadrant cylindrical alignment deflectors is located just after the energy slit to deflect the beam onto the first dynode of the EMT. A description of the detector and the coincidence pulse electronics is given in Section IV.

There are some minor differences between each output arm's electron optics. In the (e,2e) mode the outgoing electrons in the 45° arms have half the energies of those in the (e,e') arm. This is primarily compensated for by lowering V_{Z0} and all the other voltages in the (e,2e) arms by a factor of two so as to maintain the voltage ratios. Minor differences in the high voltage insulators in juxtaposition to the High Voltage lenses necessitated

slight modifications in the design of the (e,2e) High Voltage lenses; these lenses were computer modeled to achieve similar focal properties to the (e,e') lenses (see Appendix C).

Another difference relates to the size of the target beam spot imaged by the output optics. The spectrometer was designed so that the Helmholtz-Lagrange constant (see Appendix C for definition) of input and output beams are equal. The size and pencil angle of the (e,e') beam spot is equal to the input beam spot. However, geometry dictates that the optimum spot size of the 45^{o} arms is a factor of $1/\sqrt{2}$ smaller than the incident beam diameter; conservation of the emittance requires that the pencil angle be a factor of $\sqrt{2}$ larger in the (e,2e) beam. The beam spot size of the target is determined by the Field lens aperture, therefore these apertures are different for the (e,e') and (e,2e) lens columns.

The momentum analyzer selects the momentum **q** which will be accepted by the detectors by controlling the angles θ and ϕ of the electron beam. This is accomplished with electrostatic deflection by using sets of two pairs of parallel plates which act in tandem to vary the beam angle of the electron beam at the target without appreciably changing the position of the beam spot on the target.

There is one set of deflectors before the target with the plates oriented parallel the scattering plane which varies the angle ϕ thereby selecting momentum **q** in the y-direction perpendicular to the incident beam. There are two sets of deflectors after the target along the (e,2e) beam arm axes. These plates are oriented perpendicular to the scattering plane and select momentum **q** in the z-direction parallel to the incident beam. Figure III.4 shows the relative position on these deflectors in the target chamber and Figure III.5 illustrates the geometry involved.

A detailed analysis of the electron optics of these deflectors (see Appendix C) shows that if the deflector voltage $V_2 = 3V_1$ and the distance between the pairs of plated S is twice the distance between the plates and the target D then to first order the beam spot location of the target is independent of the incident angle (see Figure C.12). Further, in the small angle approximation, the deflection angle δ (i.e. either ϕ or θ), is given by

$$\delta \approx \frac{-2V_1}{\mathcal{V}} \left(\frac{L}{A}\right) \qquad \text{(III.2)}$$

where $e\mathcal{V}$ is incident energy, L is the plate length, and A is the plate separation. Higher order effects and specific dimensions are discussed in Appendix C. The deflection angle can be directly related to the momentum

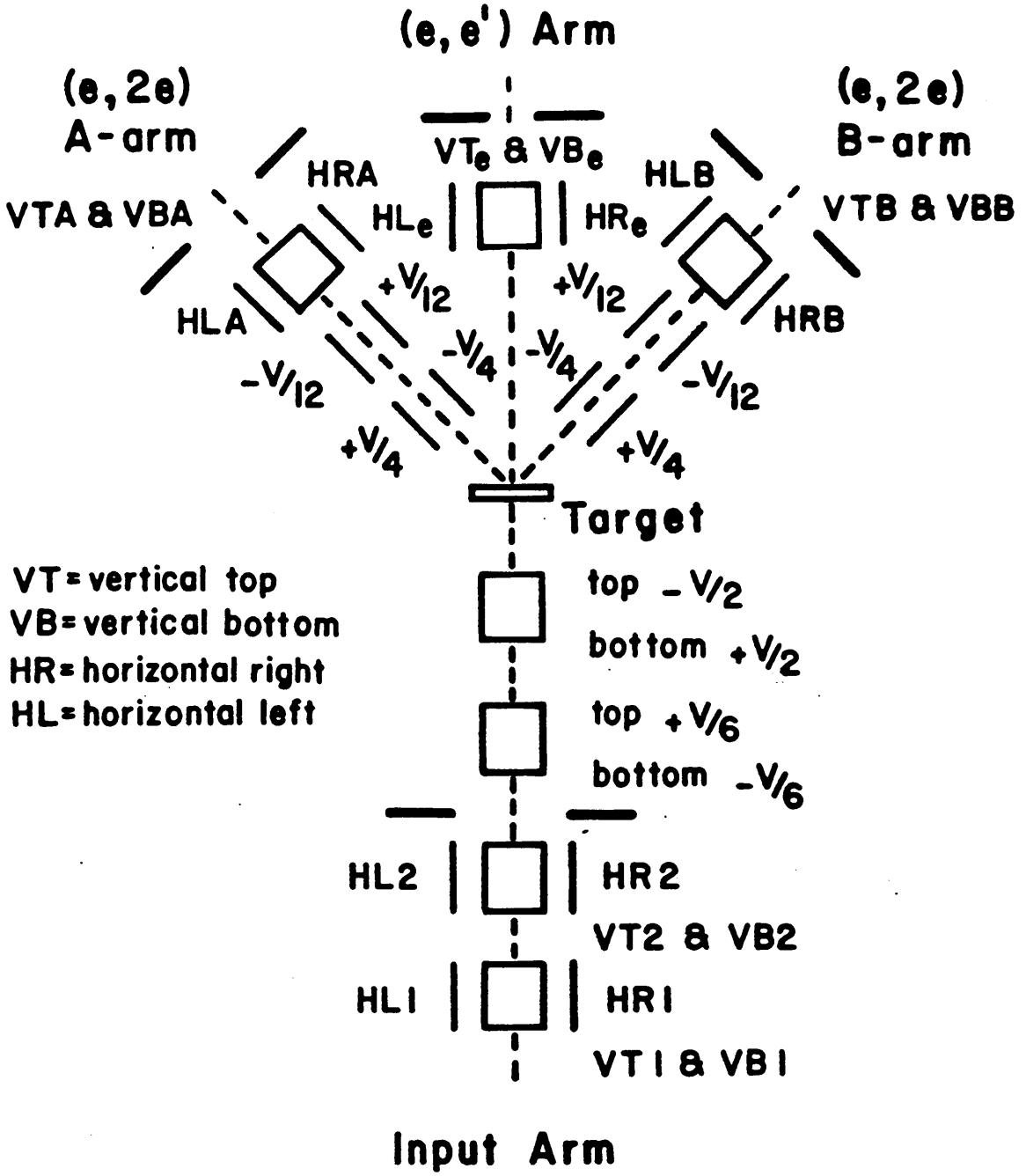

Figure III.4 Target chamber deflector positions

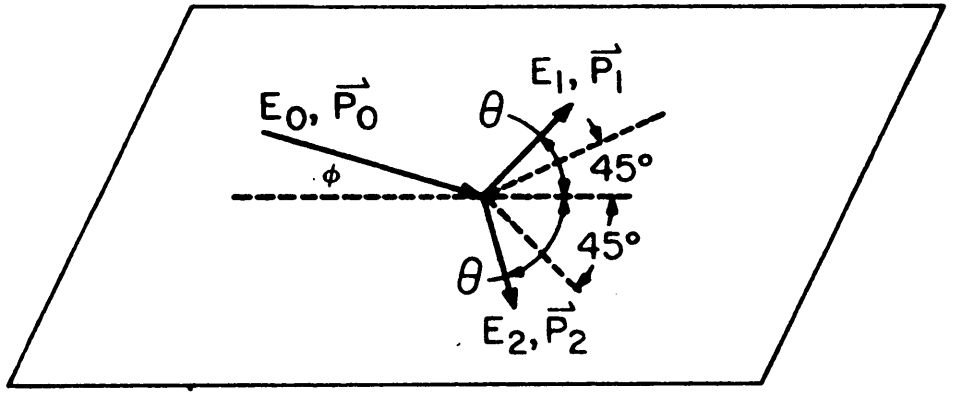

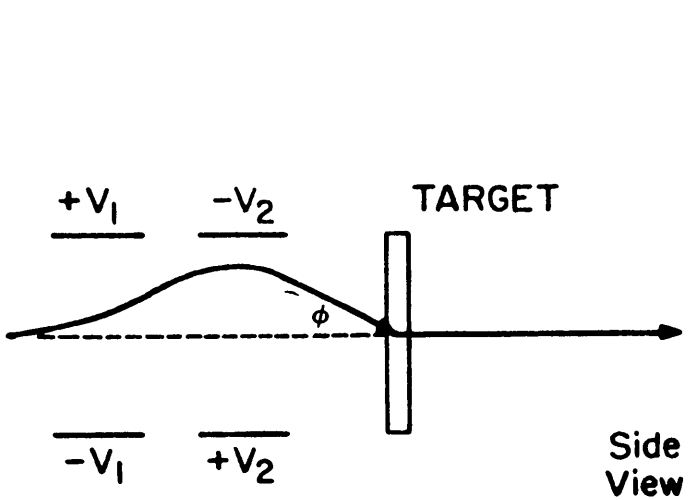

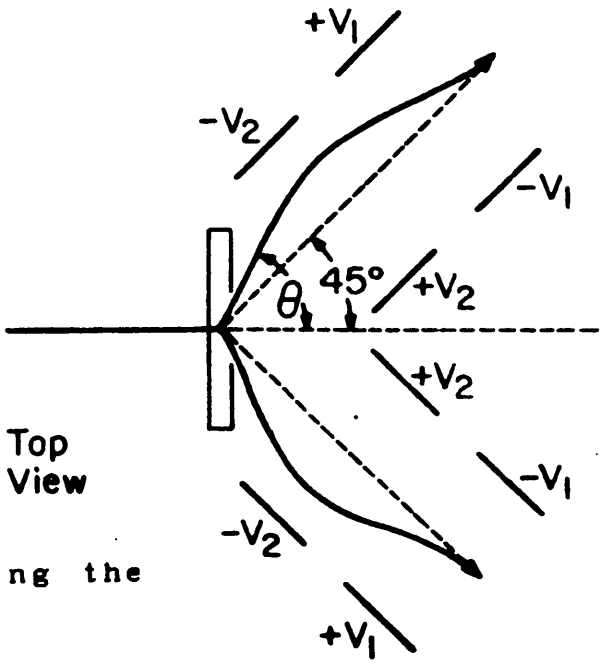

Figure III.5 Electrostatic deflectors for varying the scattering geometry.

q by Equations II.21 and II.23.

The deflector plate voltages are controlled by the computer. The automation is described in Section IV and the electronics are described in Appendices C and D. The momentum transfer was calibrated versus the computer controlled voltage by measuring the Bragg diffraction spectra of thin microcrystalline Al films (see Appendix C).

2. Voltage Distribution

A fundamental feature of high-energy (e,2e) scattering is the necessity of having two of the three major elements of the spectrometer -- electron gun, target chamber, and detectors -- at a high potential. We chose to place the output arms near room ground to facilitate coupling the signal pulses from the detectors to the pulse electronics. The target chamber is held at a positive high voltage HV_+ (typically +12.5 kV). The cathode of the electron gun is at a negative high voltage HV_- (typically -12.5 kV) and all the input electron optics voltage supplies float on this potential. The output arms, including the electron lenses, energy analyzer, and EMT, float on a variable voltage V_b which has a range of 0 to 80 V.

In the elastic scattering mode, the input arm ground (HV_-) is set to room ground and the target chamber ground is set to HV_+. Electrons from the gun are accelerated

towards the target through a potential difference of HV_+. These electrons can undergo an elastic collision and/or lose a small fraction of their energy through small angle scattering within the target. They are then decelerated by an amount $(HV_+ - V_b)$ as they move down the output arms. The energy analyzer is floating on the potential V_b, thus electrons with a potential energy eV_b (relative to room ground) are allowed to pass through the Wien filter into the detector. Therefore, the energy loss is $E_{loss} = V_b$. In the elastic mode the only voltage that must be accurately known then is V_b.

The situation is somewhat more complicated in the inelastic mode. The electron gun cathode is held at HV_- and the target chamber at HV_+, so that an electron striking the target has an energy $e(HV_+ - HV_-)$. In inelastic scattering the incident electron loses a small energy in an inelastic collision with an electron. In an (e,2e) collision at $\sim 45^\circ$ scattering angle the incident energy is shared approximately equally between the scattered and recoiled electrons. The electrons entering the output arms are decelerated by an amount $(HV_+ - V_b)$. The kinematic energy conservation expression for (e,2e) events, Equation II.9a can be expressed as

$$E_b = (2V_b - \Delta HV)e \qquad \text{(III.3a)}$$

where

$$\Delta HV = HV_+ + HV_- = |HV_+| - |HV_-| \qquad \text{(III.3b)}$$

An accurate determination of the binding energy E_b in an (e,2e) event requires knowledge of both V_b and ΔHV.

Determination of V_b poses no serious problem since it is a relatively small voltage. A standard voltmeter can measure V_b by recording the potential difference between the output arms common point CP_o and the computer control rack common point CP_c. This voltage difference can be monitored to within $\lesssim$ 10 mV by the meter used (Weston, Model 1240).

There is some discrepancy between the digital voltage signal from the computer, V_{com}, and the actual binding voltage, when the binding energy is under computer control. This can be expressed as

$$V_b = \gamma V_{com} + \Delta V_{com} \qquad \text{(III.4)}$$

The offset ΔV_{com} and the scaling factor γ depend on the range of the Voltage Booster (VPI Electronics Shop) used to amplify the computer DAC voltage. A typical value for γ is 1.01 ± .01 and for ΔV_{com} is 0.47 ± .01 V at 4X amplification.

There is also an offset due to the energy analyzer. In practice, the Wien filter does not pass electrons with energy $E_w = 0$ straight through, but rather electrons with a small energy offset eV_0. The value of V_0 can be

determined by measuring the count rate in the elastic mode as a function of V_b; the peak in transmission corresponds to a value of $E_w = e(V_b - V_0) = 0$. Typically, V_0 is 1.0 ± .25 V.

The precise measurement of ΔHV is a more complex problem due to the high voltages involved. It is measured by a voltmeter using two high voltage probes in a bridge configuration. The potential ΔHV can be expressed in terms of the meter voltage V_m as

$$\Delta HV = 2000\ V_m - 12.1 \qquad \text{(III.5)}$$

to within less than 1%. Details are given in Appendix D

The drift in ΔHV over long periods of time during data collection is an important source of uncertainty in the determination of E_b. The high voltage probes are stable to within 0.001% per month and have a temperature coefficient of 0.001% per ^{o}C which can result in an uncertainty of ± .5 V over a typical run. The high voltage power supplies drift up to 1 V per 48 hours. The drift is monitored and the supplies readjusted to their initial values from time to time over the course of a run. Altogether, drift introduces an uncertainty of 1 eV in the binding energy.

Finally, the quasi-elastic energy loss E_{loss} and the (e,2e) binding energy E_b may be expressed in terms of

measured quantities as

$$E_{loss} = e[\gamma V_{com} + \Delta V_{com} - V_0]$$
$$E_b = e[2(\gamma V_{com} + \Delta V_{com}) - (V_0^a + V_0^b) - (\alpha V_m - \beta)] \quad \text{(III.6)}$$

The electron gun, target, and detectors are each associated with a control rack which houses the electronics that float on the voltage of that element. This electronics includes the power supplies for the electron optics, the momentum deflectors, the energy analyzer, and the EMT's. A fourth control rack contains the computer, pulse electronics and 25-ℓ/s magnetic ion pump power supply. Each control rack is isolated from room ground; the local grounds on each rack are connected to a common point. This feature is designed to eliminate ground loops and to facilitate floating the racks on their respective voltages. The main features of the voltage distribution system are illustrated in Figure III.6 and details and schematics are found in Appendix D.

As a crucial safety feature the entire input arm and target chamber and their control racks are surrounded by a removable Faraday cage approximately 1.6 m by 2.0 m. Controls must be adjusted remotely through windows in the cage.

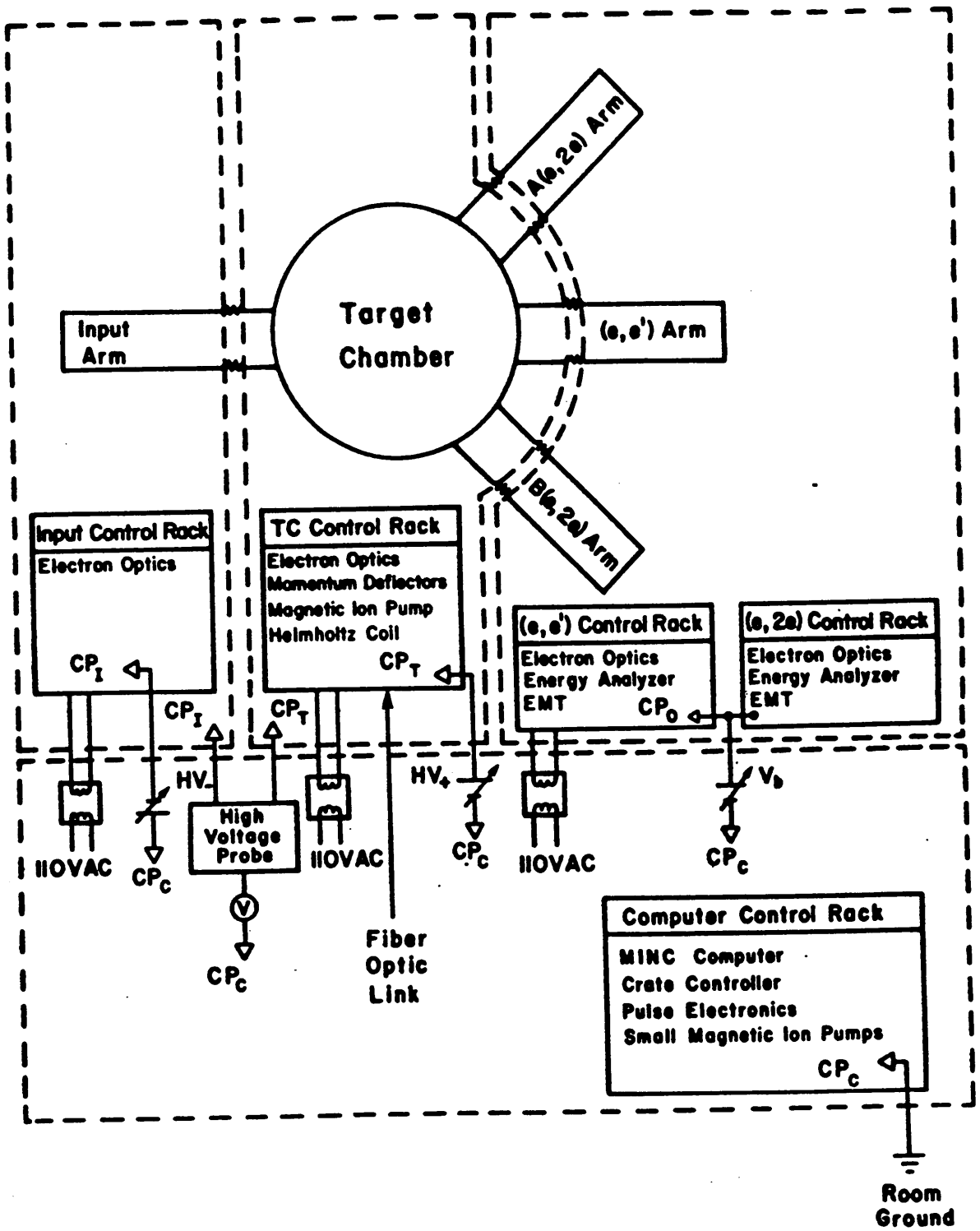

Figure III.6 High voltage distribution.

3. Vacuum System

The spectrometer is equipped with an ultra-high vacuum system which provides a base pressure of 3 x 10^{-9} Torr. The vacuum is quite stable at this pressure over the weeks required to take typical data sets. Magnetic ion pumps were chosen for the ultra-high vacuum pumping to avoid vibrations in the system and possible target contamination from gettering pumps. Sorption pumps are used as roughing pumps to avoid the chance of diffusion pump backstreaming. A schematic diagram of the vacuum system is shown in Figure D.1 and details are found in Appendix D.

4. Other components

As with all systems involving charged particle beams, care must be taken in the (e,2e) spectrometer to minimize the effects of magnetic fields. This affects the choice of materials used in construction of the spectrometer and necessitates the addition of magnetic shielding. The primary sources of the magnetic fields are static fields from the earth, the magnetic ion pumps, and magnetized materials in the lens columns. The shielding consists of extensive external mu-metal shields surrounding the beam arms and target chamber, mu-metal rings near the high

voltage insulators [67], and internal mu-metal shields around the energy analyzer and the entrance to the EMT. The target chamber shield is split in half for target access and provides insufficient shielding of the vertical component of the magnetic field. A 58 cm diameter Helmholtz coil concentric with the vertical axis of the target chamber is used to further reduce this component. The mu-metal shields were degaussed *in situ*.

The overall effect of these measures was to reduce the magnetic field transverse to the beam axis by a factor of 50 - 100 below that of the earth's magnetic field to <50 mG in the beam arms and target chamber and by another order of magnitude near the energy analyzer and EMT. Details of the magnetic shielding and magnetic profiles along the beam axes are given in Appendix D.

Thin film targets are mounted on individual metal sample holders which in turn are mounted on the target holder. The sample holders serve to support the thin film samples and provide electrical contact to the target chamber ground. The thin films are placed over holes in the sample holder (1.5 cm by 2 cm by 1-2 mm thick) which vary in size from 1.6 to 4.8 mm diameter. Most of the films studied were self-supporting, however some samples have been supported by high transmission fine copper

microscope grids. There were no discernible effects due to these grids in the (e,2e) data collected. The a-C films are mounted on Cu sample holders. However, the graphite samples are mounted on Al and Mo sample holders, because trace amounts of Cu were found to strongly inhibit sputtering of carbon [170]. Care must be taken to orient the thin films towards the analyzer side of target holder or else the edges of the sample holders can block the scattered beam.

Up to four sample holders can be mounted on the target holder. The target holder is a removable jig which aligns the samples in specific locations and fits into a cradle attached to the linear-motion feedthroughs (LMFT). The target holder can be moved in the x- and y-directions while the spectrometer is in operation to move different samples into the beam and to accurately center the samples in the beam. The maximum travel of the LMFT's is 6 cm in the x-direction (horizontal) and 4 cm in the y-direction (vertical). There is some play in the LMFT's which limits reproducability to $\sim$1 mm.

There are two sets of 45^{o}-deflectors which are also mounted on the target holder. These deflectors can deflect the main unscattered beam into either of the (e,2e) arms. The deflectors consist of two parallel plates (2.15 cm by 2.15 cm; 0.44 cm separation) oriented at $\theta = \pm 22.5^{o}$

connected to a high voltage supply (Bertan model 602B-15P). These 45°-deflector have proven invaluable in obtaining the initial electron optics settings for the (e,2e) beam arms. The current in the deflected beam is sufficient so that the current incident on various elements along the lens column can be directly measured with a picoammeter. Without the use of the 45°-deflectors the scattered beam in the (e,2e) arms can only be detected at the end of the lens column using the EMT.

A 4 cm diameter quartz viewport is provided to see inside the target chamber, particularly the target holder. There is a telescope that fits over the viewport which provides a means to view the beam spot on the target from outside the Faraday cage. This has proven useful in alignment and focusing of the beam spot. The 5 cm diameter lenses are configured as a condenser lens and mounted in a 100 cm long plastic tube. The image is brought to within about 20 cm of the viewer for a "brightness magnification" of 9X.

Very long time periods for data collection necessitate the interface of the spectrometer to a micro-computer. These time periods, measured on a scale of days or weeks, result from the low count rates inherent in coincidence experiments. The computer is designed primarily for

controlling real-time data acquisition and data storage. Although some data reduction and analysis is done on the micro-computer, most of this is reserved for more powerful mainframe computers. During real-time operation the computer controls the range and duration of data collected, selects the binding energy and momentum, and stores the data on floppy disk.

Operation of the spectrometer is controlled by a LSI 11-based MINC (DEC, Mobile INstrument Computer). The MINC is interfaced to a terminal (DEC model VT 105), two 8-inch floppy disk drives (DEC model RX02), and through a modem to the mainframe computer network. Control and coincidence electronics are interfaced to the computer by two methods ; several MINC Lab Modules are connected directly to the MINC bus and other components are interfaced by standard CAMAC hardware.

Data acquisition and the interface electronics are discussed in Section IV; details of the software are found in Appendices E and F and details of the coincidence electronics in Appendix D. Figure IV.1 shows the configuration of the computer hardware and related electronics.

Precision alignment of the spectrometer is very crucial to successful operation. The most precise angular alignment is required for the momentum analyzer deflectors

relative to the target and each other. To achieve the desired momentum resolution these angles must be accurate to within 3 mrad. This is accomplished by mounting the target, momentum analyzer, and beam alignment apertures together on a carefully machined stainless steel plate (27.9 cm diameter) which is mounted in the target chamber. The position of all of the elements on this table is determined kinematically by precision-ground sapphire balls.

The alignment of the components of each individual lens column is also very important. These elements are aligned relative to each other by bracing them against insulating alumina rods which are in turn braced against stainless steel tubes which are welded to the base flanges of the lens columns and extend the full length of the lens columns. The only exception to this, is the alignment of the electron gun assembly with the rest of the input lens column. This problem is of yet not fully resolved.

The alignment of each of the lens columns with the corresponding beam alignment aperture on the target chamber table does not require as precise alignment, because some misalignment can be compensated for by the beam deflectors at the entrance to the target chamber. However, this was still responsible for many of the problems in the initial operation of the machine and is still not sufficiently

aligned to avoid some systematic errors in the momentum determination. The arms have been aligned using a laser beam which was directed down the beam arm vacuum jackets through a series of apertures. The vacuum jackets were adjusted by alignment jacks located beneath the small magnetic ion pumps. There is still a degree of freedom in the alignment, however, since the base flanges which mount on the vacuum jacket are not at exactly right angles with respect to the stainless-steel support columns. Incorporating adjustable-angle flanges into the beam arm vacuum lines may provide a means to remove this error. The alignment can be accurately tested in the two colinear arms by measuring Bragg diffraction spectra.

The design of components for the (e,2e) spectrometer is complicated by many things. Each component may have to be compatible with the ultra-high vacuum, high voltages, precision alignment and machining, magnetic shielding, and space limitations. For example, a component of the electron optics must be made of a non-magnetic material to avoid producing stray fields; it must be conducting to avoid charging effects; it must be compatible with ultra-high vacuum requirements; it must be readily machinable to maintain the precision tolerances needed; and the part must be designed to minimize the potential for breakdown under application of high voltage. All of the components that

went inside the vacuum were first cleaned with organic solvents in an ultrasonic cleaner and then assembled with "white gloves and tweezers" to avoid vacuum contamination.

IV. DATA ACQUISITION

Data acquisition for the (e,2e) spectrometer consists of two main components, real-time data acquisition and the software used to combine the collected data. The real-time data acquisition is subdivided into two parts. The first part consists of the apparatus and computer software used to control the collection timing, momentum selection, and energy selection in the spectrometer. The second part consists of the detectors, coincidence pulse electronics, and software designed to collect the scalar count rates which comprise the raw (e,2e) data. This collected data is processed by a series of programs that combine the raw count rates into a single data file which is suitable for data analysis. The following section outlines the apparatus, software, and algorithms used in data acquisition; more details are given in the appendices as noted. A block diagram of the electronics for data acquisition is shown in Figure IV.1.

The operation of our spectrometer during data collection is controlled by a MINC (Digital Equipment Corporation, Mobile INstrument Computer) computer. Once the spectrometer has been calibrated and the electron optics manually tuned, the MINC allows complete automation of the data collection. This automation is necessitated by the low count rates of

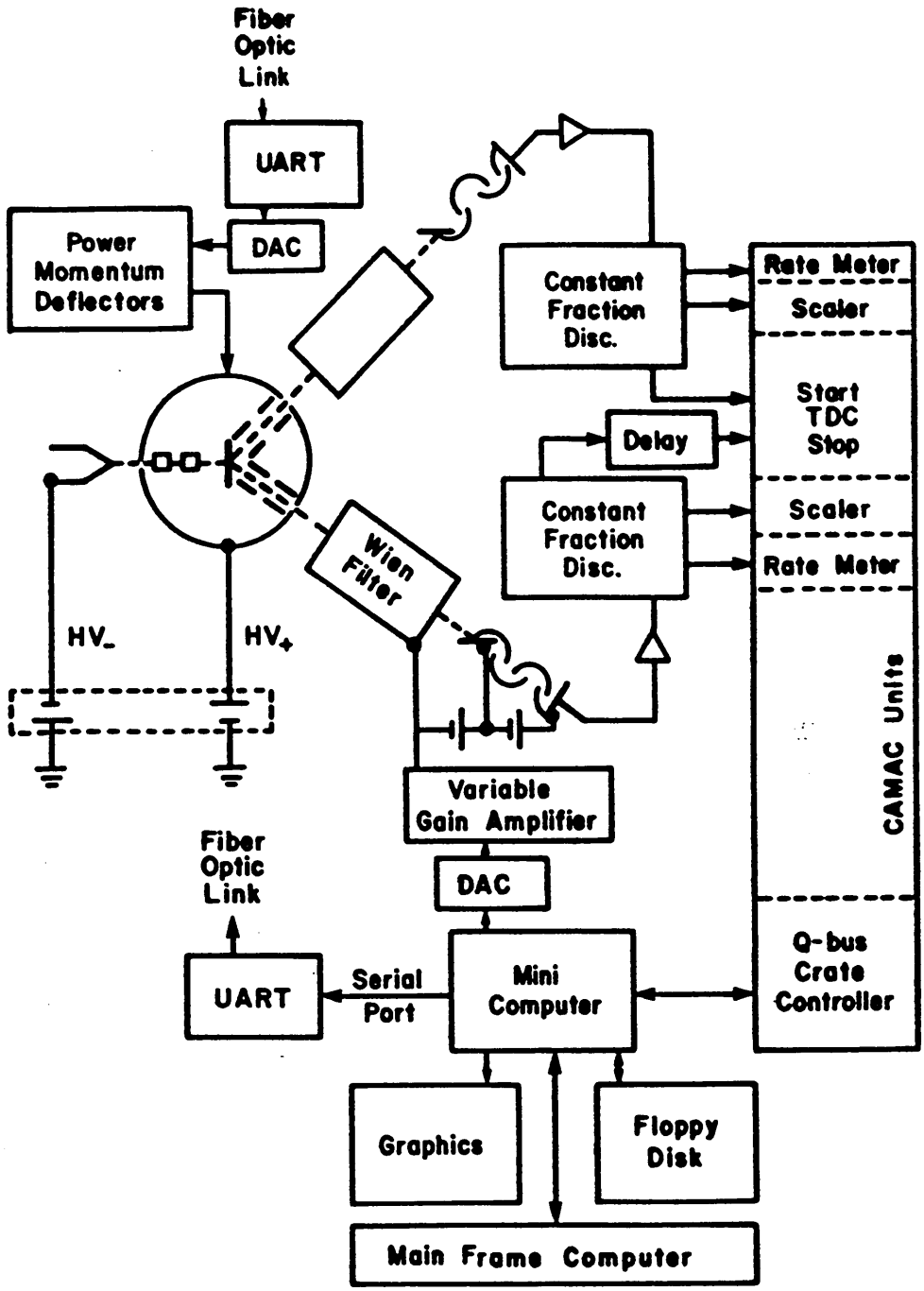

Figure IV.1 Electronics for data acquisition under computer control.

the coincidence experiment which result in data collection times on the order of days or weeks. Typically, the spectrometer can run for a few days between slight manual realignment of the beam.

The program PHYS controlling the spectrometer operation is a FORTRAN algorithm with several machine code subroutines [43]. Control parameters are set using PHYS which determine the range of energy and momentum over which data is collected and the timing of data collection. PHYS performs a wide range of functions. The program was written by Ben Cline and is described in detail in Appendix E and reference 45.

The scanning range of the binding energy is controlled by the MINC. The user selects the range by entering the minimum energy, maximum energy, and energy increment as parameters for PHYS. The MINC converts an energy value to a 0-80 VDC analog signal using a Digital-to-Analog Converter (DAC) and a variable gain amplifier. The voltage from the amplifier is connected to the common point of the (e,2e) control panel and floats the (e,2e) electron optics ground at a voltage V_b above room ground. The energy analyzer is described in more detail in Appendix C.

The scanning range of crystal momentum is also controlled by the MINC. The user selects the range by entering the minimum momentum, maximum momentum, and

momentum increment in units of inverse Angstroms as parameters for PHYS. The MINC converts a momentum value to an 8-bit digital control valve using a calibrated conversion factor C_F. The control value is transmitted over a fiber optic link to the target chamber. The fiber optic link uses optoisolators to provide the necessary isolation of the computer from the target chamber high voltage. This digital signal operates a relay and a DAC. The DAC drives two power supplies for the momentum deflector plate voltages; the relay determines the polarity of the plates. The momentum analyzer is described in more detail in Appendix C.

Collection timing is also under computer control. Input parameters for timing are the settling time before data collection, the length of data collection at each (E,**q**) point, and the number of data collection sequences completed before the data are stored on a disk file.

The program PHYS controls the order and timing of data sampling in the following manner. First, the energy and momentum of a given (E,**q**) point are set by sending the correct signals to the analyzers. The electron optics are allowed to stabilize by waiting the settling time before data collection begins. The count rates which comprise the raw (e,2e) data are collected at the (E,**q**)

point for a given length of time, the sample collection time. Data are collected in this manner over the entire (E,q) range in a random order. When all of the (E,q) points in the sampling range have been sampled, the program performs another iteration of data collection. After a specified number of iterations,. PHYS writes the raw data to a disk SUMMARY file.

This elaborate sampling pattern is designed to minimize systematic errors in the count rates due to drift in the tuning of the spectrometer. This drift includes variations in the beam current, in the transmission efficiency through the electron optics, and in the voltages supplied to the electron optics. The systematic error can largely be eliminated by sweeping over the entire (E,q) range with a sweep period that is chosen to be much less than the drift time of the spectrometer. The random order of sampling within each sweep reduces systematic errors due to drift if the drift continues for several iterations. Oscillations on time scales less than the sample collection time are reduced by measuring each count rate for many sampling periods.

In general, the settling time is on the order of a few seconds, the sample collection time on the order of a minute, and the number of (E,q) points on the order of one hundred points. This means that the iteration period

for sampling the entire (E,q) range is on the order of a couple of hours. Electron optics voltage drifts over this time span are small. The high voltage drift was measured as less than 1 V ($\pm$ 5 x 10^{-3}%) over a 48 hour period. Significant drifts in the beam current and transmission efficiency occur in times on the order of days, once the system has stabilized.

The function of the pulse electronics in our spectrometer is to identify and record the coincidence electron events. Standard coincidence techniques are used employing commercial electronics components. Two types of information are recorded for each (E,q) point during real time data acquisition, the coincidence time spectrum and the individual electron counts in each arm. The path of the pulse signal is traced chronologically in the following paragraphs.

Single electrons within the selected energy and momentum range are detected by fast, linearly focus, discrete-dynode electron multipliers located at the end of the output lens columns. The signal pulses from each electron multiplier go to a preamplifier through a high voltage decoupling capacitor and then to a discriminator. Coincidence detection is performed by a time-to-digital converter (TDC), which measures the time delay between a

pulse in one arm and a pulse in the other arm. The TDC is set to a full range of 128 nsec and has a time resolution of 250 psec/channel. The output pulse from one discriminator is used to start the TDC. The coincidence pulse from the other discriminator acts as the stop pulse for the TDC. The second pulse passes through a variable delay box before going to the TDC to reduce spurious noise. The pulses from each of the discriminators are also counted by a scalar and measured by a rate meter. The scalars record the singles count for each arm. The rate meters are used primarily for tuning the spectrometer's electron optics. Details of the coincidence electronics are found in Appendix D.

The raw data is transferred from the TDC and scalars to the MINC which stores the data on a floppy disk. The TDC and scalars interface to the MINC by standard CAMAC hardware. Data is transferred via a CAMAC crate controller to the LSI 11-based MINC using standard CAMAC commands.

During the run time, the MINC stores a complete coincidence time spectra and a total scalar count value for both arms for each (E,q) point. The coincidence time spectra consists of the count of total coincidence events occurring at each of the time interval channels over the TDC range (see Figure IV.2). During the settling time, after the MINC has set the momentum and energy, the computer

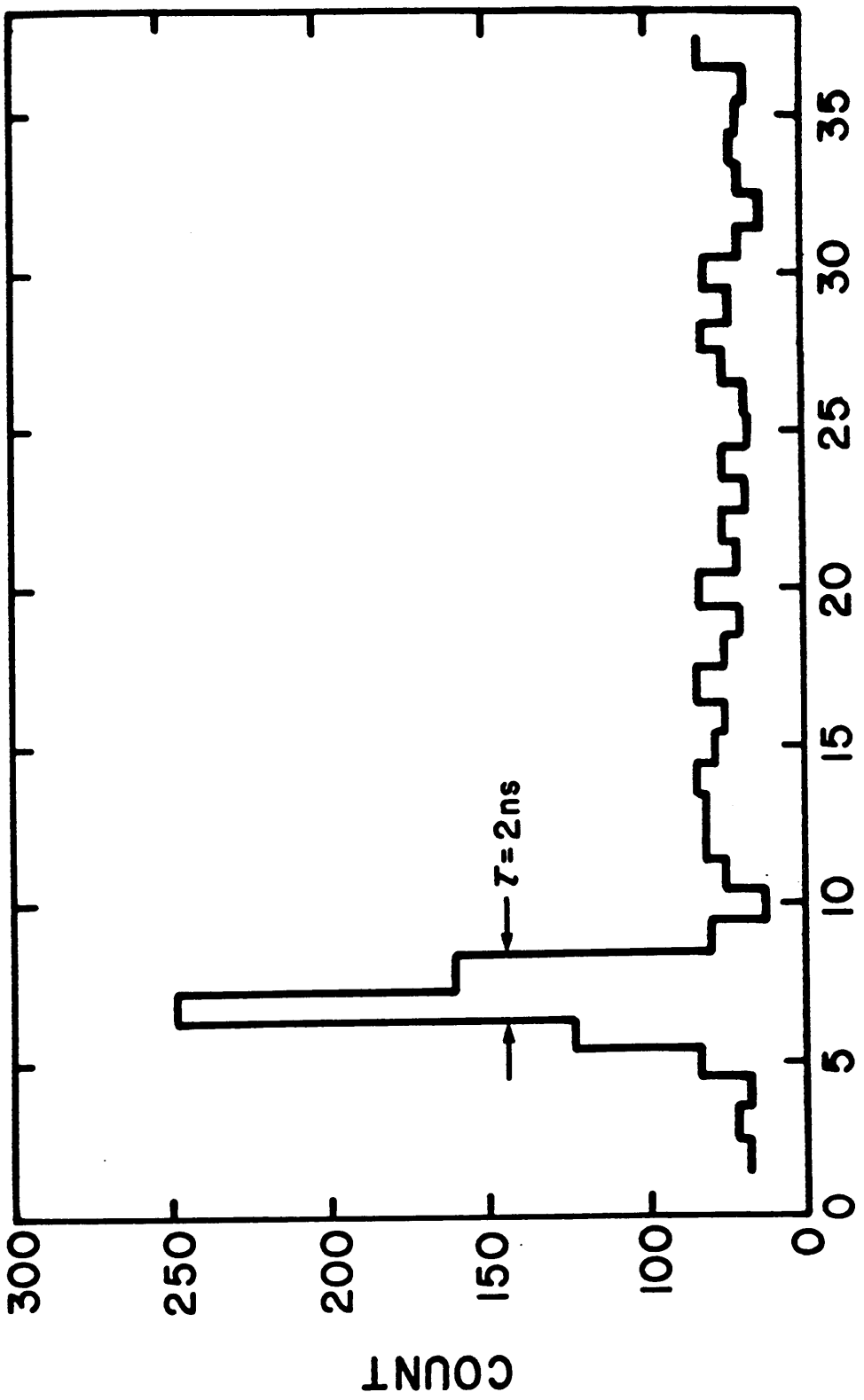

Figure IV.2 Typical time coincidence spectrum.

retrieves the appropriate coincidence time spectra and scalar counts from a data file stored on a disk. After a coincidence is registered by the TDC, the MINC increments the appropriate time coincidence spectra channel count. At the end of the sampling interval the MINC transfers the updated data back to the disk file.

The raw (e,2e) data is processed by several programs which ultimately produce a normalized array of count rates for the (E,**q**) range studied, together with an estimate of the error associated with each (E,**q**) point. This array is the final form of the coincidence data that is used in the data analysis. The software, data files, data reduction and merging algorithms, and error analysis are described in detail in Appendix E.

V: ERROR ANALYSIS

A. Count rate

The measured (e,2e) count rate is closely related to the actual (e,2e) count rate, but includes effects due to background counts and multiple scattering, as was discussed in the theory section earlier.

The elastic cross section at 45^0 is quite high (typically 60 Mhz; see Section II.A). It does not introduce any significant background into the measured (e,2e) rate, however, because the energy analyzer will not transmit these electrons which have energy $e(HV_+)$ greater than the energy of (e,2e) scattered electrons.

Inelastically scattered electrons also have a high count rate at 45^0 (typically 10 Khz). These electrons can have the correct energy and momentum to pass through the analyzers. It is possible to mimic an (e,2e) event if two such electrons are independently scattered into each (e,2e) arm almost simultaneously. These accidental coincidences produce a coincidence background which is constant over the range of delay times of the TDC because of the random nature of the events (see Figure IV.2).

In the region of the coincidence time spectrum where the true coincidence peak is found there is also a

contribution from the uniform background given by

$$N_r = N_A N_B t_c \qquad (V.1)$$

where N_A and N_B are the measured singles (non-coincidence) count rates in the (e,2e) arms and t_c is the time width of the coincidence window. The true coincidence count rate N_t is equal to the measured rate in the coincidence window N_c minus this uniform background.

An accurate measure of the count rate N_r can be obtained by measuring the background count rate over a wide time window t_b away from the coincidence peak. The count rate for this background window is given by

$$N_b = \frac{t_b}{t_c} N_r = r N_r \qquad (V.2)$$

where $r = t_b/t_c$ is the ratio of the window widths.

The true coincidence count rate is then

$$N_t = N_c - N_r = N_c - N_b/r \qquad (V.3)$$

and the standard deviation of N_t is

$$\sigma_t = (N_c + N_b/r)^{1/2} \qquad (V.4)$$

if Poisson distributions are assumed. The improvement of signal-to-noise that can be obtained by using large values of r is obvious. Typically, we use a coincidence window of 5 nsec (20 channels) and a background window of 50 nsec (200 channels).

Appendix F details the computer algorithms that

perform this background subtraction and discusses the error analysis in more concrete terms.

There are several limits that the signal-to-background ratio imposes on (e,2e) experiments. The background count rate is proportional to the product of the inelastic count rates in each arm given by Equation II.18. For the symmetric geometry these are theoretically identical rates. On the other hand, the true (e,2e) count rate is given by Equation II.30. The ratio of signal-to-noise reduces to

$$\frac{N_t}{N_r} = \frac{\sigma_6}{\left[\frac{d\sigma}{d\Omega}\right]_M^2} \quad \frac{1}{n\ I_0\ Z^2\ t_c} \quad \frac{1}{\Delta E} \qquad \text{(V.5)}$$

where σ_6 is the (e,2e) cross section given by Equation II.28, n is the number of target atoms in the interaction region, and Z is the atomic number.

The signal-to-noise ratio will decrease rapidly for higher atomic numbers and will become a limiting factor beyond perhaps the third row of the periodic table.

The coincidence count rate $N_t \propto nI_0$, while the $N_t / N_r \propto (n I_0 t_c)^{-1}$. Therefore, the optimum product of beam area times beam current times target thickness for an (e,2e) experiment must be a compromise between these two rates. The incident beam current has an upper limit set by the apparatus presently at ~100 μA: this current is used near its maximum value. The beam area is determined by the electron optics. This leaves the

target thickness as the adjustable variable. In actuality, the upper limit on target thickness is set by multiple scattering, which is proportional to an expotential of the thickness, rather than the signal-to-noise ratio. The optimum target thickness is less than or approximately equal to one mean free path, because the deconvolution techniques we employ are rather crude. If this technique could be improved significantly, then the optimum target thickness could be larger resulting in a highly desirable increase in coincidence count rate.

Beyond the random errors in the count rate, there are several potential systematic errors which have been identified. Drifts in the tune conditions, changes in the transmission efficiencies of the beam arms, and drift in the incident beam current can result drifts in N_t and/or N_r. Most such systematic errors are eliminated by the sampling algorithm described in Section IV. Long term drifts are reduced by merging the data sets on the basis of the total coincidence counts in a given region, rather than on the basis of total collection time as described in Appendix F.

The position of the beam spot on the target changes slightly as a function of the momentum selection (see Appendix C.3). This can cause a systematic error in the

count rates N_A and N_B and hence on N_t and N_r. If sample thickness varies appreciably over this range of distances, it can cause such errors. It is more likely that most such errors are caused by the mismatch between the focused areas on the target of the input and output beams as the beam spot moves. This can result in a systematic error of ~5-10% in the count rates over a typical range of momenta. The count rate should be constant for the non-coplanar geometry used to take this data.

It is possible that the target itself changes character over the time of exposure to the electron beam. Analysis of coincidence patterns on samples before and after several weeks of data collection have shown no signs of such changes. A better determination of this is possible by examining the sample in the elastic mode. Again, the energy loss spectra in the 45° arms showed no suggestions of sample degradation.

The errors introduced into the coincidence count rate by the deconvolution routines are uncertain. The primary justification for minimal deconvolution errors is that it does not appreciably alter the features or peak locations present in the original data. The deconvolution technique used and their potential errors are discussed more fully in Appendix F and in Jones and Ritter [90].

B. Energy

The energy resolution for the spectrometer is equal to the resolution of the input arm and the two output arms added in quadrature. The overall energy resolution is typically ~5-7 eV (FWHM).

The input arm energy resolution is a combination of the thermal spread from the electron gun -- typically only ~ 0.1 eV -- and the energy spread that results from the electron optics. The latter is primarily a space charge, or Beorsch [17,154] effect which increases the overall uncertainty in the input arm to ~ 2 eV [FWHM] (see Appendix D). This is modeled by a Gaussian distribution of width b_g in the deconvolution routine.

The energy resolution in the output arms can be estimated from measurements of the energy loss spectra in the elastic mode (see Figure V.1). The main energy loss feature in this spectrum is at ~25 eV loss and has a width of ~20 eV. Therefore, the broadening of the zero energy loss peak is due almost exclusively to instrumental broadening. The broadening includes both the input arm and one of the output arm resolutions.

The shape of this peak can be approximated by a

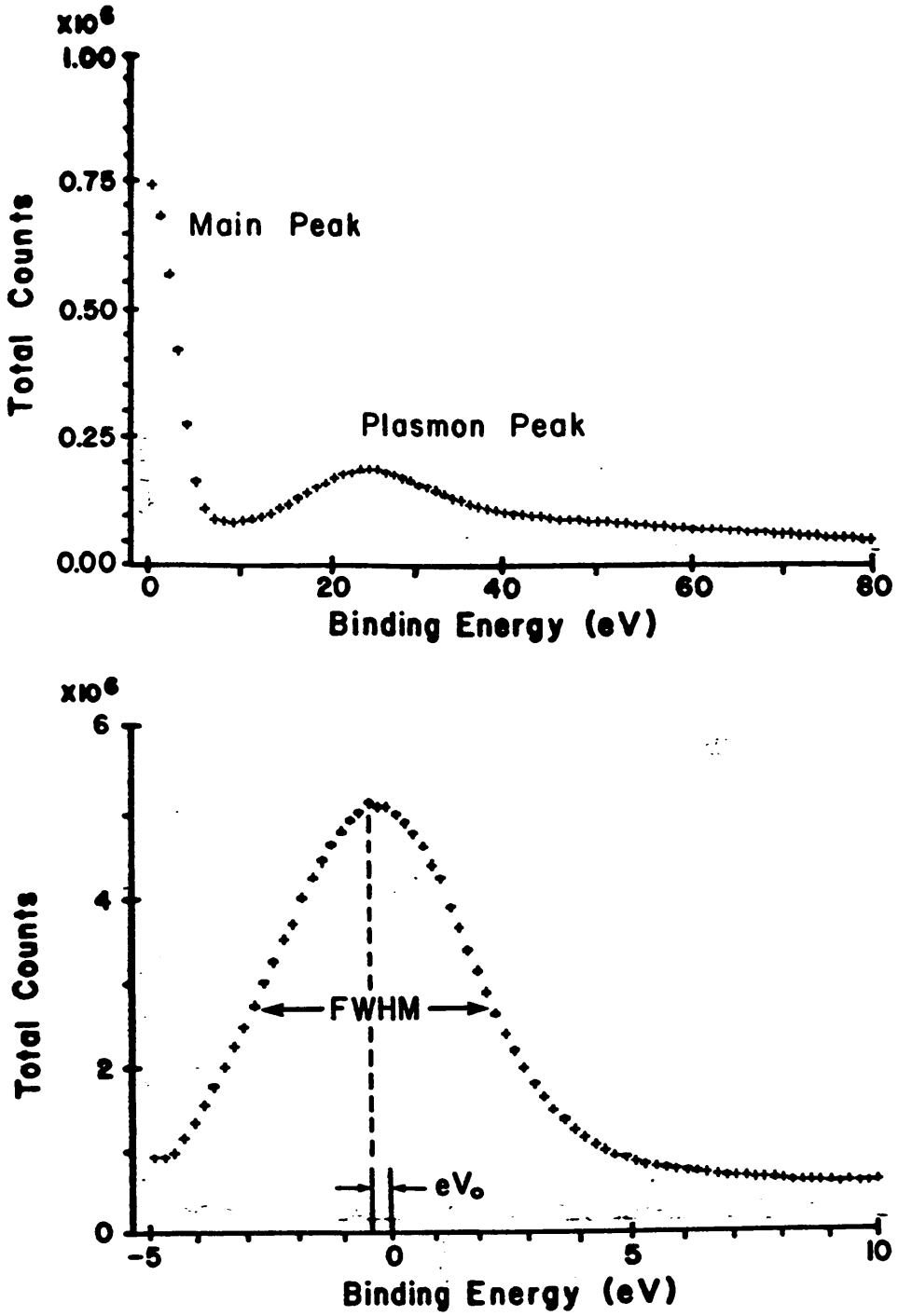

Figure V.1 Energy loss spectrum of a-C measured with ESWEEP in the elastic mode.

Gaussian distribution. The peak is slightly asymmetric and a Lorentzian line shape may provide a better model in future analysis. Typically, this peak width is 3 to 5 eV, although it has been measured as low as 2 eV. The energy resolution a_e of each output arm alone is typically 2.5 to 4.5 eV. The overall energy resolution then is 4 to 7 eV.

The uncertainty in the binding energy relative to the Fermi energy is ± 1 eV. The value of the binding energy in terms of voltages measured by the spectrometer is given by

$$E_b = e[2V_b - \Delta HV]$$

$$= e[2(\gamma V_{com} + \Delta V_{com}) - (V_o^a + V_o^b) - (\alpha V_m - \beta)] \qquad (V.6)$$

by combining the equations in Section III.2. The overall errors in E_b is typically 2% of V_{com} ± 0.7 V or ~± 1 V. The errors for the individual values in Equation V.6 are listed in Section III.2 and Appendix D. There is a drift in E_b due to the drift in the high voltage difference αV_m. This drift can be up to ± 0.5 V over an average data collection period.

There is some difficulty in determining the position of the Fermi Energy. For a semiconductor, the Fermi energy is midway between the top of the valence band and the bottom of the conduction bend. The band gap for a-C is

$\sim$ 0.5 eV [79] and $\sim$ 1.5-2 eV for a-C:H [89] (see Section VII.C). The value of the band gap in our a-C film can only be estimated as approximately 1 $\pm$ 1 eV. There is also a potential systematic error in the implicit assumption that the Fermi energy is at the target chamber ground. It is possible that the target can be at a slight negative voltage relative to the target chamber ground due to charging effects.

Taken together, these uncertainties allow the position of the Fermi energy to be assigned with an estimated accuracy of $\pm$ 2 eV. There is experimental evidence to support this estimate. The (e,2e) count rate should fall to zero above the top of the valence band (i.e. $\sim$ 0.5 eV below E_F) and does at E_b = 0 to within $\pm$ 2 eV. The calculated density of states falls to zero at $E_b \approx$ 3 eV above the assigned Fermi Energy.

C. Momentum

The momentum resolution of the spectrometer is a variable quantity. The zoom lens described in Section III.1 can vary the pupil angle of the image on the target. The overall momentum resolution Δq is related directly to the pencil angles and incident momentum by Equation II.32. The theoretical range is $0.2 \leq \theta \leq 1.1$ Å^{-1}

at 25 keV incident energy.

The momentum resolution has not yet been empirically verified. At present the value is calculated from the electron optics voltages using theoretical electron optics models in the program MODEL (see Appendix C.2). The computer simulations agree well qualitatively with experiment. The estimated accuracy of these models is 10 to 20%.

Momentum selection is described in Appendix C.3e. The momentum analyzer has been calibrated for the non-coplanar geometry by measuring the Bragg diffraction spectra of thin microcrystalline Al films (see Figure C.13). The experimental and theoretical calibration factors for the analyzer differ by about 10%. The estimated error in the momentum increment is then ~15%. This could be reduced to perhaps 5% by careful recalibration. The coplanar deflectors have not be calibrated, although they should be similar to the non-coplanar deflectors.

There is an uncertainty in the zero of momentum. This is most likely a result of misalignment of the beam arms, and in particular the electron gun as was discussed in Section III.4. The misalignment shifts the momentum analyzer setting which produces an incident beam normal to the target. The lowest band of a-C is approximately

parabolic and should be symmetric about the true q = 0. The minimum is in fact shifted to $q = 0.75 \pm 0.25$ $Å^{-1}$. A recalibration using Bragg diffraction should be able to determine this momentum offset to within 5-10%.

VI. SAMPLE PREPARATION AND CHARACTERIZATION

Preparation of samples for (e,2e) analysis is no small feat and characterization of the films is an equally difficult task. The techniques employed in making the thin films and in measuring their characteristics are described below. To date (e,2e) measurements on have been successful only on a-C films. However, significant effort has been directed toward preparation of single crystal graphite films and therefore they will also be discussed.

Samples for (e,2e) analysis must have several important properties. Foremost, the sample must be thin in order to minimize multiple scattering effects. Typically, the films must be about 1 electron mean free path thick, that is approximately 100 Å or 30 atomic layers thick for carbon. There must be a minimum of structural damage induced by the thinning techniques employed. The samples must have a reasonably uniform thickness over an area of $\sim$1 mm^2 so that the finite beam spot size and small shifts in its location do not produce significant variations in the count rates. It is particularly important to avoid surface contamination, because even a few monolayers of an oxide, etc. represent a significant fraction of such a thin film. Further, the film must be

self-supporting to allow electron transmission.

A. Amorphous carbon

Amorphous carbon films were purchased commercially from Arizona Carbon Foil Company. The manufacture and characterization of these films is described in detail by Stoner [160]. The films are made using an arc deposition evaporation technique whereby an arc is struck between spectroscopic grade carbon electrodes in a vacuum and the carbon is evaporated onto a glass microscope slide (25 mm by 70 mm) at room temperature [50]. The films contain small impurities including a few atomic percent H, ~1% O, and trace amounts (ppm) of heavy metals [161]. The films are highly uniform with variations of typically ± 10% or less over the slide area. The surface density is supplied with each film with an accuracy of ±1 $\mu g/cm^2$ as measured by a quartz oscillator. Stoner verified these surface density by using a combustion technique together with optical transmission measurements [160]. This is converted to a thickness by dividing by the density of these a-C films 1.82 ± 0.01 $g\text{-}cm^{-3}$ [93]. The conversion factor is 55 Å per 1 $\mu g\text{-}cm^{-2}$ for a-C.

One of the most important characteristics of thin

films is of course their thickness. This determines both the count rates, the signal-to-background ratio, and the extent of multiple scattering. Optical transmission measurements of the average thickness were made which agreed with surface density measurement to within <20%. Thickness variations were shown to be less than 5% over the sample area using a highly focused laser beam (~ 10μm spot size) scanned over the sample. Details of this procedure are given in Section VI.C. Several types of measurements of these a-C films were made to confirm their thickness and uniformity using the facilities of the National Research and Resource Facility for Submicron Structures (NRRFSS) on the campus of Cornell University.

A surface profile of a typical a-C film mounted on a glass microscope slide is shown in Figure VI.1. The surface varies by ~±200 Å over lengths of a few tenths of millimeters. The large variations are cracks in the films. Much of the smaller variations are due to surface irregularities in the glass slide. The profile was measured by an Alpha-Step Surface Profiler (Tencor Instruments) which uses a mechanical stylus.

Surface uniformity was measured by an Å-scope interferometer (Varian, model 980-4020). This instrument employs a sodium vapor lamp (λ = 5892 Å) and optics to direct light through a specially coated Fizeau plate, which

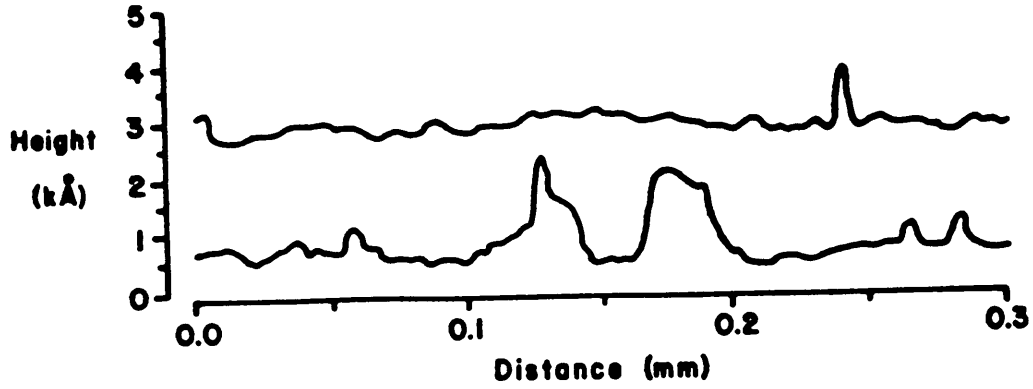

a) unetched 3.9 $\mu g\text{-}cm^{-2}$ a-C film mounted on a glass microscope slide as purchased.

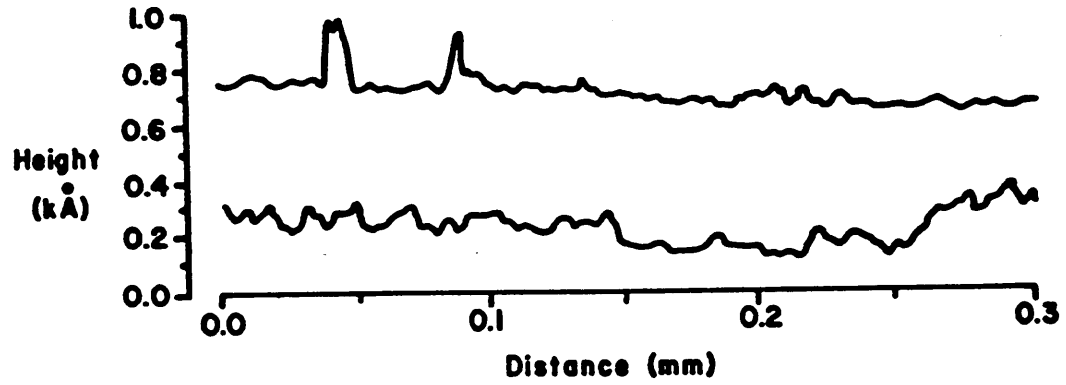

b) 9.8 $\mu g\text{-}cm^{-2}$ a-C film mounted on a glass coverslip etched to a comparable thickness using reactive ion etching.

Figure VI.1 Surface profile measurements of a-C films.

contacts the specimen at a slight angle and forms an air wedge. An interference fringe pattern is set up which effectively creates a contour map of the specimen. The fringes are parallel and evenly spaced for uniformly thick samples. A distortion of one fringe spacing corresponds to a thickness variation of one half wavelength. Interferograms were taken which show that the purchased a-C films are uniform on the scale of a couple of hundred Å .

The average thickness of an a-C sample was measured using Rutherford backscattering (RBS) by Craig Galvin at NRRFSS. RBS uses ~2 MeV He^4 ions as a probe and measures the energy loss E_L of the ions which are directly backscattered:

$$E_L = \left(\frac{M_s - M_{He}}{M_s + M_{He}} \right)^2 E_0 - 2\,t\,\frac{dE}{dx} \qquad \text{(VI.1)}$$

where E_0 is the incident He^4 energy, M_s is the mass of the scatterer, and t is the depth of the scatter below the surface. The first term results from a direct collision with the scattering atom and the second term models inelastic energy losses due to collisions with the sample electrons. The beam spot is ~1 mm square. Therefore, the measured thickness of the sample is an average value. A best fit to the experimental curve in Figure VI.2 yields an estimate of 930-990 Å for a 21.5

$\mu g - cm^{-2}$ (1180 ± 130 Å) a-C film. The 20% difference is almost within the stated experimental errors.

Analysis of the small-angle inelastic scattering data also provides an estimate of the film thickness. The thickness is derived from the extent of multiple scattering, i.e. plasmon creation, described by Equation A.4. There is a significant systematic difference between the thickness obtained by this method and all other methods. Details are discussed in Section VIII.A.

Surface contamination is not a serious problem with a-C or graphite. Graphite is very chemically inert; it is insoluble in acids, bases, and organic solvents [26]. The oxides of carbon, CO and CO_2, are both volatile gases, therefore no oxide layer can form under ordinary circumstances. However, a chemisorbed oxygen layer can form when the graphite surface is exposed to reactive oxygen [83] and layers of loosely bound CO and CO_2 molecules can form during reactive ion etching.

B. Graphite

1. Preparation

Preparation of single crystal samples pose a

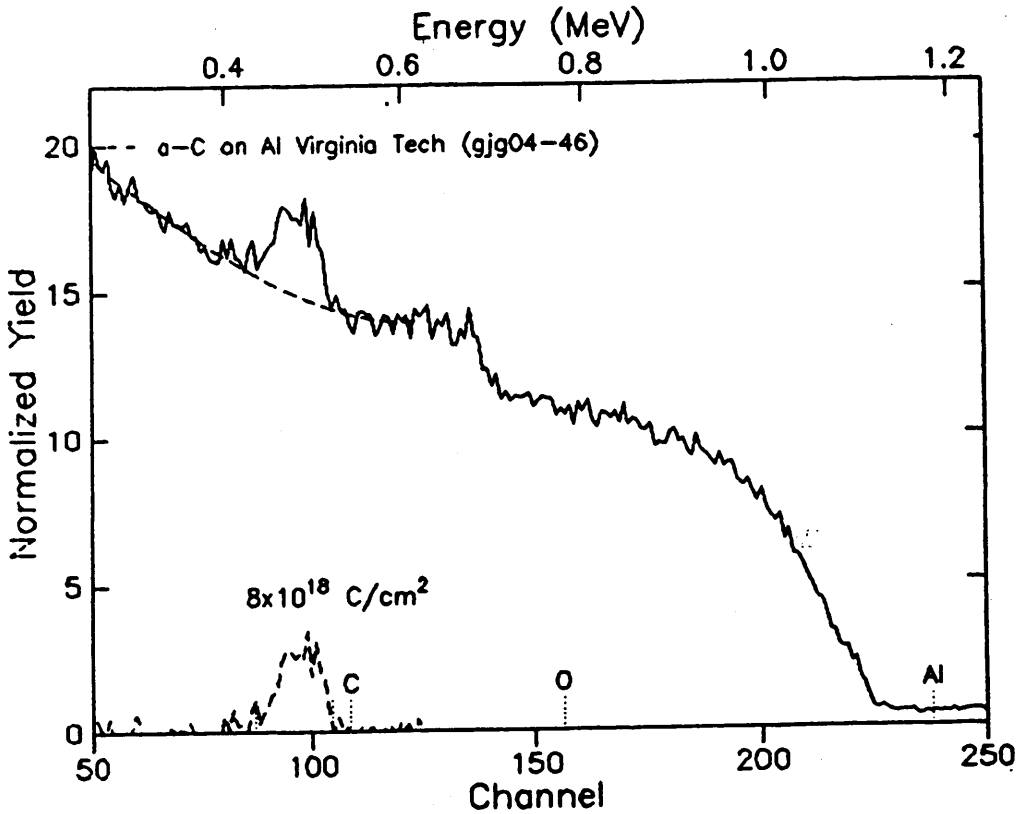

Figure VI.2 Rutherford backscattering energy loss spectra for an a-C film mounted on an oxidized Al sample holder.

Data were taken by Craig Galvin at NRRFSS.

significantly greater challenge. These samples must maintain a crystal integrity over a surface area of $\sim$1 mm^2. It is quite difficult to maintain this crystal structure down to the thicknesses needed as thinning techniques often result in target damage. In addition, there is the added problem of the alignment of the crystal axes with the spectrometer axes.

Natural crystals are used for the graphite samples, since no source of synthetic large single crystal graphite is available. The crystals are from the Ticonderoga Mine in Ticonderoga, New York and were purchased from Ward's Natural Science Establishment, Inc., Rochester, New York. The crystals have surface areas of up to $\sim$ 5 cm^2 and are up to several millimeters thick. They are embedded in calcite, which is removed with a solution of hydrofluoric acid. Synthetic, highly-oriented pyrolytic graphite (HOPG) was used during the development of the thinning techniques since it is readily available in larger samples (Union Carbide Corporatation Parma Technology Center, Parma, OH), but was not used as a target since the crystalites within the planes are randomly oriented on a scale smaller than the electron beam diameter [95] (see Section VIII).

Initial thinning of graphite is done using the "standard Scotch-tape method." Crystalline graphite and HOPG have a sheet-like structure similar to mica, therefore

they can readily be thinned by pulling layers apart with pieces of cellophane tape. Successive applications of this can result in a thin ($\sim$ .1-1 μm) film of graphite adhered to cellophane tape. The adhesive is dissolved in toluene and the crystal and cellophane are transferred to methyl alcohol to remove any residue. The cellophane is lifted off and the sample is floated onto a sample holder.

Some of these graphite samples with estimated thicknesses of a few hundred Å were examined with the (e,2e) spectrometer, however no coincidence counts were observed. It was evident that additional thinning was needed.

Several different approaches to the thinning of graphite from $\sim$ 1 μm to 100 Å have been attempted. None of these efforts have yet produced acceptable samples for (e,2e) analysis, however the techniques are outlined as a guide to future efforts in sample preparation.

The first final thinning method developed was that of ion milling. An ultra-high vacuum ion milling chamber was constructed at VPI based on initial design work by Melissa Anderson. Amorphous carbon test films were milled using both Ar (physical ion milling) and O_2 (reactive ion milling) plasmas. Serious equipment problems delayed use of the machine. It was ultimately decided that the

structural damage to the crystal resulting from high energy (~ 500-3000 eV) ions was unacceptable [126,34,35,188, 192,86].

Attempts at DC sputter etching (Edwards S150B Sputter Coater) were conducted at Poly-Scientific in Blacksburg, VA with the aid of Barry Witherspoon. Physical plasma etching using an Ar plasma and reactive ion etching using an air (N_2/O_2) plasma were tested with a DC bias of 500 V and a total power of ~ 10 W at pressures near 200 mT. Some samples were etched to a few hundred Å, however uniformity was poor and surface charging proved an insurmountable problem. The retardation of C sputtering in the presence of trace amounts of Cu was confirmed [170]. There was also evidence of a surface layer being formed on the carbon by the etching process.

Another attempt at final thinning used a Tunnel Plasma Etching (TPE) chamber [61]. The technique employs dry chemical etching where a chemical reaction takes place on the surface to be etched with a reactive plasma gas and the resulting volatile gas is pumped off. Plasma etching of carbon and organic polymers is a well established field [81] used primarily in the semiconductor industry. An oxygen plasma is produced and excited oxygen atoms and ions react with the carbon to produce CO and CO_2 [83].

Figure VI.3 shows the TPE chamber built at VPI. The

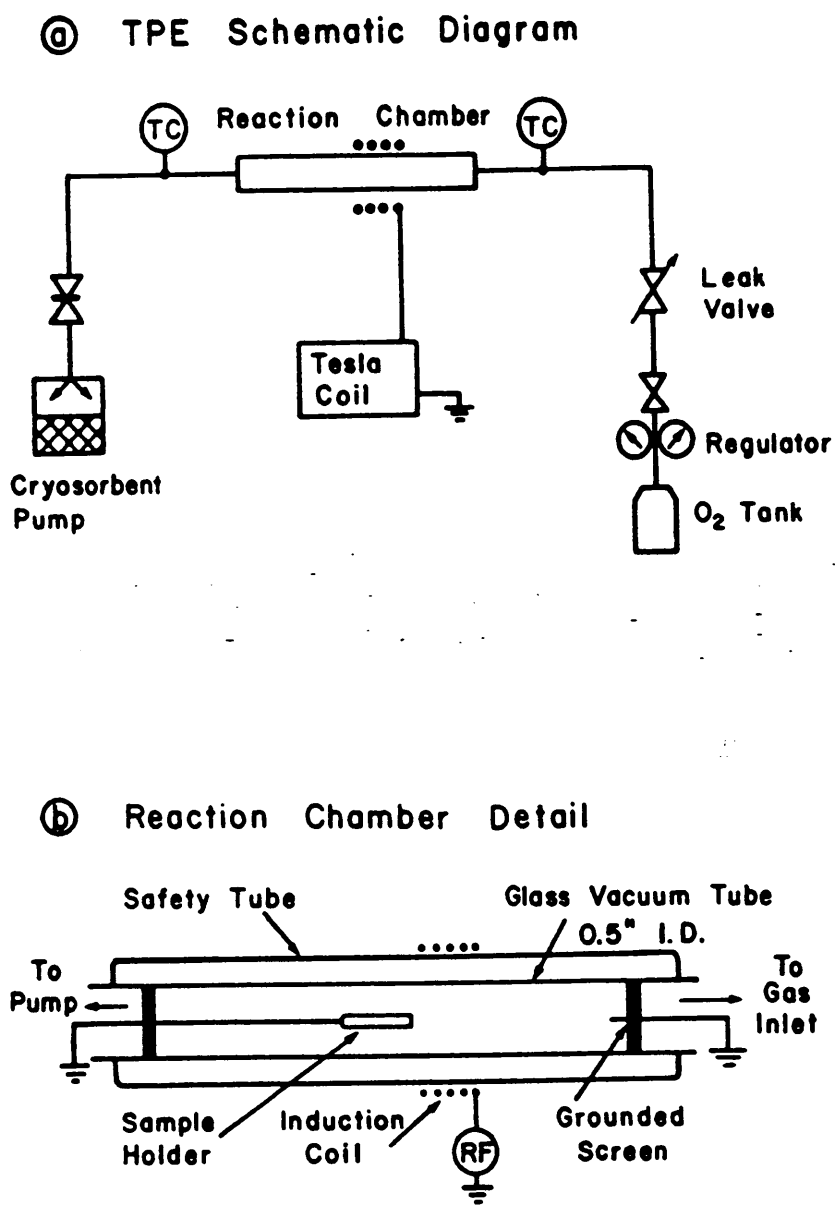

Figure VI.3 Effluent Tunnel Plasma Etching Chamber.

system has an oxygen source (welding grade oxygen with a purity of >99.9% with CO_2 and inert gasses as the major impurities) with a metering valve to control the flow of gas into the reaction chamber. A cryo-sorbent vacuum pump is attached to the opposite end of the chamber. This type of pump is sufficient since only a modest vacuum is needed and is used to avoid potential oxygen explosions that can result from the use of diffusion pumps. The plasma is produced with rf power which is supplied by a Tesla coil with a maximum output of ~10 kV at ~ 5 MHz. The rf power is coupled to the plasma through an antenna formed from a 3 cm diameter coil of copper wire. Grounded aluminum screens are used to limit the plasma within a pyrex reaction chamber ~20 cm long with a ~1.3 cm I.D. Glass was used for the reaction chamber to reduce interactions of the oxygen plasma with the walls. Aluminum is used for the grounding shields and sample holder; a thin layer of solid aluminum oxide is formed on these surfaces which then masks them from further oxidation. The sample is placed 0-5 cm downstream from the copper coil. Typical operating parameters for the TPE chamber include:

Oxygen Flow Rate: 10^4 scc/sec (10 m/sec)

Operating Power: 100 mTorr (at inlet TC)

Base Pressure: 20 mTorr

Plasma Power: ~ 1 mW

Etch Rate: ~ 10 Å/sec

Several natural Graphite films of thicknesses of ~ 75 to 300 Å and surface areas of ~ 1 mm^2 were made with the TPE. Three of these samples were tested in the (e,2e) spectrometer, but proved unsatisfactory. The characterization of these films is discussed below.

Reactive ion etching (RIE) with an rf power source was the latest thinning technique to be tried [81]. This is similar to DC sputter etching in its mechanical configuration and employs the chemical etching principles used in the TPE. The RIE was done using an Applied Materials reactive ion etcher at the NRRFSS. The use of rf power eliminated the charging problems encountered with DC sputtering and also reduced the crystal damage by lowering the incident kinetic energy of the ions to below 100 eV.

Initially only O_2 was used in the plasma, however it was found that a surface layer was produced on the carbon. This surface layer is most likely either chemisorbed O_2 or loosely bound CO and/or CO_2 molecules. Argon was introduced into the plasma to provide a mechanism for physical plasma etching in addition to the chemical plasma etching. In principle the carbon is chemically etched by the O_2 to form an oxide loosely bound to the surface and the argon physically sputters the oxide from the surface.

The argon should have enough energy to knock off the chemisorbed oxide (~ 10 eV) but not enough to sputter the carbon directly. This combination should significantly reduce damage to the graphite crystal structure. Samples etched with O_2 and Ar mixtures did not have visable surface layers which were present after etching with only O_2. The best samples were produced under the following conditions:

Oxygen Flow Rate: 30.0 ± .2 sccm

Argon Flow Rate: 10.0 ± .1 sccm

Operating Pressure: 60 ± 2 mT

Base Pressure: 10^{-5} T

rf Power: 15 W (0.05 w-cm^2)

DC Bias: 110 ± 10 V

Etch Rate: ~ 35 Å/min

Several graphite and HOPG samples of thicknesses ~ 100 to 200 Å were produced using this technique. These samples are in the process of being tested in the (e,2e) spectrometer. Evaluation of their characteristics is given below.

2. Characterization

A study of the optical transmission of a-C as a function of thickness was performed to provide an indirect

method of measuring thickness of graphite films. A He-Ne laser (λ = 6328 Å) beam was apertured and focused on the film with a spot size of $\sim$ 0.5 mm. The transmission was measured with a standard silicon photocell and a voltmeter. Figure VI.4 illustrates measurements of the transmission coefficients of a wide range of a-C films and list a linear regression analysis to an exponential decay. These measurements are in good agreement with published data [160]. The estimated accuracy of the method is ± 25% over a range of 60-1400 Å thickness.

An estimate of average thickness of graphite films can then be obtained by measuring the optical transmission coefficient of a sample. The optical properties of the a-C films are estimated by Stoner [160] to be similar to those for graphite [162]. The thickness of the graphite is obtained from Figure VI.4 by multiplying by a factor of 0.81 to correct for the difference in densities. Again, the estimate of thickness is only accurate to about ± 25%. There is good agreement between Figure VI.4 and published data [160,79].

Initial measurements of the transmission provided only a measurement of the average thickness of the samples, because the laser was focused to a spot size of $\sim$ 0.5 mm which is about twice the electron beam spot size. A more

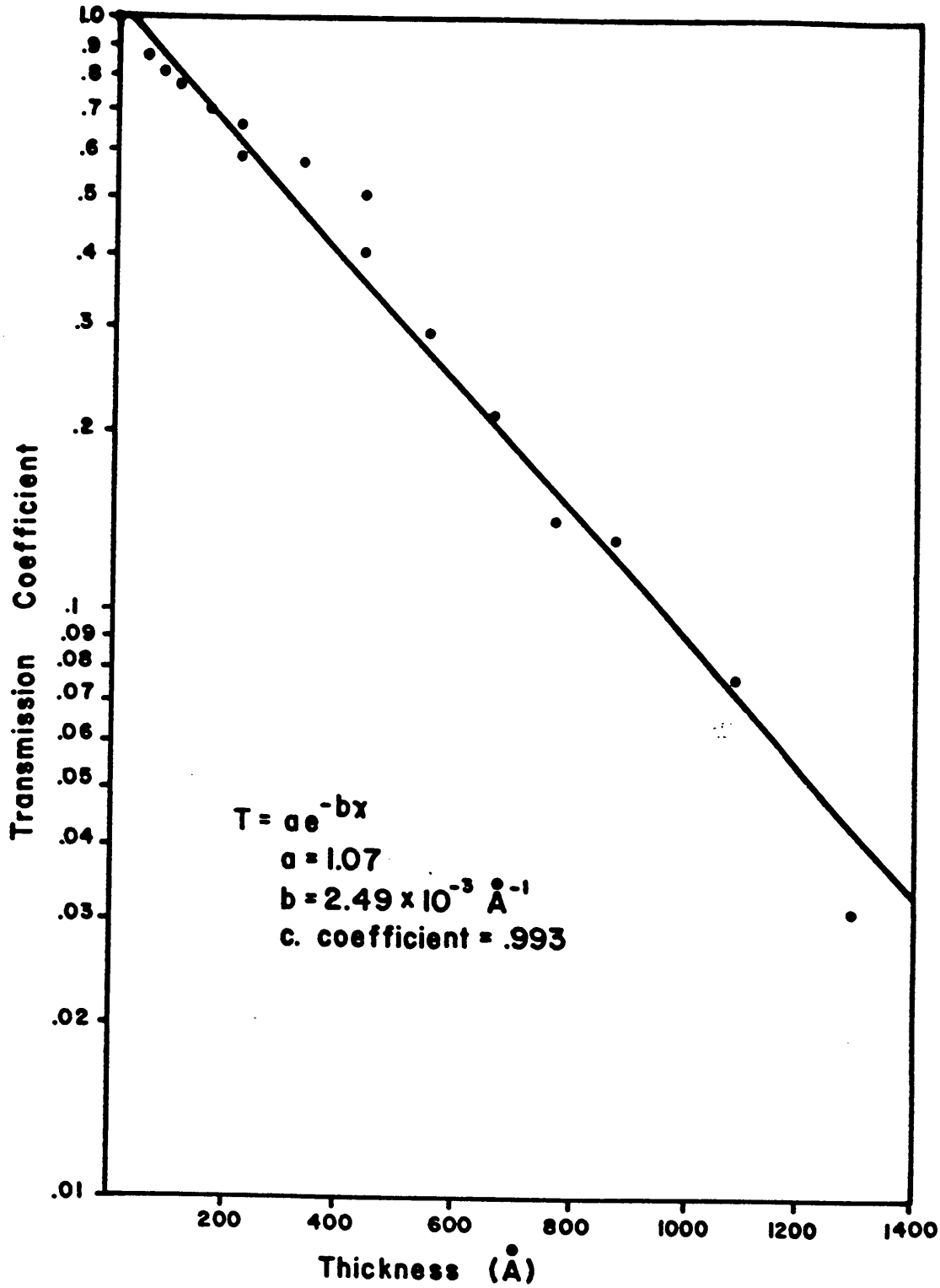

Figure VI.4 Transmission Coefficient versus Thickness for a-C films.

refined system was able to focus the laser to a spot size of $\sim$ 10 μm. The sample was mounted on an x-y-z positioning stage which allowed movement of the sample to within ± 10 μm in this system.

Transmission measurements determined that the samples prepared using the TPE were from $\sim$ 75 to 300 Å in average thickness and samples prepared using RIE were from $\sim$ 100 to 200 Å in average thickness.

Sample uniformity proved to be a difficult thing to achieve in the graphite samples. Interferograms of freshly cleaved graphite surfaces show that the surface has irregularities on the order of $\lesssim$ 1 μm over areas of $\sim$ 1 mm^2 before etching. The TPE samples were visibly uneven under a 10X optical microscope. Analysis of elastic scattering spectra and the signal-to-noise ratio in (e,2e) measurements seemed to suggest variations in thickness of a factor of 2 or more over surface areas of $\sim$ 0.25 mm^2 for these samples. The RIE samples appear to have smooth surfaces using a 10X optical microscope. Refined optical transmission measurements demonstrated that the RIE samples varied significantly over small areas. Areas of up to 0.1 mm^2 with thicknesses of 150 ± 50 Å were located on several samples.

It was not possible to use the Alpha-Step Surface Profiler on graphite because the material was too soft.

However, a-C films mounted on glass coverslips (see Figure VI.1a) were etched simultaneously with the graphite RIE samples. A surface profile of the a-C film after etching (see Figure VI.1b) exhibited variations of 50-100 Å over ~ 1 mm surface distances. This is less that variations in the film before etching. Evidently, RIE does not introduce significant surface variations in a-C films and may actually act to smooth the surface somewhat. It is reasonable to expect the same to hold for graphite.

Attempts to use RBS on graphite films were not successful. This may have been due to the wrinkled surface of the sample or channeling effects of the ions.

Further thickness information may be gained by using an electron beam to probe the graphite thin films, e.g. EELS or a STEM with an energy analyzer.

The damage to the crystal structure of graphite caused by thinning techniques can be estimated using Raman spectroscopy. The Raman spectrum of single crystal graphite and HOPG has two Raman active modes at 42 ± 1 cm^{-1} ("rigid layer shear", E_{2g_1} mode) [120,121] and 1581 ± 1 cm^{-1} (high frequency E_{2g_2} mode) [122,166,120]. The frequencies of these two in-plane modes are in exact agreement with theory developed by Al-Jishi and Dresselhaus [2]. Tuinstra and

Koenig [166] were the first to note the existence of a peak near 1355 wavenumbers present in microcrystalline graphite. The peak results from a breakdown in the k-section rule which activates a normally-inactive (in-plane, breathing A_{1g} mode) Raman mode. The exact origin of this peak is still an open question [52,106,123]. However, it is agreed that the relative intensity of the 1355 cm^{-1} mode with respect to the 1581 cm^{-1} mode varies as the inverse of the crystal planar domain size L_a [166] over a range 25 Å $\lesssim L_a \lesssim$ 1 μm [123]. Dillon *et al* have claimed that the 1355 cm^{-1} peak intensity increases in the Raman spectra of a-C films as they are annealed up to the point where ~ 20 Å islands of graphite are formed, at which point the intensity ratio begins to decrease upon further annealing [52]. The ratio of the intensities of the 1355 cm^{-1} mode and the 1581 cm^{-1} mode then provides a direct measure of the in-plane domain size of graphite microcrystals.

Raman analysis was performed by R. Zallen and Mark Holtz at VPI on samples of graphite and a-C. The spectra were obtained at room temperature in a near-backscattering or reflection geometry. Excitation was primarily by the 5145 Å green line of an argon ion laser (Coherent model 90), however spectra were confirmed using the 4880 Å

blue argon ion laser line. The power of the incident beam ranged from 10 mW to 100 mW at the sample. Scattered light was collected by an elliptical mirror or using a Micromate microscope attachment which allows the probe beam to be positioned to within ± 10 μm in the sample plane. The light was analyzed using a double monochromator (SPEX model 1403) with the spectral band pass consistently set at 5.0 cm^{-1}. A photomultiplier tube operating in the photon counting mode was used for detection. The background of the photomultiplier was less than 25 cps. The spectrometer is computer controlled and repetitive scans were taken in most cases to improve the signal-to-noise ratio. Scanning rates ranged between 0.4 cm^{-1}-sec^{-1} and 2.5 cm^{-1}-sec^{-1}.

The measured spectra for crystalline graphite and a graphite sample thinned with tape to ~ 1000 Å both exhibit a single band at 1581 cm^{-1} wavenumbers in Figure VI.5. The figure also shows spectra of crystalline graphite thinned using TPE and RIE which have additional peaks at 1360 cm^{-1} (50 cm^{-1} FWHM) and 1364 cm^{-1} (38 cm^{-1} FWHM) wavenumbers respectively. The ratio of the 1360 cm^{-1} integrated peak intensity to that of the 1581 cm^{-1} peak is 1.1 for the TPE sample. This corresponds to an in-plane domain size of 45

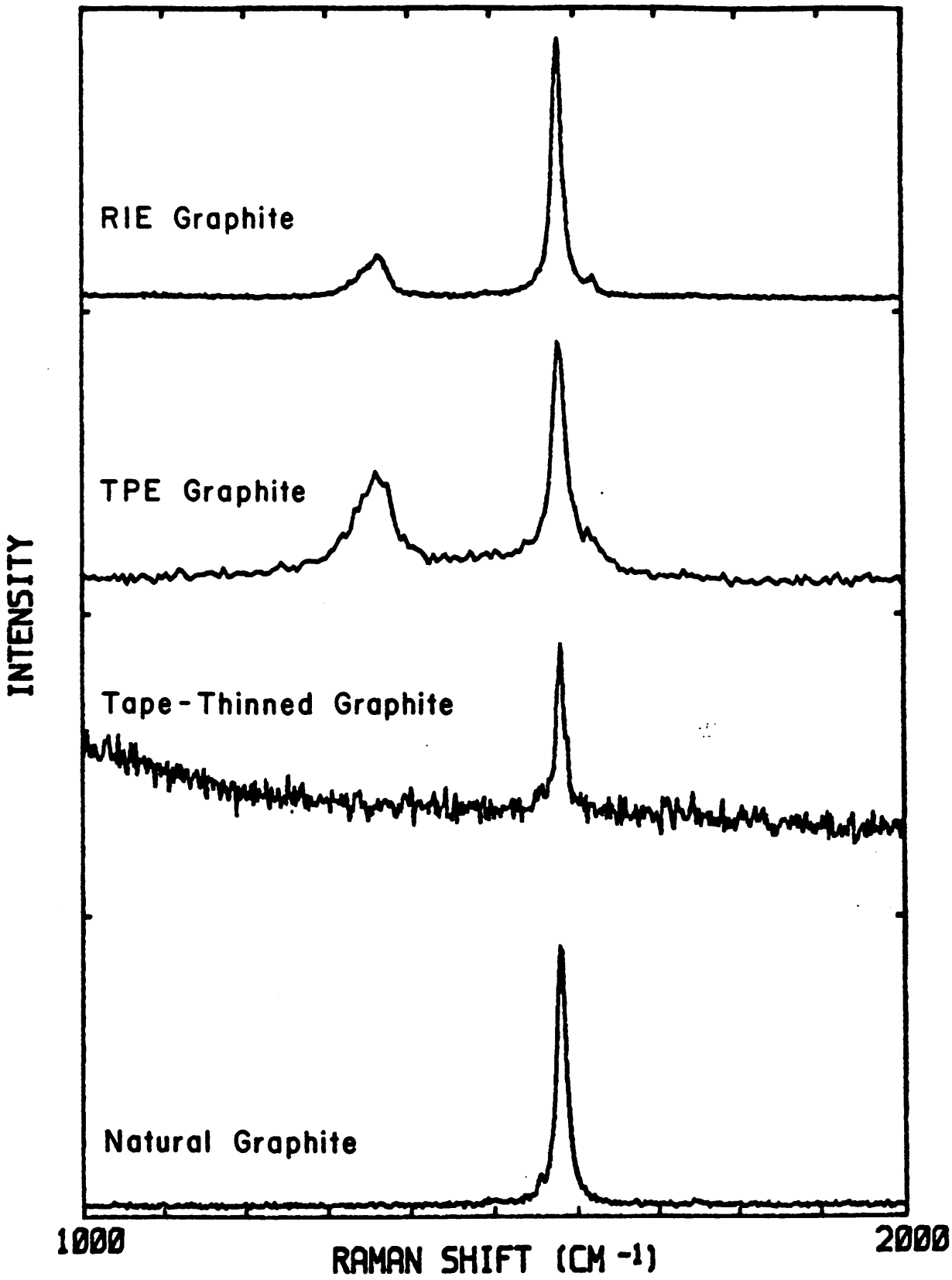

Figure VI.5 Raman Spectra of Thinned Graphite Films.

Å according to Tunistra and Koenig [166]. This ratio is 2.9 for the RIE sample which corresponds to $L_a \approx 120$ Å. Both of these etched samples exhibit a small peak at ~ 1622 cm^{-1} which Nemanich and Solin [123] also identify as a disorder-induced feature.

The width of the 1581 cm^{-1} band remained constant (14 cm^{-1} FWHM) in the natural graphite, HOPG, tape-thinned graphite, and the RIE graphite spectra. The TPE graphite sample exhibited a width of 20 cm^{-1} FWHM. Defects and buckling within the microcrystallite platelets can cause bands to broaden and/or shift. Evidence suggests that this type of damage is not induced by RIE, but does result from TPE.

These Raman spectra clearly show that damage was introduced into the graphite films during etching, however the films remain microcrystalline and graphitic in nature. It is likely that the domains show preferential alignment within the plane, because they originated from a single crystal as opposed to HOPG where the microcrystals are randomly oriented within the plane. The c-axes in the etched films are probably also somewhat misaligned due to etching.

Figure VI.6 shows Raman spectra of graphite, HOPG, and a-C. The a-C spectra has a broad amorphous band from 1000 cm^{-1} to 1650 cm^{-1} centered at 1525 cm^{-1}.

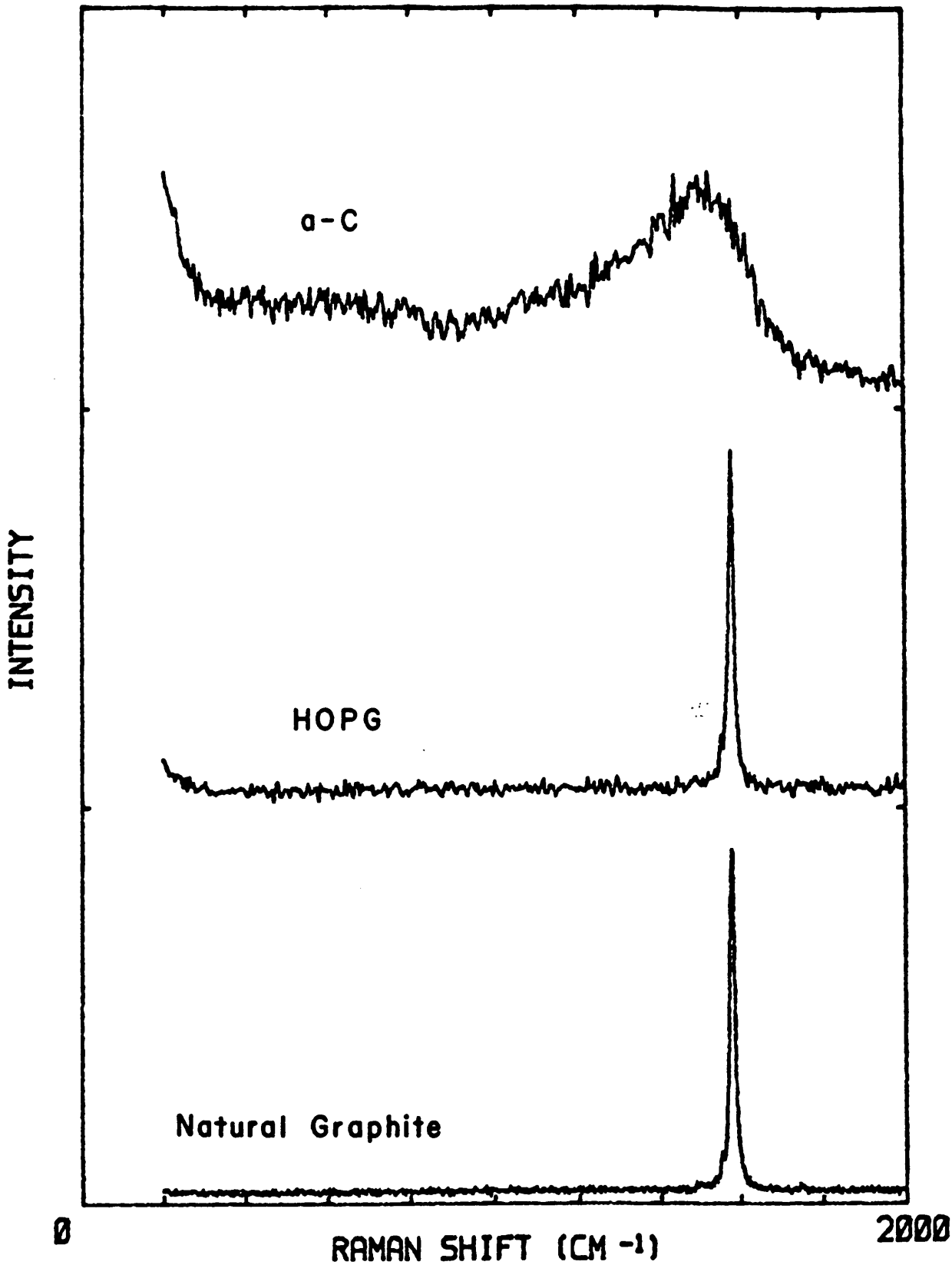

Figure VI.6 Raman Spectra of Carbon films.

This spectrum is in good agreement with measurements of other evaporated and sputtered a-C films [52,172].

The graphite crystal orientation in the spectrometer is crude, but adequate, given the resolution of the machine. The c-axis of the crystal is well known since it is perpendicular to the sheets. However, the specimen is wrinkled badly when mounted on the holder which introduces an uncertainty of at least $\pm 5^{0}$ in the alignment of the c-axis with the incident z-axis. Smaller uncertainties from the target holder alignment and crystal irregularities are therefore insignificant.

It is possible to align the in-plane axes to some extent in a simple manner. There are hexagonal crystal faces in the cleaved natural graphite visible with either the naked eye or a low power optical microscope. Noting these faces before etching the graphite allows orientation to within a few degrees. These crystal faces are still visable after RIE.

Ideally, the orientation can be found quite precisely by examining the Bragg diffraction patterns with the (e,e') arm in the elastic mode. Here, our spectrometer acts as a high energy electron diffraction (HEED) spectrometer. No attempt has been made to do this with the graphite sample yet. The present instrumental resolution of the spectrum makes it insensitive to the in-plane orientation.

VII. PHYSICS OF CARBON

Carbon has three common stable solid forms, graphite, diamond, and amorphous carbon (a-C). These form a very interesting system which exhibits perhaps the most varied range of physical properties of any element. Diamond is renowned for both its optical brilliance and extreme hardness, while graphite is a very soft material and is black in color. From a solid state viewpoint, diamond is a semi-conductor with a 3-dimensional (3D), 4-fold tetrahedrally bound crystal structure. Graphite is a semi-metal with a 3-fold bonding which is almost 2D in nature. Amorphous carbon has properties which vary over a wide range depending primarily on the temperature and method of formation. It exhibits similarities to both graphite and diamond and also has some unique properties. A fourth solid form, hexagonal diamond or white graphite, has been synthesized under high pressure and also found naturally occurring in small amounts in meteorites [42].

Crystal forms of carbon are very difficult to synthesize and to date natural crystals are of superior quality. This is due in large measure to the extremely high melting points of diamond and graphite, $\gtrsim$ 3530

°C [28,167]. Large single crystals of both graphite and diamond are rare. The properties of a synthetic form of graphite, highly oriented pyrolytic graphite (HOPG), are discussed since a significant amount of the research on graphite has been carried out on this material.

This section presents a summary of the physics of the three common forms of solid carbon, including a description of their physical properties, crystal structure, bonding, band structure, and density of states. Table VII.1 compares some important properties of these materials. These materials have been studied extensively by numerous techniques. Graphite and diamond can be characterized as well understood systems, while a-C still lacks a good theoretical framework to describe its structure.

A. Graphite

Graphite has a hexagonal crystal structure which can be considered nearly 2D. There are planes of hexagonal rings which are widely separated. The intraplanar nearest neighbor distance, 1.42 Å, is less than half of the interplanar spacing. These layers, or basal planes, are stacked with an *abab* scheme that produces two distinct types of lattice sites. These two sites are illustrated in Figure VII.1a. The solid vertical lines connect lattice sites that are located directly above and

Table VII.1 Physical properties of carbon

Property	Graphite	Diamond	a-C
Crystal Structure	Hexagonal	Diamond	
Space Group	C6/mmc[a]	Fd3m[a]	--
Lattice Constants (Å)	a_0+2.4612(1)[a] c_0=6.7079(10)@15°C[a]	3.5670(1)[a]	--
Coordination number	3	4	3 or 4
Nearest neighbor separation (Å)	1.415 (intraplanar)[b] 3.354(interplanar)[b]	1.5445[b]	--
Melting Point (°C)	~3530[b]	>3550 [d]	
Density (gm-cm^{-3})	2.2670(4)[a]	3.5155(3)[a]	1.7-2.2[a]
Index of refraction: real imaginary	2.2[c] 0.7[c]	2.4173[d]	1.4-2.7[i,j,k] 0.03-0.75[i,j,k]
Hardness (Mohs scale)	1-2[d]	10[d]	~6[d]
Resistivity (room temp.) (Ω-cm)	4x10^{-5} (interplanar)[e] 5x10^{-2} (intraplanar)[e]		1-10[l] 0.6[m]
Hall Coefficient (room temp.) (cm^3-C^{-1})	-0.05[e]		+0.25 to -0.05[e]
Band Gap (eV)	0.0[f]	5.5[g,h]	a-C 0.5[n] a-C:H 1.5-2[o]

[a] Robie et al (Ref. 147)
[b] Ubbelohde and Lewis (Ref. 167)
[c] Taft and Phillips (Ref. 162)
[d] CRC Handbook (Ref. 28)
[e] Klein (Ref. 95)
[f] Willis et al (Ref. 187)
[g] Himpsel et al (Ref. 82)
[h] Painter et al (Ref. 130)
[i] Smith (Ref. 157)
[j] Stoner (Ref. 160)
[k] Kahn et al (Ref. 91)
[l] McLintock and Orr (Ref. 118)
[m] Measured for our sample

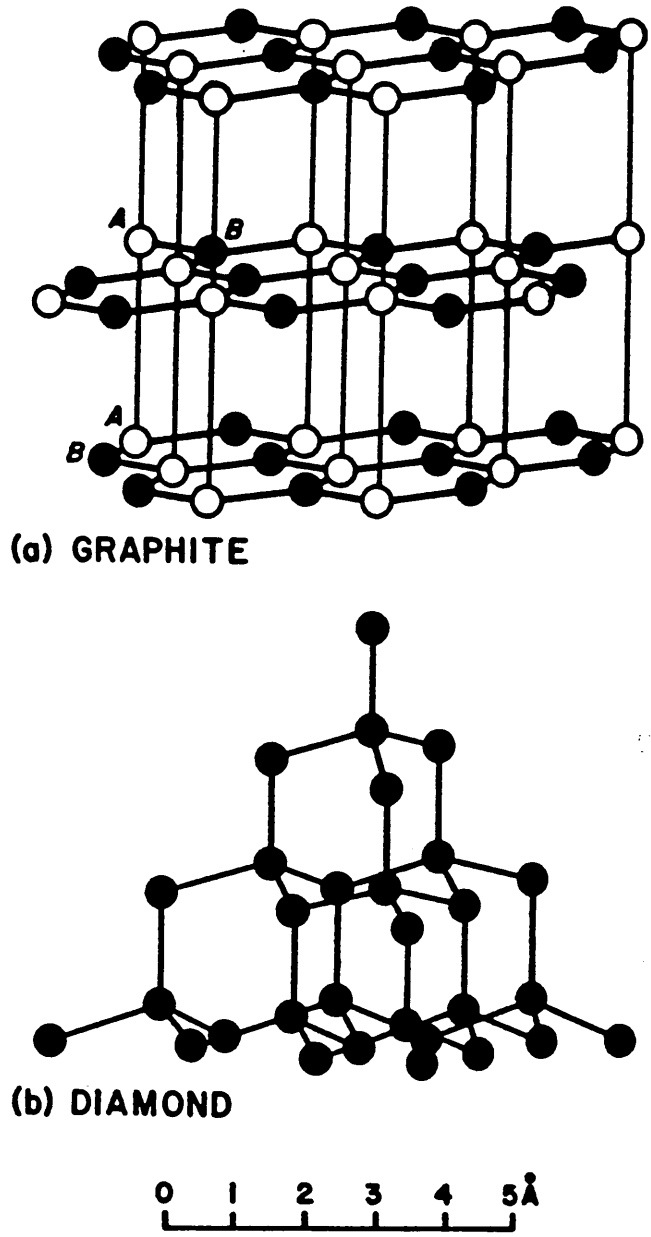

Figure VII.1 Crystal structures of carbon.

below sites in adjacent planes, whereas broken lines connect sites that are above and below empty carbon hexagon centers. The crystal has a C6/mmc space group with a basis of two atoms and four atoms per unit cell.

This planar structure is responsible for the 2D nature of graphite and for the anisotropy in many of its physical, electrical, and optical properties. Extensive reviews of the properties of graphite are given by Ubbelohde and Lewis [167] and Klein [95].

The crystal structure has been very accurately determined by x ray diffraction and is reviewed in reference 167. Reference is made to early work on graphite by pioneers in the field including Ewald [55] and Debye and Scherrer [51]. An excellent study of the valence-electron-density distribution compares x ray diffraction data [38] with pseudopotential calculations [84] and finds that the overall agreement between the two density distributions is $\pm$ 0.15 e/Å^3 throughout the entire unit cell.

The Brillouin zone (BZ) of graphite is also hexagonal. The BZ is shown in Figure VII.2 with points of symmetry labeled. The lattice vectors and reciprocal lattice vectors are also listed.

The six electrons of each carbon atom form 2 core bands and four valence bands in graphite. The two 1s electrons form nearly atomic orbitals with a binding energy

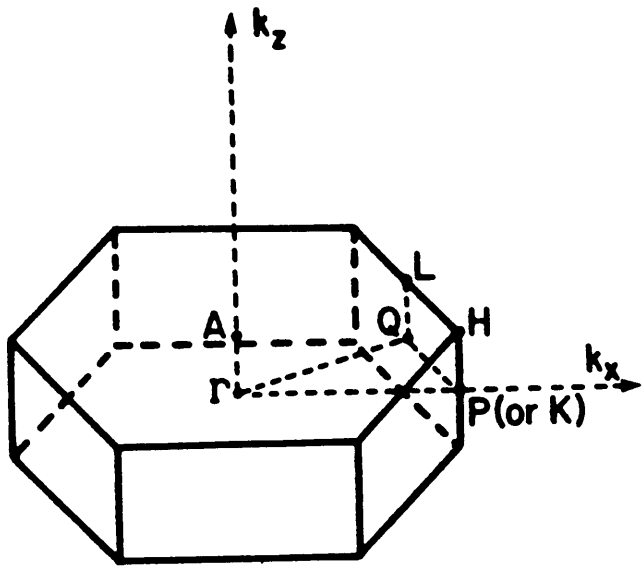

(a) 3-D Brillouin Zone

The first Brillouin zone for graphite. The point Γ is at the center of the zone. The names A, L, Q, H, and P(or K) are points of high symmetry on the zone boundary.

Lattice vectors	Reciprocal lattice vectors
$a_1 = (a_0 , 0 , 0)$	$b_1 = \left(\frac{2\pi}{a_0} , -\frac{2\pi}{\sqrt{3}a_0} , 0 \right)$
$a_2 = \left(\frac{1}{2}a_0 , \frac{\sqrt{3}}{2}a_0 , 0 \right)$	$b_2 = \left(0 , \frac{4\pi}{\sqrt{3}a_0} , 0 \right)$
$a_3 = (0 , 0 , c)$	$b_3 = \left(0 , 0 , \frac{2\pi}{a_0} \right)$

$a_0 = 2.46$ Å

$c_0 = 6.70$ Å

Figure VII.2 Brillouin zone of graphite.

of 284.5 eV [49,116,62]. The four valence electrons form two types of bonds.

The upper valence band results from the π bond formed between layers. In the 2D approximation to graphite this band is formed simply by the $2p_z$ atomic orbitals with their nodal plane being the basal plane and their axes of symmetry perpendicular to the plane. The bond can be visualized as a lobe extending at right angles to the basal plane. More careful calculations show that this band is split when one considers the two independent types of lattice sites. Electrons in these loosely bound orbitals are primarily responsible for conduction.

A second π band is the conduction band with a zero direct energy gap at the K point on the Brillouin zone boundary. The bond configurations are illustrated in Figure VII.3 where the sign of the wave function at the lattice points is designated by + or - signs. Note that the valence π band has S-symmetry whereas the conduction band has P-symmetry. This is evident since adjacent unit cells are identical for the valence band, but are of opposite phases for the conduction band. π bonds are odd with respect to the basal plane and σ bonds are even. It should also be noted that the bonding configurations in the unit cell are degenerate for the conduction and valence bands at K, as is expected.

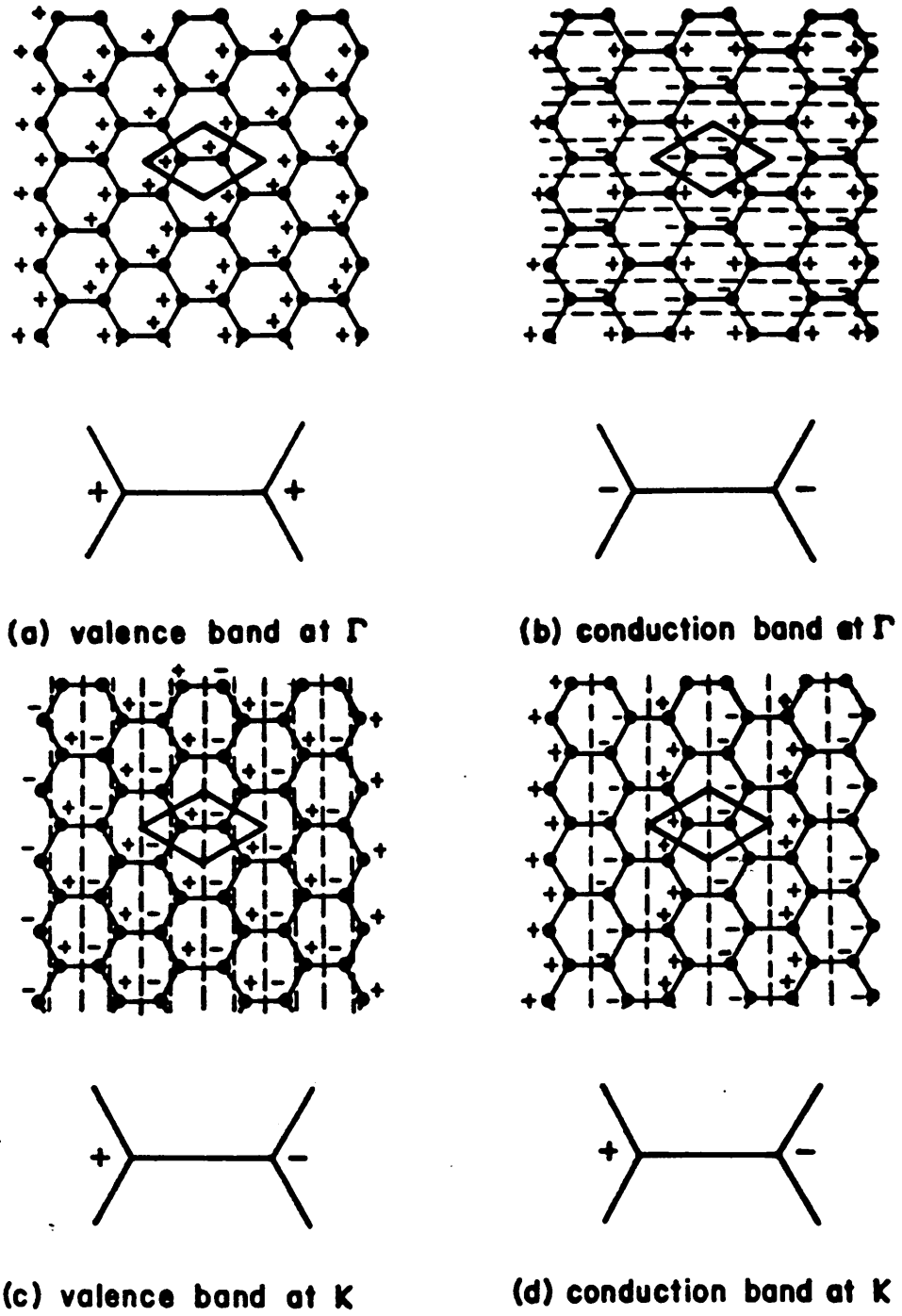

The upper figures show the basal plane structure of graphite. The sign of the p_z wave function at each lattice point is designated by + or - signs. The dashed lines separate regions of like sign. The projection of the unit cell on the basal plane is outlined in heavy lines. The lower figures show the isolated structure within the unit cell. After Wallace (Ref. 173).

Figure VII.3 π bonding in graphite.

The other three valence electrons form hybridized sp^2 orbitals. These σ electrons form tight covalent bonds with nearest neighbor atoms within the basal plane. In a simple tight binding (TB) picture, these orbitals have the form

$$\sum_j e^{i\mathbf{k}\cdot\mathbf{r}_{ij}} \left\{ \frac{1}{\sqrt{3}} \left[\Psi\,(2s) + \sqrt{2}\,\Psi_{\sigma_i}\,(2p) \right] \right\} \quad ; i = 1, 2, 3 \quad \text{(VII.1)}$$

where $\Psi(2s)$ is the carbon 2s atomic orbital and $\Psi_{\sigma_i}(2p)$ are 2p orbitals whose axes are in the directions σ_i joining the graphite atom to its three nearest neighbors [173]. There are three distinct bonding configurations which produce the three σ valence bands. Figure VII.4 illustrates these configurations where the phase of the bond wave functions are designated by + , -, and 0 signs representing phases of + $2\pi/3$, - $2\pi/3$, and 0, respectively. At the Γ-point, the upper two valence bands are composed of wave functions with equal numbers of these three bonding coefficients and the bands have P-symmetry. At the Γ-point, the lowest valence band is composed of all similar bonding coefficients and the band has S-symmetry. At the K-point, all three bands are composed of wave functions with equal numbers of the three phases. Again, note that the bonding configurations in the unit cell are degenerate for the two upper valence bands at Γ and for the lower valence band and one of the upper

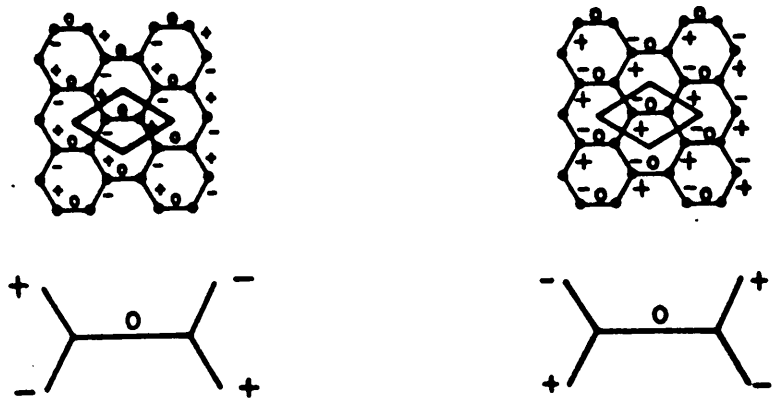

(a) Upper valence bands at Γ

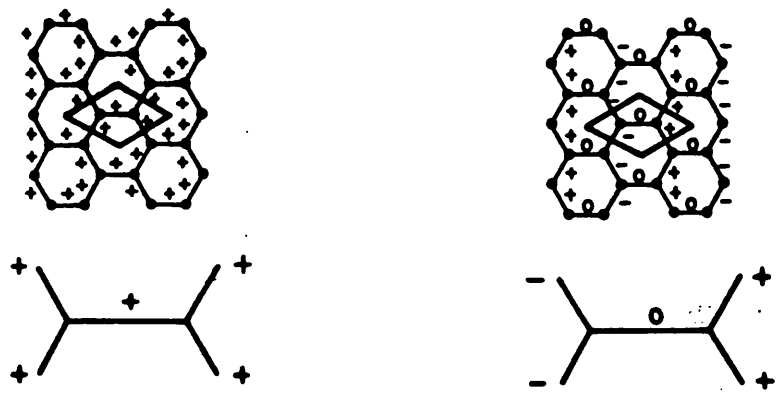

(b) Lower valence band at Γ (d) Lower valence band at K

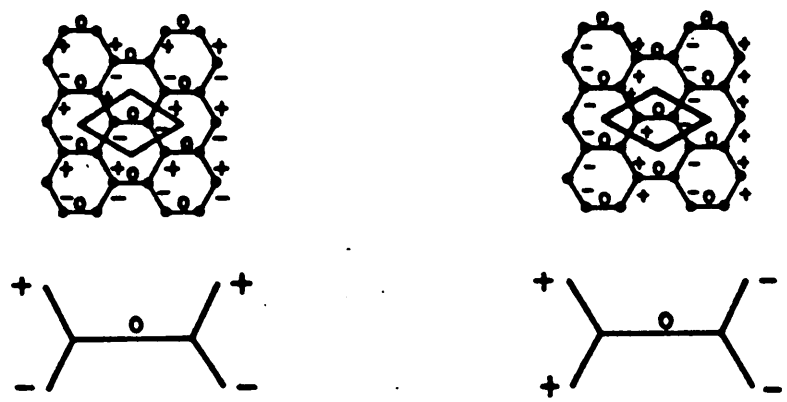

(c) Upper valence bands at K

Figure VII.4 σ bonding in graphite.

valence bands at K. Another configuration composed of anti-bonding orbitals is responsible for a σ conduction band with S-symmetry. The 3D splitting of the σ bands is much less than for the π bands.

Band structure calculations of graphite have been the focus of extensive efforts over many years. Early TB calculations by Wallace [173] have been refined and extended as listed in Table VII.2. [11,84,164,111,187]. Pseudopotential calculations by Holzwarth et al [84] and discrete variation method calculations by Willis et al [187] and Tatar and Rabii [164] are in good agreement with each other and best agreement with experiment. The band structure is illustrated in Figure VIII.12.

Table VII.3 list experimental determinations of the binding energies at symmetry points using angle-resolved ultra-violet photoemission spectroscopy (ARUPS) [112,163, 186,53,105], integrated-angle photoemission spectroscopy (PES) [15], and x ray photoemission spectroscopy (XPS) [116]. These experiments have been performed on both single crystals [163,15,112,116,105] and HOPG samples [186,53]. Synchrotron radiation [15,112,53] and Helium lamps [163,186,105] were used as ultra-violet sources and the Al Kα line was used as the x ray source [116].

The conduction and valence bands density of states has been calculated by Painter et al [129] using a

Table VII.2 Graphite Band Structure -- Theory*

Method / Band		Pseudopotential (a)	Pseudopotential (b)	(e)	Cellular (d)	Discrete Variational (e)	Discrete Variational (f)
Upper σ	Γ	3.3	4.1	2.5	1.2	4.2	4.7
	M	7.0	7.6	5.3	4.7	7.3	8.1
	K	11.2	11.6	6.0	8.8	11.0	11.9
	A	3.2	4.0			4.1	
	L					7.2	
Middle σ	Γ	3.3	4.1	2.5	1.2	4.2	4.7
	M	14.0	14.7	11.2	11.4	14.1	14.5
	K	13.3	14.3	12.3	10.8	13.7	13.9
	A	3.2	4.0			4.1	
	L					12;2	
Lower σ	Γ	20.8	21.5	13.8		19.5	20.8
	M	15.1	16.1	13.0	12.5	14.9	15.7
	K	13.3	14.3	12.3	10.8	13.7	13.9
	A	20.7	21.4			19.1	
	L					14.6	
Upper π	Γ	7.1	7.1		5.8	6.4	6.6
	M	2.2	2.7		1.8	2.0	2.0
	K	-0.2	0.0		0.0	0.0	0.0
Lower π	Γ	9.1	8.7		8.0	8.1	8.2
	M	3.1	3.9		2.6	2.5	2.7
	K	0.5	0.6		0.7	0.5	0.5
Both π	A	8.1	7.9		6.9	7.3	
	L	2.7	3.1		2.2	2.3	
	H	-0.2	0.0			0.0	

* Energies in eV below top of valence band

(a) Hedlin-Lundquist exchange correlation potential; Holzwarth et al (Ref. 84)

(b) Slater exchange correlation potential; Holzwarth et al (Ref. 84)

(c) Bianconi et al (Ref. 15)

(d) Spherically symmetric potential; Mallett (Ref. 111)

(e) Tatar and Rabii et al (Ref. 164)

(f) Willis et al (Ref. 187); Painter and Ellis (Ref. 129)

Table VII.3 Graphite band structure--experiment.

Method		XPS	PES	ARUPS					
Source		Al Kα	Synchro-tron	Synchro-tron	HeII	HeI	He	Synchro-tron	He
Band		(a)	(b)	(c)	(d)	(d)	(e)	(f)	(g)
Upper σ	Γ	5	5.7	5.3	4.3		4.6	4.6	
	M	8	8	8.8	8.3		8.3		8.0
	K	13.8		10.5	11.5				
	A								
	L								
Middle σ	Γ	5	5.7	5.3	4.3		4.6	4.6	
	M		13.6		14.5				
	K	17-19			14.6				
	A								
	L								
Lower σ	Γ	24	22.5					20.6	
	M	17-19			16.0		(15.0)		
	K	17-19			14.6				
	A								
	L								
Upper π	Γ			7.6	(8.1)	(8.0)		7.2	
	M	3-4	3	2.4	(2.8)	(2.9)			
	K			0.35	(1.2)	0.2	(1.5)		0.2
Lower π	Γ			9.0	9.3	8.9		8.1	8.6
	M	3-4	3	3.0	(2.8)	(2.9)			
	K				1.2	0.6	(1.5)		0.7
Both π	A			8.3	8.1	8.0	8.2		
	L			2.7	2.8	2.9			2.7
	H				(1.2)	0.2	(1.5)		0.2

(a) McFeely et al (Ref. 116)
(b) Bianconi et al (Ref. 15)
(c) Marchand et al (Ref. 112)
(d) Takahashi et al (Ref. 163)
(e) Williams (Ref. 186)
(f) Eberhardt et al (Ref. 53)
(g) Law et al (Ref. 105)

* Energies in eV below top of valence band. Uncertain measurements in parentheses.

variational method. A more detailed calculation for the π band density of states has been performed by Tatar and Rabii [164] using the Johnson-Dresselhaus model [88]. The structure of the density of states is well correlated with symmetry points in the band structure.

Photoemission measurements of N(E) have been made by Bianconi et al [15], McFeely et al, [116] and Thomas et al [165] which are in agreement with theory (See Figure VII.5). Willis et al performed secondary-electron emission spectroscopy and found their results in good agreement with calculations for the conduction band density of states [187]. An x ray emission spectrum was taken by Chalkin [36].

The relative contributions to the valence density of states from s and p orbitals can be inferred from comparisons of the intensities of x ray and photoemission spectra. The $2s \rightarrow 1s$ transition is forbidden in the K emission spectrum while 2p electron K x ray emission is completely allowed. By contrast, the cross section for photoemission for a 2p electron is lower by a factor of 13 than that of a 2s electron [66]. McFeely et al [116] were able to demonstrate that states with binding energies greater that $\sim$ 15 eV -- corresponding to the lower σ bands -- were almost exclusively S-bands whereas states with $E_B \lesssim 4$ eV -- corresponding to the p_z

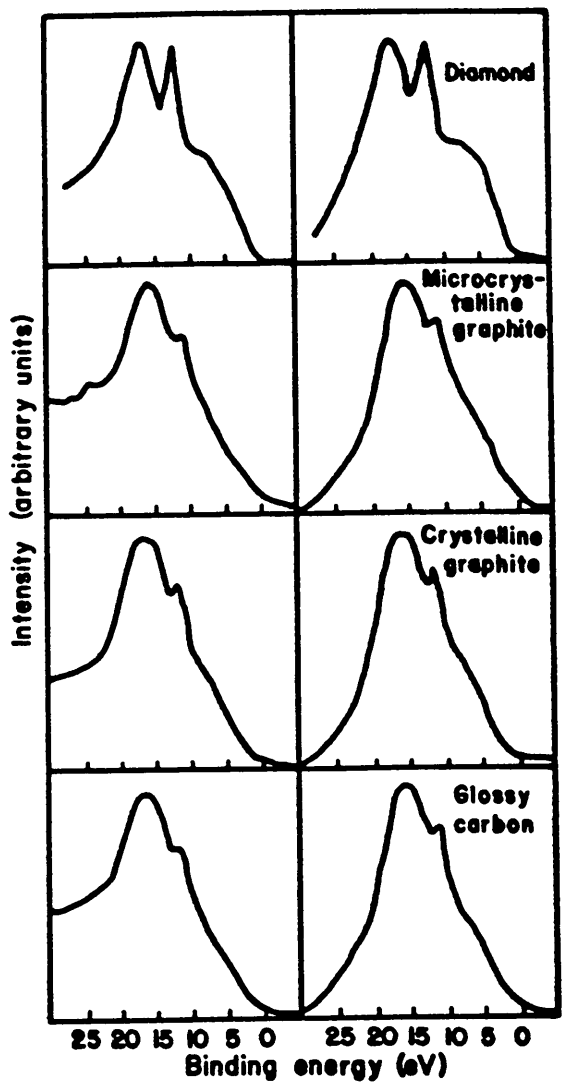

Figure VII.5 Valence band XPS spectra of carbon.

Valence-band XPS spectra, before (left) and after (right) correction for inelastic losses, of diamond, microcrystalline graphite, crystalline graphite, and glassy carbon.

orbitals in the π bands -- were almost exclusively from 2p orbitals. The intermediate energies -- corresponding to the upper σ bands -- were mixed in origin with gradually more 2p character nearer the π bands.

The electron momentum density of pyrolytic graphite summed over all bands for both **q** parallel and perpendicular to the c-axis have been calculated from several models [179,48,139]. Cooper and Leake calculated the contributions from the π and σ bands separately [48]. The band-resolved calculations show significant differences in the two directions, while the total momentum density is almost identical for both directions (See Figure VII.6). In principal, (e,2e) measurements of the momentum density can be separated by band and this difference should be apparent.

Measurements of the total electron momentum density have been made using Compton scattering [179,48,178] and positron annihilation [14] for both momentum directions in pyrolytic graphite. These are in agreement with theory.

Berko et al [14] have calculated the total momentum density for polycrystalline graphite and found that it agrees well with their positron annihilation results. Measurements of polycrystalline graphite with Compton scattering produced a broader peak [179,139].

Electron energy loss spectra have been taken by

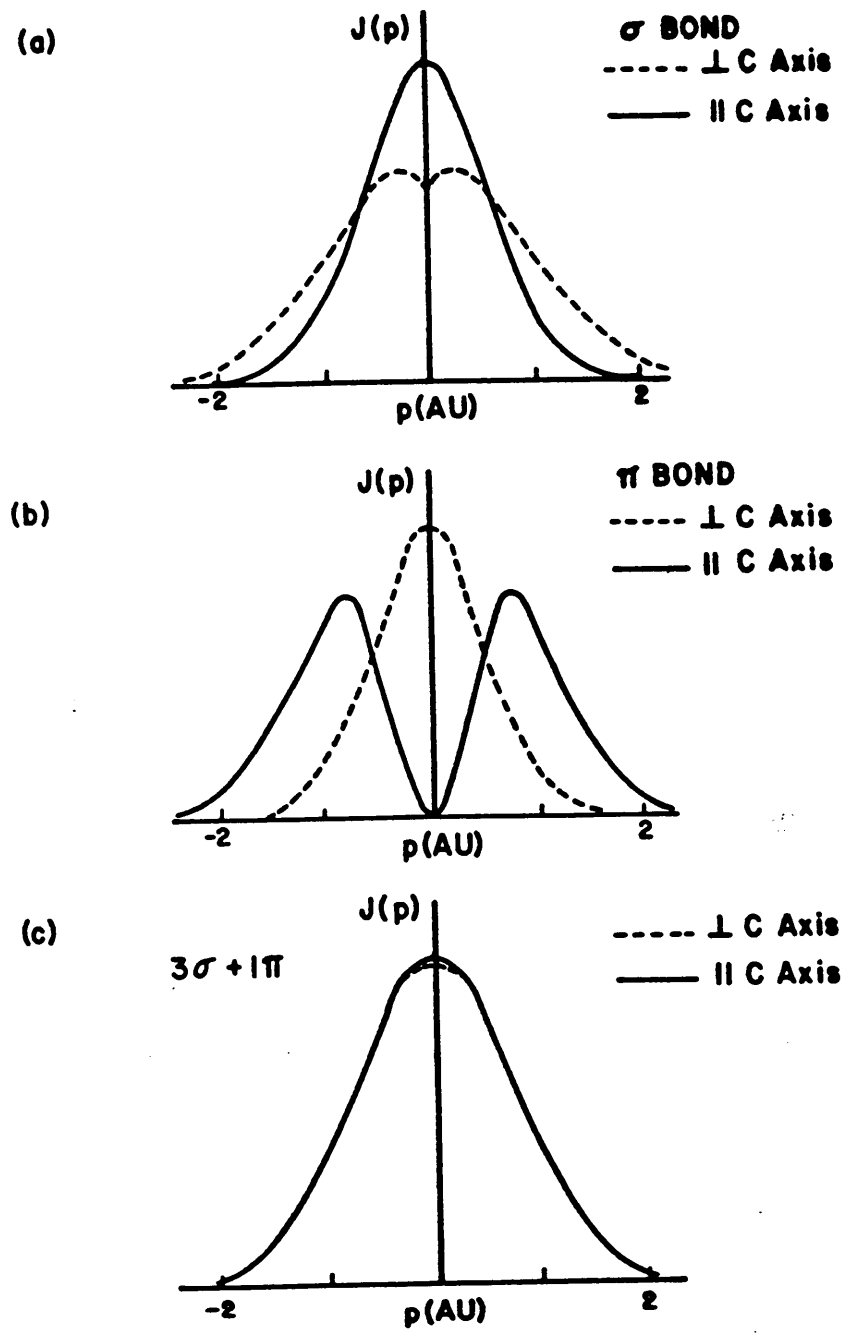

Figure VII.6 Directional Compton profiles of graphite.

The directional Compton profiles for (a) the σ and (b) the π bands of graphite. The sum of the three σ plus the π orbitals appropriate for the valence band of graphite is shown in (c). After Cooper and Leake (Ref. 48).

several groups [62,40,25,26,78]. These have been used to calculate dielectric functions and optic properties. They are discussed in more detail in Section II.A. Reflectivity measurements were performed by Greenaway et al [70]. A detailed studied of optical properties was done by Taft and Phillip [162]. Raman spectra are discussed in Section VI.

Highly oriented pyrolytic graphite (HOPG) is a synthetic form of graphite which is often used in studies of graphite properties. It is made up of small crystallites of graphite with basal plane dimensions on the order of $\sim$ 1000 Å. The c-axis of the crystallites are very highly oriented, however they are randomly oriented within the basal plane. A review of the properties of HOPG is given by Klein [95].

B. Diamond

Diamond has a diamond crystal structure with fcc symmetry. The atoms exhibit 4-fold tetrahedral bonding with a nearest neighbor distance of 1.5445 Å [167]. The crystal structure is illustrated in Figure VII.1b. Diamond has a Fd3m space group with a basis of two atom and two atoms per unit cell.

The crystal structure has been very accurately determined by x ray diffraction and is reviewed by

Ubbelohde and Lewis [167]. Early measurements were performed by Bragg and Bragg [23].

The BZ of diamond is a truncated octahedron. It is shown in Figure VII.7 with points of symmetry labeled. The primitive lattice vectors and reciprocal lattice vectors are also listed.

The 1s core bands of diamond are similar to the graphite core bands. There are four valence bands which result from the sp^3 hybridized orbitals. The bottom band is a wide dispersing band with S-symmetry, very similar to the lowest valence band in graphite. The upper three bands are degenerate at Γ and disperse downward, characteristic of P-symmetry bands. In the Γ-L and Γ-X directions the upper two bands are degenerate.

The wave functions at the Γ-points can be described in terms of 3D networks of positive and negative bonding coefficients similar to the description of graphite given above [184]. At the lower Γ-point the wave functions are formed with all positive bonding coefficients, analogous to the lowest Γ-point in graphite. These orbitals result is the S-symmetry of the lowest diamond band. The wave functions at the upper Γ-point, which is triply degenerate, are formed by three distinct configurations of equal numbers of positive and negative bonding

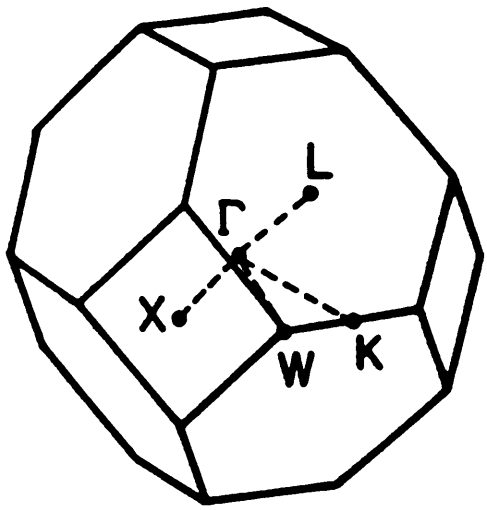

The first Brillouin zone for diamond. The point Γ is at the center of the zone. The names K, L, W, and X are points of high symmetry on the zone boundary.

Primative lattice vectors	Reciprocal lattice vectors
$\vec{a}_1 = (\frac{a_o}{2}, \frac{a_o}{2}, 0)$	$\vec{b}_1 = \frac{2\pi}{a_o}(1, 1, -1)$
$\vec{a}_2 = (0, \frac{a_o}{2}, \frac{a_o}{2})$	$\vec{b}_2 = \frac{2\pi}{a_o}(-1, 1, 1)$
$\vec{a}_3 = (\frac{a_o}{2}, 0, \frac{a_o}{2})$	$\vec{b}_3 = \frac{2\pi}{a_o}(1, -1, 1)$

$a_o = 3.567\text{Å}$

Figure VII.7 Brillouin zone of diamond.

coefficients. These configurations account for the P-symmetry nature of the upper three diamond bands.

Band structure calculations have been performed using a variety of methods including the discrete variational method [123], LCAO [39,194], augmented plane waves [94], tight binding [37], pseudopotentials [9], and variational cellular method [56]. Table VII.4 shows that all these theories are in approximate agreement with each other and the limited experimental measurements available [82]. It is interesting to note that calculations based on s^2p^2 and sp^3 orbitals yield very similar results. The band structure is illustrated in Figure VIII.14.

Himpsel et al have made measurements of the binding energies at several symmetry points using ARPES with synchrotron radiation [82].

It should be noted that energies listed in Table VII.4 are referenced to the top of the valence band. The band gap in diamond is 6 eV, [56,82,130,194] therefore the Fermi level should be $\sim$3 eV above this reference.

The conduction and valence bands density of states has been calculated by Painter et al [130] using a discrete variational method. This calculation is in very good agreement with XPS measurements by McFeely et al [116] and x ray emission spectra measured by Wiech and Zöpf [182].

Table VII.4 Diamond Band Structure

		THEORY					EXPERIMENT	
METHOD		Pseudopotential (a)	LCAO (b)	LCAO (c)	APW (d)	Discrete Variational (e)	ARPES (f)	XPS (g)
BAND								
Upper	Γ	0.00	0.00	0.00	0.0	0.0	0.0	0.0
	X	6.43	6.09	6.27	5.2	5.3		
	L	2.86	2.82	2.82	2.4	2.4		
Middle	Γ	0.00	0.00	0.00	0.0	0.0	0.0	0.0
	X	12.90	12.17	12.43	11.5	11.6		
	L	13.73	12.18	13.09	11.6	11.7		12.8 ± 0.3
Lower	Γ	21.68	20.44	21.03	19.6	19.6	24.2 ± 1.0	21 ± 1
	X	12.90	12.17	12.43	11.5	11.6		
	L	15.79	15.17	15.29	14.4	14.5		15.2 ± 0.3
Band Gap			6.3			6.0		6.0 ± 0.2

(a) Bachelet et al (Ref. 9)
(b) Zunger and Freeman (Ref. 194)
(c) Chelikowsky and Louie (Ref. 39)
(d) Keown (Ref. 94)
(e) Painter et al (Ref. 130)
(f) Himpsel et al (Ref. 82)
(g) McFeely et al (Ref. 116)

*Energies measured in eV below the top of the valence band.

The relative contribution of s and p orbitals to the density of states of diamond was also examined by McFeely et al [116] as discussed above. The fractional p mixing varied from 16% for binding energies between 24 and 20 eV monotonically to 92% for binding energies between 4 and 0 eV. Thus, the bottom band is primarily 2s in character, the middle band is of mixed character, and the upper bands are primarily 2p in character. An average hybridization of $s^{1.2} p^{2.8}$ was derived, which is in remarkable agreement with chemical intuition which would favor sp^3 over $s^2 p^2$.

The electron momentum density of diamond summed over all bands for several momentum directions have been calculated [194,138,139]. As with graphite, the total momentum densities do not differ a great deal in different momentum directions, but should show significant differences when the bands are separated. The total momentum density of diamond is quite similar to graphite although it is somewhat broader.

Experimental measurements with Compton scattering [138,178], and positron annihilation [102] for crystalline and powdered diamond are in good agreement with each other and in reasonable agreement with theory.

The theory of diamond's optical properties are discussed by Painter et al [130] and other theoretical

and experimental work is reviewed by Roberts and Walker [145]. Raman work is discussed in Section VI.

C. Amorphous Carbon

The nature of a-C is a very complex problem. Beyond the difficulty arising from the random long-range ordering in typical amorphous materials, carbon is complicated by the coexistence of the tetrahedrally bonded diamond crystal structure and the 3-fold planar structure of graphite. A central issue in understanding a-C is the relative importance of three- and four-fold bonds. Extensive experimental effort has yet to achieve a unified interpretation and theory is only in its infancy. Some possible structure models are discussed below.

Deciding exactly what materials are a-C is not an easy task. For our purposes, we can distinguish four types of carbon which will be discussed. The family of materials known as turbostatic carbons appears to be very fine grained graphitic powders. Many evaporated and sputtered a-C films appear to be primarily graphitic in character. Another class of a-C films are referred to as "diamond-like." Finally, there are hydrogenated amorphous carbons (a-C:H) which are prepared from chemical vapor deposition of organic materials.

Turbostatic carbons include carbon black (soot) and

coke. X ray [16,140,153] and electron diffraction measurements indicate that such carbons have a very finely dispersed graphite structure, i. e. small graphite regions with very little a-axis correlation. Short and Walker [153] estimate the in-plane crystal dimension of carbon black to be 15-20 Å and the c-axis thickness to be about 15 Å. They estimate a 5-10% increase in the inter-planar spacing which is consistent with reductions in bulk density. X ray PES [116], EELS [116], and Compton scattering [178] measurements for turbostatic carbons are in good agreement with data for graphite. Raman spectra show a gradual transition from crystalline graphite through microcrystalline graphite to a-C as discussed in Section VI.

The properties of a-C films differ greatly and appear to depend on the method of formation and the deposition temperature. **In general**, evaporated and sputtered films prepared at higher temperatures (room temperature and above) can be classified as graphite-like, whereas evaporated and sputtered films deposited at low temperatures and films prepared by chemical vapor deposition (CVD) can be classified as diamond-like [79]. Many of the diamond-like properties become more graphitic in nature upon annealing of the films.

It should be remembered that the films used in our (e,2e) study were prepared by arc evaporation at room

temperature (see Section VI). Therefore, these films should be expected to fall in the graphite-like category. The measured EELS and Raman spectra for these films are supporting evidence for this claim.

The hardness and semiconducting nature of graphite-like a-C films were early evidence for tetrahedral bonding. More recent measurements indicate that some a-C films are primarily graphitic in nature although some diamond-like bonding can not be ruled out.

Electron diffraction by Boiko et al of electron-beam evaporated films exhibits pronounced graphitic character [19]. They propose that their film consists of regions of oriented and unoriented graphitic islands (with coherent sizes of $\sim$ 10 Å and planar spacings of $\sim$ 4-4.5 Å) cemented with disordered carbon. Mildner and Carpenter conclude from neutron-diffraction data that tetrahedrally bonded atoms in a-C account for at most 10% and probably less than 5% of the atoms [118a]. XPS measurements by McFeely et al are very similar to graphite and differ from diamond (see Figure VII.5) [116]. The EELS spectrum of a-C shown in Figure VII.8 is also much more similar to graphite than diamond [146,172]. The EELS data of our a-C films taken by Schnatterly [149] (see Figure VIII.3) and measurements by Burge and Misell [26] are even more similar to graphite and exhibits both characteristic graphite peaks at 7 eV and 25 eV (see Section II.A).

Extended electron-energy-loss fine structure measurements by Batson and Craven on carbon K-ionization edges also show a graphite-like structure [12]. Raman spectra for evaporated and sputtered a-C were also found to be much closer to graphite than that of diamond (see Section VI) [52,172]. Based on Raman data, Wada et al have proposed a model for a-C which is based on random-network-type planar clusters of graphite structures ~ 20 Å in size, which have dangling bonds around the clusters' edges [172].

Grigorovici et al have measured the temperature dependence of electrical conductivity, piezoresistance, and thermopower, as well as optical reflectivity and transmission, for electron beam evaporated a-C films [71]. Based on electrical conductivity and optical measurements they estimate an energy gap of .65 eV. Their reflectivity measurements also show features which can be attributed solely to diamond and graphite alone. They conclude that a-C is made up of interconnected islands of both diamond and graphite structure, with a predominance of graphite.

Beeman et al [13] reviewed the radial distribution functions from electron diffraction [19,92], and the Raman and vibrational density-of-states spectra [52,172] for a-C. Their comparison of computer models of a-C structures with varying percentages of tetrahedral bonding lead them to conclude that this percentage was not likely to exceed 10%.

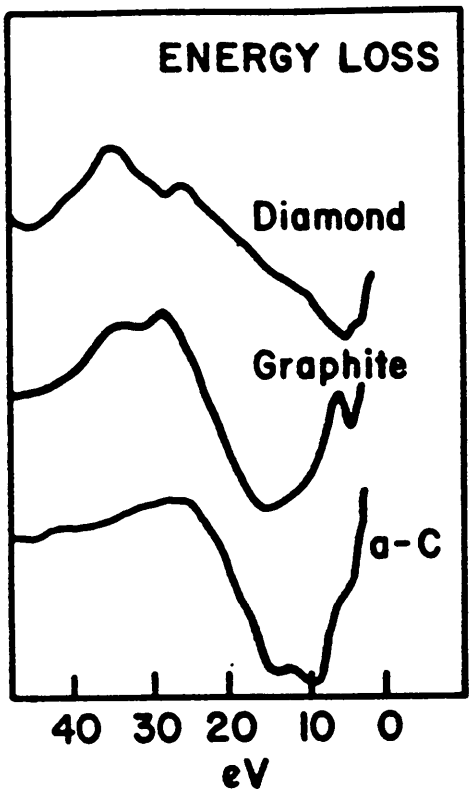

Figure VII.8 Comparison of EELS spectra of a-C, graphite, and diamond.*

* After Robertson (Ref. 146).

They propose a variation of the model by Wada et al -- similar to that mentioned by Robertson [146] -- which consists of three-coordinated planar regions with occasional four-coordinated atoms allowing changes in orientation of the planes. These graphitic regions have fairly randomly oriented planes so that the bulk material would be isotropic. Their model regions had little distortion in bond length and bond angle, yet they found that there were significant numbers of five- and seven-membered rings incorporated into the model structures. These planar regions are quite similar to the 2D random-network structure discussed by Zallen [191]. Further reference to this model is made in Section VIII.C.

Many properties of "diamond-like" a-C have been studied including, conductivity [148], resistivity [79], optical properties [79,91,148], electron diffraction [79], and electron microscopy [128]. In general, these films exhibit properties which can be attributed to the presence of both 3-fold and 4-fold bonding in varying amounts. The interested reader is referred to the literature for details.

The optical [157,89] and dielectric [103] properties, conductivity [89], EELS spectrum [60], and electron diffraction patterns [60] of a-C:H films have been studied. These films are produced from CVD from various organic compounds. In general, they exhibit significant amounts of tetrahedral bonding.

VIII. ANALYSIS OF DATA

A. Description of data

An extensive set of data has been taken for an a-C sample (Sample I.D.# C24) which extends previous measurements [144]. The normalized data, deconvoluted data, and ancillary measurements for this sample are presented below. These data are compared to published theory and experimental results for the band structure, density of state, and electron momentum density of both diamond and graphite. Finally, some conclusions are drawn regarding the structure of a-C based on this data.

Table VIII.1 lists the experimental parameters particular to the C24 data set. The incident electron energy was 20 keV. Data was collected for a range of energies $\mathcal{E}$ between -7.7 and 40.8 eV below E_F (binding voltages V_b between 2 and 25 V with a 1V increment, see Equation III.6). The range of momentum q was -4.2 to 3.1 $Å^{-1}$ with a momentum increment of 0.28 $Å^{-1}$.

Data were collected over a period of approximately two months in units of approximately one week duration. Each of the 648 (E,q) points had data collected for between 0.3 and 1.7 hours, with the central region of interest

Table VIII.1

Table VIII.1 Experimental parameters for C24 data

ENERGY

Range of binding energy	E	-7.7 to 40.8 eV
Range of binding voltage	V_{com}	2 to 25 V
Energy increment	δE	2.0 eV
Meter voltage	V_m	12.0 mV ± <1%
Meter scaling factor	α	2000.1 ± <1%
Meter offset voltage	β	-12.08 ± 0.1 V
Computer scaling factor	γ	1.01 ± 0.01
Computer offset voltage	ΔV_{com}	0.47 ± 0.01 V
Wien filter offset voltages	$V_0{}^a$	0.4 ± 0.5 V
	$V_0{}^b$	0.4 ± 0.5 V
Fermi energy relative to binding energy zero	E_F	-0.5 2 V
Incident beam energy	E_0	20.0 kV
Energy resolution	ΔE	6 eV

MOMENTUM

Range of momentum	q	-4.2 to 3.1 $Å^{-1}$
Momentum increment	δq	0.28 ± 0.05 $Å^{-1}$
Momentum offset	Q_{SHIFT}	-0.84 ± 0.28 $Å^{-1}$
Momentum conversion factor	C_F	0.064 $Å^{-1}$/step ± 10%
Momentum resolution	Δq	0.6 $Å^{-1}$

COUNT RATE

Maximum coincidence count rate	0.23 Hz
Average peak coincidence count rate	0.07 Hz
Average background count rate	0.015 Hz
Maximum signal-to-noise ratio	15
Average signal-to-noise ratio	5
Collection time per (E,q) point	0.32 to 1.68 hours
Statistical error	5 to 10%
Systematic error	10%

having the longer sampling times. The maximum coincidence rate was 0.23 Hz. The average coincidence count rate for (E,q) point in a band was approximately 0.07 Hz and the average background count rate was 0.015 Hz which is a signal-to-noise ratio of about five. The statistical error of the count rates for points in a band was from 5 to 10%. There was also a systematic uncertainty in the count rates of $\sim$ 10%, due primarily to variations of the count rates as a function of momentum.

A three-dimensional plot of the merged normalized (e,2e) data is shown in Figure VIII.1.

The parameters used in the deconvolution of multiple scattering are listed in Table VIII.2. Deconvolution was performed for the energy loss variable only, because momentum broadening was not as significant for the data set as was energy broadening. A discussion of the momentum parameters is included, however, for the sake of completeness. It should be noted that we determined all of the parameters used in the deconvolution empirically, with the exception of the mean free paths. All of these values are in good agreement with other work where it is applicable.

The four momentum broadening functions are shown in Figure VIII.2. The momentum resolution parameters were determined by theoretical electron optics modeling of the

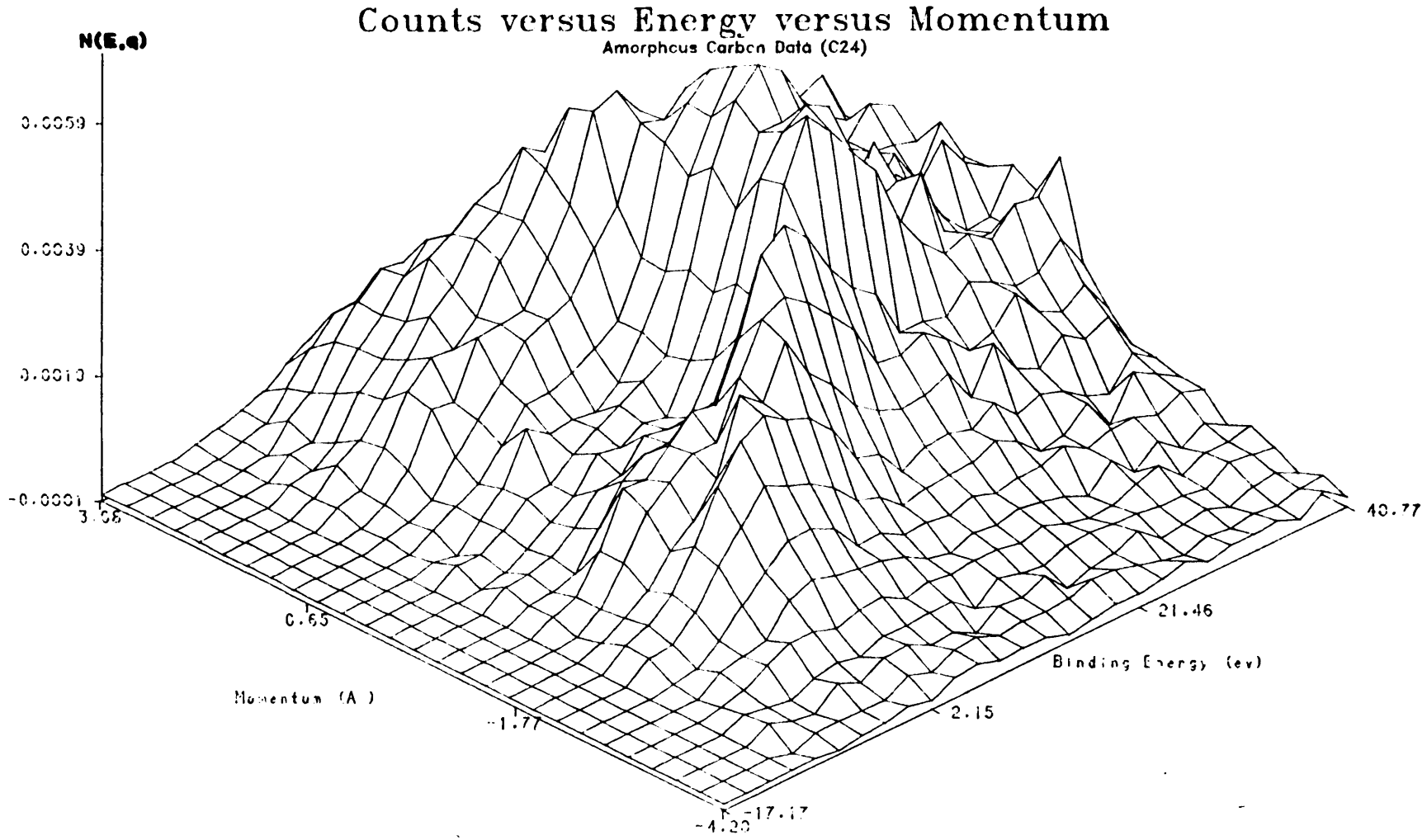

Figure VIII.1 Normalized data for the (e,2e) cross section of a-C

Table VIII.2 Deconvolution parameters for C24 data

Input arm energy resolution	$a_{\mathcal{E}}$	0.85 eV (2 eV FWHM)
Input arm momentum resolution	a_x	$0.5 Å^{-1}$ ($1.1 Å^{-1}$ FWHM)
	a_y	$0.5 Å^{-1}$ ($1.1 Å^{-1}$ FWHM)
Output arm energy resolution	$b_{\mathcal{E}}$	2.4 eV (5.7 eV FWHM)
Output arm momentum resolution	b_x	$0.3 Å^{-1}$ ($0.8 Å^{-1}$ FWHM)
	b_y	$0.3 Å^{-1}$ ($0.8 Å^{-1}$ FWHM)
Inelastic normalization constant	V_1	0.8217 [a]
Inelastic peak position	V_2	24.3 eV [a]
Inelastic peak width	m_2	15.4 eV (FWHM) [a]
Inelastic width parameter	V_3	0.00422 [a]
Elastic momentum parameter	q_0	$3.0 Å^{-1}$ [c]
Plasmon momentum parameter	q_E	$0.040 Å^{-1}$ [a]
Cutoff momentum	q_c	$20.0 Å^{-1}$ [d]
Target thickness (surface density)	t	55 Å ($1 \mu g\text{-}cm^{-2}$)
(EELS fit)		140 Å
Elastic mean free path	λ_e	530 Å (25 keV) [c]
		275 Å (12.5 keV) [c]
Inelastic mean free path	λ_i	300 Å (25 keV) [c,e,f]
		160 Å (12.5 keV) [c,e,f]
Total mean free path	λ_T	192 Å (25 keV)
		101 Å (12.5 keV)
Average mean free path	$\bar{\lambda}$	125 Å

[a] Schnatterly, (Ref. 149)
[b] Hartley, (Ref. 78)
[c] Brünger and Menz, (Ref. 25)
[d] Fields, (Ref. 59)
[e] Penn, (Ref. 132)
[f] Burge and Missell, (Ref. 26)

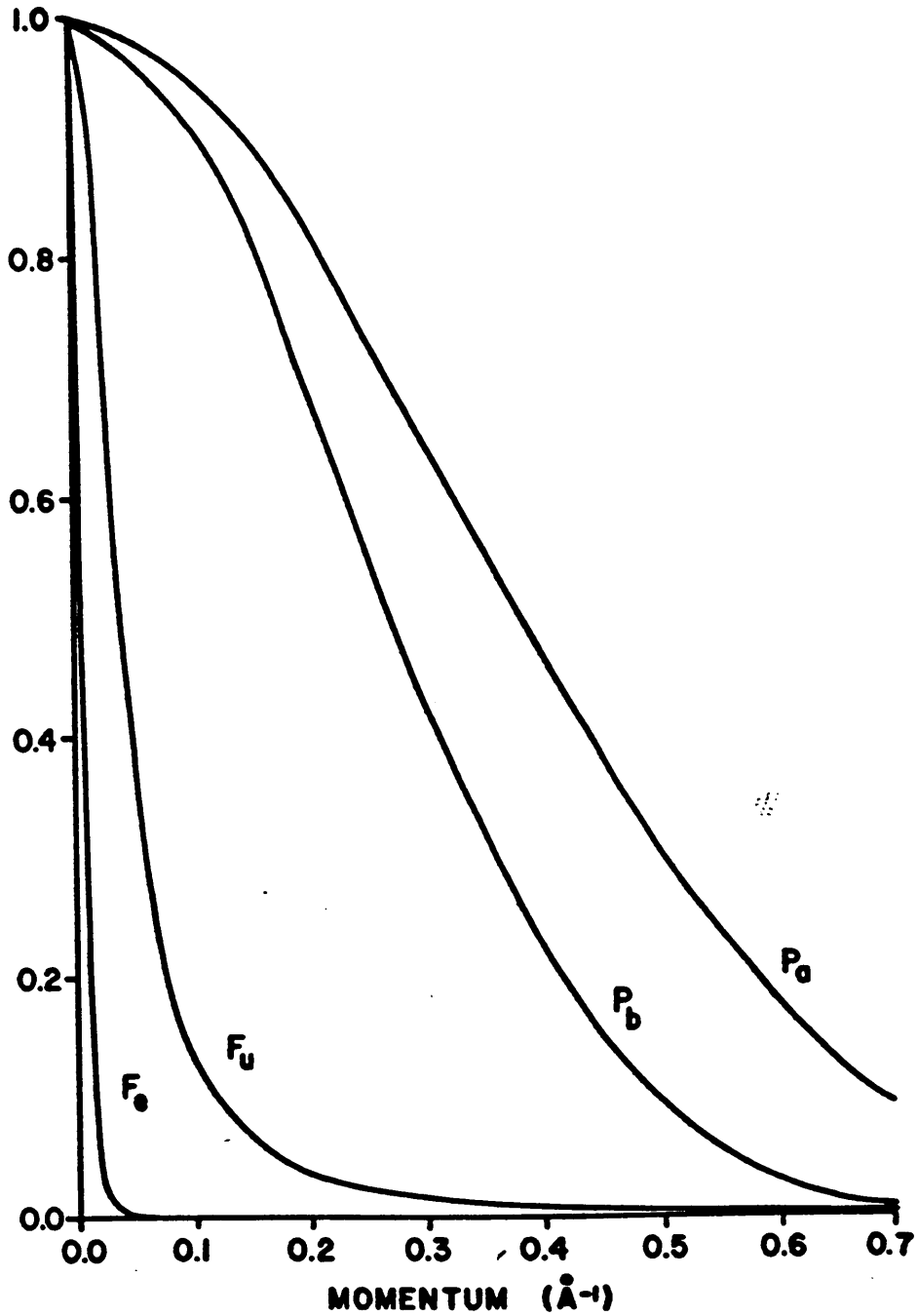

Figure VIII.2 Momentum Broadening functions.

Illustrates the four momentum broadening functions used in deconvolution normalized to one at q=0. F_e (see Equation II.6) is the small angle elastic scattering distribution. F_u (see Equation II.12) is the small-angle inelastic scattering distribution. P_a and P_b (see Equation B.10) are the output and input arm resolution Gaussian distributions, respectively.

lens systems. The input and output resolution functions are Gaussian distributions with FWHM of 1.4 and 1.0 $Å^{-1}$ respectively. A value of 3.0 $Å^{-1}$ [90] was used for the elastic momentum parameter q_0 based on measurements of a-C [25]. The plasmon momentum parameter q_E = 0.040 $Å^{-1}$ based on Schnatterly's determination of $\hbar w_p$ for a-C [149]. An empirical fit of the inelastic data of Brunger and Menz [25] to Equation II.12 yields $q_E = 0.144 \cdot ß$ [90]. The discrepancy in these values can be understood by noting that Equation II.11 is based on the assumption that the plasmon peak is narrow, which is not the case for a-C. The cutoff momentum was estimated as q_c = 20.0 $Å^{-1}$ from Equation II.13. The input arm energy resolution was estimated to have a 2 eV FWHM. The output arm energy resolution was determined from ESWEEP data shown in Figure V.2 to be 5.7 eV FWHM.

Parameters for the energy dependence of small-angle inelastic scattering were determined from high resolution EELS data taken by Cafolla and Schnatterly at the University of Virginia [149]. The data for our a-C films shown in Figure VIII.3 was taken at 150 keV and has been corrected for multiple scattering. The solid line in the figure is a fit to the data using $U(\mathcal{E})$ from Equation II.10 with a main energy loss peak position of 24.3 eV and

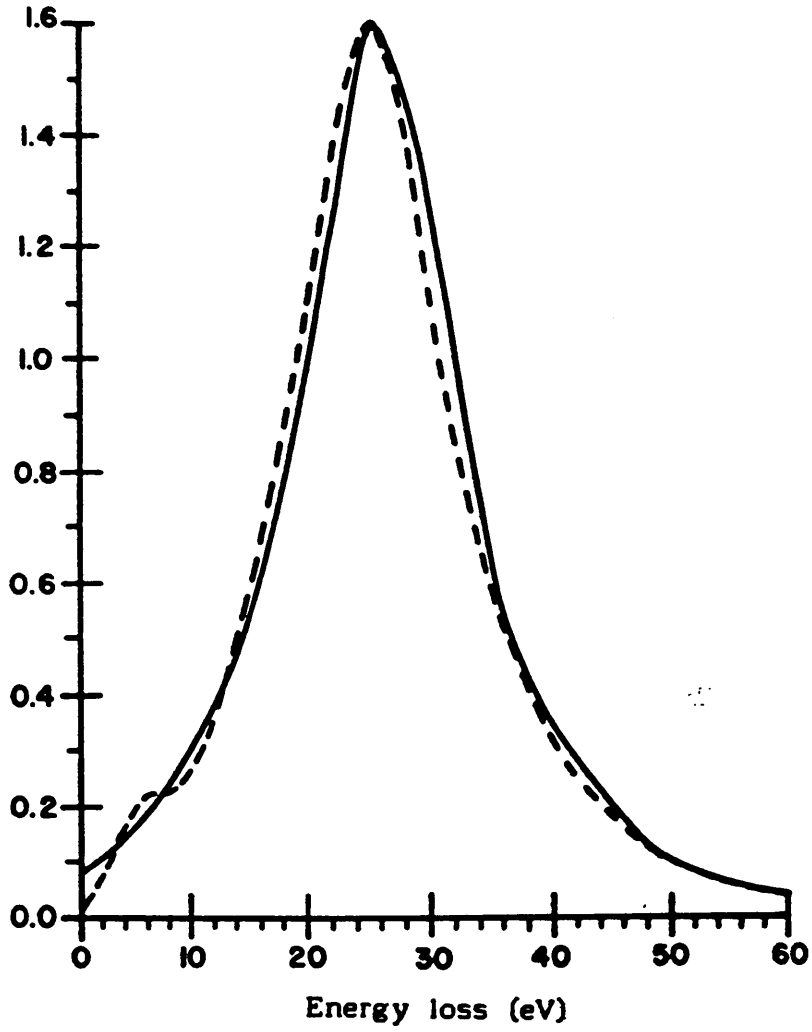

Figure VIII.3 Energy dependence of small-angle inelastic energy loss function U(ℰ).

The points represent high resolution EELS data taken by Steve Schnatterly (University of Virginia) on a-C films. The solid line is the fit to the data using Equation II.10. The vertical scale is arbitrary and normalization has been adjusted to give agreement at the peak.

a FWHM of 15.4 eV. The peak position is in good agreement with graphite data reported by Hartley [49] and a-C data in Burge and Misell [26]. However, the width is less than the value obtained by Burge and Misell (21.8 ± 0.5 eV). The Fourier transform V(t) of $U(\mathcal{E})$ is shown in Figure VIII.4.

The Fourier transform $\mathcal{T}(t)$ of the smearing function is shown in Figure VIII.5b. This is calculated from the $\mathcal{L}$-functions shown in Figure VIII.5a and the coefficients in Table VIII.3 using Equation B.7. The smearing function $\mathcal{S}(E)$, i.e. the inverse Fourier transform of $\mathcal{T}(t)$, is shown in Figure VIII.6.

The elastic and inelastic mean free paths of a-C as a function of energy are graphed in Figure VIII.7. The data are adequate for high incident energies, but must be extrapolated below about 20 keV. This introduces significant error into the mean free path estimates. However, the mean free path only enters into deconvolution calculations as a ratio of the sample thickness to mean free path. This ratio can be determined independently from ESWEEP data similar to that in Figure V.2. Comparison was made between ESWEEP data and the thicknesses for the theoretical function $\mathcal{S}(\mathcal{E})$ which produced the same plasmon ratio (the ratio of the height of the first plasmon peak to the zero loss peak height). Analysis of several

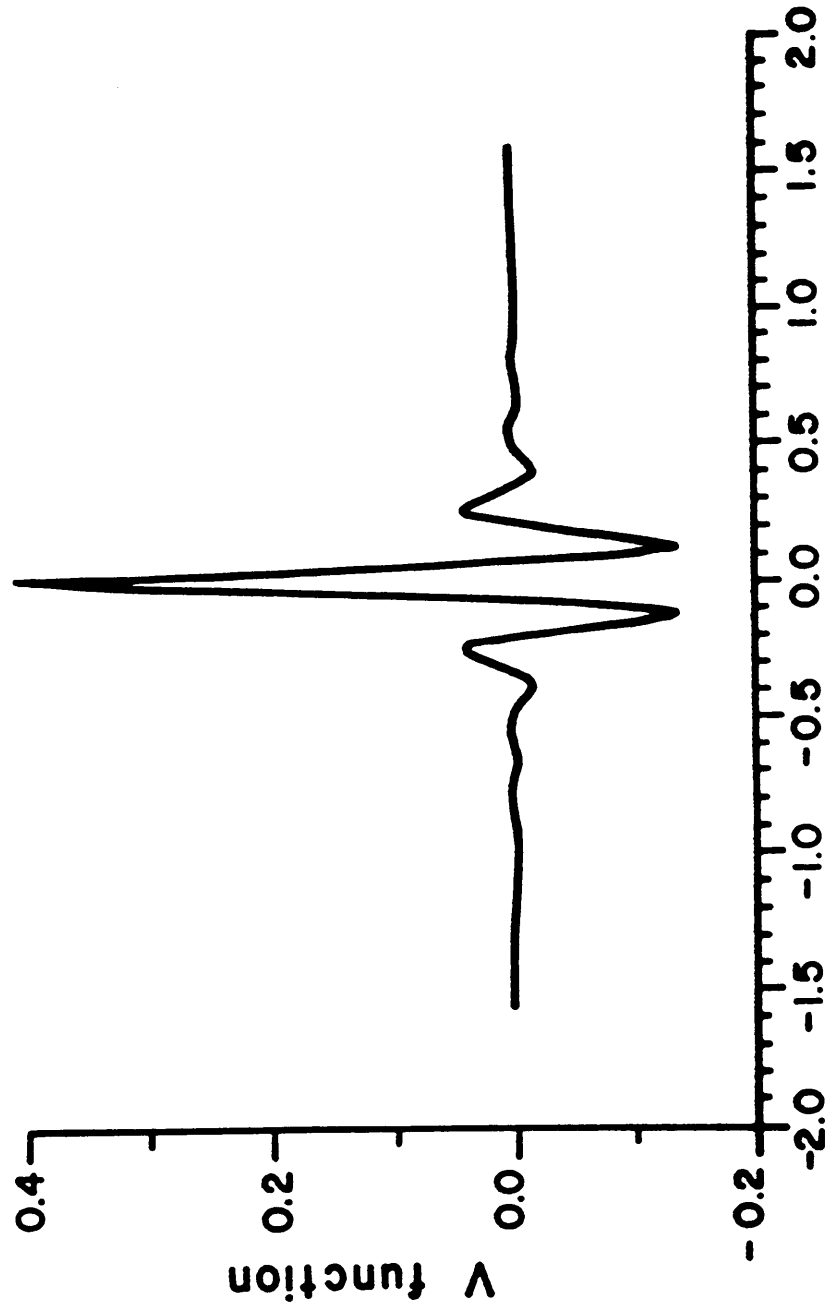

Figure VIII.4 Fourier transform V(t) of the energy dependence of the small-angle inelastic energy loss function

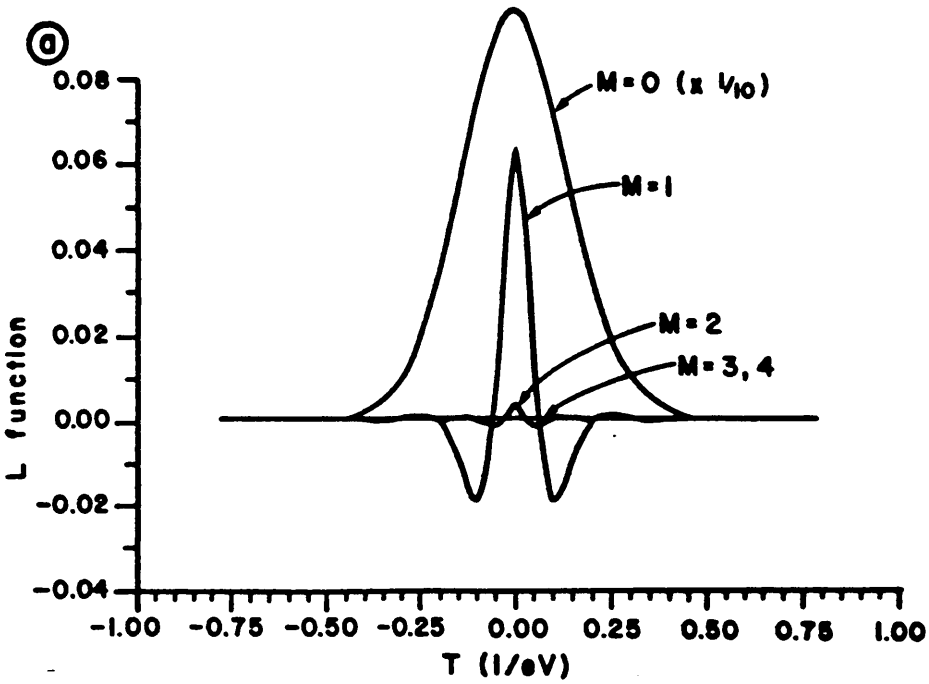

a) shows the first four $\mathcal{L}(t)$ functions (M=0,1,2,3) for the sum in Equation B.7 where M is the number of multiple scatters that occur. Note that the M=0 curve has a reduced scale.

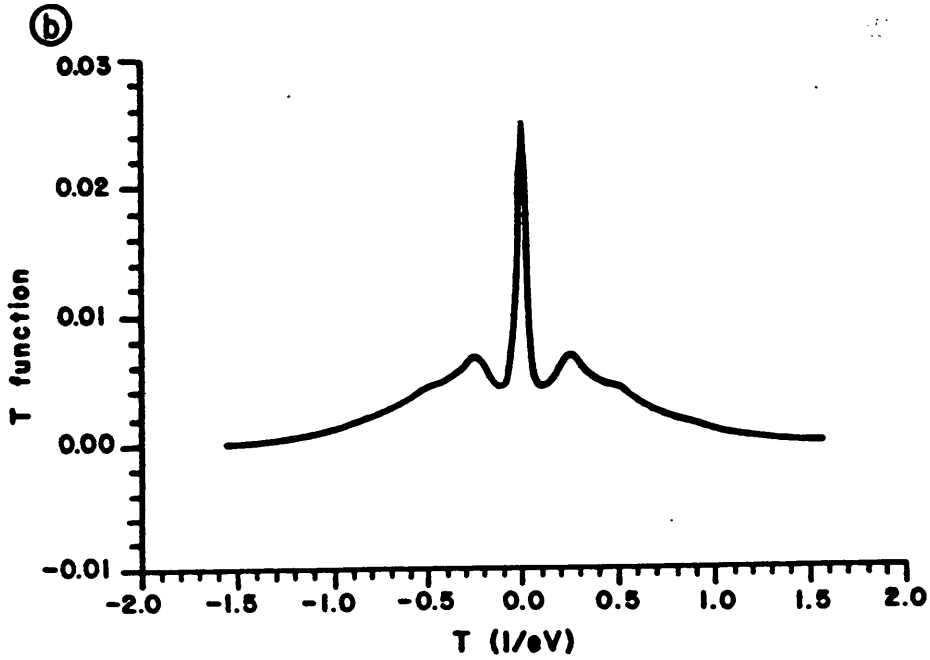

b) Fourier transform T(t) of the smearing function

Figure VIII.5 The Fourier transform T(t) of the smearing function and its compoenet functions $\mathcal{L}(t)$

Table VIII.3 Probability of multiple scattering as a function of target thickness

Number of Scatters	Thickness (Å)					
	50	100	140	150	200	250
0	0.6040	0.3805	0.2703	0.2491	0.1688	0.1178
1	0.2905	0.3365	0.3123	0.3031	0.2522	0.2040
2	0.0803	0.1776	0.2177	0.2229	0.2284	0.2133
3	0.0144	0.0699	0.1165	0.1264	0.1623	0.1766
4	0.0011	0.0208	0.0507	0.0586	0.0972	0.1255
5	--	0.0045	0.0175	0.0223	0.0499	0.0783
6	--	0.0005	0.0043	0.0065	0.0216	0.0430
7	--	--	0.0006	0.0012	0.0075	0.0204
8	--	--	--	0.0001	0.0021	0.0111
Plasmon Ratio	0.083	0.160	0.206	0.22	0.27	0.33

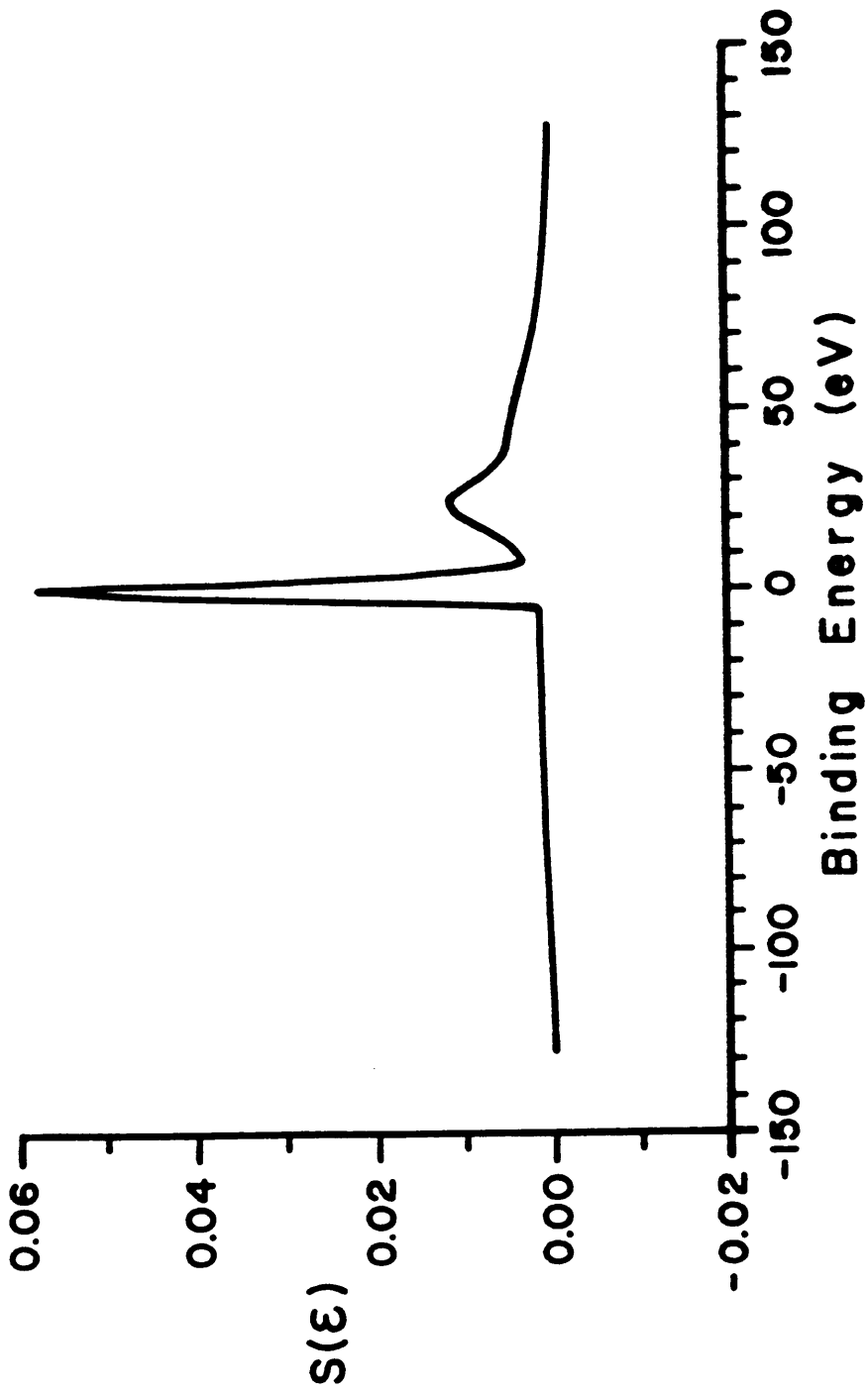

Figure VIII.6 Smearing function S(ℓ)

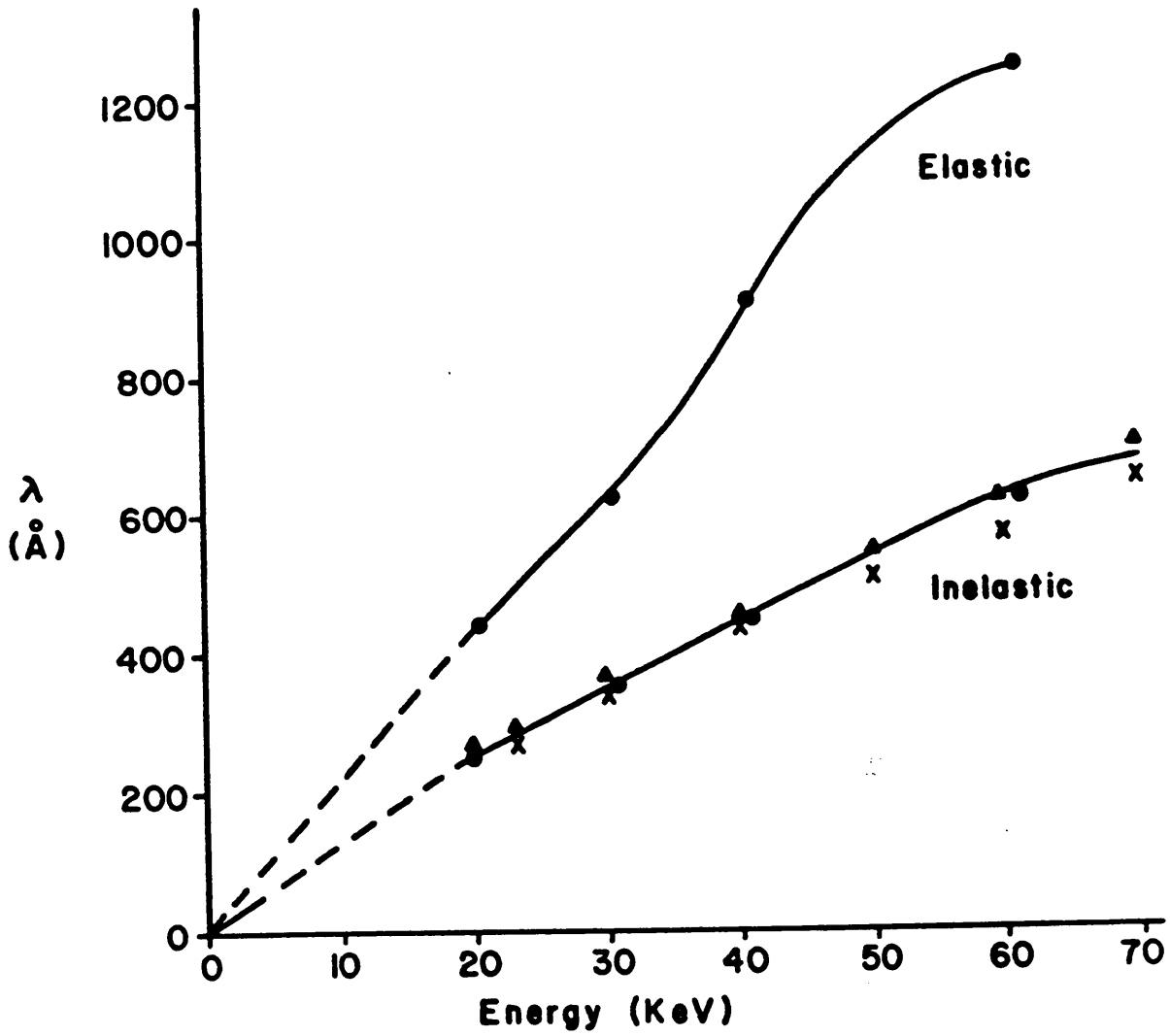

Figure VIII.7 Mean free path vs. incident energy for Carbon

Elastic mean free path curve based on data for a-C from $20<E_o<60$ keV after Brunger and Menz (ref. 25). Inelastic mean free path curve based on data for a-C from $20<E_o<70$ keV after Brunger and Menz (Ref. 25) [ ]; Burge and Misell (Ref. 26) [x]; Bohm-Pines theory in Burge and Misell [ ]; and data for graphite from $0.2<E_o<2.4$ keV after Penn (Refs. 132 and 133) and Quinn (Ref. 135).

thicknesses of a-C film suggest that estimates obtained from this method are approximately 2.5 times larger than measured film thicknesses (see Figure VIII.8). These estimates are used only in the deconvolution.

Ten iterations of the deconvolution routine were performed. Further iterations amplified noise in the data and produced larger negative count rates.

The deconvoluted data are presented in Figure VIII.9.

B. Comparison with previous results

The general trends found in the present data are the same as those we reported previously [144]. The resolution in these previous measurements was less and data were not taken at as fine an increments. The only significant discrepancy was in the assignment of the position of the Fermi level which appear to differ by about 4 eV.

The energy density of states can be calculated from the (e,2e) cross section using

$$N(E) = \int |\Phi(q)|^2 \, d^3q \qquad \text{(VIII.1)}$$

For an isotropic distribution this can be expressed as a sum over all momentum points

$$N(E) = \sum_q N(E,q) \, 2\pi q^2 \, \delta q \qquad \text{(VIII.2)}$$

where δq is the spacing between momentum points. It

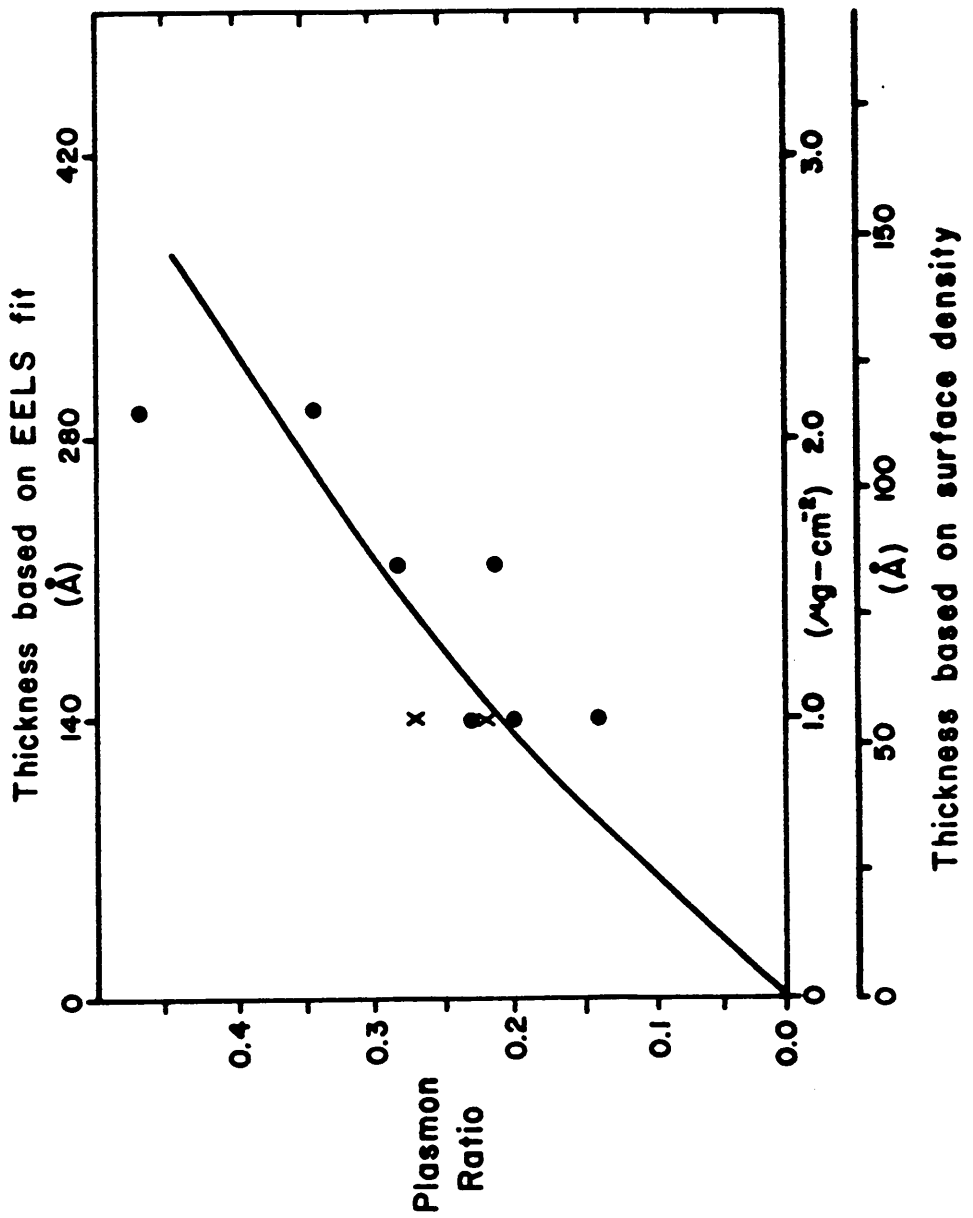

Figure VIII.8 Plasmon ratio vs. thickness

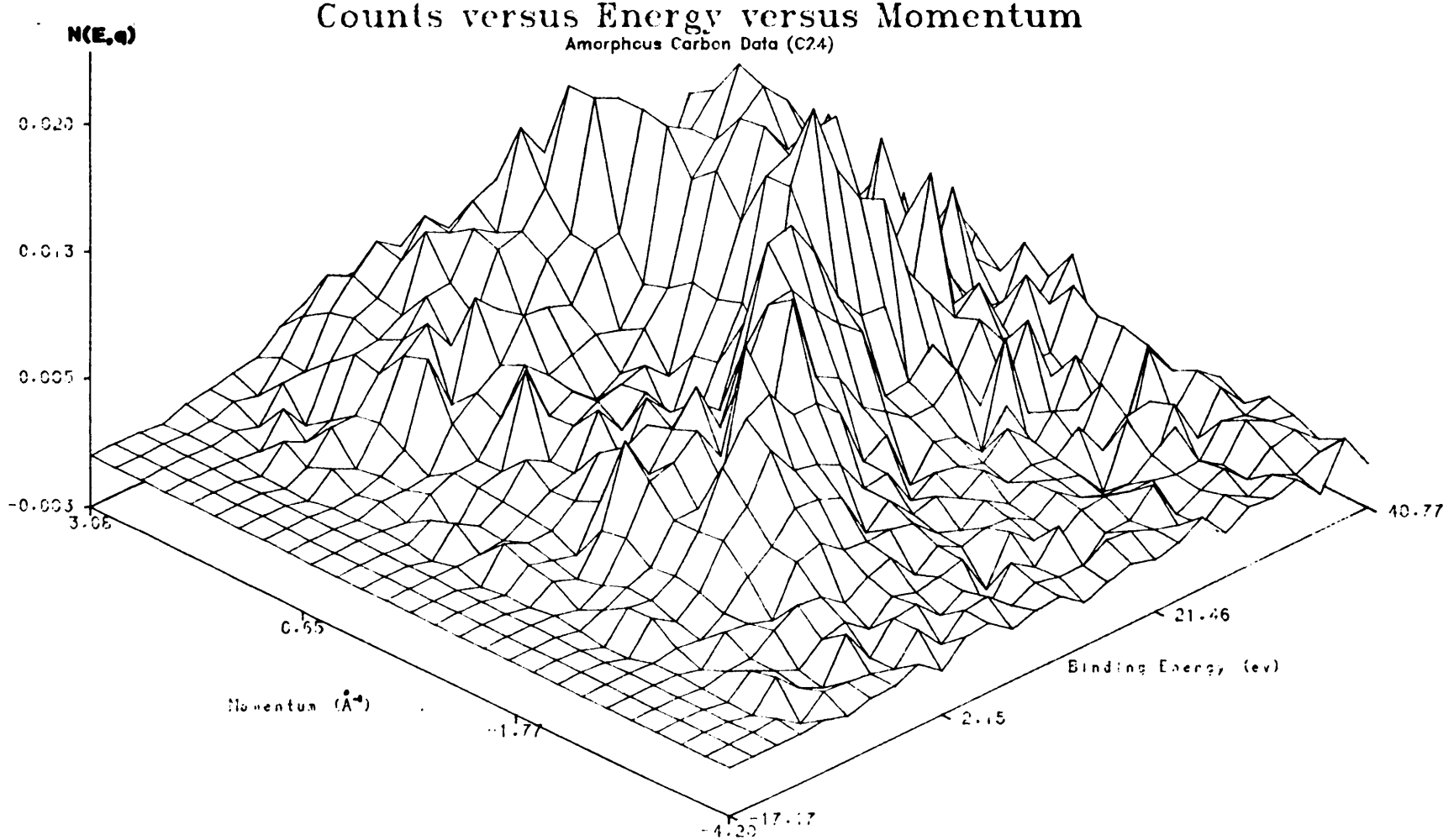

Figure VIII.9 Deconvoluted data for the (e,2e) cross section of a-C

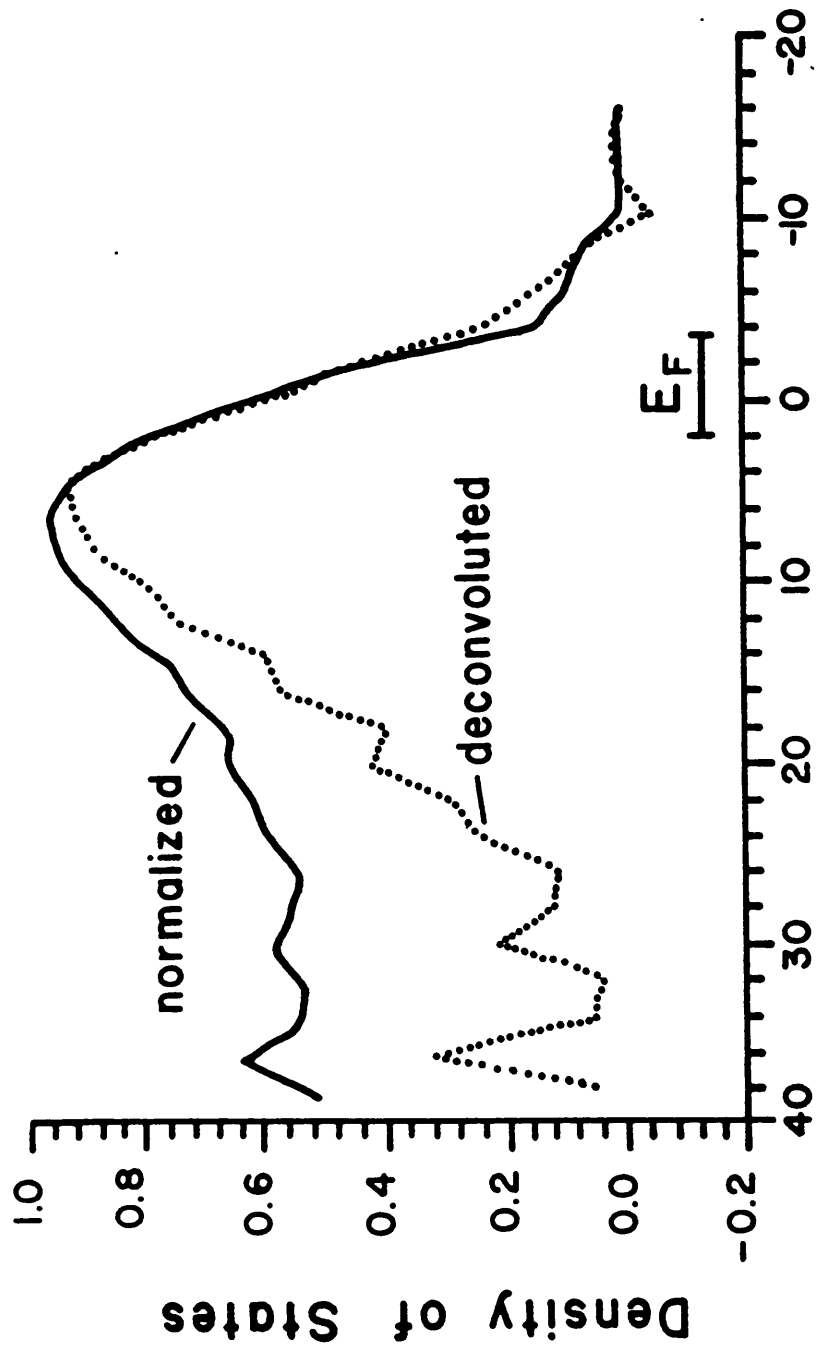

Figure VIII.10 Energy density of states calculated from a-C (e,2e) spectrum

should be noted that there is an ambiguity in this expression for N(E) for amorphous states which are degenerate in E and **q**, but can not be assigned a quantum number n. This may produce a discrepancy at small **q** due to the overlap of the wavefunctions of delocalized degenerate states. Figure VIII.10 shows N(E) calculated from the normalized and deconvoluted a-C (e,2e) spectra. The (e,2e) cross section is not measured on an absolute scale, therefore there is an arbitrary normalization factor in the calculated density of states. There is a further uncertainty in assigning the position of the Fermi Energy as -0.5 ± 2 V above the zero of the binding energy as was discussed in Section V.

Comparison of the deconvoluted a-C density of states with those of graphite [15,129] and diamond [130] are shown in Figure VIII.11. There is not enough resolution in the (e,2e) data to make detailed comparisons, however, several general conclusions can be drawn.

The (e,2e) density of states appear shifted by about 2 eV to energies above E_F. This could be an artifact of the energy resolution, be a result of a systematic error in energy measurement, or be caused by charging due to the presence of a larger energy gap. In any event, the discrepancy is within experimental error. The (e,2e) density of states is significantly wider than either

(a) a-C compared with graphite

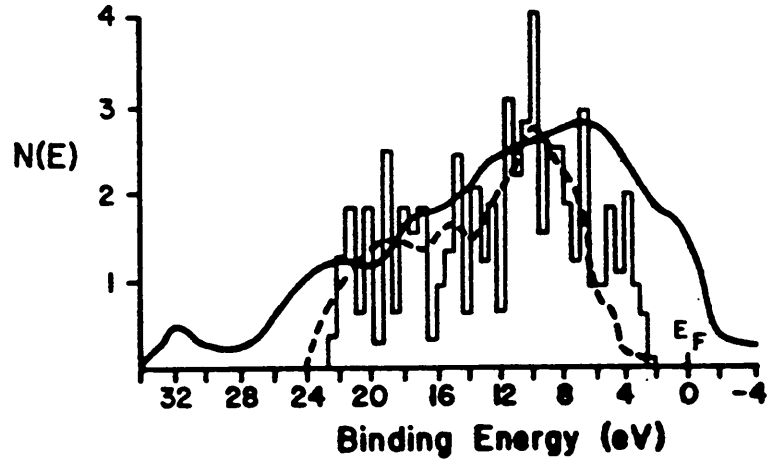

Stepped curve is after theory by Painter and Ellis (Ref. 129). Dashed curve is after XPS measurements by Bianconi et al (Ref. 15). Solid curve is based on (e,2e) data.

(b) a-C compared with diamond

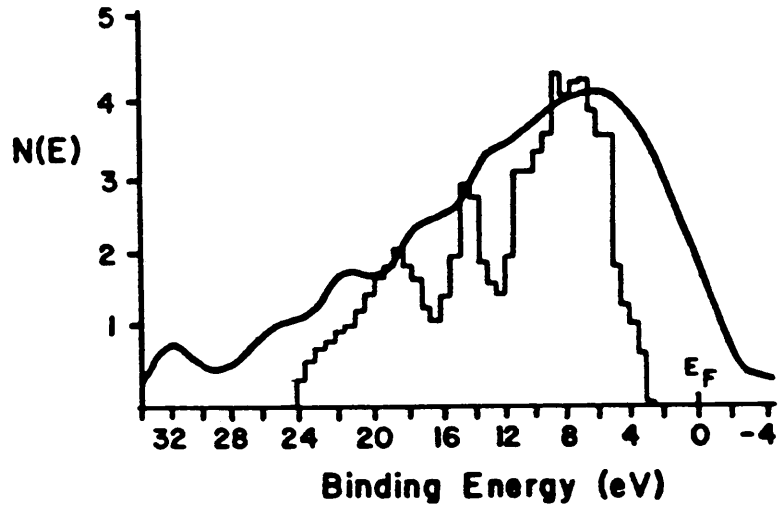

Stepped curve is after theory by Painter et al (Ref. 130). Solid curve is based on (e,2e) data.
Figure VIII.11

Figure VIII.11 Comparison of density of states of a-C, graphite, and diamond

graphite or diamond densities of state. This could also be partially a result of instrumental broadening. The small peak centered at ~ 32 eV is most likely a remnant of incomplete deconvolution, because it is one plasmon energy (24 eV) below the main feature in the density of states at 8 eV.

The 1D electron momentum density is given by

$$J(q) = \int |\Phi(q)|^2 \, dE \qquad \text{(VIII.3)}$$

which can be expressed as a sum over energy points as

$$J(q) = \sum_{E} N(E,q) \, \delta E \qquad \text{(VIII.4)}$$

where δE is the spacing between energy points. Figure VIII.12a shows J(q) calculated from the normalized and deconvoluted a-C (e,2e) spectra. A crude effort was made to calculate J(q) separately for the two bands distinguished in the data. The sum over $11 \leq E_B \leq 32$eV includes the bottom portion of the lower parabolic band. The other sum over $-2 \leq E_B \leq 9$ eV illustrates the upper band for $|q| \lesssim 1$ Å^{-1}. However, for larger q, contributions of approximately equal magnitude are present from both bands.

The electron momentum density is about twice as wide as those measured for graphite and diamond. There is some instrumental broadening in momentum, however this alone probably can not account for the marked increase in the

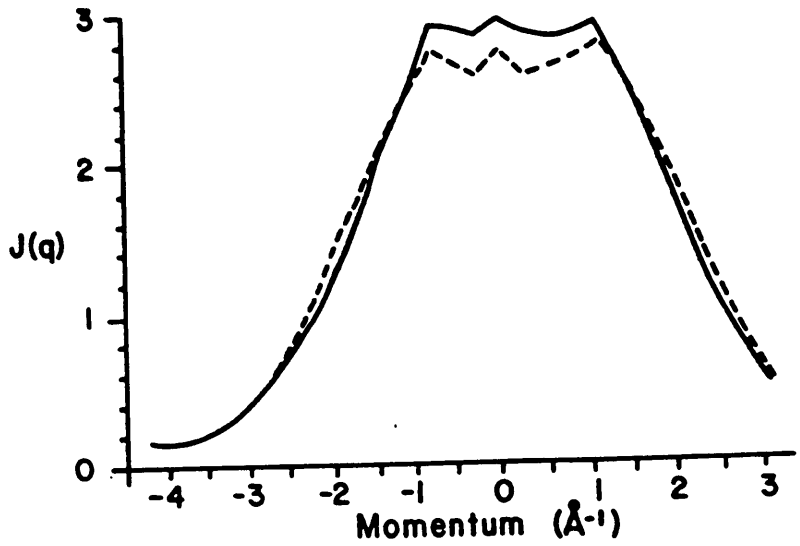

(a) Total electron momentum density from merged (dashed line) and deconvoluted (solid line) data.

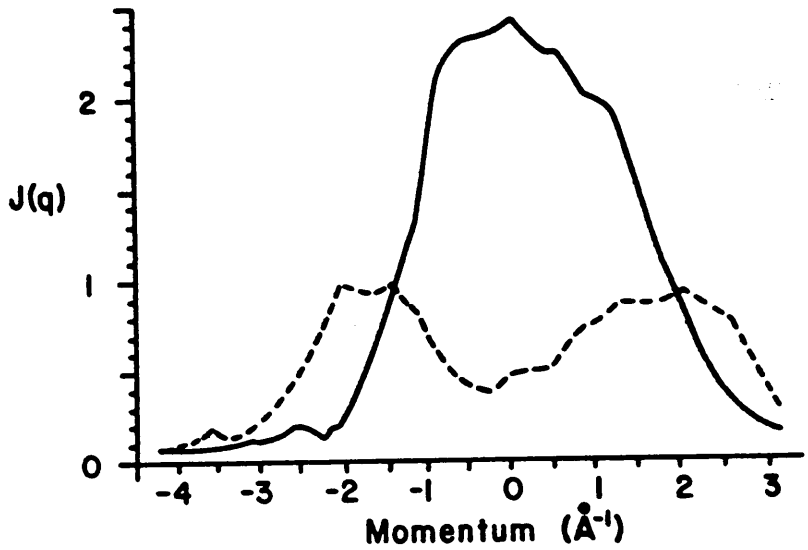

(b) Partial electron momentum density for upper part of dispersion curve (dashed line) and lower part of dispersion curve (solid line).

Figure VIII.12 Electron momentum density calculated from a-C (e,2e) spectra

width. The electron momentum density also exhibits a very broad plateau at $|q|<1$ $Å^{-1}$ which differs from the sharper shape of the crystal distributions. Here also the (e,2e) resolution is insufficient to draw any direct conclusions.

An estimate of the band structure of a-C is obtained by projecting the location of the peaks in the deconvoluted (e,2e) intensity onto the (E,q) plane. Figure VIII.13 shows the location of these points. The peaks for positive (circles) and negative momenta (squares) are mapped onto the same quadrant. These represent peaks (solid symbols) and shoulders (open symbols) in constant-momentum plots of the (e,2e) data. The triangles designate peaks in constant-energy plots of the (e,2e) data in a region where it was difficult to distinguish structure in the constant-momentum plots. Experimental resolutions (FWHM) are shown by the error bars at the bottom of the graph. Statistical errors in the count rates are shown in Figure VIII.14 by error bars, however systematic errors and errors introduced by deconvolution are not included.

There are two bands clearly visible in the data. The lower band has a minimum at q=0 with $E_B \approx$ 18 eV below the Fermi energy. The band is roughly parabolic and has a momentum width of $\sim$ 2.5 $Å^{-1}$ extending upward to near E_F. A plot of the peak heights along the band as a

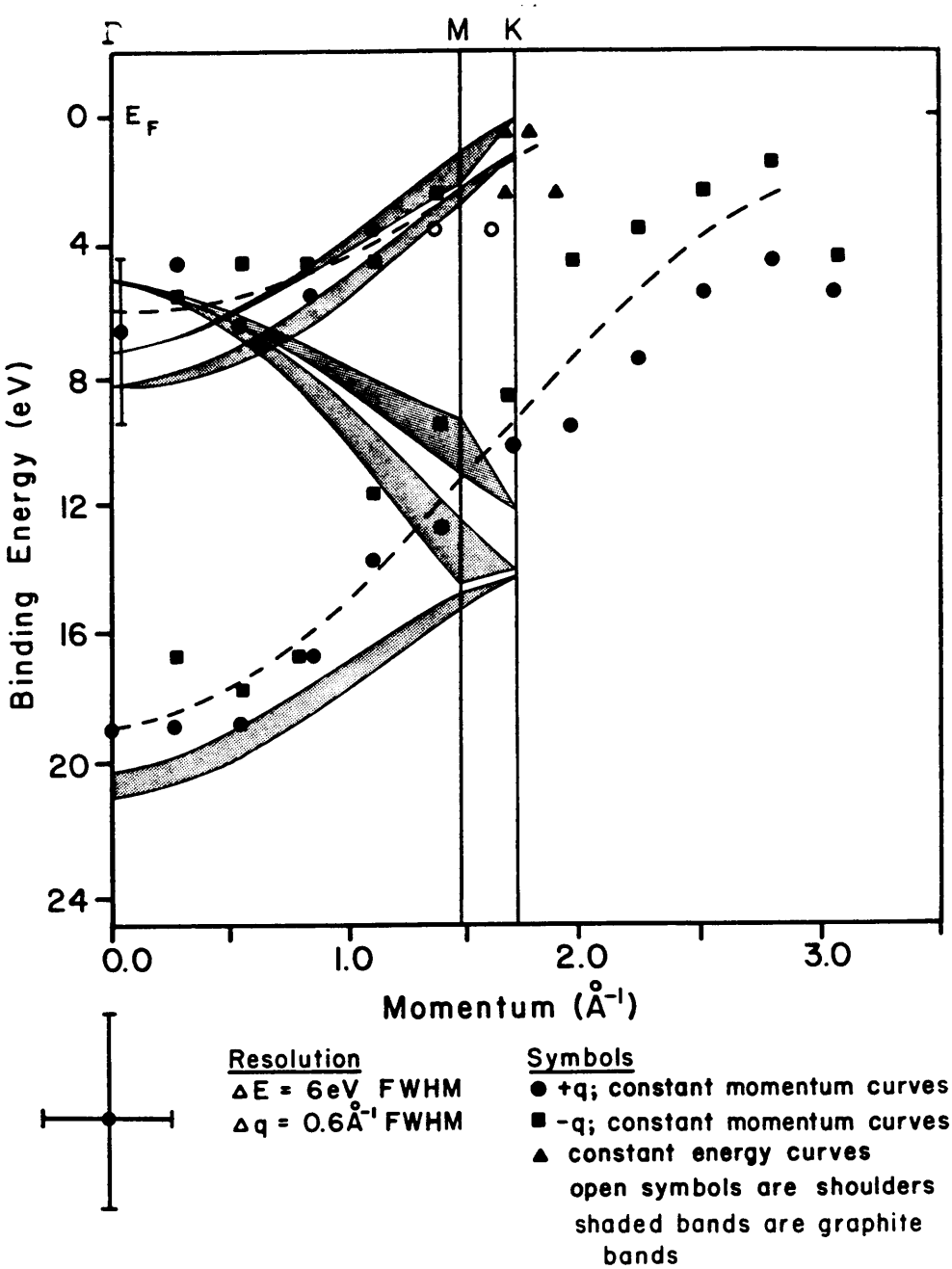

Dispersion curve for graphite after Willis et al (Ref. 187).

Figure VIII.13 Comparison of graphite band structure with a-C (e,2e) spectra

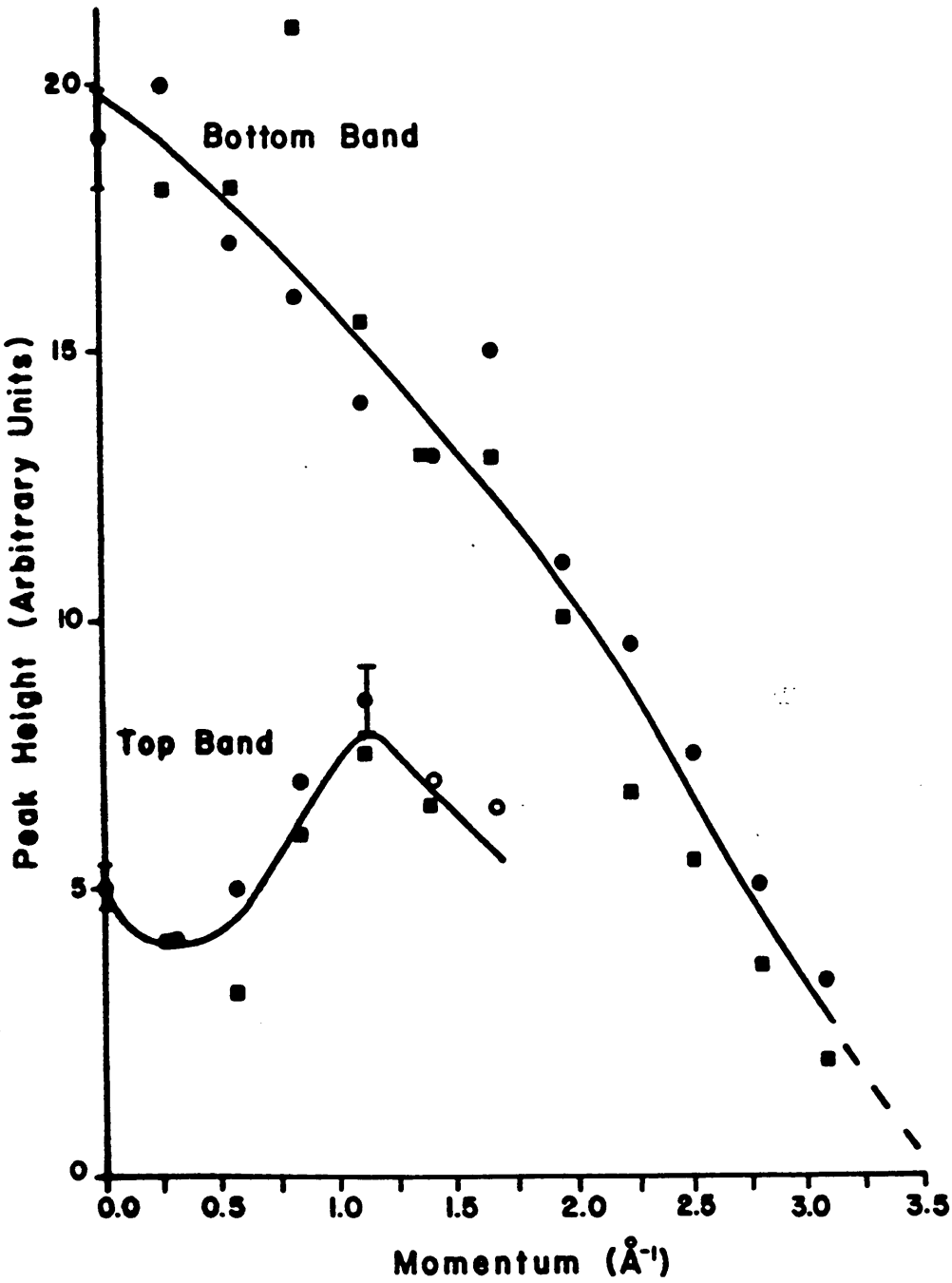

Figure VIII.14 Intensity of a-C bands as a function of momentum

function of momentum (Figure VIII.14) shows that the band intensity decreases monotonically. This is characteristic of S-symmetry bands as discussed in Section II.B.

. The upper band is not as prominent, but it is clearly visible. This band also has a minimum at q=0 with $E_B \approx 6eV$. Again, the band is upwardly dispersing to near E_F, but has an apparent momentum width of only ~ 1.7 $Å^{-1}$. However, the juxtaposition of the upper and lower bands near the Fermi level limits the certitude of this statement. A plot of the peak height versus momentum shows that there is a maximum in intensity at $q \approx 1$ $Å^{-1}$ which is $\sim 50\%$ larger than the q=0 peak intensity. Therefore, the band appears to have a mixture of S- and P-symmetry characteristics.

Most of the positive momentum peaks in the bottom band have lower binding energies than the corresponding negative momentum points. This suggests that the momentum offset is incorrect. A further shift of -1/8 to -1/4 $Å^{-1}$ improves the agreement, however the position of the band remains unchanged.

The theoretical valence band structure of graphite [187] is superimposed on the (e,2e) data in Figure VIII.13. The graphite bands in two directions, Γ-M and Γ-K, are illustrated. The 3D splitting of the bands is also included; in particular both π bands are shown. The

areas between each of the bands in the two directions are shaded. This formally represents the fact that isotropic a-C must be some kind of average over all directions. The M (1.48 $Å^{-1}$) and K (1.70 $Å^{-1}$) boundaries are included for references.

The comparison shows striking similarities. The lower σ band is comparable to the lower a-C band out to q~1.7 $Å^{-1}$ (near the graphite BZ boundary). The curvature of the two bands are quite similar, however, the a-C band is about 3 eV above the graphite band at q=0. The a-C band extends beyond the graphite BZ boundary to larger momentum. This a-C band appears to display S-symmetry as does the lowest σ band. The π bands of graphite are also in good agreement with the upper a-C band. The binding energy at q=0 for a-C is ~2 eV above the value for the center of the π bands. The upper a-C band does exhibit some P-symmetry characteristics which are contrary to the S-symmetry of the π band. The difference between the two measured a-C band energies at q=0 (~12 eV) agrees remarkably with the value for the averages of the graphite bands (~13 eV). It should be noted that earlier a-C data [144] positioned the lower band at 2 eV below the graphite band at q = 0, but had the same value for the separation of the two a-C bands at q = 0. This again emphasizes the

problem of establishing the Fermi level and suggests that there may be an error of $\sim$ 2 eV in the assignment of the Fermi level of a-C.

The apparent absence of a-C bands corresponding to the upper two σ bands is also striking. The two upper σ bands account for one half of the states in the graphite valence band, so some explanation of their absence is required. It is possible that some vestige of these bands is present, but not resolved. The width of the upper peak at q=0 (FWHM shown by error bars in Figure VIII.13) is sufficient to encompass both the π and upper σ bands. The σ bands have P-symmetry, which might help explain the P-symmetry characteristics of the upper a-C band. However, their P-symmetry would also imply that they should have high intensities at $0.5 \lesssim |q| \lesssim 1.0$ Å^{-1} where they would be most easily resolved from the other bands.

A similar comparison of the a-C data with diamond band structure is shown in Figure VIII.15. As before, the dispersion curves are illustrated for two directions, i.e. the Γ-L and Γ-X directions and the L(1.53 Å^{-1}) and X(1.76 Å^{-1}) boundaries are shown for reference. The similarities are considerably less. The lower a-C band is in comparable agreement with the lowest diamond band as it was with the lowest graphite band.

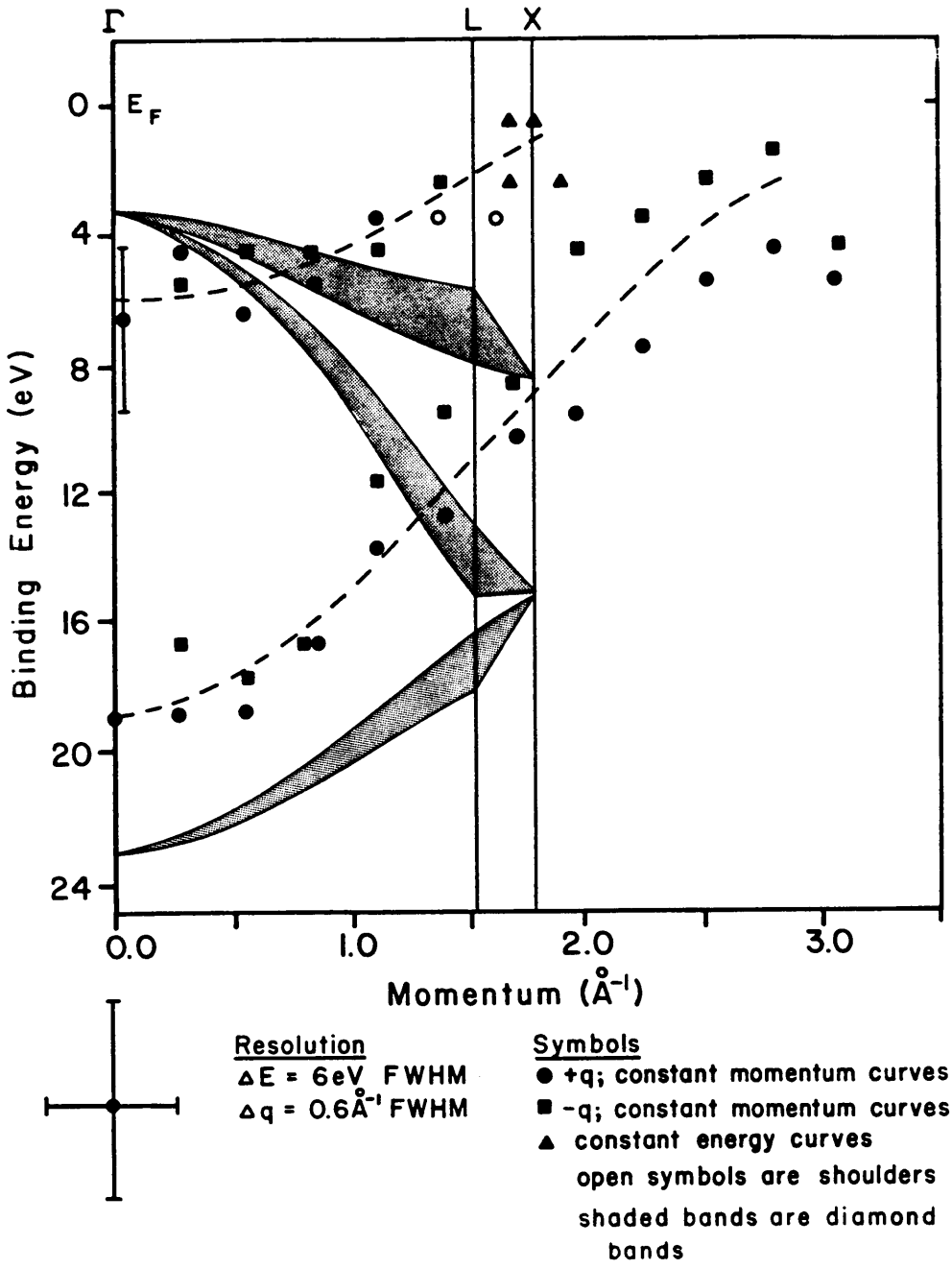

Dispersion curve for diamond after Painter and Ellis (Ref. 129).

Figure VIII.15 Comparison of graphite band structure with a-C (e,2e) spectra

Their energies differ by about 4 eV at q=0. The upper bands differ markedly and disperse in opposite directions. Their energies differ by ~3 eV at q=0. The difference between the two diamond energies at Γ is ~20 eV for diamond which is significantly larger than the corresponding ~12 eV measured for a-C.

The total number of states in the valence bands integrated over all momentum directions is $2n_vN_v$ where n_v is the number of valence electrons per unit cell and N_v is the number of unit cells in the crystal volume. An integration of the density of states N(E) over all valence energies should also equal $2n_vN_v$. This is of course equivalent to integrating the 1D density of states along all reciprocal space directions over the BZ. Individually, each band accounts for $2N_v$ states in the density of states.

It is sometimes possible to further separate the valence bands into individual bands or groups of bands if the bands are not degenerate with respect to energy over all momentum directions. This is illustrated in diamond where it is possible to equate the states with $\mathcal{E} \lesssim 15$ eV with the upper three bands and the states with $\mathcal{E} \gtrsim 15$ eV with the lowest σ band. There are three times the number of occupied states associated with the upper three bands as with the lower

band.

The theoretical density of states for diamond [130] in Figure VIII.11b shows that the number of states associated with the upper three bands ($\mathcal{E} \lesssim 15$ eV) is approximately three times that of the number associated with the lowest σ band ($\mathcal{E} \gtrsim 15$ eV). Similarly, Figure VIII.11a [129] shows that the number of states in the π-band of graphite ($\mathcal{E} \lesssim 6$ eV), the two upper σ-bands ($6 \lesssim \mathcal{E} \lesssim 14$ eV), and the lowest σ-band ($\mathcal{E} \gtrsim 14$ eV) are in the approximate ratio 1:2:1. The separation of the graphite bands is less clear, because the π-band and upper σ-bands cross.

In an amorphous sample of equal size, there must be the same total number of occupied states as in a crystal because the number of valence electrons is the same. However, the number of states in a given band is no longer predicted by Bloch's theorem, because amorphous materials lack long range order. The amorphous momentum density of states is the same along all momentum directions due to the isotropic nature of amorphous materials in real space.

The relative number of states in 3D associated with each a-C band can be determined from the density of states in Figure VIII.10. Three regions are distinguished in the band diagram in Figure VIII.13; those states with binding

energies below E = 8 eV can be assigned to the lower a-C band, those above E = 8 eV and with $q \lesssim 1.7 \text{Å}^{-1}$ can be assigned to the upper band, while states with E < 8 eV and q > 1.7 Å^{-1} cannot be unambiguously assigned. Figures VIII.9 and VIII.14 show that the cross section above E = 8 eV is approximately constant out to q = 2.8 Å^{-1} at which point the probability drops rapidly to zero. Under this approximation the number of states in the unassigned region account for 40% of the occupied area of ($\mathcal{E}$,q) space above 8 eV in Figure VIII.9. A momentum weighted sum, as in Equation VIII.2 determines that 63% of the states above E = 8 eV in the density of states are in the unassigned region. The premise that the upper band terminates near the BZ boundary would clearly assign these unassigned states to the lower band. In this case the ratio of lower band states to upper band states is 5:1. If the unassigned states are shared equally by the two bands this ratio is 2.4:1. Shifting the cutoff energy from 8 eV to 6 eV or 10 eV changes this ratio by only approximately 20%. Therefore, we can state that the ratio of the number of states in the lower band to those in the upper is between 2:1 and 5:1.

In a crystalline solid it also follows from the Bloch theorem that there are 2N states in each band in the dispersion curve along any reciprocal space direction,

where N is the number of unit cells along the corresponding crystallographic direction. Therefore, each band has an equal number of states in any given momentum direction (unless there are degenerate bands, as is the case for diamond along the Γ-L and Γ-X directions). For semi-metals (graphite) and semi- conductors (diamond), all valence states are occupied states.

(e,2e) measurements also provide information on the relative number of occupied states in each band along the measured momentum direction. It is possible to estimate the probability that an electron will be found with some energy and momentum associated with a given band by simple summation of the probabilities at each appropriate (E,**q**) point, i.e. adding the measured N(E,**q**) for each point in the band. Estimates can be based on the relative band peak heights of the curves in Figure VIII.14 or based on the relative volumes under the curve in Figure VIII.9 associated with the two bands. In both of these cases the ratio of the lower band to the upper is $3 \pm \frac{1}{2}$ to one. Again the uncertainty results from the ambiguity of assigning the large momenta states. However, this uncertainty is reduced considerably by the fact that the unassigned region is not heavily weighted by the q^2 factor present in the density of states calculation.

C. Interpretation

It can now be stated on the basis of our data that a dispersion relation $\mathcal{E}(\$25q)$ does exist for a-C. This in itself is a significant conclusion. The existence of this relation must now be integrated into any theory for such amorphous materials. Such theories may well lead to other significant results, just as the Bloch theorem which predicts bands in crystals has lead to the explanation of many other properties of crystalline solids. Most of the present morphological theories, e.g. random close packing and continuous random networks can only begin to address the existence of bands.

Ziman [193] has discussed the existence of bands in amorphous solids in the context of the expansion of wave functions in terms of linear combinations of bonding orbitals [75]. In particular, Ziman predicts the existence of bands similar to their crystal counterparts for continuous random networks (crn) of tetrahedral glasses, e.g. a-Si and "diamond-like" a-C. These glasses still possess 4-fold bonding and nearly constant bond lengths, but have a distribution of bond angles which produces long range disorder. From topological arguments, Ziman is able to demonstrate the existence of four distinct bonding configurations compatible with the amorphous structure.

The bonding configuration formed from all positive bonding coefficients is associated with the lowest Γ-point in the diamond dispersion curve. The other three amorphous bonding configurations have equal numbers of positive and negative bonding coefficients and are associated with the upper Γ-point in diamond. The existence of these bonding configurations, Ziman claims, is evidence for the existence of similar states in the amorphous and crystalline band structures at $\mathbf{q} = 0$.

Further, it is argued that at small q, that is for wavelengths much longer than the nearest neighbor distance, electrons in amorphous materials propagate in an effective medium which is not significantly different from the crystal lattice. Therefore, similar band structure should exist near $q = 0$ for crystalline and amorphous states of a particular material. The electron can be represented by a wavepacket constructed from a narrow distribution of momentum eigenstates, however this distribution broadens as the wavelength of the electron approaches the correlation length for fluctuations in the one-electron potential, that is as the wavelength becomes comparable to the short range order in the amorphous solid. This implies that in the disordered phase the bands will broaden and coalesce as $\mathbf{q}$ approaches the Brillouin zone boundary. This can be

pictured as broadening the sharp delta functions from the dispersion function $\mathcal{E}(\mathbf{k})$ in the crystalline spectral momentum density into a distribution function $\rho'(\mathcal{E}, \mathbf{k})$.

If we accept these arguments, then the band structure for "diamond-like" a-C should resemble that of diamond, particularly for small q. Figure VIII.14 indicates that this is not the case for our a-C sample. A comparison of a similar set of arguments based on "graphite-like" a-C seems in order.

Let us consider a model similar to that proposed by Beeman et al [13] described in Section VII.C. In this model, graphitic islands with basal dimensions of 10 to 20 Å are cemented together with four-coordinated atoms. These cementing atoms allow for changes in the orientations of the planes of the graphitic islands without the necessity for dangling bonds and voids that would result from unconnected, randomly oriented planes. This distribution of planes produces a long range isotropic structure. The graphitic islands are composed of layers of three-coordinated atoms arranged in a 2D continuous random network. This crn structure is discussed by Zallen [191] and is based on the work of Zachariasen [190]. In a crn, bond lengths are held nearly constant while bond angles are allowed to vary. This means that long range order is

absent, while the three-fold bonding is maintained. It is possible to form five, six, seven, and eight member rings as shown in Figure VIII.16. In a real system there would be the possibility of warping or bending of the sheets.

This model, taken together with Ziman's hypotheses, would suggest a band structure for a-C that would be similar to graphite. The p_z orbitals out of the crn planes should remain essentially unchanged, although bending or warping of the planar regions would change the distance between the out-of-plane p orbitals. Therefore, vestiges of the graphite π band should be present in the a-C band structure, which spread out at larger q.

In graphite the bonding of the lowest σ band at Γ is composed of all similar bonding coefficients (see Figure VII.4b). It is easy to picture a bond configuration of all similar bond coefficients for the crn structure in Figure VIII.16. This should be associated with the Γ-point of the lowest graphite σ band. The upper σ bands of graphite at Γ are composed of equal numbers of bonds with three phase factors (see Figure VII.4a). However it is not obvious that there are any possible bond configurations with either two or three discrete phase factors that can be fit to the 2D crn structure. It would appear that such configurations can not be satisfied for distorted graphite

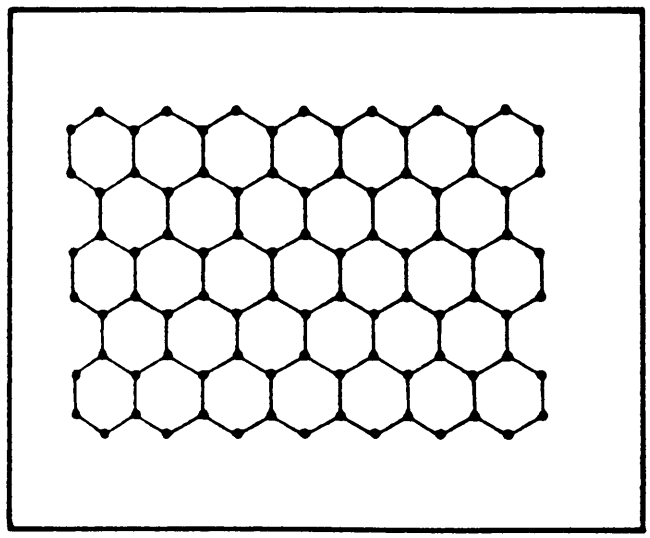

(a) graphite crystal 2D structure

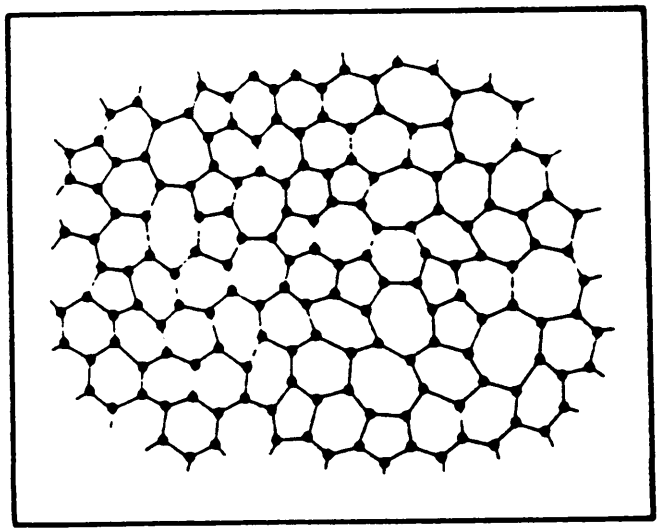

(b) 2D continuous random network

Figure VIII.16 Two dimensional continuous random network model of a-C *

* After Zallen (Ref 191).

planes with 5- and 7- member rings. This is illustrated by considering the simple example of one five-member ring in a "sea" of six-member rings. This could lead to frustration in the bonding of the amorphous structure.

If it can not be shown that there are distinct bond configurations for the amorphous structure which can be associated with the crystal Γ-point states, one of the cornerstones of Ziman's arguments for the existence of the band structure is removed. Clearly there is a need for theoretical calculations using the TB and LCBO methods to study the 2D crn model of a-C.

One possible explanation for the apparent absence of the a-C band analogous to the upper σ bands of graphite rests with the apparent continuation of the lowest a-C band to large q, well beyond the graphite BZ boundary. In the extended zone scheme the upper σ bands are extensions of the lower σ band for **k** in the second BZ. These bands can be folded back into the first BZ in the reduced zone scheme as a result of the periodicity of the crystal. It is not true *a priori* that the bands can be folded back for amorphous materials. If the upper σ bands are not folded back into the first zone, then one would expect the lowest σ band to extend upward beyond q equivalent to the first BZ boundary. Again, the amorphous band should broaden for large q. It must be noted that our resolution

is insufficient to determine the presence of any small band gap between the parts of the lower a-C band near the remnant BZ boundary.

The folding of the upper σ bands in graphite into the first BZ can be explained by the repeated zone scheme. A further consequence of a crystalline repeated zone scheme is that there will be mirror images of the bands in second and higher order BZ. For instance, the lowest graphite σ band repeated in the second BZ will produce a band dispersing downward from the zone boundary to the first reciprocal lattice vector. As discussed in Section II.3 there will be a corresponding finite probability in the spectral momentum density. The probability will fall off rapidly at larger momentum as the form factor decreases. However, the form factor should decrease continuously so that the height of the spectral momentum density should be approximately the same on both sides of the zone boundary near the boundary.

In contrast, the data in Figure VIII.9 shows the apparent absence of the remnants of the repeated zone scheme lowest σ band. At 1.7 $Å^{-1}$ (approximately the graphite and diamond BZ boundaries) the peak intensity of the lower band is still 60% of the maximum peak intensity at 0 $Å^{-1}$. This lowest a-C band and its

extension have a continuously decreasing probability across the zone boundary remnant as shown in Figure VIII.9 and VIII.14. There is no apparent evidence for the downward dispersing band that should occur if there are remnants of the repeated zone scheme in a-C. The resolution of the data is insufficient to state conclusively that this band is absent, particularly in light of the probable band broadening at larger momenta in amorphous materials. However, the absence of a downward dispersing band at $q > 1.7 \text{Å}^{-1}$ **and** the presence of an upward dispersing band with a continuously decreasing probability taken together do provide convincing evidence to discount the repeated zone scheme for a-C.

Further, this extended lower band should account for three fourths of the valence states, that is the total number of states in the three graphite σ bands. Likewise the upper a-C band should account for one fourth of the valence states, that is the states associated with the graphite π band. This is in agreement with our data.

While the model considered above may provide an explanation for the main features of the a-C (e,2e) spectra it must be viewed with some skepticism. It is by no means the only consistent explanation. It is still not entirely possible to rule out significant amounts of tetrahedral bonding. Neither is it certain that no weak bands

analogous to the upper σ bands of graphite exist.

A detailed analysis of the measured band structure is limited by two major factors. The first is instrumental resolution. The present energy and momentum resolution is simply not sufficient to measure details of the bands. The other limiting factor is the fact that (e,2e) spectroscopy on solids is an unproven technique. The analysis of a-C would be greatly aided by measurements on crystalline graphite. The measurements would serve a dual purpose. They could provide a check on the (e,2e) technique by allowing the (e,2e) data to be compared with other measurements and theory for a well understood system. Such measurements would also be invaluable in addressing the question of the extent to which a-C resembles graphite.

IX. CONCLUSIONS

There are two primary sets of conclusions to be drawn in this dissertation. The first concerns the successful operation of an (e,2e) spectrometer for the investigation of the valence band structure of solids. The major improvements over previous efforts are summarized and a brief discussion is given concerning the future improvements for our spectrometer. The second set of conclusions is in regard to what has been learned about the physics of carbon and amorphous materials in general. In addition, some suggestions for future systems of study are outlined along with a discussion of what physics the technique may potentially be able to study.

Our instrument is the first (e,2e) spectrometer with sufficient resolution to study the valence band structure of solids. The 3-5 eV energy resolution is approximately an order of magnitude better than in previous instruments. This allows the separation of the individual valence bands. Momentum resolution has also been improved by a factor of between two and ten. Our design incorporates a constant-focus variable-magnification zoom lens which provides important flexibility in balancing the conflicting

resolution. The electrostatic deflection method used for momentum selection is a major improvement over systems which employ movable detectors. The electrons are incident with energies of approximately 25 keV, which is about 3 times that of earlier spectrometers. This higher energy facilitates sample preparation and reduces multiple scattering effects by increasing the electron mean free path.

The coincidence count rate in our spectrometer is on the order of 0.1 Hz, which is comparable to count rates for other (e,2e) spectrometers, including gas spectrometers. The count rate was maintained at this level, despite reductions due to the increased energy and momentum resolution, by increasing the incident current by almost three orders of magnitude. Early problems with sample degradation, even at the lower beam currents, have been mitigated by the use of an ultra-high vacuum system. There is no evidence of sample damage from 50 μA beam currents incident on the target for weeks at a time.

At present work is underway to design and install an upgraded energy analyzer which has an estimated energy resolution of 0.5 eV. Recalibration and realignment is also being done which should significantly reduce the systematic errors in momentum selection. This increased

resolution should prove sufficient to investigate many of the details of the band structure that are presently inaccessible.

The low count rate is presently the major impediment to further application of the technique. This will become an even more serious problem if the energy and momentum resolution are improved or if the incident energy is increased. There appears to be no technical reason that data at different energies and momenta could not be taken simultaneously. Moore et al [117] have successfully used a multi-detector system with their gas (e,2e) spectrometer. A multi-detector system utilizing multi-channel plate arrays and position-sensitive detectors is being considered for our system. We estimate that to double the incident energy, the energy resolution and the momentum resolution simultaneously will require approximately 64 data collection channels to maintain the present data rate. It is not inconceivable to have several hundred data channels.

In principle, the count rate can be increased by use of even higher beam currents. The present electron gun can deliver more current at higher anode voltages, however this would necessitate major revisions in the input lens optics to avoid electrical breakdown. Magnetic focusing lenses may allow significantly higher beam currents. Sample degradation is a potential problem at higher incident

currents.

Operation of the spectrometer at higher incident energies is also desirable. The major difficulty is the problem of electrical breakdown mentioned above. Again, it will be necessary to make major revisions to the input lens optics. This must be coupled with some way to maintain the present count rate.

Much has been accomplished in the field of data manipulation and analysis that will be useful in studying other systems. A more accurate method of multiple scattering deconvolution must be developed and the analysis needs to be generalized to include inhomogeneous structure in single crystals.

The analysis of extensive data on a-C has lead to several interesting conclusions. The existence of a dispersion relation $\mathcal{E}(\mathbf{q})$ in a-C has been clearly demonstrated. Two distinct bands are discernible in the data. One band has a minimum at approximately 6 eV below the Fermi level at q=0 and disperses upward to near the Fermi level at $q \approx 1.5$ Å^{-1}. the lower band is much more prominent, extending from a minimum of $\sim$ 18 eV below the Fermi energy at q=0 to near the Fermi level at $q \approx 2.5$ Å^{-1}.

These two bands are similar to the lower σ band and

the π band in graphite. However, the instrumental resolution is not sufficient to exclude the possibility of 4-fold bonds as are found in diamond. There are several notable differences between the a-C band structure and either graphite or diamond. The lower band extends well beyond the momenta corresponding to the BZ of graphite and diamond and appears to account for about three times the number of occupied valence states as does the upper band. There is also an absence of any downward dispersing bands that might correspond to the middle bands in graphite and diamond.

Some conjectures have been made as to possible explanations for these differences. In particular, a model for a-C based on small randomly-oriented islands of quasi-2D graphite-like continuous-random-network structures may offer an explanation compatible with the data. It must be noted, however, that the inadequate resolution and lack of concrete theoretical frameworks make such explanations speculative. No definitive interpretations can be given until higher resolution experiments are performed on both a-C and single crystal graphite.

Work is presently continuing on single crystal graphite, both as an extension of the work on a-C, as a characterization study of a well studied system, and as an interesting measurement on a semi-metal. Work has begun on

the study of microcrystalline Al, which will probe the physics of a simple metal. Al has also been extensively studied with other techniques and some limited theoretical studies of the (e,2e) cross section have been performed [124]. Another interesting system is the semiconductor Si, in both crystalline and amorphous forms.

In addition to studying the properties of specific materials, there is a wealth of physical phenomena which may be able to be studied. The comparison of amorphous and crystalline samples of the same material should provide valuable information about the structure of amorphous materials. It may be possible to study the nature of the transition from localized to delocalized states in amorphous solids. The momentum broadening of the spectral momentum density as the states become localized is a characteristic signature which may be observable with higher resolution measurements. It may also be possible to study the nature of hybridized s-d orbitals in transition metals [107] and the evolution of the valence electron wave function in the metal-insulator transition.

It is obvious that the tremendous potential of (e,2e) spectroscopy in solids has just begun to be explored.

REFERENCES

[1] M. Abramowitz and I. A. Stegun, Editors, Handbook of Mathematical Functions, (National Bureau of Standards, Washington, D. C., 1972).

[2] R. Al-Jishi and G. Dresselhaus, "Lattice-dynamical model for graphite," Phys. Rev. B **26**. 4514 (1982).

[3] U. Amaldi, A. Egidi, R. Marconero, and G. Pizzella, "Use of a two channeltron coincidence in a new line of research in atomic physics," Rev. Sci. Instrum. **40**, **1001 (1969).**

[4] William F. Ames, Numerical Methods for Partial Differential Equations, (Academic Press, New York, 1977).

[5] W. H. J. Andersen, "Optimum adjustment and correction of the Wien filter," Br. J. Appl. Phys. **18**, 1573 (1967).

[6] G. D. Archard, Proceedings of the Third International Conference on Electron Microscopy, as cited in Klemperer and Barnett.

[7] N. W. Ashcroft and N. D. Mermin, Solid State Physics, (Holt, Rinehart, and Winston, New York, 1976).

[8] A. Azim Khan, David Mathine, John A. Woollam, and Y. Chung, "Optical properties of 'diamondlike' carbon films: An ellipsometric study," Phys. Rev. B **28**, 7229 (1983).

[9] G. B. Bachelet, H. S. Greenside, G. A. Baraff, and M. Schlutter, Phys. Rev. B **24**, 4745 (1981).

[10] G. A. Baker, Jr., I. E. McCarthy, and C. E. Porter, Phys. Rev. **120**, 254 (1960).

[11] F. Bassani and G. Pastori Parravicini, Nuovo Cimento **50**, 95 (1967).

[12] P. E. Batson and A. J. Craven, Phys. Rev. Lett. **42**, 893 (1979).

[13] D. Beeman, J. Silverman, R. Lynds, and M. R. Anderson, "Modeling studies of amorphous carbon," Phys. Rev. B **30**, 870 (1984).

[14] S. Berko, R. E. Kelly, and G. S. Plaskett, "Angular correlation of annihilation radiation from oriented graphite," Phys. Rev **106**, 824 (1957).

[15] A. Bianconi, S. B. M. Hagstrom, and R. Z. Bachrach, "Photoemission studies of graphite high-energy conduction-band and valence-band states using soft-x-ray synchrotron radiation excitation," Phys. Rev. B **16**, 5543 (1977).

[16] J. Biscoe and B. E. Warren, J. Appl. Phys. **13**, 364 (1942).

[17] H. Boersch, Z. Physik **139**, 115 (1954).

[18] D. Bohm and D. Pines, Phys. Rev. **92**, 609 (1953).

[19] B. T. Boiko, L. S. Palatnik, A. S. Derevyanchenko, and A. A. Nechitailo, "Intermediate stages of graphitization in thin films of condensed carbon," Sov. Phys. -- Solid State **12**, 381 (1970).

[20] Russell A. Bonham and Manfred Fink, High Energy Electron Scattering, (Van Norstrand Reinhold Co., New York, 1974), pp. 232-255.

[21] M. Born and E. Wolf, Principles of Optics, (Pergammon Press, Oxford, 1980).

[22] R. N. Bracewell, The Fourier Transform and its Applications, (McGraw-Hill, New York, 1978).

[23] W. H. Bragg and W. L. Bragg, Proc. Roy. Soc. A **89**, 277 (1913).

[24] G. R. Brewer, "High-intensity electron guns," Focusing of Charged Particles, Volume II, Edited by A. Septier (Academic Press, New York, 1967), pp. 23-73.

[25] W. Brünger and W. Menz, "Absolute intensities for elastic and inelastic electron scattering in a-C and germanium", Z. Physik **164**. 21 (1961).

[26] R. E. Burge and D. L. Misell, "Electron energy loss spectra of evaporated carbon films", Philos. Mag. **18**, 251 (1968).

[27] B. T. Burke, Sov. Phys. -- Solid State **12**, 381 (1970).

[28] CRC Handbook of Chemistry and Physics, 60th Edition, (CRC Press, Boca Raton, FL, 1979).

[29] R. Camilloni, A. Giardini Guidoni, I. E. McCarthy, and G. Stefani, "Mechanism of the (e,2e) reaction with atoms," Phys. Rev. A **17**, 1634 (1978).

[30] R. Camilloni, A. Giardini Guidoni, R. Tiribelli, and G. Stefani, "Coincidence measurement of quasifree scattering of 9-keV electrons on *k* and *l* shells of carbon," Phys. Rev. Lett. **29**, 618 (1972).

[31] A. F. Carley and R. W. Joyner, "The application of deconvolution methods in electron spectroscopy -- a review," J. Electron Spectrosc. Relat. Phenom. **16**, 1 (1979).

[32] B. A. Carré, "The determination of the optimum accelerating factor for successive over-relaxation," Computer J. **4**, 73 (1961).

[33] G. Carter and J. S. Colligon, Ion Bombardment of Solids, (American Elsevier Publishing Co. Inc., New York, 1968).

[34] G. Carter, J. S. Colligen, and M. J. Nobes, "The equilibrium topography of sputtered amorphous solids II," J. Materials Sc. **6**, 115 (1971).

[35] G. Carter, J. S. Colligon, and M. J. Nobes, "The growth of topography during sputtering of amorphous solids," **8**, 1473 (1973).

[36] F. C. Chalklin, Proc. R. Soc. A **194**, 42 (1948).

[37] R. C. Chaney, C. C. Lin, and E. E. Lafon, Phys. Rev. B **2**, 459 (1970).

[38] R. Chen, P. Trucano, and R. F. Stewart, Acta Crystallogr. Sect. A **33**, 823 (1977).

[39]J. R. Chelikowsky, and S. G. Louie, "First principle linear combination of atomic orbitals method for the cohesive and structural properties of solids: Application to diamond," Phys Rev. B **29**, 3740 (1984).

[40]T. T. P. Cheung, "Orientation dependance of the carbon K edge in graphite measured by reflection electron-energy-loss spectroscopy," Phys. Rev. B **31**, 4792 (1985).

[41]G. L. Clark, Encyclopedia of X-Rays and γ-Rays, (Reinhold, New York, 1963), p. 439.

[42]R. Clark and C. Uher, "High pressure properties of graphite," Adv. in Physics **33**, 469 (1984).

[43]Ben Cline, computer code PHYS, V. P. I. Systems Development Office (1983).

[44]Ben Cline, computer code TOTAL2, V. P. I. Systems Development Office (1983), modified by J. R. Dennison (1984).

[45]Ben Cline, "Physics User's Guide," unpublished, 1983.

[46]Ben Cline and Mark Smith, V. P. I. Systems Development Office (1983).

[47]M. J. Cooper, "Compton scattering and electron momentum determination," Rep. Prog. Phys. **48**, 415 (1985).

[48]M. J. Cooper and J. A. Leake, Phil. Mag. **15**, 1201 (1967).

[49]D. W. Davis and D. A. Shirley, J. Electron Spectrosc. **3**, 137 (1974).

[50]G. Dearnaley, Rev. Sci. Instrum. **31**, 197 (1960).

[51]P. Debye and P. Scherr, Phys. Z. **18**, 291 (1917).

[52]R. O. Dillon, John A. Wollam, and V. Katkanant, "Use of Raman scattering to investigate disorder and crystalline formation in as-deposited and annealed films," Phys. Rev. B **29**, 3482 (1984).

[53]W. Eberhardt, I. T. McGovern, E. W. Plummer, and J. E. Fisher, "Charge-transfer and non-rigid-band effects in graphite compounds," Phys. Rev. Lett. **44**, 200 (1980).

[54]H. Ehrhardt, M. Schulz, T. Tekaat, and K. Willmann, "Ionization of helium: angular correlation of the scattered and ejected electrons," Phys. Rev. Lett. **22**, 89 (1969).

[55]P. P. Ewald, Sitzungsber. Munch. Akad. **4**, 7 (1914).

[56]A. C. Ferraz, M. I. T. Chagas, E. K. Takahashi, and J. R. Leite, "Variational cellular model of the energy bands of diamond and silicon," Phys. Rev. B **29**, 7003 (1984).

[57]R. A. Ferrell, "Angular Dependence of the Characteristic Energy Loss of Electrons Passing Through Metal Foils," Phys. Rev. **101**, 554 (1956).

[58]R. A. Ferrell, "Characteristic Energy Loss of Electrons Passing Through Metal Foils. II. Dispersion Relation and Short Wavelength Cutoff for plasma oscillations," Phys. Rev. **107**, 450 (1957).

[59]J. R. Fields, Inelastic Electron Scattering in Lithium Fluoride, Princeton University, Ph.D. (1976).

[60]J. Fink, Th. Müller-Heinzerling, J.Pflüger, B. Scheerer, B. Dischler, P. Koidl, A. Bubenzer, and R. E. Sah, "Investigation of hydrocarbon-plasma-generated carbon films by electron-energy-loss spectroscopy," Phys. Rev. B **30**, 4713 (1984).

[61]S. J. Fonash, "Advances in dry etching processes -- a review," Solid State Technol. **28**(1), 150 (1985).

[62]C. P. Frank, S. E. Schnatterly, F. J. Zutavern, A. Aton, T. Cafolla, and R. D. Carson, "1s core-level spectroscopy of graphite: The effects of phonons on emission and absorption and validity of the final-state rule," Phys. Rev. B **31**, 5366 (1985).

[63]L. Frost, and E. Weigold, "(e,2e) on solids -- a

progress report," E. Weigold, ed. Momentum Wave Functions -- 1982, AIP Conference Proceedings No. 86 (Am. Inst. Physics, New York, 1982).

[64]A. Galejs and P. H. Rose, "Optics of electrostatic accelerator tubes," Focusing of Charged Particles, vol II, Edited by A. Septier (Academic Press, New York, 1967).

[65]R. Gans, Z. Tech. Phys. **18**, 41 (1937) as cited in Gibbons, et. al.

[66]U. Gelius, in Electron Spectroscopy, edited by D. A. Shirley (North-Holland, Amsterdam, 1972), p. 311.

[67]P. C. Gibbons, J. J. Ritsko, and S. E. Schnatterly, "Inelastic electron scattering spectrometer," Rev. Sci. Instrum. **46**(11), 1546 (1975).

[68]A. E. Glassgold, VICPEAC, abstract of papers 646 (1967).

[69]A. E. Glassgold and G. Ialongo, "Angular distrubution of the outgoing electrons in electron ionization," Phys. Rev. **175**, 151 (1968).

[70]D. L. Greenaway, G. Harbeke, F. Bassani, and E. Tosatti, "Anisotropy of the optical constants and the band structure of graphite," Phys. Rev. **178**, 1340 (1969).

[71]R. Grigorovici, A. Devenyi, A. Gheorghiu, and A. Belu, "Properties of amorphous carbon films," J. Non-Crystalline Solids **8-10**, 793 (1972).

[72]P. Grivet, Electron Optics, (Pergamon Press, Oxford, 1972).

[73]H. Hafner, J. Arol Simpson, C. E. Kuyatt, "Comparison of the spherical deflector and cylindrical mirror analyzers," Rev. Sci. Instrum. **39**, 33 (1968).

[74]M. Hattori and K. Yamada, J. Phys. Soc. (Japan) **18**, 200 (1963).

[75]G. G. Hall, Phil. Mag. **43**, 338 (1952).

[76]G. G. Hall, Phil. Mag. **3**, 429 (1958).

[77]David Halliday and Robert Resnick, Physics, 3rd ed., (Wiley, New York, 1978), p. 818.

[78]B. M. Hartley, "The excitation of polarization waves in bound electronic states", Phys. Stat. Sol. **31**, 259 (1969).

[79]J. J. Hauser, "Electrical, structural, and optical properties of amorphous carbon," J. Non-crystalline Solids **23**, 21 (1977).

[80]P. W. Hawkes, ed., Magnetic Electron Lenses: Topics in Current Physics, (Springer-Verlag, Berlin, 1982).

[81]C. J. Heslop, "Fundamental aspects of reactive plasma etching," in Proceedings of the Ninth International Vacuum Congress and Fifth International Conference on Solid Surfaces (Madrid, Spain, 1983), pp. 462-471.

[82]F. J. Himpsel, J. F. Van der Veen, and D. E. Eastman, "Experimental bulk energy bands for diamond using hν-dependant photoemission," Phys. Rev. B **2**, 1967 (1980).

[83]L. Holland and S. M. Ojha, "The chemical sputtering of graphite in an oxygen plasma," Vacuum **26**(2), 53 (1976).

[84]N. A. W. Holzwarth, S. G. Louie, and S. Rabii, "X-ray form factors and the electronic structure of graphite," Phys. Rev. B**26**, 5382 (1982).

[85]S. T. Hood, I. E. McCarthy, P. J. O. Teubner and E. Weigold, Phys. Rev. Lett. **33**, 459 (1974).

[86]R. I. Jacobson and G. K. Wehner, "Study of ion-bombardment damage on a Ge(111) surface by low-energy electron diffraction," J. Appl. Phys. **36**, 2674 (1965).

[87]P. A. Jansson, J. Opt. Soc. Am. **60**, 184 (1970).

[88]L. G. Johnson and G. Dresselhaus, Phys. Rev. B

7, 2275 (1973).

[89]D. I. Jones and A. D. Stewart, Phil. Mag. B **46**, 423 (1982).

[90]R. Jones and A. L. Ritter, "Analysis of multiple scattering for (e,2e) experiments on thin films," (submitted to J. Elec. Spectrosc. Rel. Phenom.).

[91]A. A. Kahn, D. Mathine, J. A. Woollam, and Y. Chung, "Optical Properties of 'diamond-like' carbon films: An ellipsometric study," Phys. Rev. B **28**, 7229 (1983).

[92]J. Kakinoki, K. Katada, T. Hanawa, and T. Ino, Aca. Crystallogr. **13**, 171 (1968).

[93]E. F. Kennedy, D. H. Youngblood, and A. E. Blaugrund, Phys. Rev. **158**, 897 (1967) as cited in Stoner.

[94]R. Keown, Phys. Rev. **150**, 568 (1966).

[95]Claude A. Klein, "Electrical properties of pyrolytic graphites," Rev. Mod. Phys. **24**(1), 56 (1962).

[96]O. Klemperer and M. E. Barnett, Electron Optics, (Cambridge University Press, Cambridge, 1971).

[97]Chris E. Kuyatt, Electron Optics Notes, (1967) (unpublished).

[98]C. E. Kuyatt and J. Arol Simpson, "Electron monochromator design," Rev. Sci. Instrum. **38**, 103 (1967).

[99]N. A. Kzasilnikova and N. M. Persiatseva, Zh. T. F. Pis'ma **1**, 266 (1975).

[100]N. A. Kzasilnikova and N. M. Persiatseva, Sov. Tech. Phys. Lett. **1**, 127 (1975)

[101]N. A. Kzasilnikova and N. M. Persiatseva, Phys. Lett. A **69**, 287 (1978).

[102]G. Lang and S. deBenedetti, Phys. Rev. **108**,

911 (1957).

[103]Joel D. Lamb and John A. Woollam, "Dielectric properties of 'diamondlike' carbon prepared by rf plasma deposition," J. Appl. Phys. **57**, 5420 (1985).

[104]R. E. LaVilla and H. Mendlowitz, Appl. Optics **6**, 61 (1967).

[105]A. R. Law, J. J. Barry, and H. P. Hughes, Phys. Rev. B **28**, 5332 (1983).

[106]P. Lespade, R. Al-Jishi, and M. S. Dresselhaus, "Model for Raman scattering from incompletely graphatized carbon films," Carbon **20**, 427 (1982).

[107]V. G. Levin, V. G. Neudachin, and Yu. F. Smirnov, "On investigation of the structure of energy bands using quasielastic knock-out of an electron by an electron (e,2e)," Phys. Stat. Sol. (b) **49**, 489 (1972).

[108]K. L. Lim and I. E. McCarthy, "Analysis of (p,2p) angular correlation experiments," Phys. Rev. **133**, B1006 (1964).

[109]B. Lohmann and E. Weigold, "Direct measurement of the electron momentum probability distribution in atomic hydrogen", Phys. Lett. **86A**, 139 (1981).

[110]D. H. Madison, R. V. Cahoun and W. N. Shelton, Phys. Rev. **A16**, 552 (1977).

[111]C. P. Mallett, J. Phys. C **14**, L213 (1981).

[112]D. Marchand, C. Fretigny, M. Lagues, F. Batallan, Ch. Simon, I. Rosenman, and R. Pinchaux, "Three-dimensional band structure of graphite studied by angle-resolved photoemission using ultraviolet synchotron radiation," Phys. Rev. B **30**, 4788 (1984).

[113]I. E. McCarthy, "Theory of the (e,2e) reaction," E. Weigold, ed. Momentum Wave Functions -- 1982, AIP Conference Proceedings No. 86 (Am. Inst. Physics, New York, 1982).

[114]I. E. McCarthy and E. Weigold, "(e,2e) Spectroscopy," P. Reports **27C**, 277 (1976).

[115]I. E. McCarthy and E. Weigold, "Observing the

[115]I. E. McCarthy and E. Weigold, "Observing the motion of electrons in atoms and molecules," Contemp. Phys. **24**, 163 (1983).

[116]F. R. McFeely, S. P. Kowalezyk, L. Ley, R. G. Cavell, R. A. Pollak, and D. A. Shirley, "X-ray photoemission studies of diamond, graphite, and glassy carbon valence bands," Phys. Rev. B **9**, 5268 (1974).

[117]J. H. Moore, M. A. Coplan, T. L. Skillman, Jr., and E. D. Brooks III, Rev. Sci. Instrum. **49**, 463 (1978).

[118]I. S. McLintock and J. C. Orr, Chemistry and Physics of Carbon, Volume II, edited by P. L. Walker (Dekker, New York, 1973), p. 243.

[118a]D. F. R. Mildner and J. M. Carpenter, J. Non-Cryst. Solids **47**, 391 (1982).

[119]M. Morgan, "Electrical conduction in amorphous carbon films," Thin Solid Films **7**, 313 (1971).

[120]R. J. Nemanich, G. Lucousky, and S. A. Solin, "Long wavelength vibrations in graphite," Sol. St. Comm. **23**, 417 (1977).

[121]R. J. Nemanich, G. Lucousky, and S. A. Solin, in Proceedings of the International Conference on Lattice Dynamics, edited by M. Balkanski (Flammarion, Paris, 1975), p. 619.

[122]R. J. Nemanich, G. Lucousky, and S. A. Solin, Mater. Sci. Eng. **31**, 157 (1977).

[123]R. J. Nemanich and S. A. Solin, "First- and second-order Raman scattering from finite-size crystals of graphite," Phys. Rev. B **20**, 392 (1979).

[124]V. G. Neudachin, G. A. Novoskol'tseva, and Yu. F. Smirnov,"Quasielastic knock-out of an electron by a fast electron from atoms, molecules, and very thin crystalline films," Sov. Phys. JETP **28**, 540 (1969).

[125]V. G. Neudachin, and F. A. Zhivopistsev, "Manifestations of collective properties of the degenerate electron gas in the (e,2e) quasielastic knockout process," Phys. Rev. Lett. **32**, 995 (1974).

[126]M. J. Nobes, J. S. Colligon, and G. Carter, "The equillibrium topography of sputtered amorphous solids," J. Materials Sc. **4**, 730 (1969).

[127]P. Nozieres and D. Pines, Phys. Rev. **113**, 1254 (1959).

[128]A. Oberlin, M. Oberlin, and M. Maubois, "Study of thin amorphous and crystalline carbon films by electron microscopy," Phil. Mag. **36**, 833 (1976).

[129]G. S. Painter and D. E. Ellis, "Electronic band structure and optical properties of graphite from a variational approach," Phys. Rev. B **1**, 4747 (1970).

[130]G. S. Painter, D. E. Ellis, and A. R. Lubinsky, "*Ab initio* calculations of the electronic structure and optical properties of diamond using the discrete variational method," Phys. Rev. B **4**, 3610 (1971).

[131]G. Peach, "The impulse approximation revisited," Comments on Atomic and Molecular Physics **15**, 165 (1984).

[132]D. R. Penn, "Electron mean free paths for free-electron-like materials," Phys. Rev. B **13**, 5248 (1976).

[133]D. R. Penn, "Quantitative chemical analysis by ESCA," J. Elec. Spec. Rel. Phenom. **9**, 29 (1976).

[134]Powder Diffraction File, Joint Committee on Powder Diffraction Standards, 1979.

[135]J. J. Quinn, "Range of excited electrons in metals," Phys. Rev **126**, 1453 (1962).

[136]F. H. Read, "Calculated properties of electrostatic Einzel lenses of 3-apertures," J. Phys. E **2**, 679-684 (1969).

[137]A. Recknagel, Zeit. Für Phys. **111**, 61 (1938).

[138]W. A. Reed, and P. Eisenberger, "Gamma-ray Compton profiles of diamond, silicon, and germanium," Phys Rev B **6**, 4596 (1972).

[139]W. A. Reed, P. Eisenberger, K. C. Pandey, and L. C. Snyder, "Electron momentum distribution in graphite and diamond and carbon-carbon bonding," Phys. Rev. B **10**, 1507 (1974).

[140]G. Reinhold, Phys. Lett. **2**, 230 (1963).

[141]R. H. Ritchie, Phys. Rev. **106**, 874 (1957).

[142]John J. Ritsko, Inelastic Electron Scattering, Princeton University, Ph.D. (1974).

[143]A. L. Ritter, J. R. Dennison, and J. Dunn, "(e,2e) spectrometer for investigating the spectral momentum density of thin films," Rev. Sci. Instrum **55**, 1280 (1984).

[144]A. L. Ritter, J. R. Dennison, and R. Jones, "Spectral momentum density of amorphous carbon from (e,2e) spectroscopy," Phys. Rev. Lett. **53**, 2054 (1984).

[145]R. A. Roberts and W. C. Walker, Phys Rev. **161**, 730 (1967).

[146]John Robertson, "Electronic structure of amorphous semiconductors," Adv. Phys. **32**, 361 (1983).

[147]R. A. Robie, P. M. Bethke, and K. M. Beardsley, U. S. Geological Survey Bulletin 1248 as cited in Handbook of Chemistry and Physics, 60th Edition (CRC Press, Boca Raton, FL, 1979).

[148]N. Savvides, "Four-fold to three-fold transition in diamond-like amorphous carbon films: A study of optical and electrical properties," J. Appl. Phys. **58**, 518 (1985).

[149]S. Schnatterly and T. Cafolla, private communications.

[150]Kenneth D. Sevier, Low Energy Electron Diffraction, (Wiley, New York, 1972), p. 37.

[151]K. D. Sevier, Low Energy Electron Spectrometry, (Wiley, New York, 1972).

[152]"Shop Talk," (Magnetic Shield Division -- Perfection Mica Co., Bensenville, IL, 1984).

[153]M. A. Short and P. L. Walker, Jr., "Measurement of interlayer spacings and crystal sizes in turbostratic carbons," Carbon **1**, 3(1963).

[154]J. Arol Simpson and C. E. Kuyatt, "Anomalous energy spreads in electron beams," J. Appl. Phys. **37**, 3805 (1966).

[155]Yu. F.Smirnov and V. G. Neudachin, "Investigation of the electronic states of atoms, molecules, and solids by quasielastic knock-on of an electron by a fast electron (e,2e)," JETP Lett., (1966).

[156]Andrew B. Smith, "Notes on the performance and application of EMI windowless particle detectors," R/P034, Valve Division, EMI Electronics Ltd., 1965, p. 5.

[157]F. W. Smith, "Optical constants of a hydrogenated amorphous carbon film," J. Appl. Phys. **55**, 764 (1984).

[158]B. Stenhouse, P. J. Grout, N. H. March, and J. Wenzel, "Chemical bonding effects on the diffraction intensities in amorphous silicon and carbon," Phil. Mag. **36**, 129 (1977).

[159]G. Stefani, R. Camilloni, and A. Giardini Guidoni, "Absolute (e,2e) differential cross section measured in coplanar conditions: He," Phys. Lett. **64A**, 364 (1978).

[160]John O. Stoner, Jr., "Accurate determination of carbon-foil surface densities," J. Appl. Phys. **40**, 707 (1969).

[161]John O. Stoner, Jr., private communications.

[162]E. A. Taft and H. R. Phillip, "Optical properties of graphite," Phys. Rev. **138**A, 197 (1965).

[163]T. Takahashi, H. Tokailin, and T. Sagwa, "Electronic band structure of graphite studied by highly angle-resolved ultraviolet photoelectron spectroscopy," Solid State Comm. **52**, 765 (1984).

[164]R. C. Tatar and S. Rabii, "Electronic properties of graphite: A unified theoretical study," Phys. Rev. B **25**, 4126 (1982).

[165]J. M. Thomas, E. L. Evans, M. Barber, and P. Swift, Trans. Faraday Soc. **67**, 1875 (1972).

[166]F. Tuinstra and J. L. Koenig, "Raman spectra of graphite," J. Chem. Phys. **53**, 1126 (1970).

[167]A. R. Ubbelohde and F. A. Lewis, Graphite and Its Crystal Compounds, (Oxford University Press, Oxford, 1960).

[168]A. Ugbabe, E. Weigold, S. T. Hood, and I. E. McCarthy, "(e,2e) reaction in inert gasses: coplanar symmetric geometry," Phys. Rev. A **11**, 576 (1975).

[169]P. H. van Cittert, Z. Phys. **69**, 298 (1931).

[170]J. L. Vossen, "Inhibition of chemical sputtering of organics and C by trace amounts of Cu surface contamination," J. Appl. Phys. **47**, 544 (1976).

[171]L. Vriens, "Angular correlation of scattered and ejected electrons in ionzing collisions. II," Physica **47**, 267 (1969).

[172]N. Wada, P. J. Gaczi, and S. A. Solin, "'Diamond-like' 3-fold coordinated amorphous carbon," J. Non-Cryst. Solids **35**, 543 (1980).

[173]P. R. Wallace, "The band theory of graphite," Phys. Rev. **71**, 622 (1947).

[174]C. Weber, "Numerical solution of Laplace's and Poisson's equations and the calculation of electron trajectories and electron beams," Focusing of Charged Particles, Volume I, edited by A. Septier (Academic Press, New York, 1967).

[175]E. Weigold, Editor Momentum Wave Functions -- 1982, AIP Conference Proceedings Number 86 (Am. Inst. Physics, New York, 1982).

[176]E. Weigold and I. E. McCarthy, "(e,2e) Collisions," Ad. At. and M. Phys., (1978).

[177]E. Weigold, S. T. Hood, and I. E. McCarthy, "Structure of inert gases from the (e,2e) reaction," Phys. Rev. A **11**, 566 (1975).

[178]R. J. Weiss, and W. C. Phillips, "X-ray

determination of the electron momentum density in diamond, graphite, and carbon black," Phys. Rev. **176**, 900 (1968).

[179]R. J. Weiss, W. C. Phillips and A. Harvey, Philos. Mag. **17**, 146 (1960).

[180]G. K. Wertheim, "Deconvolution and smoothing: Applications in ESCA," J. Elec. Spec. Rel. Phenom. **6**, 239 (1975).

[181]G. K. Wertheim, "Novel smoothing algorithm," Rev. Sci. Instrum. **48**, 1414 (1975).

[182]Wiech and Zöpf, in Electronic Density of States, Nat. Bur. Stand. (U.S) Spec. Pub. 323 (U.S. GPO, Washington, D.C., 1969), p. 335.

[183]W. Wien, Verh. Dt. Phys. Ges. **16**, 165 (1897).

[184]B. G. Williams, "The experimental determination of electron momentum densities," Physica Scripta **15**, 92 (1972).

[185]J. F. Williams, S. Dey, D. Sampson, and D. McBrinn, "Progress report on (e,2e) collisions in thin films," E. Weigold, Ed. Momentum Wave Functions -- 1982, AIP Conference Proceedings No. 86 (Am. Inst. Physics, New York, 1982).

[186]P. M. Williams, "The direct evaluation of electronic band structures of layered solids using angle-resolved photoemission," Nuovo Cimento **38B**, 216 (1977).

[187]R. F. Willis, B. Fitton, and G. S. Painter, "Secondary-election emission spectroscopy and observation of high energy excited states in graphite: Theory and experiment," Phys. Rev. B **9**, 1926 (1974).

[188]M. J. Witcomb, "Predection of the apex angle of surface cones on ion-bombarded crystalline materials," J. Materials Sc. **9**, 1227 (1974).

[189]A. G. Wright, "Design of photomultiplier output

circuits for optimum amplitude of time response," R/P065, Electron Tube Division, EMI Industrial Electronics Ltd., 1977, p.2.

[190]W. H. Zachariasen, J. Am. Chem. Soc. **54**, 3841 (1932).

[191]R. Zallen, The Physics of Amorphous Solids, (Wiley, New York, 1983), pp. 60-72.

[192]P. C. Zalm and L. J. Beckers, "Consequences of sputtering with molecular ions," J. Appl. Phys. **56**, 220 (1984).

[193]J. M. Ziman, "Electron states in glassy semiconductors," J. Phys. C: Solid St. Phys. **4**, 3129 (1971).

[194]A. Zunger and A. J. Freeman, "Ground-state electronic properties of diamond in the local-density formalism," Phys. Rev. B **15**, 5049 (1977).

Appendix A. Derivation of (e,2e) Scattering Amplitude

The object of the following analysis is to derive an expression for the (e,2e) scattering amplitude M_{if} and in so doing keep track of all of the necessary approximations. This analysis is specific to solids and the approximations necessary for this are emphasized.

The work by McCarthy, Weigold, et al has been used as a guideline throughout this derivation. Their review article [114] contains an excellent explanation of their analysis and further details are found in other works by them [29,109,177]. They have concentrated on the theory of atomic and molecular targets, however much of the analysis can be generalized to the case of solid targets. In relating the scattering amplitude to the cross section and calculating the form factor for specific situations with solid targets, use has been made of several early sketches of theories for the (e,2e) reaction in solids, in particular work by Smirnov, Neudachin, and collaborators [107,124,155].

The (e,2e) scattering amplitude M_{if} can be formally expressed in terms of a scattering matrix S as

$$M_{if} = \langle \Psi^f \mid S \mid \Psi^i \rangle \qquad (A.1)$$

The initial wave function $|\Psi^i(x_1, x_2, \xi)\rangle$ is an (N+1)-body wave function which describes the initial state of the incident electron and the target. The target is an N-body system which includes the electron to be ejected and all of the other electrons in the target. The coordinates x_i include the position r_i and spin σ_i coordinates of the incident electron (i=1) and the ejected electron (i=2). All of the internal degrees of freedom of the ion are included in the coordinates ξ.

The term ion is used here as a general expression for the (N-1)-body system of the target after an electron has been ejected.

The final wave function $|\Psi^f(x_1, x_2, \xi)\rangle$ is also an (N+1)-body wave function which describes the final states of the scattered electron, ejected electron, and ion.

It is advantageous to make a few initial approximations at the outset. These are not too restrictive. First, the problem is considered as *non-relativistic*. The major implication is that spin-orbit coupling is unimportant which implies that electron spin enters into the problem only through the Pauli exclusion principle. In most of the equations below, explicit spin dependence is not shown. The center of mass motion of the target and ion are neglected; this amounts

to an assumption of *infinite target mass*. Finally, the target is assumed to be initially in a *ground state*. This implies that finite temperature effects are ignored.

The Schrodinger equation for the (e,2e) reaction can formally be expressed as

$$\left[E - \left\{K_1 + K_2 + H_I(\xi) + V_1(E_1 ; x_1,\xi) + V_2(E_2 ; x_2,\xi) + v(r)\right\}\right] \Psi^f(x_1,x_2,\xi) = 0 \qquad (A.2)$$

where $H_I(\xi)$ is the Hamiltonian of the ion, K_i are the electron kinetic energy terms, and V_i are the electron-ion potentials. The electron-electron Coulomb potential $v(r)$, which includes a non-local exchange term, depends on the relative coordinate of the electrons r. At the outset the potentials V_i are generalized as non-local and energy dependent to allow for the possibilities of inelastic channels in the reaction.

The (N+1)-body wave functions can be written in a multi-channel expansion as

$$\Psi(x_1,x_2,\xi) = \sum_{\mu} \psi_\mu(x_1) \, |\mu\rangle \qquad (A.3)$$

where the sum is over all possible channels. The expansion is in terms of the bases of target wave functions $|\mu\rangle$ which satisfy the Schrodinger equation

$$\left[\epsilon_\mu - (K_2 - H_I + V_2)\right] |\mu\rangle = 0 \qquad (A.4)$$

We want to separate the wave function for the incident

electron from these general target wave functions. In fact, we are only interested in two channels, that involving the target ground state $|g\rangle$ and the channel in which the target eigenstate $|w\rangle$ represents an ejected electron-ion system with a well defined energy and momentum. To achieve this separation, we make the approximation of *weak coupling between channels*. This approximation depends on the experimentally-observed fact (for gases) that elastic scattering is much more probable that any particular non-elastic channel [114]. This allows the separation of the incident electron wave function from the target wave function.

A further *two-body weak coupling approximation* allows the separation of $|w\rangle$ into a product of an ejected electron wave function and an (N-1)-body wave function of the final ion state $|f(\xi)\rangle$ which satisfies the Schrodinger equation

$$\left[\epsilon_f - H_1(\xi) \right] \left| f(\xi) \right\rangle = 0 \qquad \text{(A.5)}$$

At this point an optical potential model is introduced with the goal of reducing the (e,2e) amplitude from an (N+1)-body system to one involving wave functions computed in the optical model potential (distorted waves) and the structure wave functions of quantum chemistry. This is done in a series of approximation referred to by McCarthy

and Weigold [114,85] as the *distorted-wave off-shell impulse approximation.* An optical model potential $\tilde{V}_{\mu\nu}$ is derived [114] for two target states $|\mu>$ and $|\nu>$. The optical model potential allows the separated wave functions for the incident, scattered and ejected electrons to be expressed in terms of distorted wave functions which are products of a spatial wave function and a spin wave function. For the incident electron

$$\psi_{\mu}(x_1) = X_1^{i}(r_1) \quad X^{m}(\overleftrightarrow{\sigma}_1) \tag{A.6}$$

where the spatial wave function satisfies the approximate Schrodinger equation of the optical model potential

$$\left[E - \epsilon_{\mu} - K_1 - \tilde{V}_{\mu\mu}\right] X_1^{i}(r_1) \cong 0 \tag{A.7}$$

The spin component is not explicitly expressed in the rest of this section. There are analogous expressions for the scattered and ejected electron distorted wave functions $X_1^{f}(x_1)$ and $X_2^{f}(x_2)$.

Combining the weak coupling approximations and the optical potential model allow the initial and final (N+1)-body wave functions to be written as

$$\Psi^{i}(x_1,x_2,\xi) = X_1^{i}(x_1) \; |g(x_2,\xi)>$$

$$\Psi^{f}(x_1,x_2,\xi) = X_1^{f}(x_1) \; X_2^{f}(x_2) \; \left|f(x_2,\xi)\right] \tag{A.8}$$

Using these wave functions and expressing the optical model potential explicitly, the scattering amplitude can be

expressed as

$$M_{if} \cong \langle X_1^f(x_1)\, X_2^f(x_2) \,| \times \left[f(\xi) \right| \tilde{v} + v + v\, G_3(E)\, v \left| g(x_2,\xi) \right\rangle \left| X_1^i(x_1) \right\rangle \tag{A.9}$$

Antisymmetry is implied in this equation. The electron-electron potential is v. The potential $\tilde{v}$ produces inelastic scattering of the incident electron from the ion which is responsible for exciting non-elastic channels by changing the state of the ion and gives rise to a term representing ionization by core excitation. The total 3-body Green function is

$$G_3(E) = \lim_{\epsilon \to 0^+} \left[E - i\epsilon - (K_1 + K_2 + H_1 + \tilde{V}_1 + \tilde{V}_2 + v) \right]^{-1} \tag{A.10}$$

It is still necessary to reduce the problem further, to a 2-body problem. A simple albeit crude, approximation reduces the entire operator to only the electron-electron potential v. This is known as the *distorted-wave Born approximation* [110]. The addition of the plane-wave approximation for the distorted waves yields the *plane-wave Born approximation*; Reference 69 discusses the (e,2e) cross-section with regard to this approximation. A derivation of the scattering amplitude in this approximation is given in Section II.

McCarthy and Weigold [114] describe a less drastic approximation for reducing the problem to a form which

contains only 2-body wave functions and operators; the set of approximations is referred to as the *quasi-three body approximation*. The inelastic potential term in the Green function is assumed negligible. The electron-ion potentials $\tilde{V}_i$ are expanded in a Taylor series about the electron-electron center-of-mass coordinate **R**. For equal energies $E_1=E_2$, i.e., for symmetric geometries, the first term in $V_1(\mathbf{R})$ vanishes. Higher order terms, i.e., gradient $\vec{\nabla}_R$ terms, are expected to be ineffective if the electron-electron potential is short range. However, v is a Coulomb potential; higher order terms will be small only if the experiment is designed to have high energy incident, scattered, and, ejected electrons. For atoms the gradients are quite small except at the canter of the atom where the integrand is cut off by bound-state orbitals except for the 1s case. The reduced two-body Green function is

$$G_2(E) = [p^2 - K_r - v]^{-1} \qquad \text{(A.11)}$$

where $p = \frac{1}{2}(p_1 - p_2)$ and K_r is the electron kinetic energy in relative coordinates. The scattering amplitude is given by

$$M_{if} \cong \langle X_1^f | \langle X_2^f | \left[f \left| \tilde{v} + T_M(p^2) \right| g \right\rangle | X_1^i \rangle \qquad \text{(A.12)}$$

where $T_M(p^2)$ is the two-body Coulomb t-matrix including exchange (Mott scattering) which describes the removal of

the ejected electron by the incident electron. This Coulomb t-matrix is given by

$$T_M(p^2) = (1 - P_{12})\,[v + v\,G_2(E)\,v] \qquad (A.13)$$

where P_{12} is the exchange operator.

All of the approximations made thus far constitute what McCarthy and Weigold refer to as the *distorted-wave off-shell impulse approximation* for the (e,2e) reaction [114].

An additional effect of the quasi-three-body approximation is that the term involving $\tilde{v}$ in Equation A.12 may be neglected. Weigold and McCarthy [114,177] review neglect of this term extensively from both a theoretical view and by examining extensive data on atomic and molecular systems. They conclude that it is negligible above an incident energy $E_0 \gtrsim 100$ eV.

Note that the scattering amplitude now depends on the target and ion structure only through the overlap function $\langle f|g\rangle$ since T_M is independent of the internal coordinates ξ. The operator T_M commutes with $\langle f|$ and

$$M_{if} \cong \langle X_1^f|\langle X_2^f|\,T_M(p^2)\,\big|\,\big[\langle f|g\rangle|X_1^i\rangle \qquad (A.14)$$

Evaluation of the scattering amplitude using the fully distorted optical model wave functions is limited to only very simple cases. The primary difficulty in evaluation of this integral arises from the complexity in transforming

the t-matrix to the same coordinate system in which the distorted waves are expressed. A series of approximations to these wave functions provides less and less exact alternative wave functions; the less exact approximations are valid for higher and higher electron energies. McCarthy and Weigold provide a detailed description of these alternative wave functions and discuss the validity of the approximations and the accuracy of theoretical fits to gas scattering data using them [114].

The *phase-distortion approximation* is a five parameter approximate wave function. It has been used particularly for low-incident energy high-atomic number atoms and molecules and provides excellent fit to all symmetric non-coplanar data. It is, however, too complex for present theories in (e,2e) solid scattering.

The *eikonal approximation* describes a distorted optical model wave as a plane wave with an effective propagation constant $\vec{K} = (1+\beta+i\gamma)\mathbf{k}$,

$$X(\mathbf{k},\mathbf{r}) \cong \exp(-\gamma kR)\exp[i(1+\beta+i\gamma)(\mathbf{k}\cdot\mathbf{r})] \qquad (A.15)$$

The phase modification parameter β represents an average change of wave length in the relevant region. The attenuation parameter γ represents loss of flux due to excitation on nonelastic channels. The model wave function is normalized so that its magnitude is one at a point R, just before the beam enters the interaction region.

The *plane-wave approximation* is simply a special case of the eikonal approximation where $\gamma = \beta = 0$. All present calculations of (e,2e) reactions in solids use this approximation.

The expression for the scattering amplitude can be greatly simplified by factoring the t-matrix and overlap function components; this is called the *factorization approximation*. In the eikonal approximation this factorization is exact:

$$M_{if} \cong \left\langle \tfrac{1}{2}(K_1 - K_2) \middle| T_M\left(\tfrac{\hbar^2}{4m}|K_1 - K_2|^2\right) \middle| \tfrac{1}{2}(K_0 + q) \right\rangle \times \langle X_1^f | \langle X_2^f | \left(f \middle| g \right\rangle | X_1^i \rangle \qquad \text{(A.16)}$$

Including the effects of the exclusion principle, the t-matrix term is given by

$$\langle T \rangle = C_0^2(\eta) \left\{ \frac{1}{|K - K'|^4} + \frac{1}{|K + K'|^4} - \frac{1}{|K + K'|^2 \, |K - K'|^2} \cos\left(\eta \ln\left[\frac{|K + K'|^2}{|K - K'|^2} \right] \right) \right\}$$

$$\text{where } C_0^2(\eta) \equiv \frac{2\pi\eta}{[\exp(2\pi\eta) - 1]}$$

$$\eta \equiv \frac{m e^2}{2 \hbar^2 K'}$$

$$K \equiv \tfrac{1}{2}(K_0 + q)$$

$$K' \equiv \tfrac{1}{2}(K_1 - K_2) \qquad \text{(A.17)}$$

McCarthy and Weigold [114] have determined empirically that this term is described adequately by the plane wave approximation for realistic values of β and γ by reducing

the effective propagation constants $\vec{K}_i$ to the momenta $\vec{k}_i$. This term is then related to the Mott electron-electron cross section (see Equation II.17). In the non-coplanar symmetric geometry the Coulomb t-matrix term is essentially constant over a relevant range of q but varies somewhat more rapidly in the coplanar symmetric geometry.

We can now turn our attention to the overlap function $\langle f|g\rangle$ which remains as the last quantity to calculate. Evaluation requires that the dependence on the coordinate x_2 be separated from the target wave function. To do this we must evoke one final approximation, the *single particle or independent electron approximation*. It is at this point that the analysis for solid targets begins to differ significantly from that of gasses.

The target wave function can be expanded either in term of a Hartree-Fock configuration [114] or in the form of a Slater determinate made up of the single electron wave functions [124]. Employing the Hartree-Fock configuration, the overlap integral can be expressed as a sum over these states

$$\langle f|g\rangle = \sum_c f_c \, \psi_c(x_2) \qquad \text{(A.18)}$$

where f_c are the coefficients for the expansion in terms of the Hartree-Fock wave functions for the target ground

state. This expansion makes the implicit assumption that there are no significant configuration interactions in the ion. The single particle approximation consists of assuming that only one of the expansion coefficients is non-negligible. Then the overlap integral reduces to the characteristic wave function of the electron in the target before it was ejected $\psi_n(x_2)$: n denotes the specific characteristic wave function.

It is often useful to use the Slater determinate form to express the characteristic wave function of an electron in a solid in terms of the atomic orbital basis functions. In this case the expansion coefficients for the overlap integral are just the coefficients derived in the tight-binding model expansion of the target electron orbital.

In the eikonal approximation the overlap function can be expressed as a form factor

$$F_{ij}(\mathbf{q}) = \frac{1}{(2\pi)^{3/2}} \int d\mathbf{r}_2 \; \psi_n(\mathbf{r}_2) \; e^{-i\,\mathbf{q}\cdot\mathbf{r}_2} \qquad \text{(A.19)}$$

Extending this to the plane wave approximation, the form factor is equal to the Fourier transform $\phi_n(\mathbf{q})$ of target electron wave function where the momentum

$$\mathbf{q} = \mathbf{k}_1 + \mathbf{k}_2 - \mathbf{k}_o \qquad \text{(A.20)}$$

as we found from kinematic arguments earlier.

The final expression for the (e,2e) scattering amplitude is

$$M_{if} = \langle T_M \rangle \; F_{if}(\mathbf{q}) \qquad \text{(A.21)}$$

Appendix B. Derivation of Multiple Scattering Function

In order to evaluate the smearing function $\mathcal{S}$, we must have some knowledge of the $\mathcal{F}$-functions.

$\frac{d^4\,\mathcal{F}}{d^3\,q\,d\,\epsilon}$ $\frac{d^4\,\mathcal{F}}{d^3\,q\,d\,\epsilon}$ $\frac{d^4\,\mathcal{F}''(\epsilon,\,\mathbf{q};\,E,\,T)}{d^3\,q\,d\,\epsilon}$ is the probability density that an electron traveling in the direction $\mathbf{k}$, $\mathbf{k}'$, $\mathbf{k}''$ with initial energy E will lose energy ϵ and momentum $\mathbf{q}$ in traveling through a target of thickness T. Considering the approximations in Equations II.50 and II.51, it can be seen that $\mathcal{F}$, $\mathcal{F}'$, and $\mathcal{F}''$ are all the same function, except that their coordinate systems are rotated with respect to each other to align them with their corresponding beam axis. We need to find an expression for $\mathcal{F}$ in terms of more elementary functions.

Consider first the function $\mathcal{F}$, related to $\overline{\mathcal{F}}$, which does not include the effects of instrumental energy-momentum broadening. When the scattering thickness goes to zero,

$$\frac{d^4\mathcal{P}}{d^3q\ d\epsilon}(\epsilon,q;E,0) \equiv P_0(\epsilon,q) = \delta(E)\ \delta^3(q) \qquad (B.1)$$

This insures the normalization of $\mathcal{P}$ and express the fact that no energy or momentum was exchanged. Extending this to include instrumental broadening,

$$\frac{d^4\bar{\mathcal{P}}}{d^3q\ d\epsilon}(\epsilon,q;E,0) \equiv \bar{P}_0(\epsilon,q) \qquad (B.2)$$

where $\bar{P}_0$ is the resolution function of the spectrometer normalized to unity. In the limit of thin films

$$\frac{d^4\mathcal{P}}{d^3q\ d\epsilon}(\epsilon,q;E,\delta\tau) = [1-\mu_1(E)\delta\tau]\ P_0(\epsilon,q) + \mu_1(E)\ \delta\tau\ \bar{P}_1(\epsilon,q) \qquad (B.3)$$

where $\bar{P}_1(\epsilon,q)$ is also normalized to unity and $\mu_1(E)$ is the probability of single scattering per unit thickness of the scatter (the reciprocal of the mean free path). Equation B.3 shows that the unscattered beam is depleted by the amount scattered and that the function $\bar{P}_1$ describes the distribution of the scattered particles. This equation is valid for thicknesses such that $\mu_1(E)\delta t << 1$, i.e. for films of thickness much less than the mean free path. The equation is extended to finite thicknesses using the Poisson distribution [26] in the form

$$\frac{d^4\bar{\mathcal{P}}}{d^3q\ d\epsilon}(\epsilon,q;E,\tau) = \exp(-\mu_1(E)\tau) \sum_{n=0}^{\infty} \frac{(\mu_1(E)\tau)^n}{n!}\ \bar{P}_n(\epsilon,q) \qquad (B.4)$$

where $\bar{P}_n(\epsilon,q) = P_1 \otimes \bar{P}_{n-1}$; $n = 1,2,3...$

In practice it will be advantageous to separate the function

$$\not{h}_1(E)\ P_1(\epsilon,\mathbf{q}) = {}_0\not{h}_1(E)\ {}_0P_1(\epsilon,\mathbf{q}) + {}_1\not{h}_1(E)\ {}_1P_1(\epsilon,\mathbf{q})$$

$$\not{h}_1(E) = {}_0\not{h}_1(E) + {}_1\not{h}_1(E) \qquad \text{(B.5)}$$

where the prescript 0 refers to elastic processes and 1 refers to inelastic processes. ${}_0P_1$ and ${}_1P_1$ are separable into product functions of ϵ and $\mathbf{q}$ separately, whereas P_1 is not. The literature also reports ${}_0P_1$ and ${}_1P_1$ separately. This separation was discussed in a physical context in Section II.A. The approximations of Equations II.50 and II.51 are somewhat relaxed when applied to elastic and inelastic scattering separately and are in good agreement with experiment. Equation B.4a is modified so that

$$\overline{P}_n(E;\epsilon,\mathbf{q}) = \left\{ \frac{{}_0\not{h}_1(E)}{\not{h}_1(E)}\ {}_0P_1 + \frac{{}_1\not{h}_1(E)}{\not{h}_1(E)}\ {}_1P_1 \right\} \otimes \overline{P}_{n-1}$$

$$;n = 1,2,3... \qquad \text{(B.4b)}$$

Making use of the expansion

$$(a+b)^n = \sum_{m=0}^{n} \binom{n}{m} a^m\ b^n$$

$$\overline{P}_n(E;\epsilon,\mathbf{q}) = \sum_{m=0}^{n} \binom{n}{m} \left(\frac{{}_0\not{h}_1(E)}{\not{h}_1(E)} \right)^m \left(\frac{{}_1\not{h}_1(E)}{\not{h}_1(E)} \right)^{n-m}$$

$$x \left[{}_0P_m \otimes {}_1P_{n-m} \otimes \overline{P_0} \right] \qquad ;n = 1,2,3... \qquad \text{(B.4c)}$$

where the notation ${}_0P_n$ means ${}_0P_1$ convoluted with itself (n-1) times. All of the $\overline{P}_n$ can now be calculated solely from the functions ${}_0P_1$, ${}_1P_1$, and $\overline{P}_0$ and the inverse of the mean free paths at the appropriate beam energy.

The smearing function can now be expanded in terms of the $\overline{P_n}$ functions by substituting Equation B.4c into Equation II.54 as

$$\mathcal{S}(\epsilon,\mathbf{q};E,T) = \sum_{j_0,k_0,l_0=0}^{\infty} \sum_{j_1,k_1,l_1=0}^{\infty} C^{j_0,k_0,l_0}_{j_1,k_1,l_1}(E,T) \; \mathcal{K}^{j_0,k_0,l_0}_{j_1,k_1,l_1}(\epsilon,\mathbf{q})$$

$$\text{where } C^{j_0,k_0,l_0}_{j_1,k_1,l_1}(E,T) = \int_0^T d\tau \left\{ \exp[-\mathcal{h}_1(E)\tau - 2\mathcal{h}_1(E/2)T'] \right.$$

$$\left. \tau^{j_0+j_1} T'^{,k_0+k_1+l_0+l_1} \right\}$$

$$\times \left[\frac{{}_0\mathcal{h}_1(E)^{j_0}}{j_0!} \frac{{}_1\mathcal{h}_1(E)^{j_1}}{j_1!} \frac{{}_0\mathcal{h}_1(E/2)^{k_0+l_0}}{k_0!\; l_0!} \frac{{}_1\mathcal{h}_1(E/2)^{k_1+l_1}}{k_1!\; l_1!} \right]$$

$$\text{and } \mathcal{K}^{j_0,k_0,l_0}_{j_1,k_1,l_1}(\epsilon,\mathbf{q}) = \{[\overline{P}_0 \otimes {}_0P_{j_0} \otimes {}_1P_{j_1}] \otimes [\overline{P}_0' \otimes {}_0P'_{k_0} \otimes {}_1P'_{k_1}]$$

$$\otimes [\overline{P}_0'' \otimes {}_0P_{l_0}'' \otimes {}_1P_{l_1}'']\} \qquad \text{(B.6a)}$$

The subscripts j_0 and j_1 refer to the number of elastic and inelastic multiple scatterings in the input beam; k and l refer to the output beams. Evaluation of the distance integral yields

$$C^{j_0,k_0,l_0}_{j_1,k_1,l_1}(E,T) = \frac{\alpha^j\ \beta^{k+1}}{(\alpha-2\beta)\ (j_0!\ j_1!\ k_0!\ k_1!\ l_0!\ l_1!)} \times \Bigg\{ e^{-2\beta T}\ T^{j+k+1} \times \Bigg[\sum_{i=0}^{j} \binom{j}{i} (i+k+1)!\ (-1)^i \Bigg[\sum_{m=0}^{i+k+1} \frac{1}{(i+k+1-m)!\ [(2\beta-\alpha)T]^m} \Bigg] \Bigg] - e^{-\alpha T} \Bigg[\sum_{i=0}^{j} \binom{j}{i} \frac{(i+k+1)!\ (-1)^i\ T^{j-i}}{(2\beta-\alpha)^{i+k+1}} \Bigg] \Bigg\}$$

where $j \equiv j_0 + j_1$, etc.

$$\alpha \equiv \hbar_1(E)$$

$$\beta \equiv \frac{\hbar_1(E/2)}{(\hat{k} \cdot \hat{k}')} \qquad \text{(B.6b)}$$

The convolutions in the expression for the smearing function are most easily evaluated by using the convolution theorem of Fourier analysis [22]. Let x and t be the Fourier transform pairs of q and ϵ, respectively. Since the Fourier transform is linear, operation on Equation B.6 yields the Fourier transform of the smearing function,

$$\mathcal{T}(t,x;E,T) = \sum_{j_0,k_0,l_0=0}^{\infty} \sum_{j_1,k_1,l_1=0}^{\infty} C^{j_0,k_0,l_0}_{j_1,k_1,l_1}(E,T)\ \mathcal{L}^{j_0,k_0,l_0}_{j_1,k_1,l_1}(t,x)$$

where $\mathcal{L}^{j_0,k_0,l_0}_{j_1,k_1,l_1}(t,x) = (4\pi^2)^{2+j+j+1} \cdot \Big\{ \bar{Q}_0 \cdot \bar{Q}_0' \cdot \bar{Q}_0'' \cdot [\ {}_0Q_1]^{j_0} \cdot [\ {}_1Q_1]^{j_1} \cdot [\ {}_0Q_1']^{k_0} \cdot [\ {}_1Q_1']^{k_1} \cdot [\ {}_0Q_1'']^{l_0} \cdot [\ {}_1Q_1'']^{l_1} \Big\}$ (B.7)

$\mathcal{L}$ is the Fourier transform of $\mathcal{K}(\epsilon,\mathbf{q})$ and the Q-

functions are the Fourier transforms of the corresponding P-functions.

Nine functions are required to describe the three $\mathcal{P}$-functions. This can be reduced to four independent functions by noting that the ${}_0P_1$ and ${}_1P_1$ functions are the same for each beam with an appropriate rotation of axes and that the two output arms have identical resolution functions. These four basic functions are:

$P_a(\epsilon,\mathbf{q})$: the normalized probability density that the *output analyzers* will detect a particle at momentum $\mathbf{q}$ and energy ϵ below its selected value.

$P_b(\epsilon,\mathbf{q})$: the normalized probability density that an electron in the *incident beam* is at an energy ϵ and momentum $\mathbf{q}$ below the selected value.

$P_e(\epsilon,\mathbf{q})$: the normalized probability density that an *elastically* scattered electron will lose energy ϵ and momentum $\mathbf{q}$ to the target.

$P_u(\epsilon,\mathbf{q})$: the normalized probability density that an *inelastically* scattered electron will lose energy ϵ and momentum $\mathbf{q}$ to the target.

By introducing three rotation matrices, the nine P-functions can be expressed as

$$\bar{P}_o(\epsilon,\mathbf{q}) = P_b(\epsilon,\bar{\mathcal{O}}\mathbf{q}) \qquad \bar{P}_o'(\epsilon,\mathbf{q}) = P_a(\epsilon,\bar{\mathcal{O}}'\mathbf{q}) \qquad \bar{P}_o''(\epsilon,\mathbf{q}) = P_a(\epsilon,\bar{\mathcal{O}}''\mathbf{q})$$

$${}_oP_1(\epsilon,\mathbf{q}) = P_e(\epsilon,\bar{\mathcal{O}}\mathbf{q}) \qquad {}_oP'_1(\epsilon,\mathbf{q}) = P_e(\epsilon,\bar{\mathcal{O}}'\mathbf{q}) \qquad {}_oP''_1(\epsilon,\mathbf{q}) = P_e(\epsilon,\bar{\mathcal{O}}''\mathbf{q})$$

$${}_1P_1(\epsilon,\mathbf{q}) = P_u(\epsilon,\bar{\mathcal{O}}\mathbf{q}) \qquad {}_1P'_1(\epsilon,\mathbf{q}) = P_u(\epsilon,\bar{\mathcal{O}}'\mathbf{q}) \qquad {}_1P''_1(\epsilon,\mathbf{q}) = P_u(\epsilon,\bar{\mathcal{O}}''\mathbf{q})$$

(B.8)

The rotation matrices $\mathcal{O}$, $\mathcal{O}'$, $\mathcal{O}''$ rotate the fixed target axes into the beam axes. The fixed target axes as illustrated in Figure B.1 are:

$\hat{q}_z$: In the direction of the input arm axis parallel to the beam arm plane.

$\hat{q}_x$: Perpendicular to $\hat{q}_z$ and in the beam arm plane.

$\hat{q}_y$: Perpendicular to $\hat{q}_z$ and the beam arm plane.

Each of the three beam coordinate systems have axes:

$\hat{q}_{11}$: Parallel to the beam direction.

$\hat{q}_1$: Perpendicular to $\hat{q}_{11}$ and parallel to the beam arm plane.

$\hat{q}_2$: Perpendicular to $\hat{q}_{11}$ and $\hat{q}_1$

The rotation matrices for the fixed coordinates into the beam coordinates are:

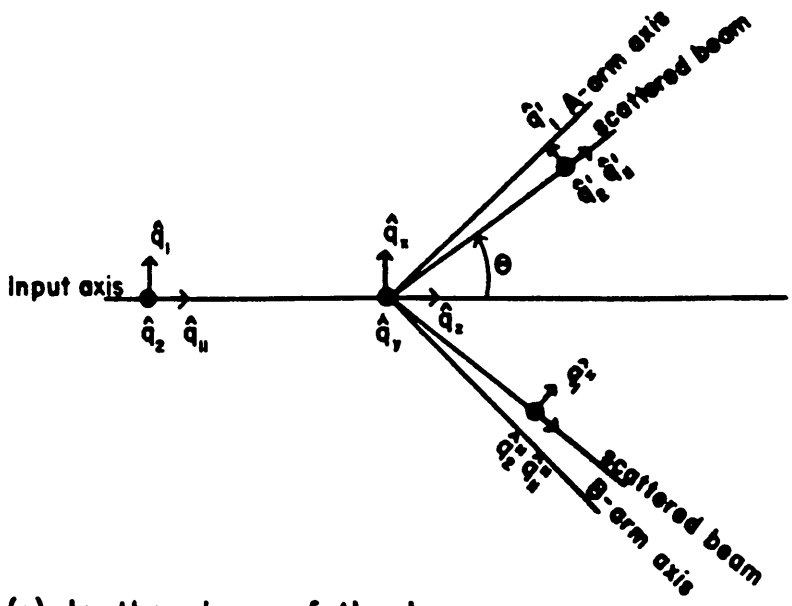

(a) In the plane of the beam arms

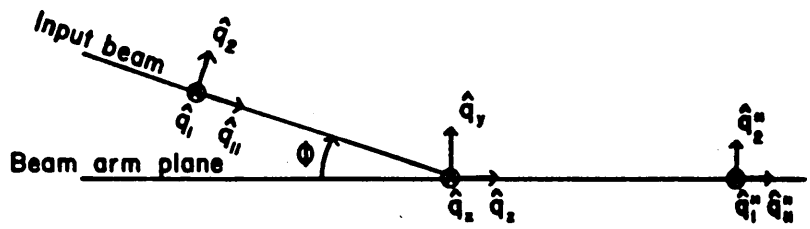

(b) Out of the plane of the beam arms

Figure B.1 Spectrometer coordinate systems.

$$\overline{\theta} = \begin{pmatrix} 1 & 0 & 0 \\ 0 & \cos\phi & \sin\phi \\ 0 & -\sin\phi & \cos\phi \end{pmatrix}$$

$$\overline{\theta}' = \overline{\theta}'' = \begin{pmatrix} \cos\theta & 0 & -\sin\theta \\ 0 & 1 & 0 \\ \sin\theta & 0 & \cos\theta \end{pmatrix} \qquad \text{(B.9)}$$

In the symmetric geometry $\theta' = \theta'' \equiv \theta$.

The instrumental broadening functions $P_a(\mathcal{E},q)$ and $P_b(\mathcal{E},q)$ can be model as Gaussian distributions

$$P_a(\epsilon,q) = \frac{1}{(2\pi)^{3/2}} \frac{1}{a_x\, a_y\, a_\epsilon} \exp\left[\frac{-\epsilon^2}{2a_\epsilon^{\,2}} + \frac{-q_x^{\,2}}{2a_x^{\,2}} + \frac{-q_y^{\,2}}{2a_y^{\,2}} \right] \delta(q_z)$$

$$P_b(\epsilon,q) = \frac{1}{(2\pi)^{3/2}} \frac{1}{b_x\, b_y\, b_\epsilon} \exp\left[\frac{-\epsilon^2}{2b_\epsilon^{\,2}} + \frac{-q_x^{\,2}}{2b_x^{\,2}} + \frac{-q_y^{\,2}}{2b_y^{\,2}} \right] \delta(q_z) \qquad \text{(B.10)}$$

where a and b are the widths of the Gaussian distributions. The delta function in q_z is a result of the negligible effect of broadening on the large momentum along the beam axis.

The elastic and inelastic distributions can be expressed as

$$P_e(\epsilon,q) = F_e(q_\perp)\, \delta(\epsilon)\, \delta(q_\parallel)$$

$$P_u(\epsilon,q) = F_u(q_\perp)\, U(\epsilon)\, \delta(q_\parallel) \qquad \text{(B.11)}$$

These are the normalized versions of the quasi-elastic scattering cross sections described in Section II.A. Using the parameterized forms (see Equations II.6, II.10, and II.12) together with the added constraints imposed by normalization

$$P_e(\epsilon,q) = \left\{ \frac{q_o^2 / \pi}{(q_\perp^2 + q_o^2)^2} \right\} \delta(\epsilon)\ \delta(q_\parallel)$$

$$P_u(\epsilon,q) = \left\{ \frac{\frac{1}{2\pi} \frac{\left(q_c^2 - q_e^2\right)}{\ln\left(q_c/q_E\right)}}{\left(q_\perp^2 + q_c^2\right)\left(q_\perp^2 + q_E^2\right)} \right\}$$

$$\times \left\{ \frac{V_1 \epsilon}{\left(\epsilon^2 - V_2^2\right)^2 V_3 + \epsilon^2} \right\} \delta(q_\parallel)$$

where $q_\perp < q_c$ and $\epsilon > 0$ (B.12)

Here q_0, q_c, q_E, V_2, and V_3 are free parameters left to fit data for quasi-elastic scattering; V_1 can be determined from normalization.

To find the Q-functions for the evaluation of Equation B.7 one needs to merely find the Fourier transform of the four functions above. The Fourier transform of a function whose coordinates have been rotated is equal to the Fourier transform of the function prior to rotation with the transform coordinates rotated in the same manner; therefore the Q-functions can be constructed in an identical manner as the P-functions in Equation B.8 from

$$Q_a(t,x) = \frac{1}{4\pi^2} \exp\left[\frac{-1}{2} a_\epsilon^2 t^2 + \frac{-1}{2} a_x^2 x^2 + \frac{-1}{2} a_y^2 y^2 \right]$$

$$Q_b(t,x) = \frac{1}{4\pi^2} \exp\left[\frac{-1}{2} b_\epsilon^2 t^2 + \frac{-1}{2} b_x^2 x^2 + \frac{-1}{2} b_y^2 y^2 \right]$$

$$Q_\epsilon(t,x) = \frac{q_o L}{4\pi^2} K_1(q_o L) \qquad ; L \equiv \sqrt{x^2 + y^2}$$

$$Q_u(t,x) = \tilde{F}_u(x_\perp)\, \tilde{U}(t)$$

where $$\tilde{F}_u(x_\perp) = \frac{1}{(2\pi)^{3/2} \ln(q_c/q_E)} \left\{K_o(q_E L) - K_o(q_c L)\right\}$$

with $L \equiv \sqrt{x^2 + y^2}$

and $$\tilde{U}(t) = \frac{-V_1}{\sqrt{\left(\frac{2\pi}{V_3}\right)\left[V_2^2 - (4V_3)^{-1}\right]}} \left\{ \mathcal{Im}\left[\cos(\rho)\, Ci(\rho) + \sin(\rho)\, Si(\rho)\right] - \frac{i\pi}{2} \exp\left(\frac{-|t|}{2\sqrt{V_3}}\right) \sin\left(t\sqrt{V_2^2 - (4V_3)^{-1}}\right)\right\}$$

with $$\rho \equiv -|t| \left[\sqrt{V_2^2 - (4V_3^2)^{-1}} + \frac{i}{2\sqrt{V_3}}\right]$$

(B.13)

where K_o and K_1 are modified Bessel functions of order zero and one and Si and Ci are the sine and cosine integral functions, respectively [1]. Plots of these functions for parameters characteristic of a-C are found in Section XIII.

APPENDIX C: ELECTRON OPTICS

This appendix relates to electron optics. The first section provides a review of the basic principles of electron optics and the definitions of terms used in this work. It is not intended to be a thorough treatise on the subject; for that, the reader is referred to the more complete treatments by Klemperer [96], Grivet [66], and Kuyatt [97]. The second section discusses the matrix method of calculations for electron optics trajectories and some of the software developed to model electron optics systems. Section three contains specific information on the theory of electron optics components used in our spectrometer together with diagrams and dimensions of the system.

1. Theory

The fundamental concepts of electron optics are based on the identity of the optical description of the path of a light ray through a refractive medium and the mechanical description of the motion of a point mass through a potential field. This follows from a comparison of Fermat's principle of least time as applied to the path of a light ray, with Maupertuis' principle of least action as applied to any mechanical motion. In direct analogy with light

optics, a refractive index of an (non-relativistic) electron in an electrostatic field of potential V can be written as

$$n = \sqrt{\frac{2eV}{mc^2}} \qquad (C.1)$$

which leads to an analog of Snell's Law for an electron traversing the boundary of two regions of constant potential V_1 and V_2:

$$\frac{\sin\alpha_1}{\sin\alpha_2} = \sqrt{\frac{V_2}{V_1}} \qquad (C.2)$$

A similar, though somewhat more complicated, treatment of the motion of electron can be performed for motion of an electron in a magnetostatic field [96]. These "indices of refraction" provide the necessary ties to light optics.

This analogy becomes particularly useful for cylindrically symmetric fields. The paraxial approximation limits the theory to rays which are close to the axis and make a very small angle with it. For electron lenses, this in effect, is equivalent to assuming that all the rays pass through potentials gradients equal to the axial potential, that is that there are no radial fields. For such fields, it can be shown that the equations of Newtonian or thick lens light optics can be applied directly (see for instance Born and Wolf [21]). Thick lens optics must be used since

the finite extent of potential distributions imply that all electron lenses are fundamentally "thick lenses." The cardinal elements of a thick lens are shown in Figure C.1. Newton's lens equation states that

$$f_1 f_2 = p\ q \tag{C.3}$$

Another useful relation that follows is

$$f_1 / f_2 = \sqrt{V_1 / V_2} \tag{C.4}$$

The electron optics form of Abbe's sine law is

$$\sqrt{V_1}\ y_1 \sin\theta_1 = \sqrt{V_2}\ y_2 \sin\theta_2 \tag{A.5}$$

where θ_1 and θ_2 are the semi-aperture angles of the bundles of rays at the object and image respectively (that is the pencil angles θ_p). We can define the Helmholtz-Lagrange constant as

$$HL = \sqrt{V}\ 2\ y\ \theta_p \tag{C.6}$$

which is a conserved quantity for images, assuming the small angle approximation. The quantity $2y\theta_p$ is defined as the emittance.

An image in electron optics can be described by three parameters. One method of characterization is to specify the image radius r_p, its pencil angle θ_p, and its beam angle θ_b. Another equivalent method uses two apertures to define the image, specifying the pupil radius r_p,

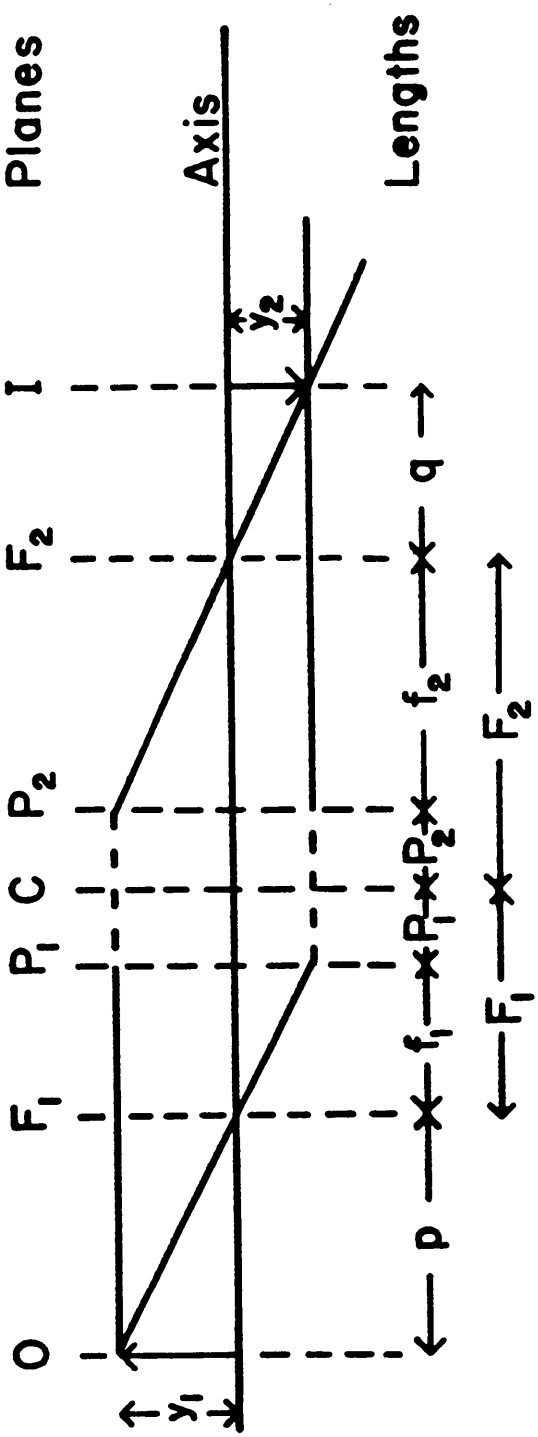

An object of height y_1 at plane O is focused by a lens centered at plane C to an image of height y_2 at plane I. The focal planes F and the principle planes P of the lens are subscripted by 1 and 2 for the object and images side of the lens, respectively.

Figure C.1 Thick lens cardinal elements.

window radius r_w, and the distance between the pupil and window d [97]. Figure C.2 illustrates the relationship between these methods.

. R-θ diagrams [97] provide a convenient method for displaying the trajectories of the rays from an image (see Figure C.6). Radius is plotted versus angle of slope for the nine principle rays at a given point along the beam axis. These nine rays delimit the maximum range of radii and angles for all rays emanating from the image, that is there are rays from the image for all (r,θ) inside the region bounded by the parallelogram formed by the principle rays. It should be noted that the sides of this parallelogram are parallel to the θ-axis when an image is formed at the given axial position z.

An alternate approach to trajectory calculation is the ballistic method. The differential equations of motion for a given set of fields are solved for the trajectories of an electron with some initial position and velocity. This approach is useful for system where the paraxial approximation is invalid. The theory of deflector plates and the Wien filter described below use this approach. Grivet [66] derives the theories of electron optics using the differential equations of motion.

As with light optics, the quality of electron lenses suffer from aberrations. Hawkes [80] identifies five

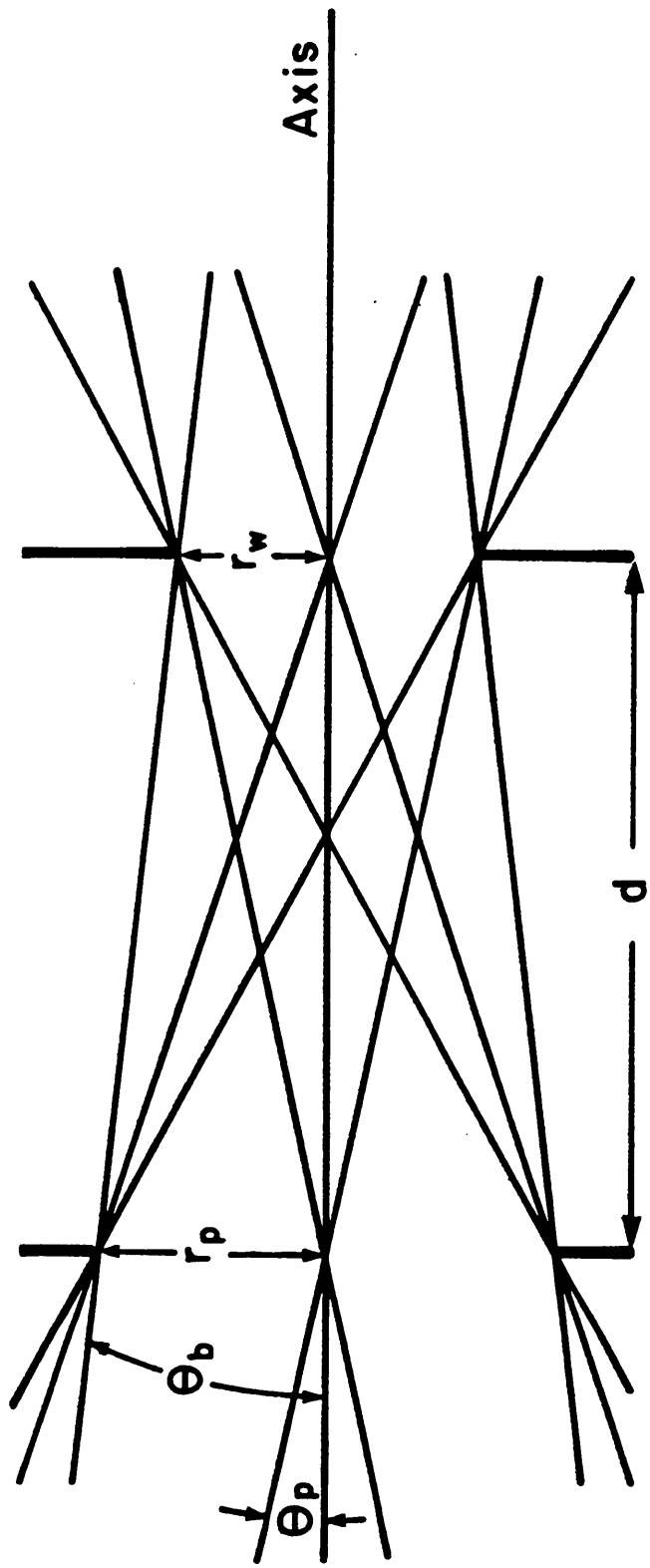

Figure C.2 Characterization of Images.

The radius r_p, pencil angle θ_p, and beam angle θ_b for an image at the pupil are shown. The equivalent representation using a pupil radius r_p, window radius r_w, and separation d is also shown.

common types of aberrations. Mechanical aberrations result from imperfections in the machinery and alignment of lens elements; this is the most important type of aberrations in most electron optics systems. Chromatic aberrations result from different focal properties of an element for different energy electrons. Geometrical aberrations are caused by discrepancies that arise from using the Gaussian and paraxial approximations. Assuming non-relativistic electron properties results in relativistic aberrations. Interaction between the electrons in the beam themselves can produce space-charge aberrations, particularly in very high current density beams. The requirements for the precision of the electron optics in our spectrometer are not that demanding, and for the most part aberrations can be neglected.

A standard convention for the coordinate system for electron optics calculations has been adopted: The positive z-axis is chosen as the forward beam axis; the positive y-axis is chosen as up out of the plane of the spectrometer; the x-axis then lies in the spectrometer plane.

2. Matrix method

The matrix method is a standard technique borrowed from thick lens optics that allows the radial distance y

and slope y' of a ray at some later position to be calculated by multiplying the initial radial distance y_0 and the initial slope y_0' by an appropriate matrix. In general the matrix is derived by reducing the differential equations of motion for the fields to equations for y and y' which are linear in y_0 and y_0'. Several important matrices are discussed below and additional use of the matrix method is made in Section C.3. References 97 and 64 provide a good outline of the matrix method for electron optics.

As a trivial example, the radial distance y and the slope y' after traversing an axial distance z in a field free region are given by the equation

$$\begin{bmatrix} y \\ y' \end{bmatrix} = \begin{bmatrix} 1 & z \\ 0 & 1 \end{bmatrix} \cdot \begin{bmatrix} y_0 \\ y_0' \end{bmatrix} \qquad \text{(C.7)}$$

In analogy with Newtonian Optics, the matrix for an electrostatic lens can be written as [97]

$$\begin{bmatrix} y \\ y' \end{bmatrix} = \begin{bmatrix} 1 & 0 \\ \frac{-1}{f_2} & \frac{f_1}{f_2} \end{bmatrix} \cdot \begin{bmatrix} y_0 \\ y_0' \end{bmatrix} \qquad \text{(C.8)}$$

where f_1 and f_2 are defined in Figure C.1. This matrix propagates a ray from the first principle plane P_1 to the second principle plane P_2. There are a wide range of electrostatic elements which constitute lenses and are described by this matrix in one form or another; these

include gap lenses, einzel lenses, aperture lenses, and deflector plates which will be discussed later individually.

For a traverse through a region of length L with a constant electric field E perpendicular to the axis, the equation of motion is

$$y = \frac{eE}{2m} \cdot \left(\frac{L}{v_z}\right)^2 + \left(\frac{L}{v_z}\right) \cdot \dot{y}_0 + y_0 \qquad \text{(C.9)}$$

where the zero of the potential energy is chosen such that the potential energy $e\mathcal{V}$ is equal to the kinetic energy i.e., $e\mathcal{V} = mv_z^2/2$. This yields a matrix form

$$\begin{bmatrix} y \\ \dot{y} \end{bmatrix} = \begin{bmatrix} 1 & L \\ 0 & 1 \end{bmatrix} \cdot \begin{bmatrix} y_0 \\ \dot{y}_0 \end{bmatrix} + \frac{E}{2\mathcal{V}} \cdot \begin{bmatrix} \frac{1}{2}L^2 \\ L \end{bmatrix} \qquad \text{(C.10)}$$

If the electric field is instead parallel to the beam axis the matrix equation can be written

$$\begin{bmatrix} y \\ \dot{y} \end{bmatrix} = \begin{bmatrix} 1 & \left(\frac{2L}{1 + \sqrt{V_2 / V_1}}\right) \\ 0 & \frac{}{\sqrt{V_1 / V_2}} \end{bmatrix} \cdot \begin{bmatrix} y_0 \\ \dot{y}_0 \end{bmatrix} \qquad \text{(C.11)}$$

where V_1 and V_2 are the voltages at the entrance and exit to the region [64,67].

When an electron beam traverses a discontinuity in the axial electric field, the beam is focused. This is the situation illustrated in Figure C.3, where three equipotential planes V_1, V_2, and V_3 define two regions of uniform electric field with a field

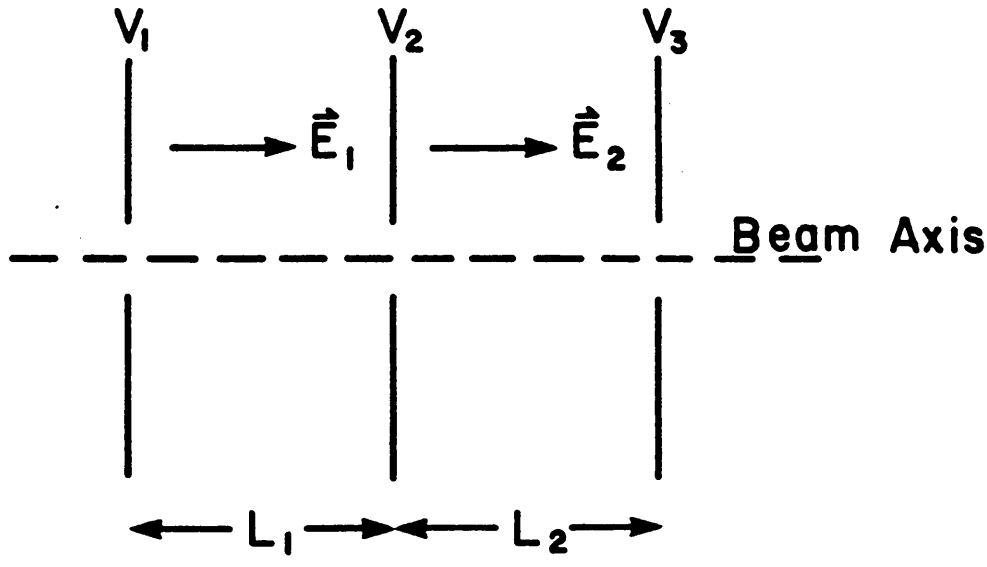

Figure C.3 Voltage distribution for VFIELD.

discontinuity at the V_2 plane. Kuyatt [97] shows that traversing the discontinuity from one side of the V_2 plane to the other can be represented in the matrix form as

$$\begin{bmatrix} y \\ y' \end{bmatrix} = \begin{bmatrix} \frac{1}{E_2-E_1} & 0 \\ \frac{}{4V_2} & 1 \end{bmatrix} \cdot \begin{bmatrix} y_0 \\ y'_0 \end{bmatrix} \qquad \text{(C.12)}$$

Comparison with Equation C.8 shows that this is equivalent to a lens with $f_1 = f_2$ and $f_2 = 4V_2/(E_1-E_2)$. Lenses based on this concept, known as Calbick or aperture lenses, are in common use; such lenses are formed by placing a thin plate with a small axial aperture held at a potential V_2 between two beam tubes both held at the same potential, V_0.

The matrices for uniform axial fields and field discontinuities can be used together to provide a way of estimating the focal properties of optics elements with arbitrary shape and voltage distribution [65]. For a given geometry and potential, the axial voltages at given intervals can be calculated by solving Laplace's or Poisson's equation using numerical techniques. Once the axial potential is known, the paraxial approximation allows the entire optics element to be treated as a series of stepwise applications of the matrix

$$\begin{bmatrix} y \\ y' \end{bmatrix} = \begin{bmatrix} \left\{ 1 + \dfrac{2V_2 - (V_1 + V_3)}{2\,(V_2 + \sqrt{V_2\,V_3})} \right\} & \dfrac{2\,L}{1 + \sqrt{V_3 / V_2}} \\ \dfrac{2\,V_2 - (V_1 + V_3)}{2(V_2 + \sqrt{V_2\,V_3})} & \sqrt{\dfrac{V_2}{V_3}} \end{bmatrix} \cdot \begin{bmatrix} y_0 \\ y_0' \end{bmatrix} \qquad \text{(C.13)}$$

This matrix is derived by multiplying the matrix for uniform axial field by the one for a field discontinuity; assuming that $L_1 = L_2 = L$ and describes a ray which propagates from the left of the V_2 plane to the left of the V_3 plane as illustrated in Figure C.3. Multiplying the matrices for each potential step, yields a single matrix which describes the entire lens element. It is a simple matter to calculate the thick-lens cardinal elements for the lens element from the final matrix [64].

Two programs were written to calculate the matrix for an arbitrary lens element. The first, VFIELD, uses a successive overrelaxation (SOR) method to iteratively solve Laplace's Equation for the lens element geometry. The SOR method uses a finite difference equation to successively estimate the potential at a given grid point based on the potential at neighboring points. Convergence is greatly enhanced by using an accelerating factor, β. An overview of numerical methods for partial differential equations is given by Ames [4] and the specifics for

solving Laplace's Equation using the SOR method are given by Weber [174]. Details of calculating the optimum acceleration factor are given by Carrè [32]. In VFIELD, a subroutine specific to the lens element defines the geometry and potential distribution of the lens element with regard to a 2-D rectangular grid (radius and z) of points. The voltage on the lens elements are held fixed and the potential at the rest of the points are then calculated for these boundary conditions. Once the solution has converged, the grid density can be increased by a factor of H^2 (typically a factor of 16) and the values from the previous grid used as initial values for the denser grid. When an adequate solution is found, the voltages for the grid points on the lens axis are transferred to a second program, AXMATRIX. AXMATRIX calculates the matrix and thick-lens cardinal elements of the lens element as outlined above. These programs were used to calculate the focal properties of several lenses for the spectrometer including the High Voltage lenses and the electron gun Einzel lens (details of these lenses are given in section C.3). As an example of results from AXMATRIX, the cross-section potential distribution for the input High Voltage lens are shown in Figure C.4 along with plots of the axial potential.

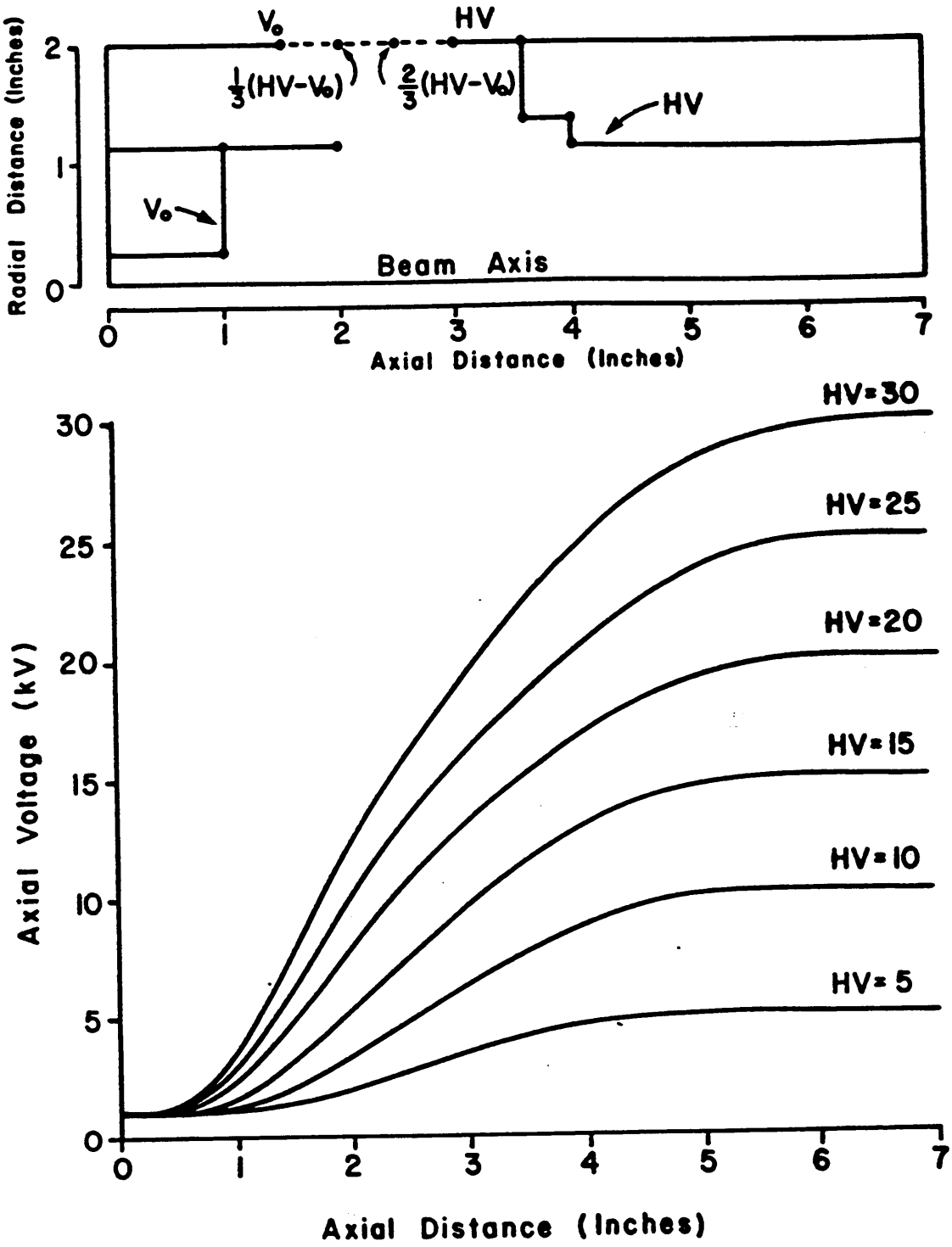

Figure C.4 Example of VFIELD results: input High Voltage lens.

Table C.1 Results of AXMATRIX: input High Voltage lens.

```
(E,E') HV LENS: 25 / 1 VOLTAGE RATIO

TIME: 13:50:51                DATE: 27-OCT-83

SEE KUYATT, P.2.2, FOR DEFINITIONS OF PARAMETERS.
LENGTH OF LENS =          1.77800E+01 CM
DISTANCE BETWEEN VOLTAGE INCREMENTS =       0.12700E+00 CM
INITIAL MOMENTUM =          0.53702E-14 G-CM/S
                            0.81052E+04 1/A
FINAL MOMENTUM =          0.26849E-13 G-CM/S
                          0.40523E+05 1/A
FM1 =        0.87380E+01 CM
FM2 =       -0.12272E+01 CM
FM1        0.18647E+01 CM
FM2        0.93229E+01 CM
PM1        0.68733E+01 CM
PM2       -0.10550E+02 CM

                (                                    )
                (     -0.10852E+01      0.16673E+01  )
MARTIX =        (                                    )  (CGS UNITS)
                (     -0.10726E+00     -0.16306E-01  )
                (                                    )

DET |MATRIX| =          0.19653E+00
SQRT(V_I/V_F)=          0.20001E+00
PERCENT ERROR =         1.741 %
F1 / F2 =           0.20001E+00
PERCENT ERROR =         0.000 %

INITIAL RADIUS =          0.10000E+02 CM
INITIAL SLOPE =         0.10000E-01
INITIAL TRANSVERSE MOMENTUM =          0.53699E-16 G-CM/S
                                       0.81048E+02 1/A

FINAL RADIUS =       -0.10835E+02 CM
FINAL TRANSVERSE MOMENTUM =          -0.19040E-13 G-CM/S
                                     -0.29642E+05 1/A

FINAL SLOPE =       -0.10728E+01,
LATERAL MAGNIFICATION =       -0.13403E+02
ANGULAR MAGNIFICATION =        0.33314E+01
```

Computer modeling of electron optics calculations can greatly facilitate the often complex and laborious calculations necessary for the design and use of such systems. The program MODEL is designed to calculate ray diagrams and image positions for electron optics elements using the matrix formulation described above. The two main purposes of the program are to model the experimental settings for the spectrometer and to aid in design of other electron optics assemblies. There are two corresponding modes of operation of MODEL.

The spectrometer mode of MODEL calculates ray diagrams, r-θ diagrams, lens focal properties, and pupil and window positions, angles, radii, and Helmholtz-Lagrange factors for user-input lens voltages. The program stores the position and dimensions of all of the elements of the lens columns and has subroutines to calculate the cardinal lens elements and/or matrix elements for each of these lens elements. Beginning with either a pupil and window or a radius, beam angle, and pencil angle the nine principle rays are traced through the lens column. The characteristics of the pupil and window images of each lens are also calculated from these initial conditions. R-θ diagrams can be plotted for a number of locations along each lens column. A representative set of output for the input lens column from MODEL is shown in Figures C.5 and C.6 and Tables C.2 and C.3.

a) entire input lens column

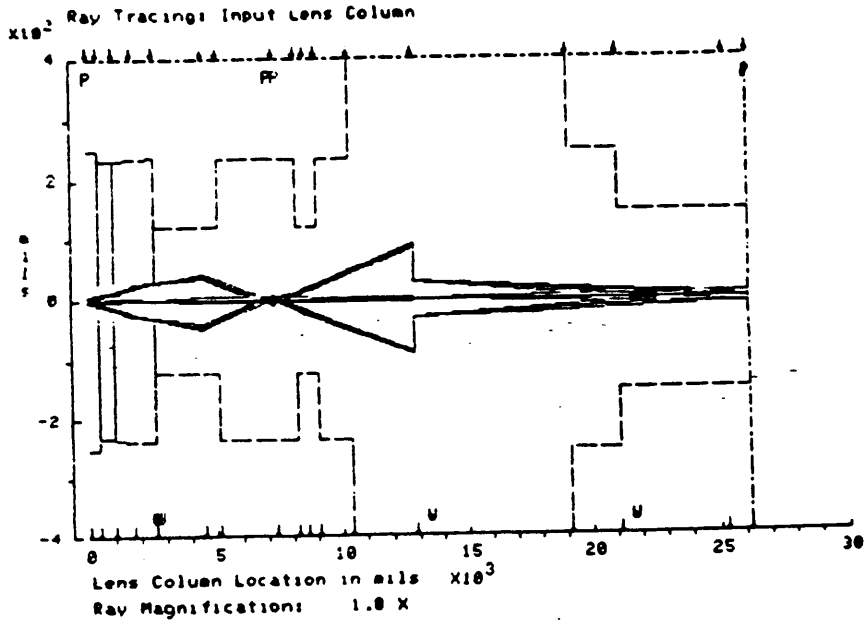

b) Enlargement of zoom lens region

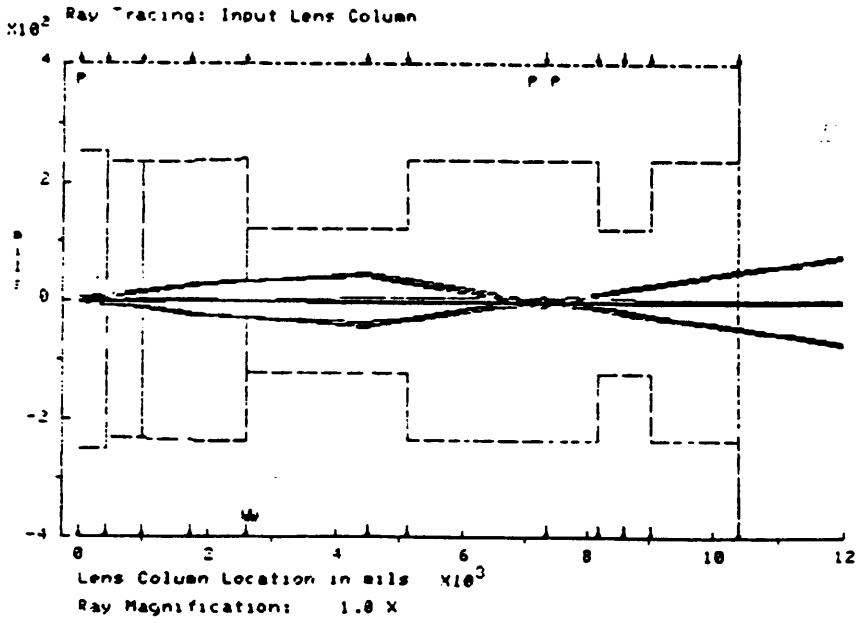

Figure C.5 Ray diagram of input lens column using MODEL.

The solid lines are ray trajectories of the nine principle rays. The lens column profile is outlined with dashed lines. The P's and W's locate the positions of pupil and window images, respectively. The arrows indicate each of the positions of lens elements listed in Table C.2.

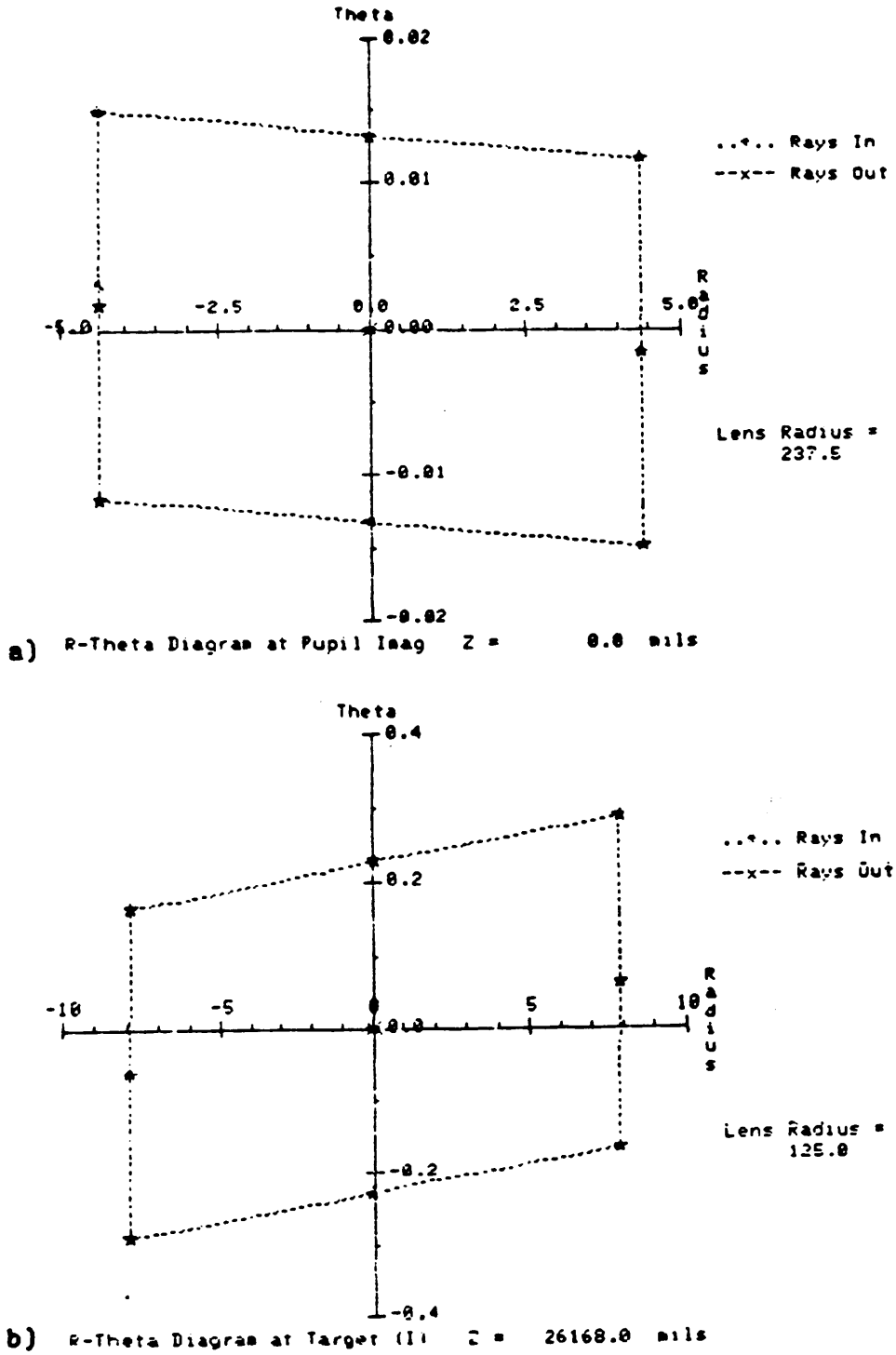

Figure C.6 R-θ diagrams of input lens column using MODEL.

R-θ diagrams of the pupils images at a) the electron gun cathode and b) the target are shown.

Table C.2 Input lens column dimensions using MODEL.

Input Lens Column

Lens Calculations from Pupil Imag to Target (I)

POSITION	LOCATION	LENS RADIUS	VOLTAGE	BEAM RADIUS	BEAM SLOPE	FILLING FACTOR
Pupil Imag	0.00	237.50	2.3750	4.380	0.14901	1.8442E-02
Anode App	438.00	30.00	2.3750	9.490	0.14901	0.3163
1st Gun Ap	983.00	32.50	2.3750	15.85	0.14901	0.4877
Gun Enzl L	1724.00	250.00	4.7000	26.91	0.14901	0.1076
2nd Gun Ap	2580.00	30.00	2.3750	30.44	0.07933	1.015
Inp Fld L	4500.00	121.00	4.5000	45.67	0.16187	0.3775
Dia Ch 1	5121.00	121.00	2.3750	35.55	0.16187	0.2938
Inp Zm 1	7346.50	234.50	1.7620	7.637	0.16340	3.2568E-02
Dia Ch 2	8191.00	142.00	2.3750	15.02	0.16340	0.1052
Inp Zm 2	8607.00	142.00	2.3750	21.76	0.16340	0.1533
Dia Ch 3	9013.00	142.00	2.3750	28.51	0.16340	0.2008
Dia Ch 4	10326.00	234.50	2.3750	49.93	0.16340	0.2129
In HVolt L	12866.00	1125.00	25.0000	89.51	0.16340	7.9567E-02
In Algn Ap	19143.00	250.00	25.0000	19.47	0.02896	7.7865E-02
En Defl Pl	21143.00	150.00	25.0000	16.16	0.02896	0.1078
Ex Defl Pl	25293.00	150.00	25.0000	9.312	0.02896	6.2079E-02
Target (I)	26168.00	125.00	25.0000	7.957	0.02896	6.3657E-02

Table C.3 Input lens column locations using MODEL.

a) pupil image characteristics

Input Lens Column

Lens Calculations from Pupil Image to Target (I)

Pupil Image Locations

LENS	PENCIL ANGLE	BEAM ANGLE	PUPIL POSITION	PUPIL RADIUS	PUPIL HEL-LAGRN
Pupil Image	0.01728	-0.00162	0.00	4.4	8.97E-02
Gun Enzl L	0.00603	-0.00071	-2468.77	9.6	8.97E-02
Inp Fld L	0.01615	0.00197	7095.31	-3.6	8.97E-02
Inp Zm 1	0.01609	0.00196	7456.96	-3.6	8.97E-02
In HVolt L	0.00227	-0.00028	26148.19	7.9	8.97E-02

b) window image characteristics

Input Lens Column

Lens Calculations from Window Img to Target (I)

Window Image Locations

LENS	PENCIL ANGLE	BEAM ANGLE	WINDOW POSITION	WINDOW RADIUS	WINDOW HEL-LAGRN
Window Img	0.00162	-0.01328	2710.00	36.	8.97E-02
Gun Enzl L	0.00190	-0.01564	2580.87	30.	8.97E-02
Inp Fld L	0.00003	0.00026	11967[illegible].64	-1.82E+03	8.97E-02
Inp Zm 1	0.00025	0.00205	21695.48	-2.29E+02	8.97E-02
In HVolt L	0.00062	0.00511	13453.69	-29.	8.98E-02

c) electrostatic lens cardinal elements

Input Lens Column

LENS POSITION	LENS LOCATION	LENS VOLTAGE	F1 DISTANCE	F2 DISTANCE	f1 DISTANCE	f2 DISTANCE
Gun Enzl L	1724.00	4.7000	3423.80	4024.17	1729.78	1744.76
Inp Fld L	4500.00	4.5000	1887.37	1887.37	1866.66	1896.66
Inp Zm 1	7346.50	1.7620	16794.99	16794.99	16212.52	16212.52
In HVolt L	12866.00	25.0000	4652.36	1257.43	1696.55	5474.53

This mode has proven useful in two different ways. Experimentally obtained lens voltages can be input into the computer and the calculated trajectories used to aid in analysis of the optical properties of the beam. In particular, MODEL can determine the location of the pupil image near the target and yields a theoretical value for the pencil angle at the target. This theoretical value determines the momentum resolution. MODEL can alternately be used to calculate the lens voltages that give a desired output, and these voltages used as initial values to begin experimentally tuning the system.

The theoretical properties of the electron lens elements calculated by MODEL are only accurate to within about 10%. We have had quite good success with using the program to model the optics, particularly for the input arm.

The second mode of MODEL allows the user to custom design his own lens column from a list of possible electron lens elements. This list includes most of the matrices described above, allowing for arbitrary dimensions and voltages. The lens elements specific to the spectrometer, e.g., the High Voltage lenses and the Electron Gun Einzel lens, can also be incorporated in the custom lens columns. The voltages on the lens elements can be modified and the entire custom lens column design can be stored in a data file for later reference and modification. Output similar

to that shown for the spectrometer mode can be generated. In addition, the focal properties of any of the lens elements can be listed and plotted; this option was used to produce the graphs for the individual lens elements described above.

3. Description of components

a. Deflector plates

In many different regions along its path, the electron beam is directed by electrostatic deflectors. These deflectors are basically parallel plate capacitors with an electric field E, perpendicular to the beam axis due to a voltage 2V applied across the plates. Ritsko [142] gives a nice discussion of the design of such deflector plates where he shows that to first order the transverse momentum transfer to an electron of velocity v_z and energy $e\mathcal{V}_0$ is

$$q = \frac{2eV}{v_z} \cdot \frac{L}{A} \qquad (C.14)$$

and that the angle of deflection is

$$\theta = \frac{V}{\mathcal{V}_0} \cdot \frac{L}{A} \qquad (C.15)$$

where L is the length of the plates and A is the separation (see Figure C.7). The matrix for a deflector plate from Equation C.10 is given by

$$\begin{bmatrix} y \\ y' \end{bmatrix} = \begin{bmatrix} 1 & L \\ 0 & 1 \end{bmatrix} \cdot \begin{bmatrix} y_0 \\ y_0' \end{bmatrix} + \frac{V}{\mathcal{V}_0 A} \cdot \begin{bmatrix} \frac{1}{2} L^2 \\ L \end{bmatrix} \quad \text{(C.16)}$$

There are two important higher order effects to be considered for these deflectors. The first is that fringe fields result in an increase in the effective length of the plates. Recknagel [137] has shown that this increase in length is

$$\Delta L = \frac{A}{\pi} \cdot \left[1 - \ln\left(\frac{A}{2\pi L} \right) \right] \quad \text{(C.17)}$$

The second effect is that parallel plate deflectors act as an astigmatic lens focusing the beam only in a plane perpendicular to their surfaces. The focal length is given by Ritsko [142] as

$$\frac{1}{f} = \frac{2L}{A^2} \cdot \left(\frac{V}{\mathcal{V}_0} \right)^2 - \frac{2}{L} \cdot \theta^2 \quad \text{(C.18)}$$

For the deflector plates in our system the focal lengths are quite long and the angular aberration is negligible at present momentum resolution. The electric field plates of the Wien filter, however, do focus the beam significantly; the Wien filter is treated separately below.

There are two types of deflectors employed in the system. The momentum deflectors and 45° deflectors use actual parallel plates. The alignment deflectors in the target chamber and the lens columns are actually two sets

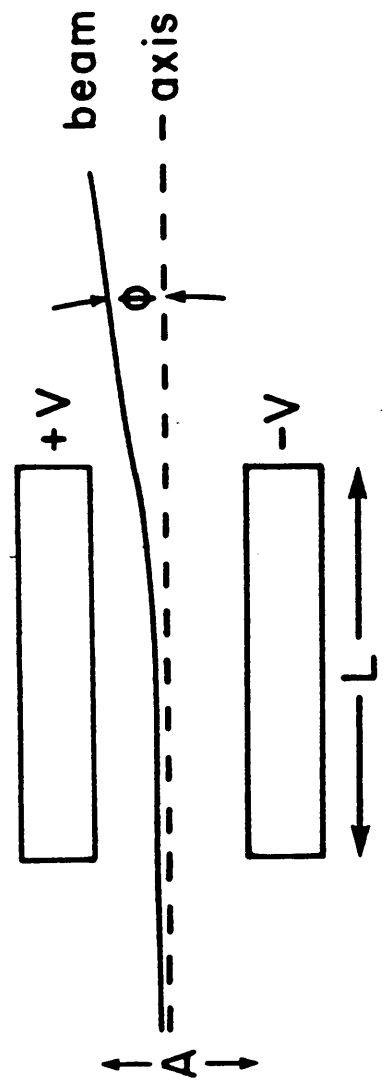

Figure C.7 Diagram of deflector plates.

of deflectors formed by longitudinally splitting a cylindrical piece into four equal isolated parts. The two sets can be controlled separately and provide deflection in the two orthogonal transverse directions.

b. Electrostatic lenses

The simplest type of electrostatic lens is a gap lens. This lens is formed by two cylinders of equal diameter held at different potentials V_1 and V_2, whose separation is small compared with their diameter. The focal properties depend on the voltage ratio; note that lenses with voltage ratios of V_2/V_1 and V_1/V_2 have the same focal properties where $f_1 \leftrightarrow f_2$ and $F_1 \leftrightarrow F_2$. Tabulations of empirical values of the thick-lens cardinal elements can be found in many references [97] and are plotted in Figure C.8. The decelerating (accelerating) lens at the entrance (exit) of the energy analyzer is of this type. The High Voltage lenses are modified gap lenses.

An einzel lens is a symmetric combination of two identical gap lenses with the first and third voltages the same. Einzel lenses have the advantage of being able to focus the beam without changing the final velocity of the electrons. The dimensions and a plot of the cardinal elements of an einzel lens are shown in Figure C.9. The

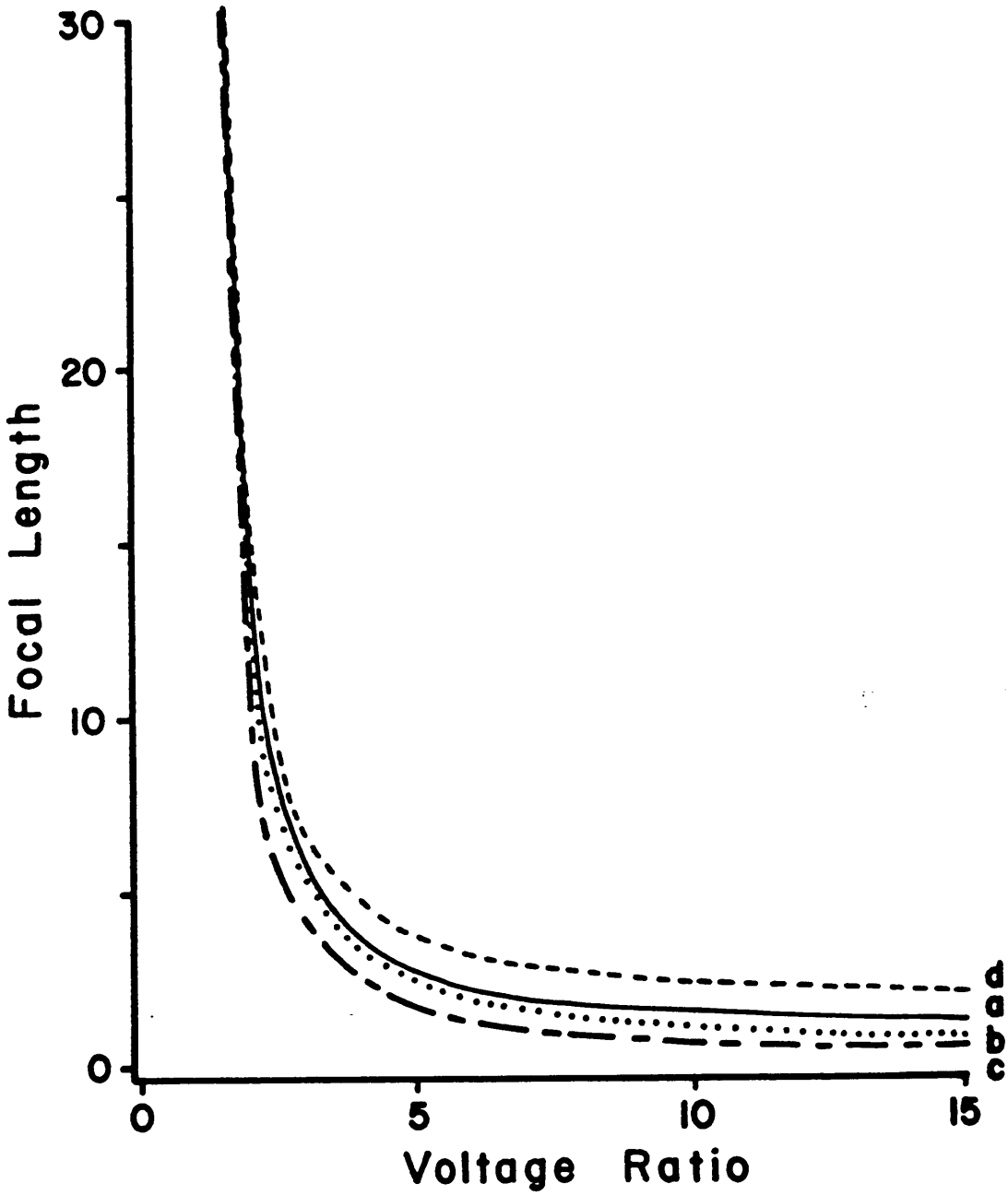

Figure C.8 Cardinal elements of a gap lens.

Graph shows a) F_1 divided by the diameter D, b) F_2/D, c) f_1/D, and d) f_2/D.

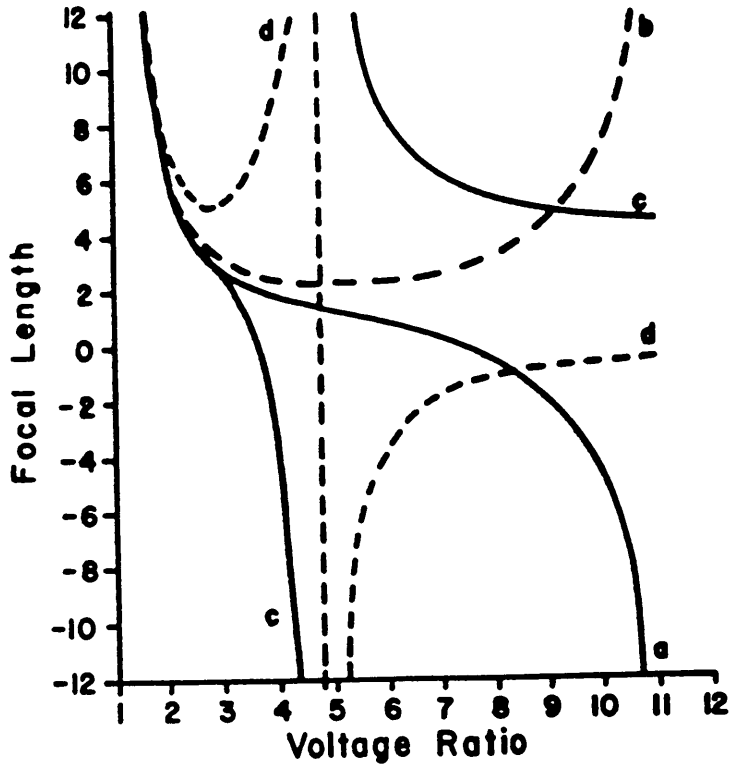

(a) The curves show: a) F^*/D and b) f^*/D for $D/L = 2$, and c) F^*/D and d) f^*/D for $D/L = 5$.

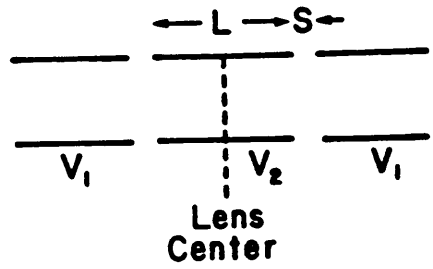

(b) Einzel lens geometry

Figure C.9 Cardinal elements of an Einzel lens.

two identical lenses must be sufficiently far apart so that the electric fields of the two gap lenses have a small overlap; a two diameter spacing is sufficient. Kuyatt [97] shows that an einzel lens can be treated as a single lens with effective thick-lens cardinal elements related to the component gap lens cardinal elements by

$$f_1^{ez} = f_2^{ez} = \frac{f_1 f_2}{2F_2 - L}$$

$$F_1^{ez} = F_2^{ez} = F_1 - f_1^{ez} + \frac{L}{2} \qquad \text{(C.19)}$$

Therefore, the matrix for an einzel lens is simply

$$\begin{bmatrix} y \\ y' \end{bmatrix} = \begin{bmatrix} 1 & 0 \\ \frac{-1}{f^{ez}} & 1 \end{bmatrix} \cdot \begin{bmatrix} y_0 \\ y_0' \end{bmatrix} \qquad \text{(C.20)}$$

Most of the lenses in the spectrometer are einzel lenses. The Electron Gun Einzel lens has a length of less than twice its diameter, so its focal properties were calculated using AXMATRIX.

A three-aperture lens is a modification of the einzel lens which has three small diameter apertures in place of the cylindrical tubes of the standard einzel lens (see Figure C.10). In this type of lens the thickness of the electrodes is very small compared with the spacing between the electrodes or the diameters of the apertures. Read [136] gives the theory and details of focal property calculations of these lenses. The output Field lenses are

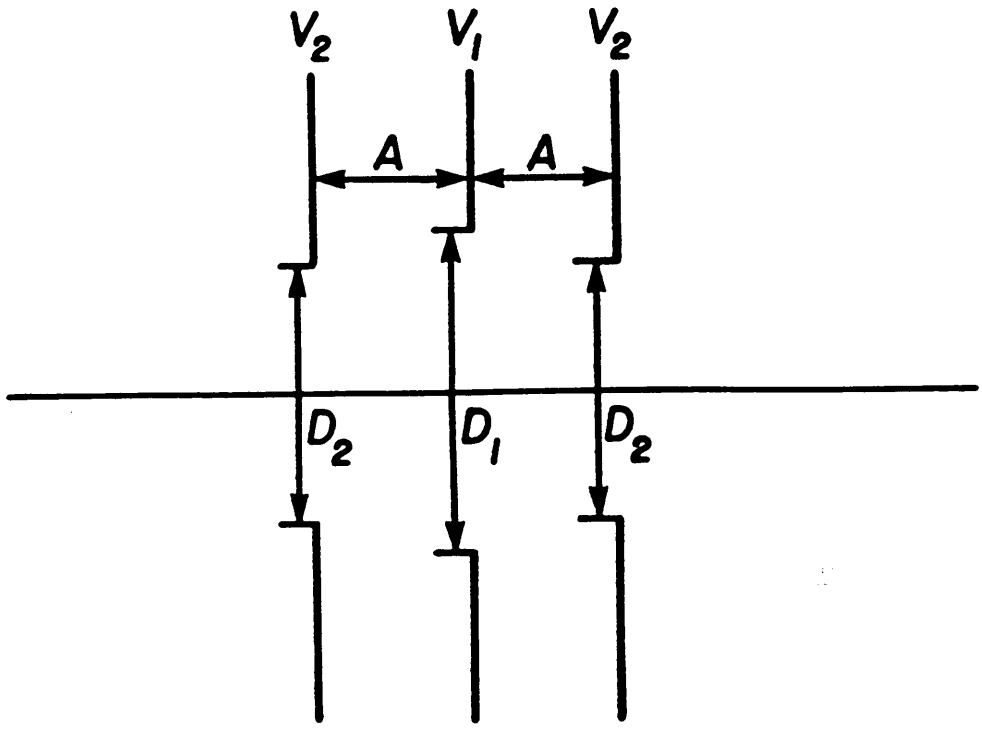

Figure C.10 Diagram of three-aperture lens.

three-aperture einzel lenses.

The quadrupole (quad) lens has two distinctive properties different from other electrostatic lenses discussed. The most important of these is that the quad lens allows different focusing in the two orthogonal transverse planes; in fact, it acts as a diverging lens in one direction and as a converging lens in the other. One can, however, combine two or more quad lenses, each rotated 90° about the beam axis with respect to the previous lens, and with potentials and geometric dimensions chosen in such a way that the same converging effect results in both planes. Quad lenses, also known as strong-focusing lenses, produce a much stronger convergence than circular symmetrical lenses since the transverse nature of the quad lens' active fields is more effective than those of the latter which are primarily longitudinal with respect to the beam axis. Detailed discussions of the properties of quad lenses are found in Grivett [66] and Klemperer and Barnett [96].

Cross-sections of several geometries for quad lenses are shown in Figure C.11. The two pole pieces perpendicular to the x-axis are held at a positive potential $+V_q$, and the other two at a potential $-V_q$, which results in convergent focusing in the x-plane and diverging focusing in the y-plane. The potential distribution for the

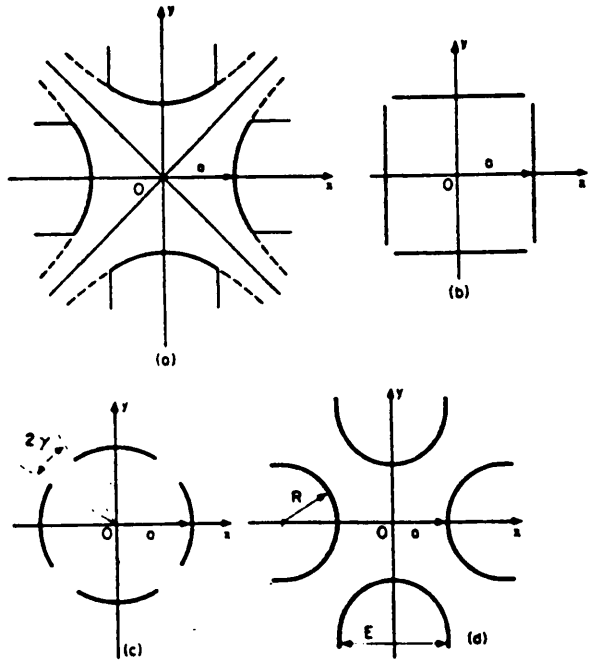

	K_1	K_2
a) Hyperbolic segments	1	0
b) Plane electrodes	1.037	0.009
c) Concave circular electrodes	$1.273\frac{\sin 2\gamma}{2\gamma}$	$0.042\frac{\sin 6\gamma}{6\gamma}$
d) Convex circular electrodes	-	-

Figure C.11 Quadrupole lens geometries.

hyperbolic geometry can be solved exactly and the other geometries can be considered as perturbations expressed as

$$V(x,y) = = V_q\left\{K_1\left[\frac{x^2 - y^2}{a^2}\right] + K_2\left[\frac{x^6 - 15x^2y^2(x^2 - y^2) - y^6}{a^6}\right] + \cdots\right\} \quad (C.21)$$

Figure C.11 lists the values of the expansion coefficients for the different geometries. In general all these types of quad lenses are similar to the hyperbolic case and the exact solutions for the hyperbolic case provide an adequate approximation. For the hyperbolic case it can be shown that [96]

$$f_x = \frac{1}{\beta \sin(\beta L)} \qquad f_y = \frac{-1}{\beta \sinh(\beta L)} \quad (C.22)$$

$$F_x = \frac{1}{\beta \tan(\beta L)} - \frac{1}{2L} \qquad F_y = \frac{-1}{\beta \tanh(\beta L)} + \frac{1}{2L}$$

where the excitation constant β is related to the accelerating voltage of the electron beam $\mathcal{V}_0$ by

$$\beta^2 = \frac{1}{a^2}\left(\frac{V_q}{\mathcal{V}_0}\right) \quad (C.23)$$

and the effective length L is equal to

$$L = L_0 + 1.1\ a \quad (C.24)$$

where L_0 is the actual length of the lens and a is its characteristic radius. The matrices for a quad lens can be written as

$$\begin{bmatrix} x \\ x' \end{bmatrix} = \begin{bmatrix} \cos\beta L & \frac{1}{\beta}\sin\beta L \\ -\beta \sin\beta L & \cos\beta L \end{bmatrix} \cdot \begin{bmatrix} x_0 \\ x_0' \end{bmatrix}$$

$$\begin{bmatrix} y \\ y' \end{bmatrix} = \begin{bmatrix} \cosh\beta L & \frac{1}{\beta}\sinh\beta L \\ \beta \sinh\beta L & \cosh\beta L \end{bmatrix} \cdot \begin{bmatrix} y_0 \\ y_0' \end{bmatrix}$$

(C.25)

For the special case of convex circular electrodes [6]

$$f_{x,y} \approx \pm \frac{V_0}{V_q} \frac{a^2}{4R} \qquad \text{(C.26)}$$

For a doublet, comprised of two identical quadruple lenses arranged coaxially, separated by a small distance D and rotated by 90^0 with respect to each other the focal length of the doublet is [96]

$$f_x = f_y \approx \frac{1}{L^2 \beta^4 (L + D)} \qquad \text{(C.27)}$$

In the (e,2e) spectrometer, single quad lenses are used before and after the Wien filter to compensate for the astigmatic converging focusing of the electric field plates.

c. Electron Gun

Space-charge-limited theory must be used to describe our electron gun. The gun has a perveance 0.3 $\mu A\text{-}V^{-3/2}$ under normal operation which is above the limit of 0.1 $\mu A\text{-}V^{-3/2}$ cited by Brewer [24] above which space-charge effects are of predominant importance.

The perveance is the ratio of the total current to the anode voltage to the three-halves power.

The details of the space-charge-limited diode type electron gun are given by Kuyatt [97] and Brewer [24]. The theory is based on the assumption that the electrons have space-charge-limited laminar flow with such effects as thermal velocities and lens aberrations treated as perturbations of this laminar flow condition.

The space-charge-limited current density can be calculated from the geometry of the gun and the anode voltage V_{An} as

$$J\left(\frac{\mu A}{\text{unit area}}\right) = 2.33\ \frac{V_{An}^{3/2}}{D^2} \qquad \text{(C.28)}$$

where D is the cathode-anode apertures separation. If we consider the anode aperture as a Calbick lens (see Section C.2), it can be shown that the virtual cathode image is at a distance 3D before the anode aperture in the space-charge limit (4D below the space-charge limit) [97]. It follows that the initial pupil conditions are:

$$\begin{aligned} r_p &= 3D\ \sqrt{\frac{V_k}{V_{An}}} \\ \tan\theta_p &= r_p\ /\ 3D \\ \tan\theta_b &= r_w\ /\ 3D \end{aligned} \qquad \text{(C.29)}$$

where r_w is the anode aperture radius and $eV_K = kT$ is

the thermal energy of the electrons. For this type of electron gun, $eV_k \approx 1.0$ eV. It should be noted that in our spectrometer under normal operating conditions the last aperture in the electron gun assembly, not the anode aperture, is the limiting window aperture; this does not change the theory.

The total current from the diode is just the product of the current density times the beam area, that is,

$$I_{Total} = J\ A = 7.32\ V_{An}^{3/2} \left(\frac{r_w}{D}\right)^2 \qquad (C.30)$$

The emittance of the electron gun was crudely measured using a thin aperture and Faraday cup prior to use in the spectrometer. The emittance value was 0.4 ± 0.2 cm-mrad which agrees with theoretical calculations to within the limits of error.

d. Energy analyzer

The basic principle of a Wien filter is quite simple. The filter has a homogeneous electric field $\mathbf{E} = E\hat{y}$ perpendicular to the beam axis and the plane of the spectrometer and a homogeneous magnetic field $\mathbf{B} = B\hat{x}$ in the spectrometer plane perpendicular to both **E** and the beam axis. A normally-incident charged particle of velocity $v_0 = E/B$ will be subject to equal and opposite forces due to these two fields and will pass undeflected through the filter, while particles with other velocities

will be dispersed. A slot at the exit of the filter can then provide energy selection and the size of the aperture can determine the energy resolution.

Determination of the optical properties of the Wien filter requires a sophisticated analysis which will only be outlined here. Bonham and Fink [20] go through a detailed derivation of the electron optics of a Wien filter, beginning from the differential equations of motion. Their analysis is greatly simplified by five approximations: 1) the influence of space charge is neglected; 2) no relativistic effects are considered; 3) electric and magnetic fields are assumed to have sharp cutoffs at the edges of the analyzer; 4) the acceptance angle is assumed to be small; 5) the initial velocity distribution can be written in the form $v = v_0(1+\beta)$ where β is a small correction representing the spread of the electrons emitted from the source.

The equations of motion in the field region can be written as:

$$\ddot{x} = 0 \qquad \text{(C.31a)}$$

$$\ddot{y} = \frac{-e}{m}\left(|E| + |B|\dot{x}\right) \qquad \text{(C.31b)}$$

$$\ddot{z} = \frac{-e}{m}\left(|B|\dot{y}\right) \qquad \text{(C.31c)}$$

It is obvious from Equation C.31a that the Wien filter does

not affect trajectories in the x-plane; this plane is referred to as the non-dispersive plane. On the other hand, the Wien filter acts as a converging lens in the y-plane, that is the dispersive plane. The focal properties of the Wien filter are symmetric and can be expressed as

$$f = \frac{a}{\sin(L/a)}$$
$$F = a \cot(L/a) \qquad \text{(C.32)}$$

where L is the length of the electric field plates and a is a parameter which describes the radius of an electron in the magnetic field alone:

$$a = \frac{mv_0}{e|B|} = \frac{m|E|}{e|B|^2} \qquad \text{(C.33)}$$

Since F is a periodic function, the focal point can have the same value for many different values of a and the magnetic field, each corresponding to a different mode of operation of the filter. The first mode is when 1/a is between 0 and π, that is when a trajectory crosses the beam axis only once. The maximum dispersion occurs for $L/a = \pi$ which is the mode used in our spectrometer. An object at the entrance of the analyzer is focused to the exit of the analyzer with unity magnification. An object at infinity is focused to infinity in this mode.

The key principle of the energy dispersion can be understood as an exploitation of the chromatic aberration of this focusing effect. A point image on the axis at the

entrance to the Wien filter is focused at a distance

$$y_D = \frac{2m\beta v_0}{e|B|} = 2\beta a \qquad (C.34)$$

from the axis. In our spectrometer the image from the Wien filter is at the exit plane of the filter, therefore the width of the image of the energy slit on this plane directly determines the range of energies that pass through the slit. The finite size of the image at the entrance plane results in a finite image size at the exit plane related by a magnification (assuming $\beta=0$) of

$$\gamma = -\cos(L/a) \qquad (C.35)$$

The energy distribution at the exit plane can be thought of as a convolution of the point-wise spectrum with this finite image size. This suggests that the transmission curve as a function energy will be Gaussian-like with a maximum transmission of electrons with energy eV_E, and tapering off symmetrically for both higher and lower energies.

Further aberrations due to the finite size of the image at the entrance plane and the angle of incidence to this plane provide a limit to the ultimate resolution of the Wien filter. Sevier [151] states that the ultimate theoretical resolution for a Wien filter such as the one used in our spectrometer is given by

$$\Delta E_{theor} = V_{E_1} \left(\frac{3\ h^2\ \pi^2}{2me\mathcal{V}L^2} \right)^{1/2} \qquad (C.36)$$

where V_{E_1} is the potential of the analyzer tube. For our spectrometer operating at $e\mathcal{V}$ = 25 keV this gives ΔE_{theor} = 70μeV. In practice this ultimate resolution can not be achieved with any reasonable transmission efficiency.

The Wien filter electric field is produced by two 2.54 cm x 2.54 cm square stainless steel electric field plates with a separation of 0.508 cm held at a voltage difference V_{Anz} which floats on V_{E_1}. The magnetic field is produced by a current I_{Anz} through two pairs of coils wrapped on the surface of a 1.27 cm diameter cylindrical form. The coils are wrapped in a manner described by Anderson [3] which maximizes the homogeneity of the magnetic field. The analyzer voltage and current are supplied by a hybrid voltage-current supply (VPI electronics shop). Details of the voltage distribution are given in Section III.B and schematics are found in Appendix D. A mu-metal shield fits closely around the analyzer extending from before the entrance plane to just before the accelerating lens. The energy slit is a 0.635 x 2.54 mm slit in a 0.254 mm thick molybdenum disk; the slit is longer in the non-dispersive direction.

e. Momentum analyzer

The momentum deflectors consist of two sets of square parallel plate deflectors which act in tandem to vary the beam angle of the electron beam at the target without changing the position of the beam spot. The design goal was to do this in such a way that the electron trajectories were independent of the absolute voltages and the absolute distances of the momentum selector. Figure C.12 shows a schematic of the momentum deflectors and their dimensions.

Using the matrix for a field free region, Equation C.7 and for a displacement through a region of electric field perpendicular to the beam axis, Equation C.10, the matrix for the region from the entrance of the momentum deflectors to the target can be written as,

$$\begin{bmatrix} y \\ y' \end{bmatrix} = \frac{V_1 L}{2\mathcal{V}A} \cdot \begin{bmatrix} L(1-\eta) + 2[S + L + D(1-\eta)] \\ 2(1-\eta) \end{bmatrix} \qquad (C.37)$$

where $e\mathcal{V}$ is the electron kinetic energy, $\eta \equiv V_2 / V_1$, and it is assumed that $y_0 = y_0' = 0$. The constraints that $y = 0$ and that y' is independent of S and D and dependent on only the ratios L/A and η are satisfied when $\eta = 3$ and $S = 2D$. The matrix thus reduces to

$$\begin{bmatrix} y \\ y' \end{bmatrix} = \frac{-2V_1}{\mathcal{V}} \cdot \frac{L}{A} \cdot \begin{bmatrix} 0 \\ 1 \end{bmatrix} \qquad (C.38)$$

The major error in Equation C.38 is due to fringing fields about the plates; according to Recknogel [137] the

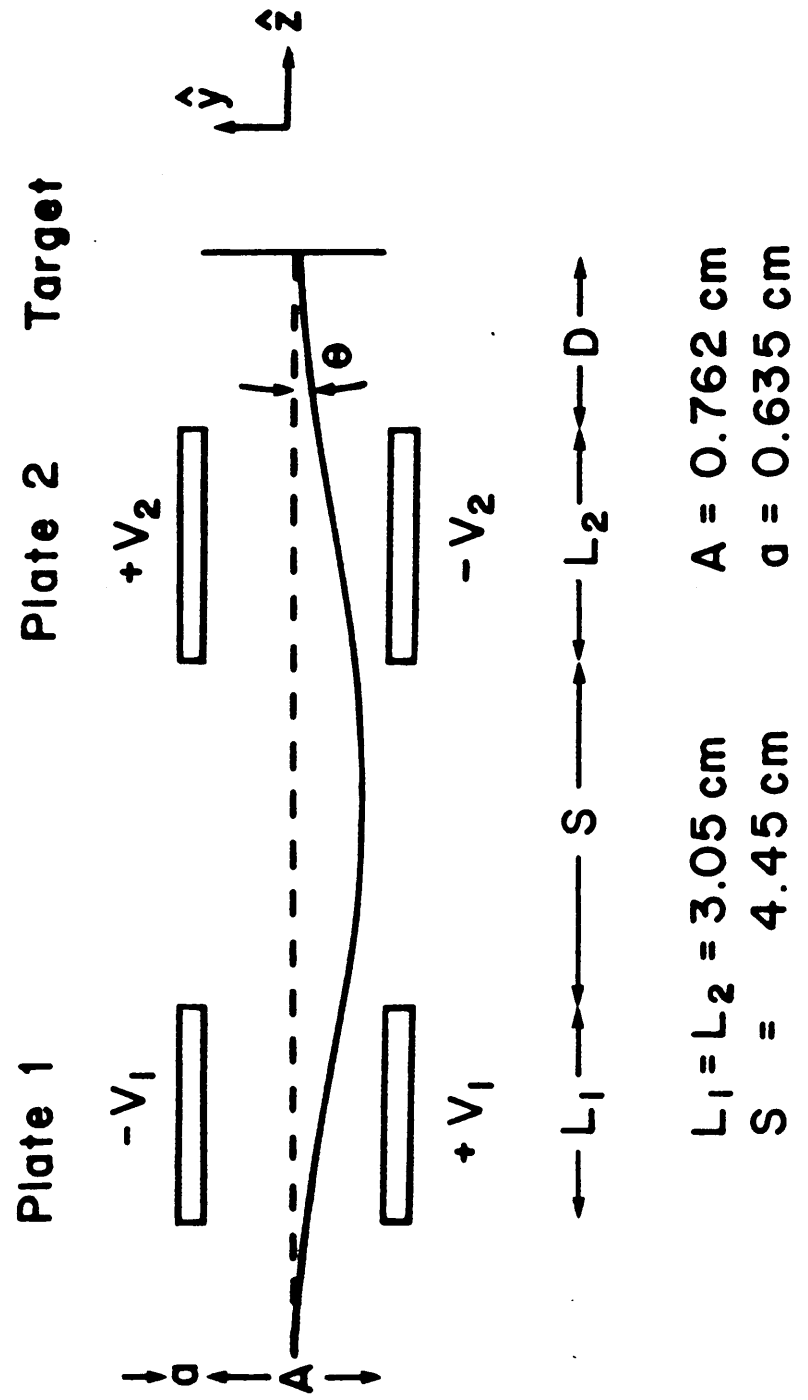

Figure C.12 Momentum Deflectors Dimensions.

fringing increase the effective length of the plates by $\sim$ 33% . In practice, this correction probably somewhat overestimates the increase due to fringe effects because both sets of plates are in close proximity to grounded surfaces in one direction and separated from each other by less than 1 1/2 times their length in the other direction. The increase in effective length results in a corresponding increase in the theoretical momentum conversion factor discussed below. This effect is uniform for all deflection angles and is therefore incorporated into any empirical determination of the momentum conversion factor.

Higher order errors are included in the expression

$$\begin{bmatrix} y \\ y' \end{bmatrix} = \begin{bmatrix} 1 & (2L + 3D) \\ 0 & 1 \end{bmatrix} \cdot \begin{bmatrix} y_0 \\ y'_0 \end{bmatrix} + \frac{L_{eff} V_1}{A\mathcal{V}} \cdot \begin{bmatrix} \frac{1}{2}(L + 2D) \cdot (3 - \eta) \\ (1 - \eta) \end{bmatrix} \quad \text{(C.39)}$$

The first term in this equation allows the beam to enter the momentum analyzer with a non-zero initial radius and slope. Since this is independent of deflector voltage, it is unimportant in determination of the momentum conversion factor. The second term in Equation C.39 allows for η to differ from the ideal value of 3. A 1% deviation in the deflector voltage ratio would result in a displacement of 0.2 mm over the full deflector range at $e\mathcal{V}$ = 25 keV.

The voltage distribution for the momentum analyzer is

controlled by the MINC computer via an opto-isolated fiber optic link (see Section IV). The signal from the MINC is converted to an 8-bit digital signal by a UART (universal asynchronous receiver-transmitter) located on the target chamber control rack. The lowest 7 bits of the signal are then converted to a 0 to -5 VDC signal by a DAC; this voltage is used to drive the output of two high voltage power supplies (BERTAN, models 602B-15P and 602B-15N). These power supplies produce 0 to ±600 VDC which are connected to the momentum deflector plates via a voltage divider network. (Schematics and power supply specifications are given in Appendix D). The supplies are designed to provide a positive voltage on one deflector plate and a negative voltage of equal magnitude on the other plate; both voltages float on the target chamber high voltage. The eighth bit of the digital signal controls a relay which determines the polarity of the deflector plates.

The momentum voltage correction panel on the target chamber rack is an additional feature that allows for adjustment of the momentum voltages to minimize movement of the beam spot on the target as a range of momentum voltages are swept. The ratio of the deflector voltages to the computer momentum control step and the ratio η are varied with two dual-tandem potentiometers as shown in the

schematic in Figure D.6. These ratios were adjusted to minimize the beam spot movement as viewed through the viewport telescope and the variation in count rate as a function of momentum as controlled by QSWEEP (see Appendix E).

A theoretical expression for the momentum calibration factor can be derived from Equation C.39 and the relation $q = y'P_0$:

$$C_F = \frac{\Delta q}{\Delta N} = \frac{\Delta V_1}{\Delta N} \sqrt{\frac{2me}{\gamma\hbar^2}} \frac{L_{eff}}{A} (1 - \eta) \qquad (C.40.a)$$

where momentum is expressed as a wave number, $0 \leq N \leq 255$, and C_F is in units of $Å^{-1}$ per incremental step of the computer momentum control number N. At the time when momentum calibration was performed, measurements of the characteristics of the perpendicular momentum analyzer plate voltages showed that $\Delta V_1/\Delta N = 1.555$ V and $\eta = 2.967$, both to within $\lesssim 0.1\%$. At an incident energy of 25 keV, C_F is equal to 0.0398 $Å^{-1}$ per step using the actual length of the plates and 0.0532 $Å^{-1}$ per step using the theoretical L_{eff}. The momentum calibration factor is proportional to the inverse of the square root of the incident electron voltage; therefore, corresponding theoretical values for C_F at 20 keV are

0.0445 $Å^{-1}$ per step and 0.0595 $Å^{-1}$ per step, respectively.

The coincidence data for both the a-C and graphite were taken after the momentum voltage correction panel was adjusted to minimize motion of the beam spot on the target. For these measurements $\Delta V_1/\Delta N$ = 1.750 V and η = 2.745 which yield values of C_F which differ by < 0.5% from those listed above.

Alternately, the momentum calibration factor can be expressed in terms of mrad/V as

$$C_F' = \frac{\Delta\delta}{V_1} = \frac{1}{\mathcal{V}} \frac{L_{eff}}{A} (1 - \eta) \qquad \text{(C.40b)}$$

For a 25 keV incident energy electron this is C_F' = 0.421 mrad/V_1 with η = 2.967 and L_{eff} = 1.336 L for perpendicular deflection.

The momentum calibration factor C_F' for the parallel momentum will be a factor of two larger than that for perpendicular momentum deflection because the energy of the outgoing electrons in the (e,2e) mode is half that of the incident electrons. However, the resistance divider network is designed so that $\Delta V_1/\Delta N$ is approximately twice as large for perpendicular deflection as for parallel deflection. This means that the perpendicular momentum calibration factor C_F will be $\sqrt{2}$ times that of the parallel momentum deflectors when expressed in $Å^{-1}$

per step.

The momentum deflectors were calibrated by measuring the Bragg diffraction spectra of thin microcrystalline Al films. The spectrometer was operated at 25 kV in the elastic mode using the (e,e') beam arm as the detector and acted as a HEED apparatus. A typical diffraction pattern is shown in Figure C.13. Comparison of the peak positions of the first four Bragg peaks from these measurements to published values for Al [134] predict that the calibration factor is 0.057 ± .001 $Å^{-1}$ per step at 25 keV incident energy. Adjusting for the difference in incident momentum, this corresponds to an experimental value of 0.064 ± .01 $Å^{-1}$ per step at 20 keV. The experimental conversion factor is about 8% larger than the theoretical estimate using the theoretical effective plate length; it corresponds to an effective plate length of L_{eff} = 1.4 L. Similar comparisons of theory and experiment for ThCl and a-C [134] were in approximate agreement.

The coincidence data shown in this dissertation all use a value of 0.064 $Å^{-1}$ per step with an estimated uncertainty of ~15%.

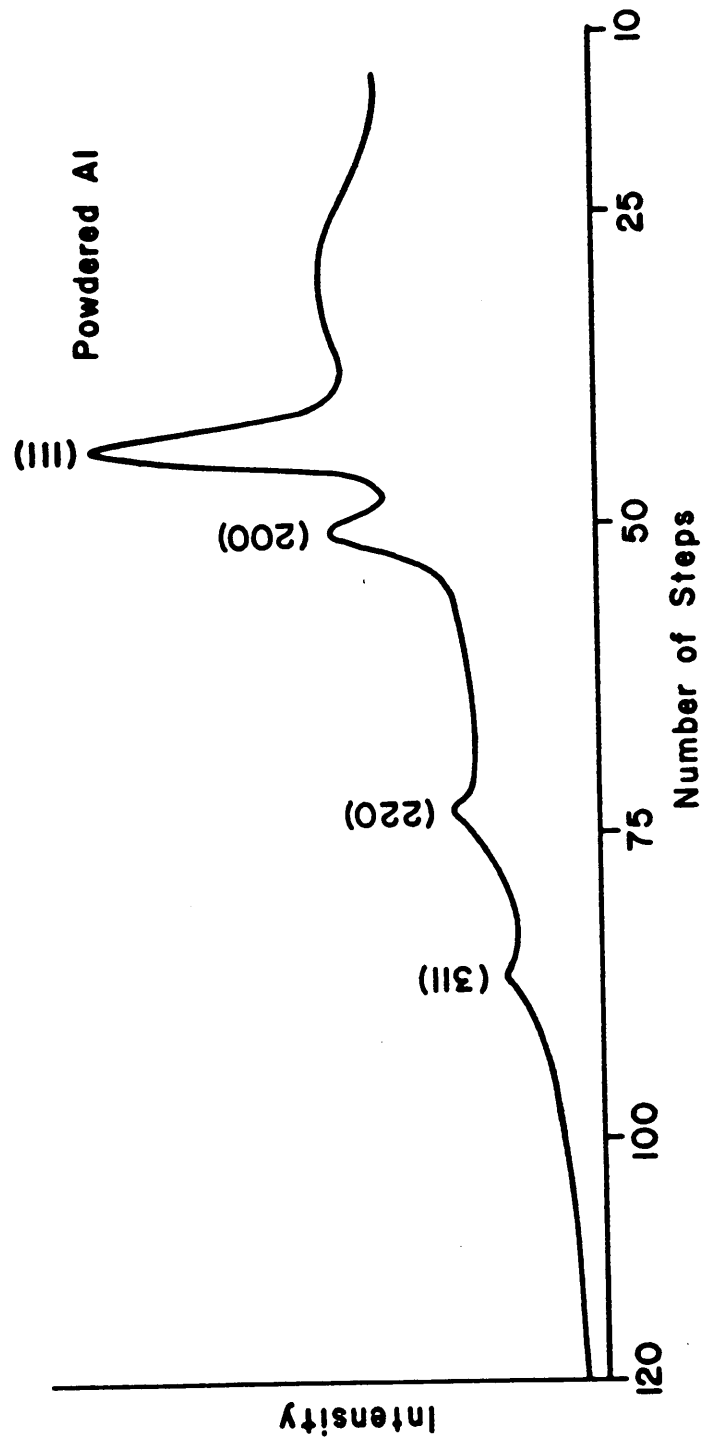

Figure C.13 Bragg diffraction pattern for momentum analyzer callbration.

f. Electron lens assemblies

The electron gun assembly includes the electron gun filament, cathode, anode, and an einzel lens. The filament is a soft-cathode oxide filament which is heated by a voltage supply (VPI electronics shop) driven typically with 5 to 7 VDC at ~ 3 A. The anode is held at a voltage V_{AN} (Bertan model 602B 50P) typically from 1.0 to 2.5 kV above the input common point. There are four apertures in the assembly designated, from left to right as shown in Figure C.14, as the cathode, anode, first gun, and second gun apertures.

The Electron Gun Einzel lens has a length to diameter ratio of less than two and therefore must be modeled using an axial step-wise potential. The results of an analysis using VFIELD and AXMATRIX are shown in Figure C.15. The input Field lens, Zoom 1, and Zoom 2 lenses are conventional Einzel lenses.

The high voltage lenses are modified gap lenses which have a complex geometry (see Figure C.4). Their axial potential distributions were modeled with VFIELD and AXMATRIX and calculated cardinal elements are shown in Figure C.16. The input and (e,e') high voltage lenses are identical and differ slightly from the (e,2e) high voltage lenses.

The output Field Lenses are 3-aperture lenses. These

LENS NAME	Anode	Einzel	Anode	Cathode
VOLTAGE	V_{AN}	V_{Ez} (<5kV)	V_{AN} (0.5 to 2.5 kV)	V_{CP_1} (0V)
LENS LENGTH	325	340	1300	435
LENS DIA.	375 500	500	475	500
AP. DIA.	60		75	60 31
GAP LENGTH	92	92		140

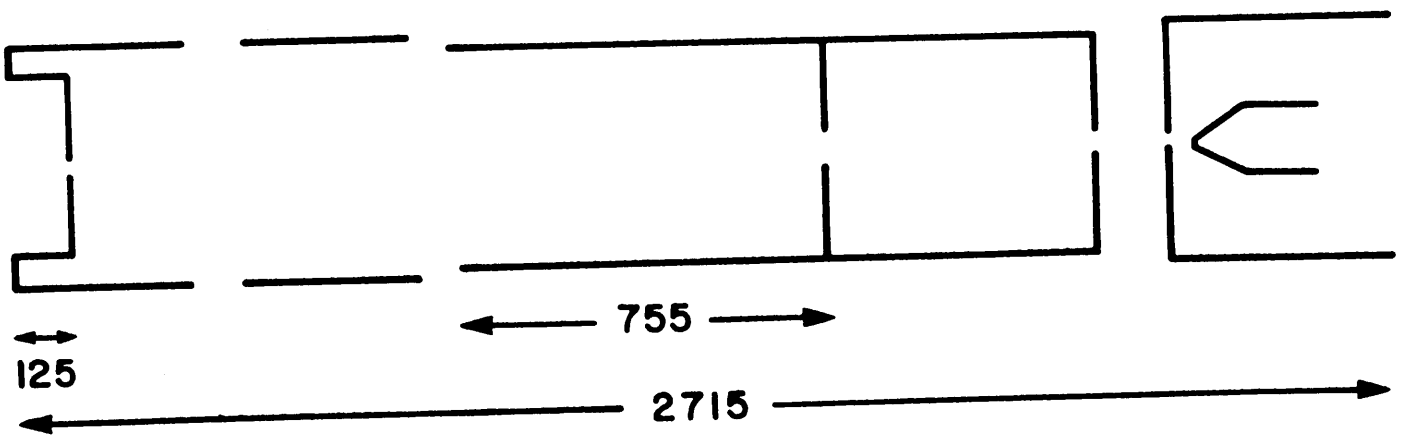

Distances in mils

Figure C.14 Electron gun assembly.

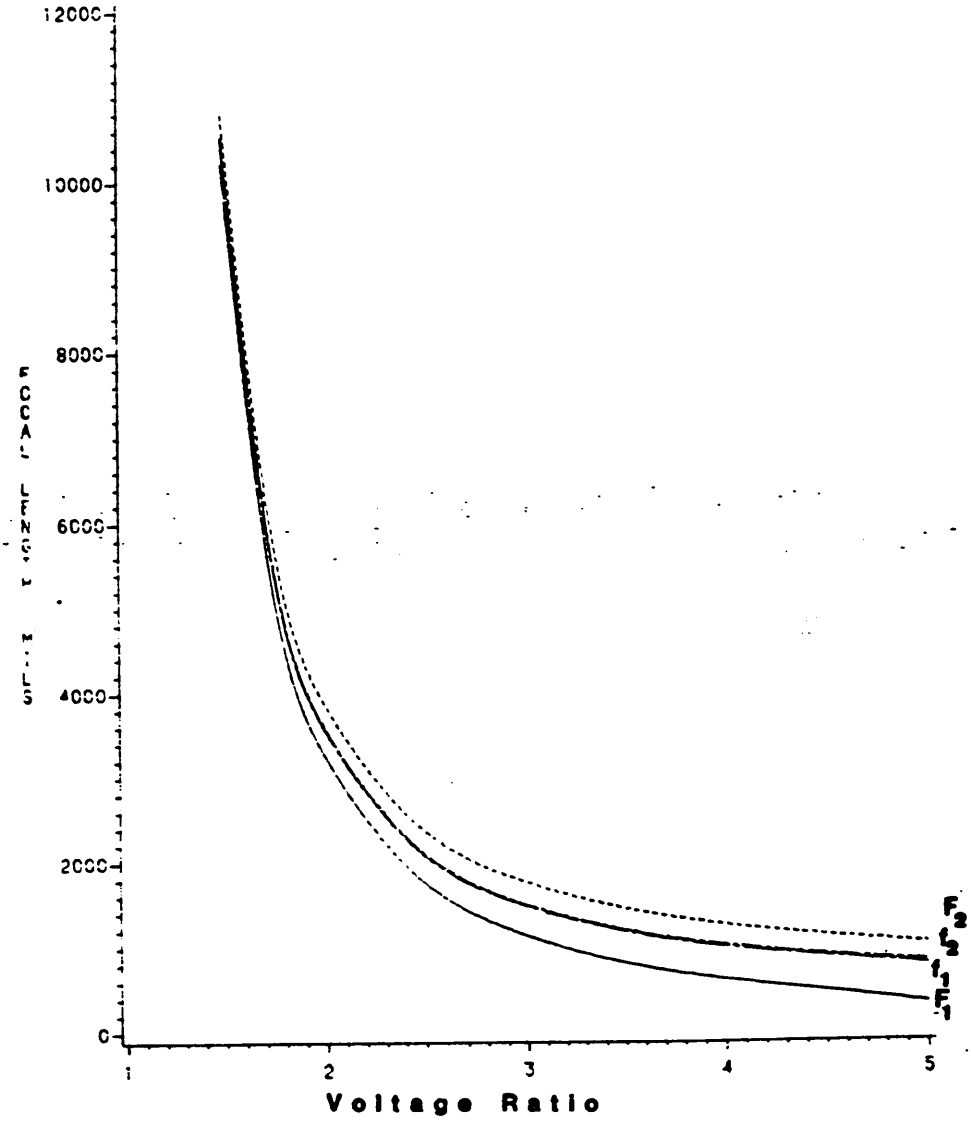

Figure C.15 Cardinal elements of Electron Gun Einzel Lens.

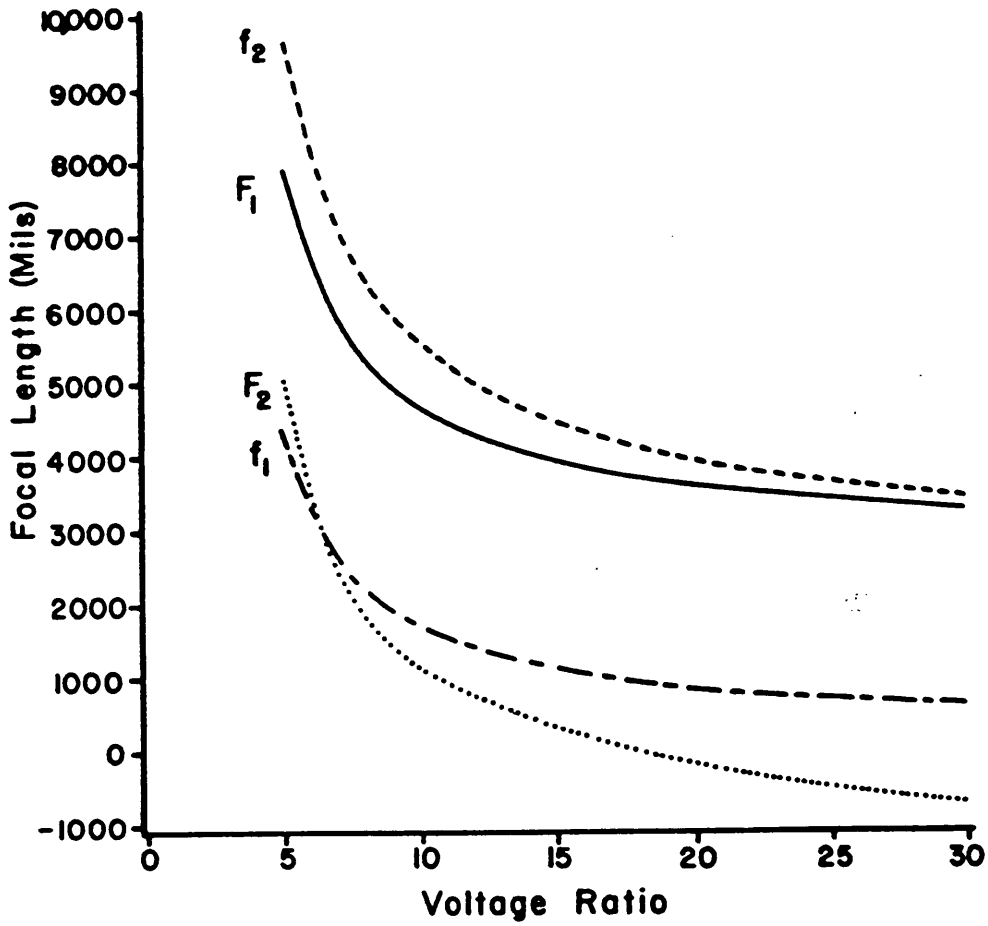

Figure C.16 Cardinal elements of the High Voltage lenses.

lenses differ slightly for each beam arm. The differences are noted and each set of cardinal elements plotted in Figure C.17.

The first and second apertures and the energy slit are made of 0.25 mm thick Mo stock. Molybdenum is used because its oxide is also a metal. This limits the aberrations that could result from even a small surface charge of such tiny apertures.

The cardinal elements for the quad lenses, which differ slightly in the (e,e') and (e,2e) arms, are shown in Figure C.18.

Figure C.19 is an approximate scale drawing of the input lens column from the electron gun to the target. The drawing includes the dimensions of the various pieces. A similar drawing of the output arm from the target to the EMT is shown in Figure C.20.

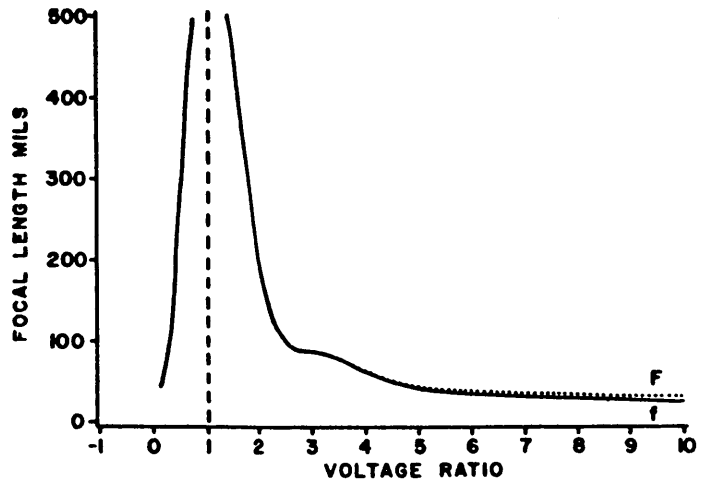

(a) A(e, 2e) Field Lens

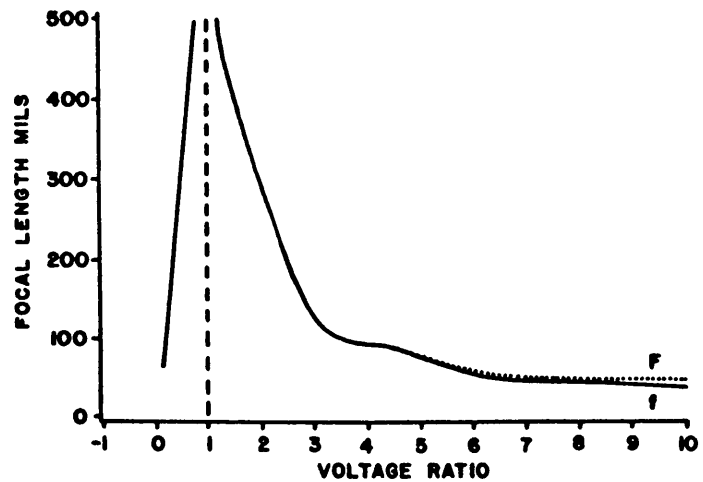

(b) B(e, 2e) Field Lens

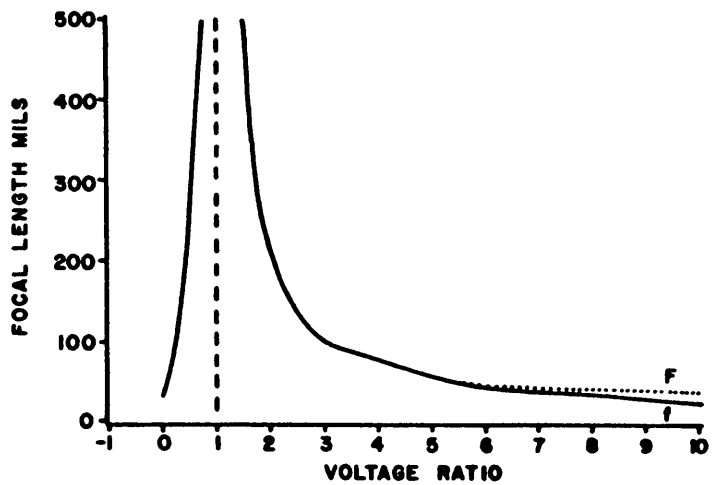

(c) (e, e') Field Lens

OUTPUT FIELD LENS DIMENSIONS *

Lens	A	D_1	D_2	A/D_1	D_2/D_1
A(e, 2e)	26 mils	13.5 mils	2.0 mils	1.98	1.56
B(e, 2e)	20	10.0	15.6	2.00	1.50
(e, e')	20	13.5	20	1.50	1.50

* See Reed (Ref. 136).

Figure C.17 Cardinal lens elements of the three-aperture Field Lenses.

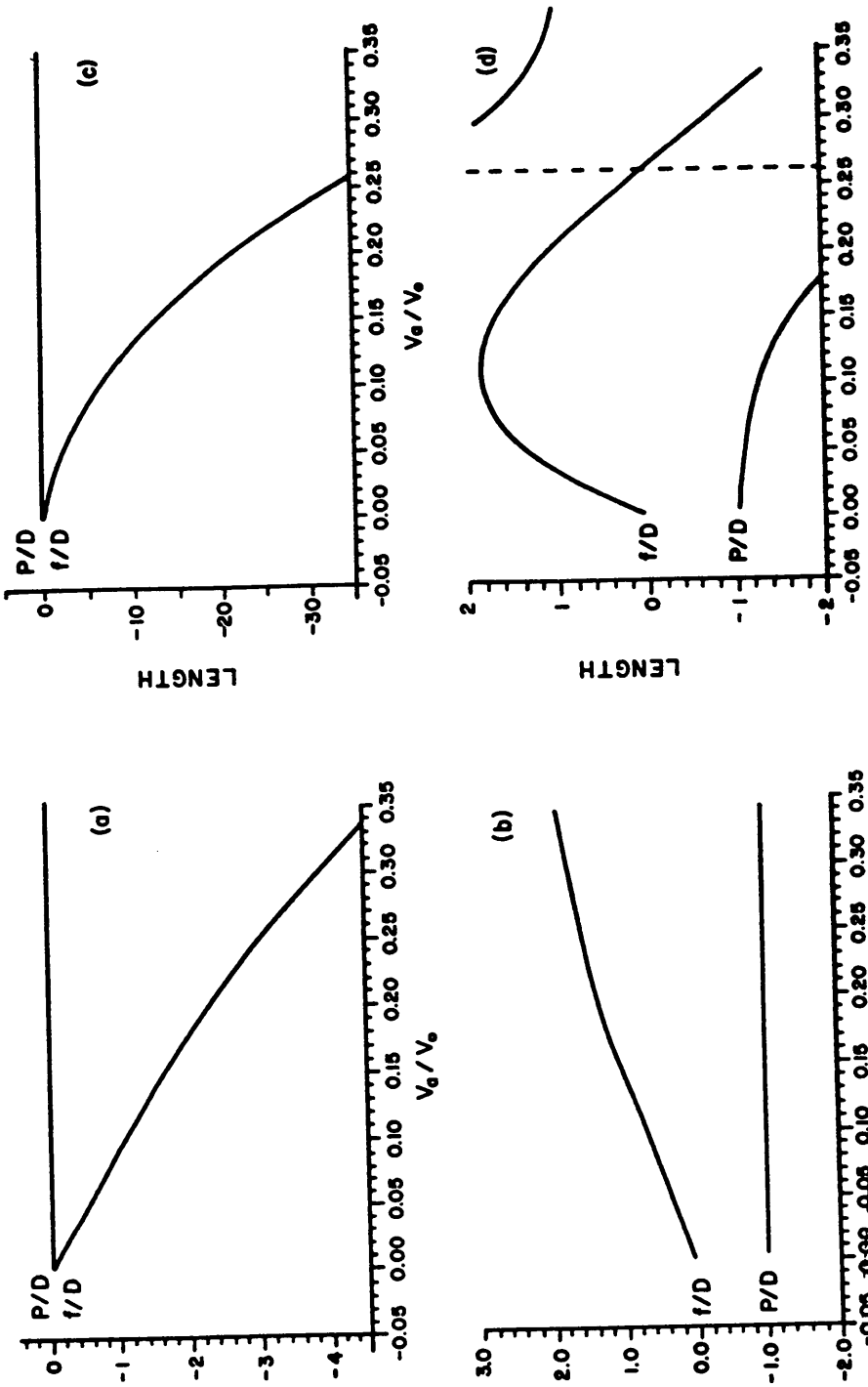

Figure C.18 Cardinal elements of electrostatic quadrupole lenses.

The diverging (a) and converging (b) (e,e') quadrupole cardinal lens elements f/D and P/D with K_1=1.2592 and K_2=0.0380. The diverging (c) and converging (d) cardinal lens elements for the (e,2e) quadrupole lens with K_1=1.2661 and K_2=0.4187.

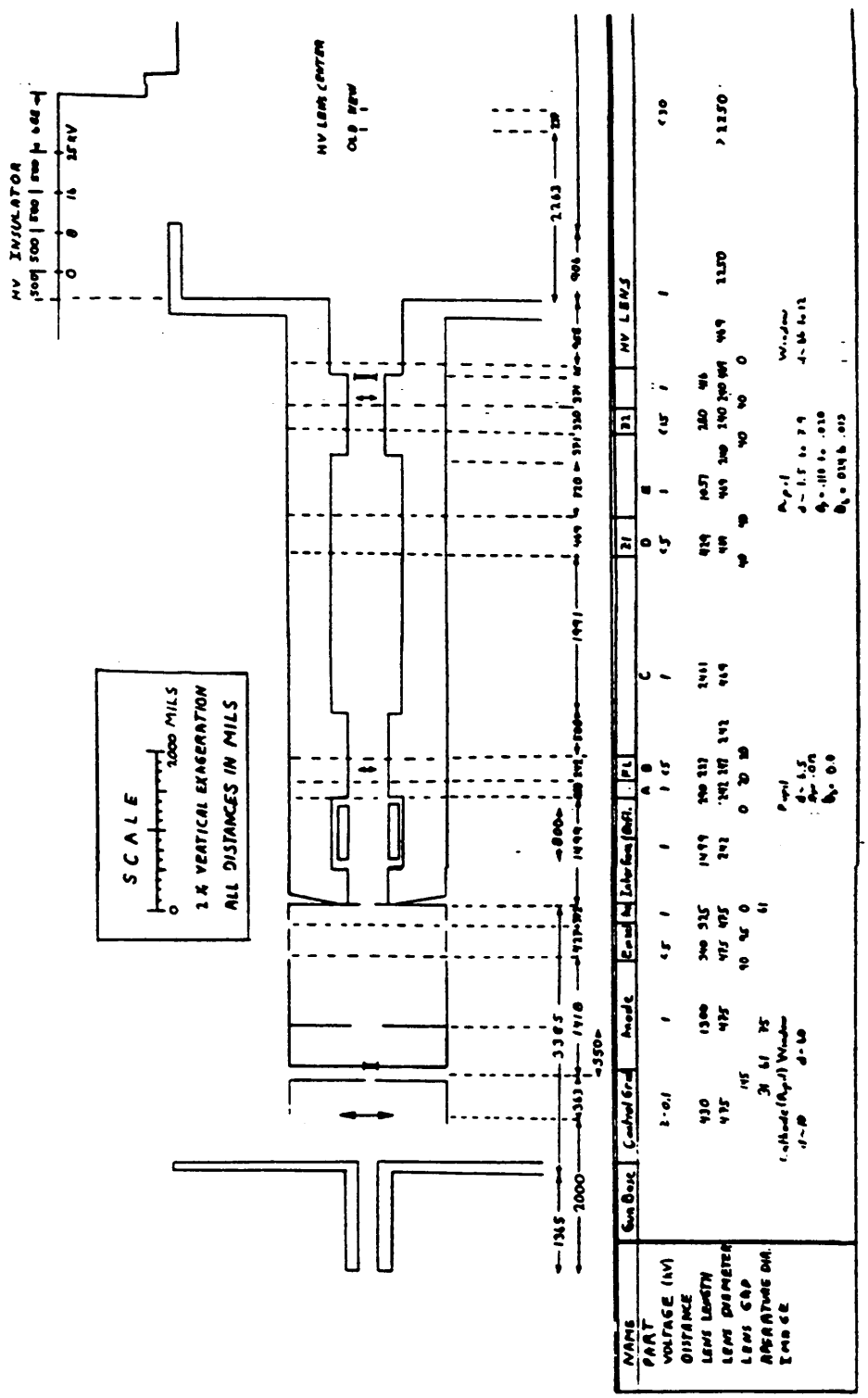

Figure C.19 Input arm lens column.

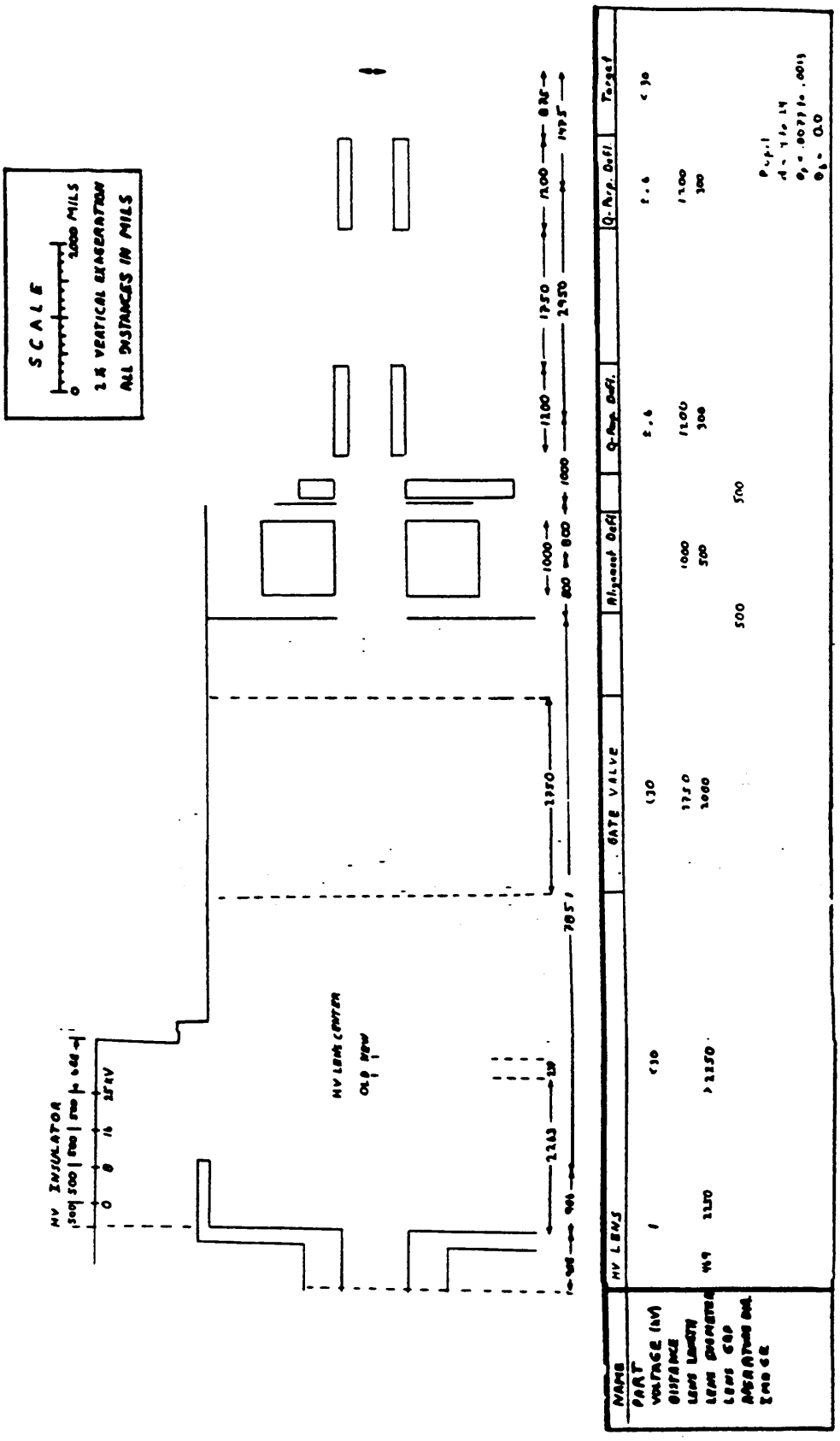

Figure C.19 Input arm lens column (continued).

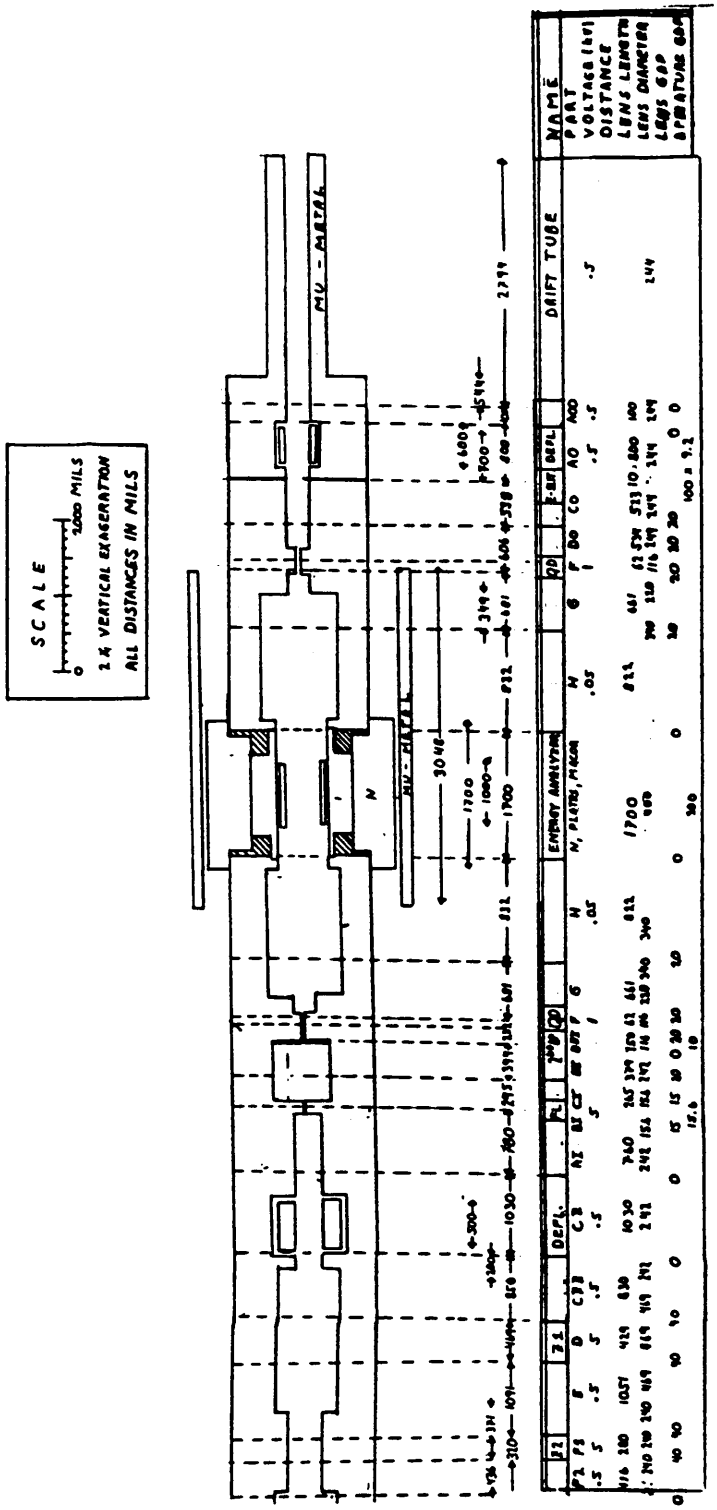

Figure C.20 Output arm lens column.

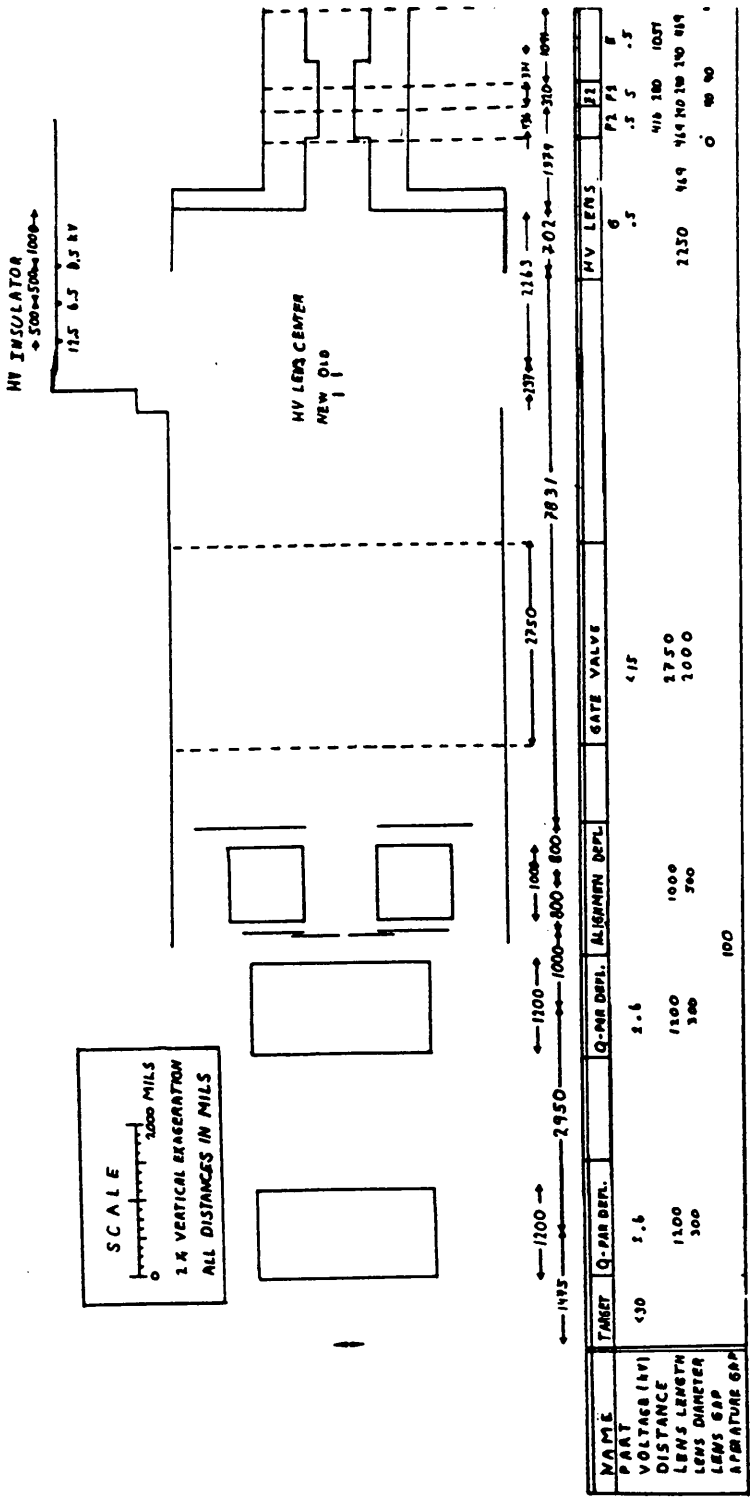

Figure C.20 Output arm lens column (continued).

APPENDIX D: SPECTROMETER SUBSYSTEMS

1. Vacuum system

The (e,2e) spectrometer is equipped with an ultra-high vacuum system to provide a base pressure of 3×10^{-9} Torr. A schematic diagram of the vacuum system is shown in Figure D.1. The vacuum jackets are constructed of stainless steel and all materials inside the vacuum were designed to meet the ultra-high vacuum requirements. Standard Conflat flanges with Cu gaskets are used throughout the system. The vacuum system has a volume of approximately 65 ℓ. The chamber and beam arms can be isolated by gate valves (Thermonics Laboratory, Inc., 2 inch Viton Sealed Gate Valve) so that samples can be changed without cycling the electron gun and EMT to atmosphere each time.

Rough pumping is done by two 40 ℓ sorption pumps (Thermonics Laboratory, Inc. model SP-11). These pumps are isolated from the main chamber by an ultra-high vacuum shut off valve (Varian, model 951-5091). On occasion a dry-vane vacuum pump (Gast Manufacturing Co., model 0522-V103) has been employed.

The high vacuum is accomplished with 5 magnetic ion pumps, a 200-ℓ/s pump (Thermonics Laboratory, Inc.; pump model IP-200, power supply model PS-1000) on the target

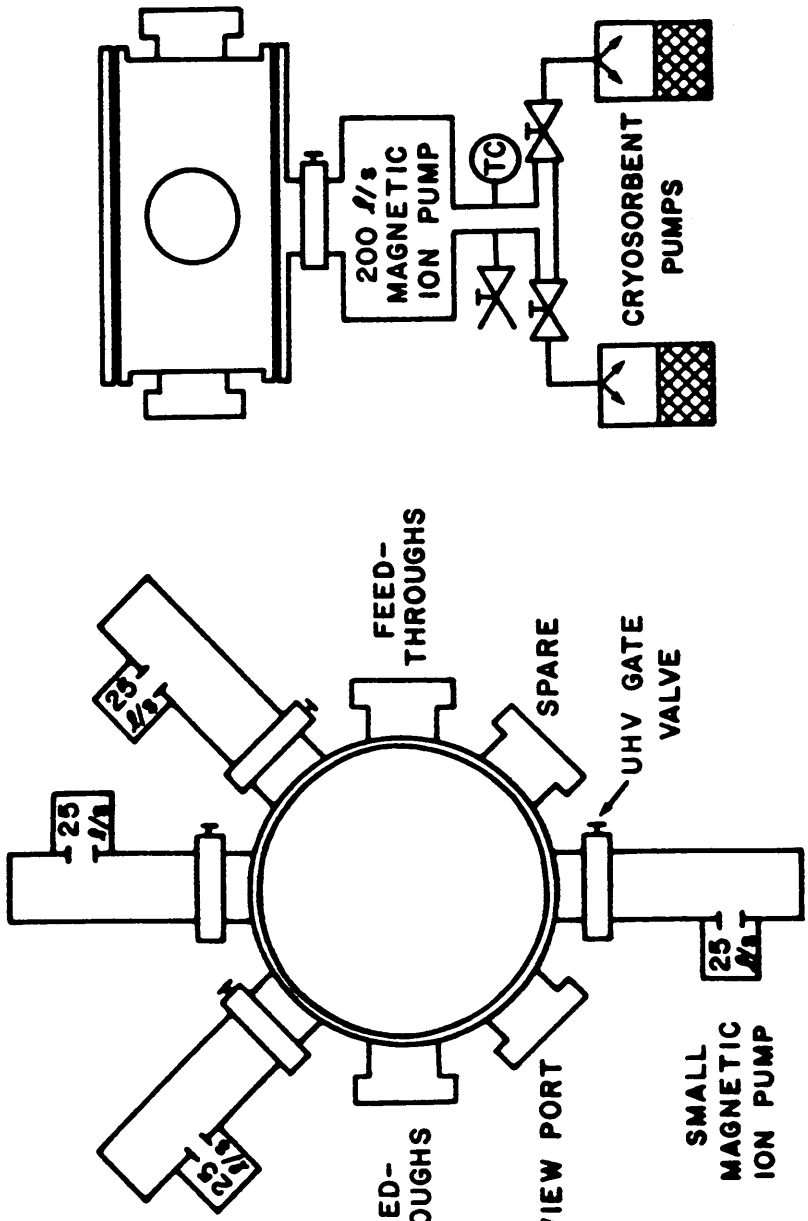

Figure D.1 Vacuum system for (e,2e) spectrometer

chamber and a 25-ℓ/s pump (Thermonics Laboratory, Inc.; pump model IP-025, power supply model PS-150) on each of the four beam arms. The large pump is configured so that it can operate floating at the target chamber high voltage once a good vacuum has been established. The input arm pump is electrically isolated by a ceramic beam arm insulator made by National Electrostatics Corporation.

To achieve the base pressure the system must be baked out at $\sim$ 200°C for 2-3 days after each time it is opened to atmosphere. In general the vacuum turn around time for opening the system is 4-5 days.

Pressure is monitored by measuring the current drawn by the magnetic ion pumps; the ion pump is essentially a large Penning type cold cathode gauge in which the current drawn is a function of the pressure in the system. Since the four small pumps are all connected to the same power supply, only a pressure reading in the target chamber and the average pressure in the arms are available. At times a quadrupole residual gas analyzer (Spectrum Scientific, Ltd., model SM 100) has been connected to the vacuum; this has verified the pressures measured with the magnetic ion pumps.

In general, the pressure is quite stable in the low 10^{-9} Torr range. There is a slight rise in the pressure as a function of the electron beam current.

2. Magnetic shielding

This section of Appendix D describes the magnetic environment for the spectrometer, including the sources of the magnetic fields, the types and designs of magnetic shielding employed, and measurements of the effectiveness of the shielding.

The magnetic fields to be shielded are almost exclusively static fields. Three primary sources are the earth's magnetic field, fields from the permanent magnets in the magnetic ion pumps, and stray fields due to magnetized materials in the spectrometer. The earth's field has an approximate strength of $\sim$500 mG and a declination of $\sim 60^{\circ}$ below the horizontal at a latitude of 35° N [77]. The strong fields of the large permanent magnets in the five magnetic ion pumps are localized and are on the same order as the earth's field along the beam axes.

Stray magnetic fields due to magnetized parts of the electron optics column provided some difficulty, since they were hard to identify and in general were produced within the mu-metal shielding. Care was taken to use non-magnetic materials, e.g., Everdur, 304 stainless-steel, Cu, and Mo, in construction of the optics parts. However, some stainless-steel parts became magnetized and had to be

replaced or de-magnetized. Other magnetized parts, i.e. the gate valves and Ni leads of some vacuum feedthroughs, were unable to be corrected.

Magnetic shielding is accomplished with high permeability mu-metal shields. Most of the electron optics are surrounded by such shielding and critical areas have a second layer within the vacuum chamber.

The target chamber is shielded by a mu-metal can that fits tightly over the target vacuum chamber. This shield is constructed of 1.6 mm thick mu-metal with an ideal attenuation of $\sim$700 (shielding efficiency $\sim$55 dB) [142] with overall dimensions of 36 cm diameter and 35 cm height. The shield has a number of openings for vacuum ports and is split in half horizontally to allow access to the target chamber. This reduces the efficiency of the shield, particularly for the vertical component of the magnetic field. A Helmholtz coil (58 cm diameter) concentric with the vertical axis of the target chamber is used to buck the vertical field component.

The beam arms are surrounded by continuous cylindrical mu-metal shields (15 cm diameter) that extend from the end flange to just past the 25-ℓ/s magnetic ion pumps. This shielding is 1.6 mm thick and has an ideal attenuation of $\sim$800 (shielding efficiency $\sim$60 dB). There are sections of 0.25 mm thick mu-metal foil wrapped around the

vacuum tube walls at the entrance to the small magnetic ion pumps, on either side of the high voltage insulators underneath the mu-metal rings, around the gate valves, and at the beam arm entrances to the target chamber. These foils have an ideal attenuation of ~250 (shielding efficiency ~45 dB).

Continuous mu-metal shielding cannot extend across the high voltage insulators. These sections were shielded with a series of mu-metal rings (30.5 cm O.D., 17.8 cm I.D., and 1.6 mm thick) which are spaced 1.9 cm apart and are mounted on Plexiglass rods. These rings shield the components of the field perpendicular to the beam axis by factors of 10 to 100. The parallel component is not shielded, but the effect of this component on the electron beam trajectory can be compensated for by the electron optics. The theory of this shielding technique is described in Gibbons *et al* [67].

Local magnetic shielding is added inside the vacuum chamber at two critical locations on the output beam arms, around the energy analyzer and at the entrance to the EMT. The energy analyzer is particularly sensitive to magnetic fields because the electrons are decelerated to much slower velocities there than at any other point in the system. The energy analyzer shield is a solid mu-metal cylinder

(3.4 cm I.D. and 1.6 mm thick) that fits closely over the lens column. It is 12 cm long -- the energy analyzer is 8.5 cm long -- with an ideal attenuation of ~3500 (shielding efficiency of ~70 dB). The entrance to the EMT is a critical region because the electrons are still moving with low velocity and fringing fields due to the end of the main beam arm shield are present. The EMT shield is also a solid mu-metal cylinder (95 mm I.D. and 1.6 mm thick); it extends 11 cm from the entrance of the EMT with an ideal attenuation of ~12500 (shielding efficiency ~80 dB).

All the external magnetic shielding was degaussed *in situ* using a 60 Hz AC signal.

The magnetic shielding reduced the magnetic field in the beam arms and target chamber by an overall factor of approximately 100. Magnetic beam arm profiles (Figure D.2) show that the maximum fields were on the order of 70 mG and that the rms field was about 10 mG. Using an impulse approximation, the effect of small magnetic fields on the electron path can be expressed as

$$y = -3.02 \times 10^{-8} \left(\frac{B}{\sqrt{V}} \right)^2 x^2 \qquad (D.1)$$

where x is the distance of flight along the beam axis (in cm), y is the perpendicular deflection distance, B is the magnetic field (in Gauss), and V is the accelerating

(a) Output (A) Arm Magnetic Profile

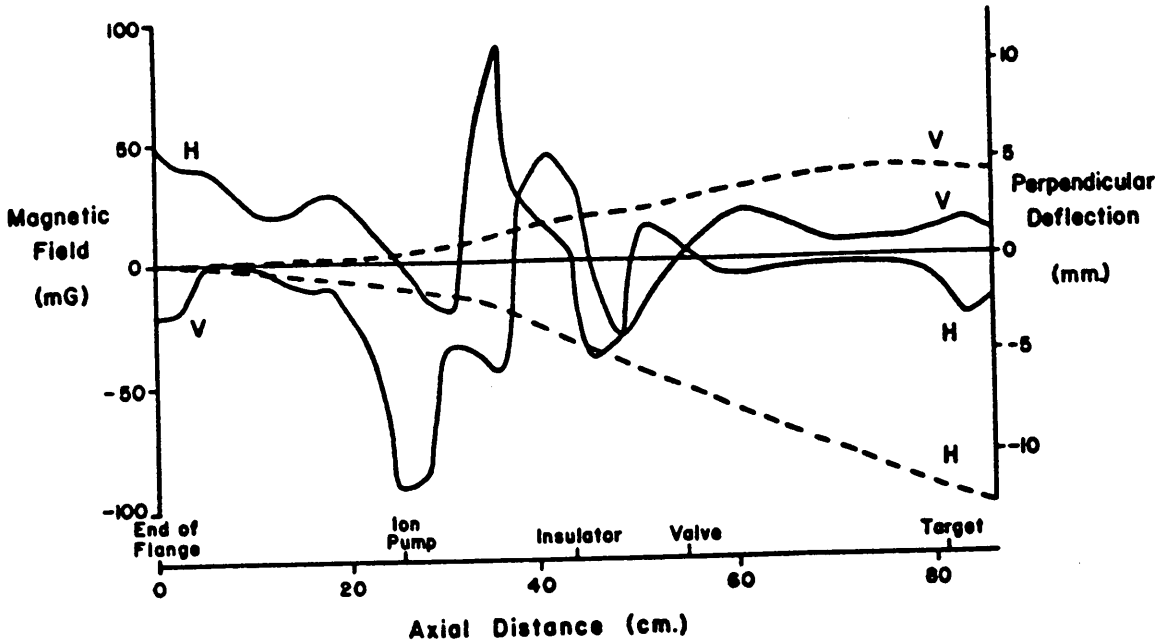

(b) Input Arm Magnetic Profile

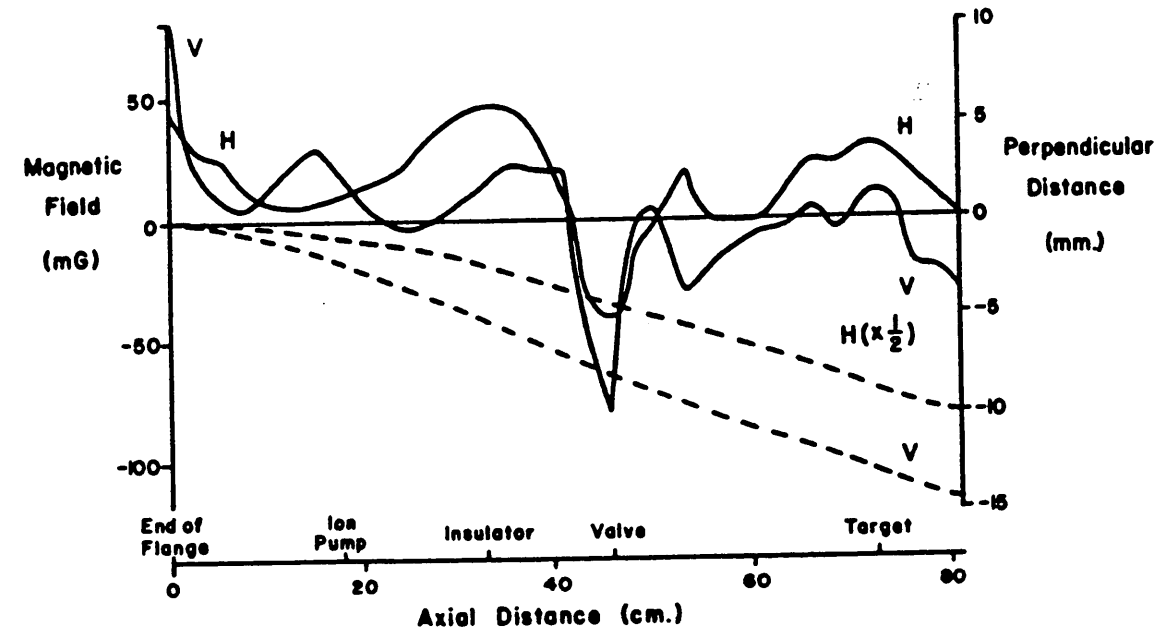

Figure D.2 Magnetic Profile of beam axes.

The solid lines are measured profiles for the horizontal (H) and vertical (V) components of the magnetic field. Dashed lines are the approximate electron trajectories calculated using the impulse approximation. The horizontal axis is the distance along the beam axis in cm.

voltage of the electron (in kV). The approximate trajectory of an electron along the beam axes is also plotted.

3. Voltage distribution

Two high precision high voltage probes (Fluke model 80 F-15) are connected to a voltage bridge which measures the voltage difference between the two probes as shown in the schematic in Figure D.3a. The voltage measured across R_m is equal to one thousandth of the voltage difference $|HV_+| - |HV_-|$ with an accuracy of ± 0.01%.

To achieve this high precision, the voltage bridge is calibrated periodically. Calibration is performed by measuring the voltage difference over a wide range with the connected probes in different arrangements. With Probe #1 connected to HV_+ and Probe #2 connected to HV_- analysis of the equivalent circuit in Figure D.3b shows that the meter voltage is

$$V_m = IR = \frac{R_2\ HV_+ + R_1\ HV_- - I\ R_1\ R_2}{(R_1 + R_2)} \qquad (D.2)$$

By reversing the position of the HV probes, the measured voltage is

$$V_m^* = \frac{R_1\ HV_+ + R_2 HV_- - I\ R_1\ R_2}{(R_1 + R_2)} \qquad (D.3)$$

and

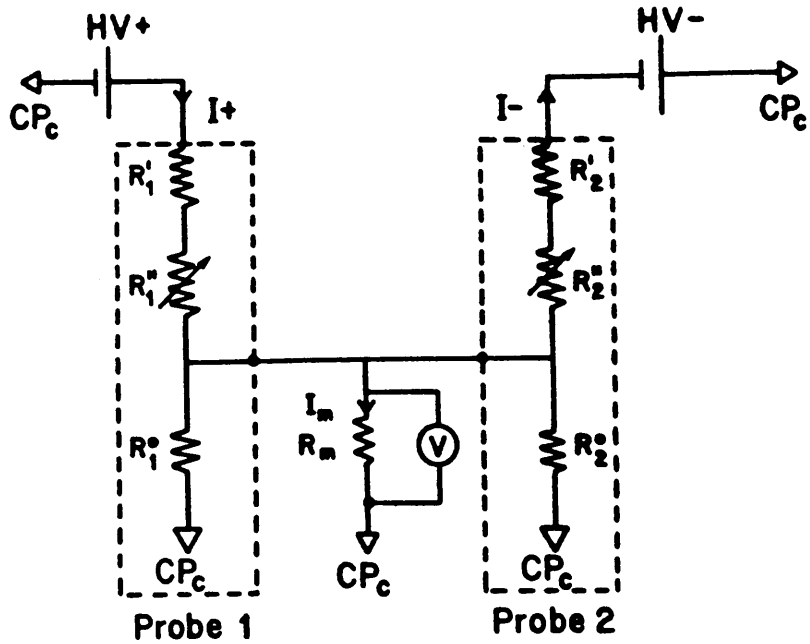

(a) Schematic of high voltage divider

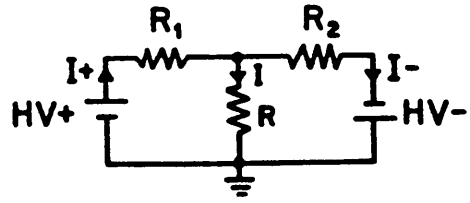

$R_1 \equiv R_1' + R_1'' \approx 1000 R_1^\circ$

$R_2 \equiv R_2' + R_2'' \approx 1000 R_2^\circ$

$\frac{1}{R} \equiv \frac{1}{R_1^\circ} + \frac{1}{R_2^\circ} + \frac{1}{R_m}$

(b) Equivalent circuit

Figure D.3 High Voltage Divider

Table D.1 High Voltage Probe Specifications

Fluke Model 80F-15 High Voltage Probe*

Input voltage range	1-15 kV
Input resistance	100MΩ
Division ratio	1000:1
Ratio Accuracy	±0.01% of input
Stability of ratio	±0.001%/month
	±0.05%/year
Temperature coefficient	0.001%/°C
Voltage coefficient	<±0.002%

* John Fluke Manufacturing Company, Inc.

$$V_m + V_m^* = (HV_+ + HV_-) \cdot [\mathcal{R} - \mathcal{R}^2 + \mathcal{O}(\mathcal{R}^3)] \qquad (D.4)$$

where

$$\mathcal{R}^{-1} \equiv \frac{R_1 R_2}{(R_1 + R_2)R} = 1000 \pm <1\% \qquad (D.5)$$

To avoid the necessity of reversing the probes during operation, $(V_m + V_m^*)$ was calibrated as a function of V_m:

$$(V_m + V_m^*) = \alpha V_m + \beta \qquad (D.6)$$

where $\alpha = 2000.1$

$\beta = -12.078$ V

Finally,

$$HV_+ + HV_- = 2000\ V_m - 12.1 \qquad (D.7)$$

to within less than 1% (or .1 V if greater) uncertainty.

4. Pulse electronics

The purpose of the pulse electronics in our spectrometer is to identify and record the coincidence electron events. This section of the appendix describes the pulse electronics in detail, tracing a pulse from the electron multiplier to the MINC computer where it is recorded as data. Details of the components are also given. Refer to the text section on data acquisition for a general description of the pulse electronics and to Figure IV.1 for a block diagram of the system.

Electron detection is performed by a fast, linearly

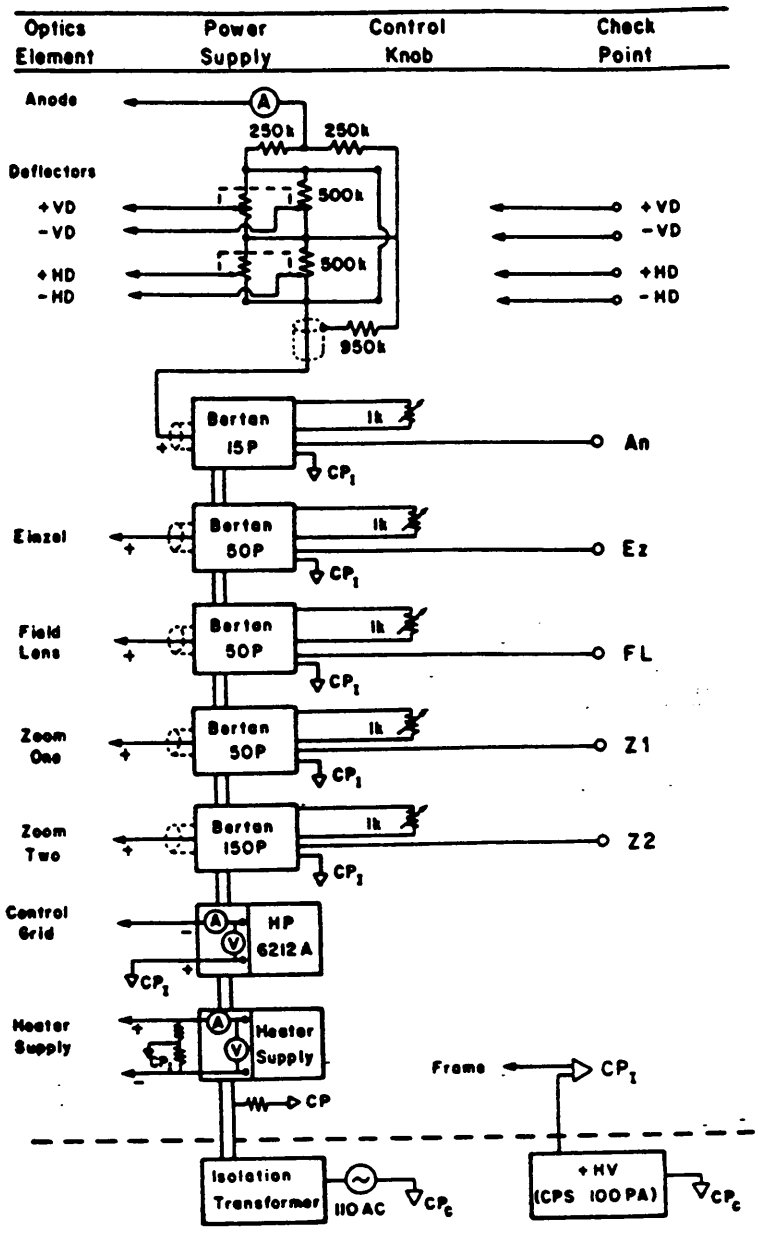

Figure D.4 Input Arm Electronics

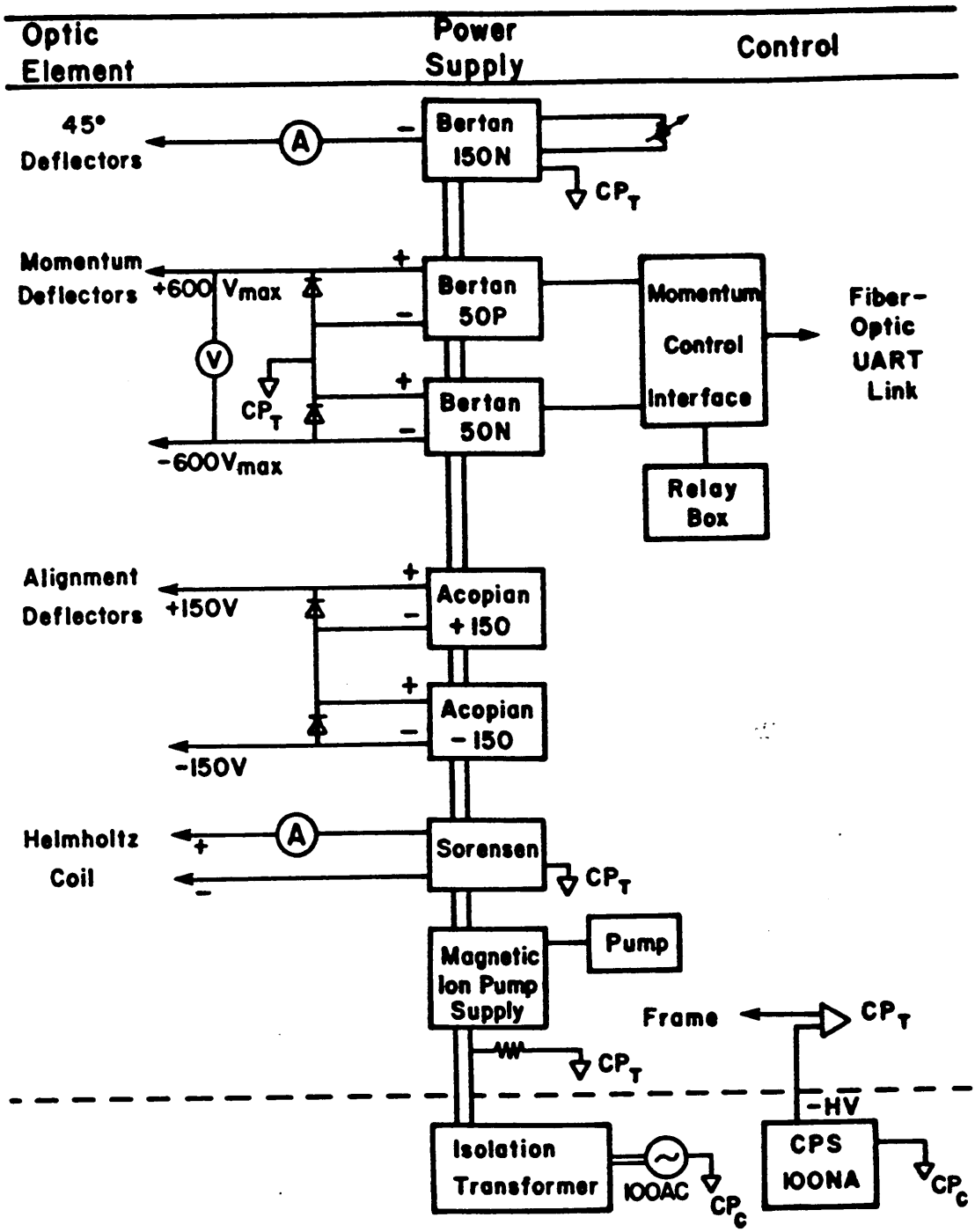

Figure D.5 Target Chamber Electronics

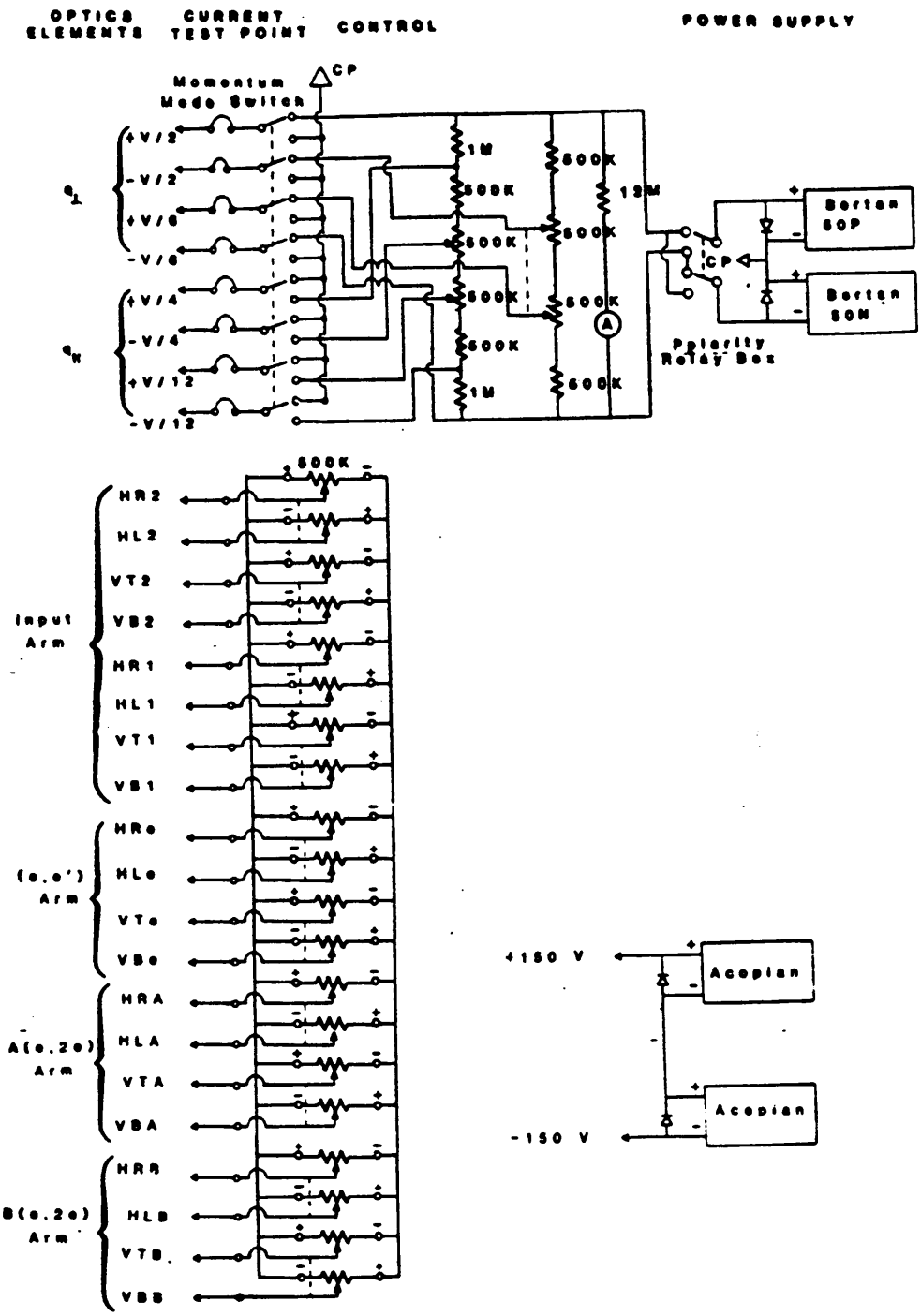

Figure D.6 Target Chamber Deflector Schematic

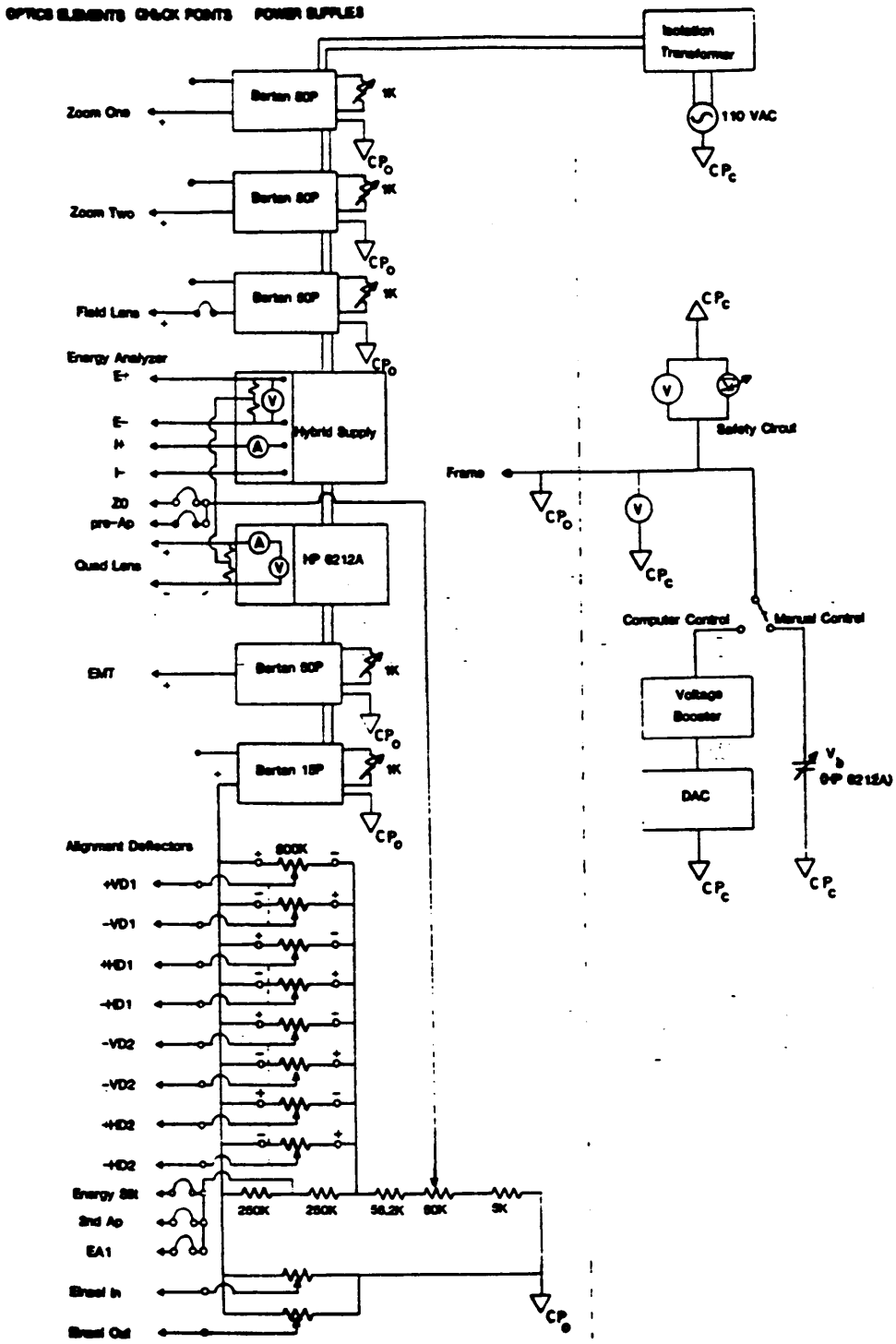

Figure D.7 Output Arm Electronics

Table D.2 Power Supply Specifications

Power Supply	Voltage	Current	Notes
Acopian[a]	Range: 0-600V		Temp. Coeff.: 0.01%/°C
Bertan[b] 602B-15P,N	Range: 0-1.5kV Max. Ripple: 15mV	Max: 10mA	Regulation:0.001%line;0.001%load Stability: 0.01%/hr;0.02%/8hrs. Temp. Coeff.: 50ppm/°C
Bertan[b] 602B-5P,N	Range: 0-3kV Max. Ripple: 30mV	Max.: 2mA	same as 602B-15
Bertan[b] 602B-150P,N	Range: 0-15kV Max. Ripple: 150mV	Max: 0.6mA	same as 602B-15
CPS[c] 100PA,100NA	Range:0-30kV Max. Ripple: 150mV	Max: 1mA	Regulation:0.001%line;0.001%load Stability:0.005%/hr;0.01%/8hrs. Repeatability: 0.05% Temp. Coeff.: 25ppm/°C
Hewlett-Packard[d] 6212A	Range:0-100V Max.Ripple:200μV_{rms}	Range:0-100mA Max.Ripple:150μA_{rms}	Regulation:4mV,500μAline 8mV,500μAload Stability:Voltage 0.1%/8hrs. Current-1.3mA/8hrs. Temp. Coeff.: Voltage-0.02%/°C Current-0.5mA/°C
Hewlett-Packard[d] 6516A	Range:0-1.6kV Max.Ripple: 5mV	Max:5mA	Regulation:0.001%line;0.001%load Stability:0.05%/8hrs. Temp.Coeff.: 0.02%/°C
Heater Supply[e]	Range:0-10V	Range:0-10A	
Hybrid Voltage-Current Supply[e]	Range:0-200V	Range: 0-3A	
Sorensen[f] QRB-40	Range:0-40V	Range: 0-800mA	

(a)Acopian Corporation
(b)Bertan Associates, Inc.
(c)CPS, Inc.
[d]Hewlett-Packard Company
[e]VPI Electronics Shop

focused, discrete-dynode electron multiplier (EMI Gencom, model D233). The electron multiplier is housed in a glass envelope which is attached by a glass-to-metal adapter to a standard (3.4cm O.D.) Conflat flange at the end of the beam arm vacuum jacket. The electron multiplier tube (EMT) has 14 BeCuO dynodes that operate at a maximum of 4 kV anode-to-cathode voltage with a typical gain of 2×10^6. The detection efficiency is rated at 90-100% for electrons of energy of 300 to 500 eV [156]. This is the typical energy of the electrons reaching the EMT. The anode pulse typically has a width of 4 nsec (FWHM) with a rise time of 2.5 nsec.

The signal from the EMT goes to a preamp (EMI Gencom, model VA.02) through a high voltage decoupling capacitor [189]. The preamp uses an integrated circuit amplifier (LeCroy Research Systems, model VV100B) with a gain of 10. Pulses from the preamp have a typical width of 2 nsec and a rise time of 0.7 nsec. A schematic of the EMT circuitry is shown in Figure D.8.

The signal pulse from each preamp goes to a discriminator (Canaberra, model 1428A) operating in the constant fraction timing mode. The discriminator level is adjusted to slightly above the background level, so that the singles scalar rate is negligible when the beam is deflected out of the beam path. The discriminator produces

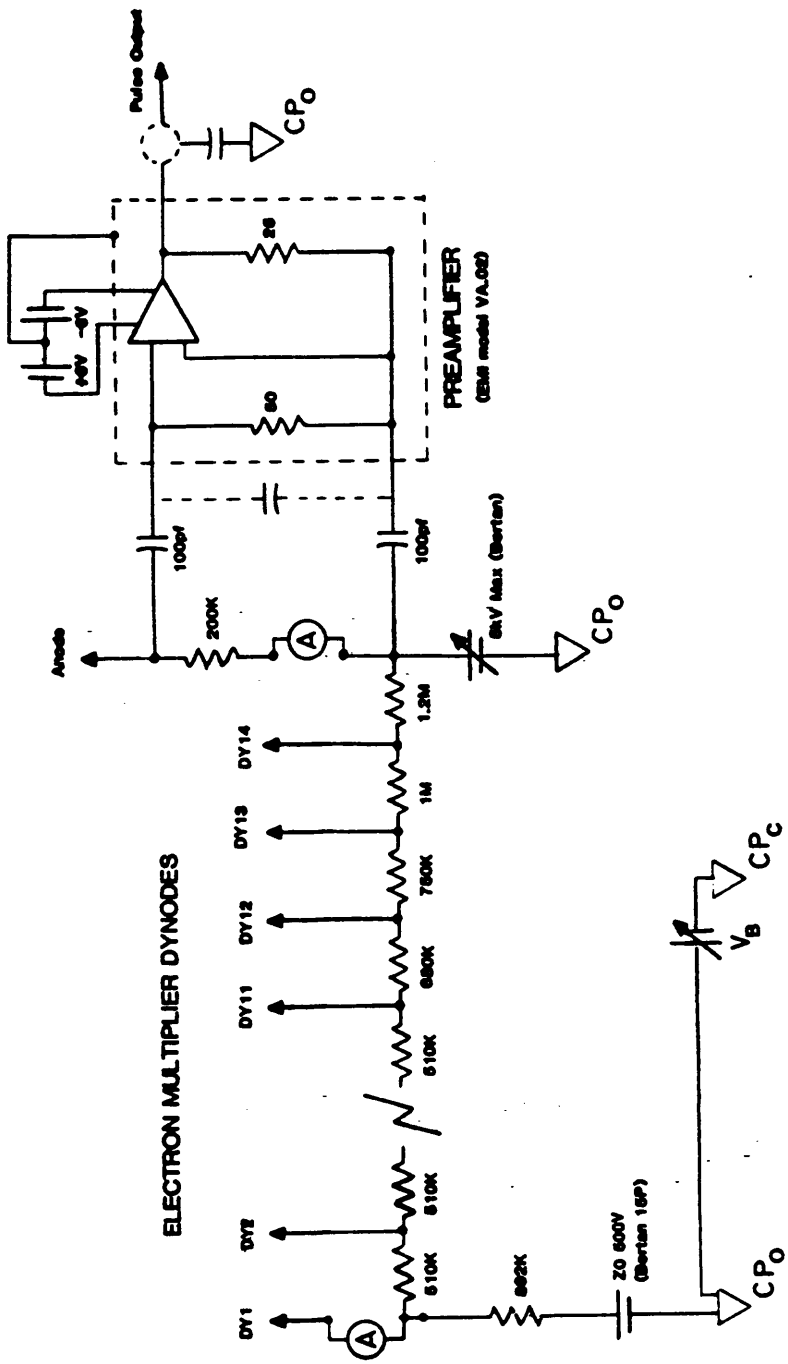

Figure D.8 Electron Multiplier Schematic

a negative-going pulse with a rise time of <3 nsec and a pulse width of 20 nsec nominal that is used to trigger the TDC. The discriminator also produces two independent positive-going pulses with rise times of <10 nsec that drive the scalars and rate meters. This positive pulse has a width of ~ ??? nsec, which determines the dead time of the discriminator following a given pulse.

Each discriminator is connected to a 32-bit scalar (Kinetic Systems, model 3640) which records the singles count for each arm. Each discriminator is also connected to an analog ratemeter (TENNELEC, model TC 525). The rate meters are used primarily for tuning the spectrometer's electron optics to a maximum transmission level.

Coincidence detection is performed by a time-to-digital converter (LeCroy Research Systems, CAMAC model 2228A). The signal from one discriminator acts as a start pulse for the TDC. The TDC waits up to 128 nsec to receive a stop pulse from the second discriminator. The signal from the second discriminator passes through a variable delay box (VPI Physics Electronics Shop) before it reaches the TDC. The signal is delayed approximately 25 nsec to minimize false stop pulses and to compensate for internal delays in the TDC. If a stop pulse is received, the TDC records a potential coincidence event by transferring to the MINC computer a digital number which is proportional to

the time between signals. The TDC is set to a full scale range of 128 nsec with a time resolution of 250 psec/channel. There are 512 TDC channels. The conversion time of the TDC is $\lesssim$ 30 μsec, which determines the dead time of the TDC. Using the signal from the arm with the lower single scalar rate as the start pulse will increase the coincidence rate by reducing the dead time in the pulse electronics.

The TDC and scalars interface to the MINC by standard CAMAC hardware. Data is transferred via a CAMAC crate controller (Interface Standard, model IS-11/CC) to the LSI 11-based MINC using standard CAMAC commands. The transfer takes ~30 msec to execute. The data transfer accounts for the limiting dead time of the pulse electronics system. Some data is lost as the rate of the TDC start pulse exceeds ~3 kHz and at ~32 kHz the transfer becomes inoperable.

APPENDIX E: DATA ACQUISITION SOFTWARE

The program PHYS provides the real-time control of the spectrometer during (e,2e) data acquisition, performs the initial data reduction, and displays a listing and graphics of the data [43]. PHYS is an RS-11 FORTRAN program with a number of machine code subroutines. Standard CAMAC commands and MINC lab module subroutines facilitate the control of peripheral devices. The process of real-time data acquisition is described in the main text section on data acquisition. This appendix details the software, data files, data reduction, and merging algorithms, and the error analysis associated with count rates. A flow chart of the (e,2e) data acquisition software is shown in Figure E.1.

Data are collected by the MINC at each (E,**q**) point; the range of (E,**q**) points defines an (E,**q**) space over which data is collected. PHYS directs the MINC to sample each (E,**q**) point in a random order that eventually samples all of the (E,**q**) space. After a specified number of sweeps through (E,**q**) space, the time coincidence spectrum for each (E,**q**) point undergoes a data reduction process and a SUMMARY data file is created. Only four numbers per (E,**q**) point are stored in the summary file; the total counts in the coincidence-plus-

Figure E.1 Flowchart of data acquisition software.

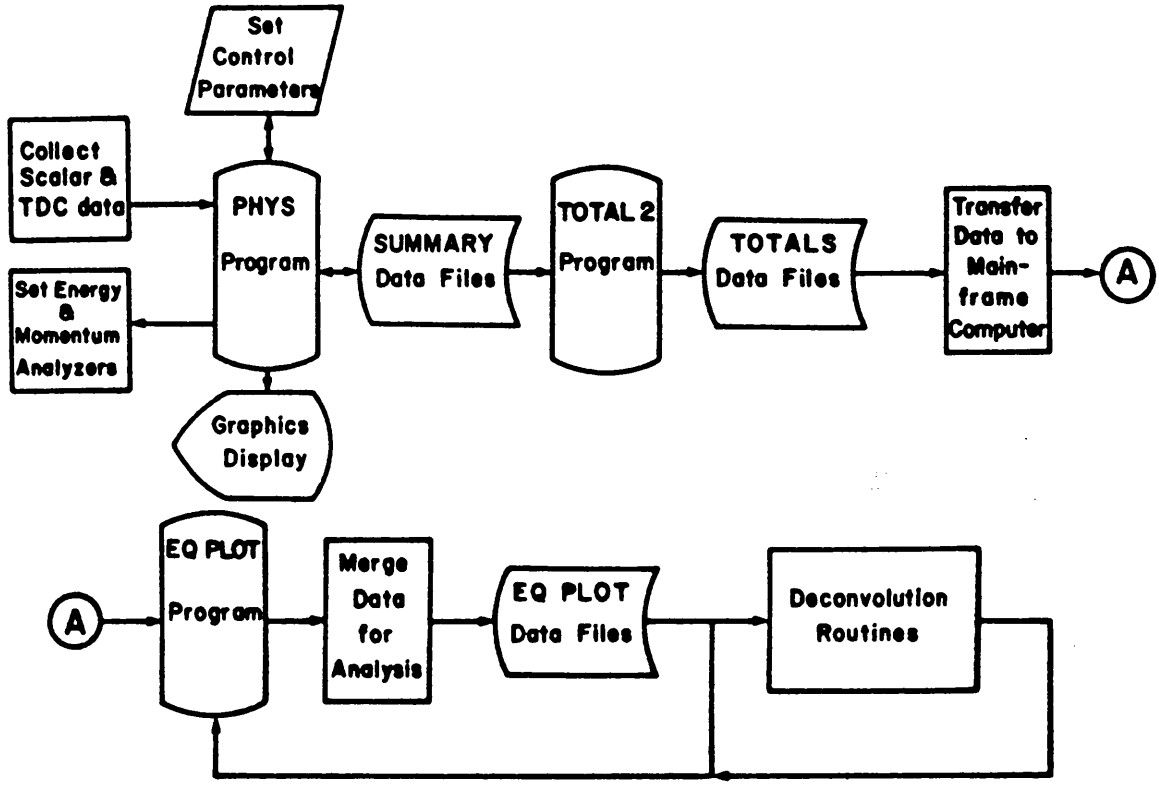

Figure E.1 Flowchart of data acquisition software.

background time window, the total counts from the background time window, and the total scalar counts from each beam arm. The significance of the time windows is discussed in the main text section on data analysis. The software allows the user to set the ranges of these time windows before data collection has begun. Typically, the coincidence-plus-background window is 5 nsec (20 TDC channels) and the background window is 50 nsec (200 TDC channels).

PHYS allows the user to graphically display the time coincidence spectrum of each (E,**q**) point during the data collection process. Once a SUMMARY data file is created the coincidence-minus-background count at each (E,**q**) point can be listed.

The program TOTAL2 combines data from one or more SUMMARY files, together with a listing of PHYS control parameters and annotations, into a TOTALS data file [42]. This data file is in a form that can easily be printed, read by other FORTRAN programs, and transferred to the main frame computer. The TOTALS data file contains a listing of the data from each SUMMARY data file which includes the energy, momentum, coincidence-plus-background window count, background window count, and scalars counts for each (E,**q**) point. A summation over all SUMMARY files combined of the four counts at each (E,**q**) point is also

included in the data file.

The TOTALS data files are transferred to the VPI mainframe computers, a DEC VAX 11/780 and an IBM 370, for further analysis. Elaborate data transfer packages are used which check the transferred data byte by byte, using appropriate handshaking and transmission error detection [46].

There are several related real-time command programs that control operation of the spectrometer while it performs auxiliary functions. This section briefly outlines the most important of these programs [45].

PHYS is designed to operate in two modes, the coincidence mode described above and the pulse mode. In the pulse mode, PHYS scans an (E,**q**) space just as detailed in the text section on (e,2e) data acquisition. However, only the scalar count output for one channel is monitored; there is no coincidence detection. The mode is designed primarily for use in (e,e') data acquisition when our spectrometer acts as an EELS instrument.

QSWEEP is used to collect scalar count data over a range of momenta at a fixed energy value. Momentum selection is performed in sequential order over the range; only one sweep of the momenta is made. The collected data can be displayed graphically by the MINC or it can be

stored in a data file, transferred to the mainframe computer, and plotted and listed by EQPLOT. QSWEEP is used primarily as an aid in measuring the momentum calibration factor (see Appendix C.3) and in aligning the spectrometer.

ESWEEP is used to collect scalar count data over a range of binding energy at a fixed momentum value. ESWEEP is similar to QSWEEP in operation and data display. The program is used to collect (e,e') data. It also looks at wide angle inelastic scattering in the (e,2e) arms which is used to measure the resolution of the energy analyzer.

ZEROMD is used to set the momentum and energy analyzers to zero.

APPENDIX F. DATA ANALYSIS SOFTWARE

1. Data merging

The program EQPLOT analyzes the data stored in the TOTALS data files by the MINC computer. EQPLOT uses the four measured counts, coincidence-plus-background, background, and the two scalars rates, to combine one or more TOTALS data files into a single array of the coincidence count rate over (E,**q**) space. The program also calculates the random error associated with the coincidence count rate at each (E,**q**) point.

EQPLOT establishes an (E,**q**) array that covers a range of energy and momentum large enough to incorporate all of the TOTALS data to be combined. The data is merged into this array one SUMMARY data file at a time. After the data from each SUMMARY file is read into EQPLOT, a check is made for suspect data points that may represent glitches in the data collection process. A comparison is made between the scalar (background) count at each (E,**q**) point and the average scalar (background) count for the entire summary file. Data not within tolerance (typically ± 10%) can be rejected as invalid data.

The background count at each valid data point is subtracted from the coincidence-plus-background count using the technique described in Section V. This coincidence count data is incorporated into two arrays. One array, CTOT(I,J), contains the total number of actual coincidence counts from all of the combined SUMMARY files at each (E,**q**) point. Note that I and J are the energy and momentum indices of the (E,**q**) point, respectively.

The second array, CNORM(I,J), that utilizes the coincidence count data is a merged, normalized coincidence count rate. This array is designed to merge data file collected over different subspaces of (E,**q**) space for varying time periods in such a way as to minimize errors and accurately weight the contribution of each SUMMARY data file to the complete data set. Data is often taken in several subsets that cover different regions of (E,**q**) space. Each subset, or TOTALS data file, overlaps adjacent data subspaces; this overlap region plays a key role in merging the data.

One column of the overlap region, with momentum index J=JMERG, is designated as the merging column. All (E,**q**) points with J=JMERG and that have both old and new data comprise the merging region. NRMNEW is the sum of the coincidence counts in the merging region for the new data, i.e. the SUMMARY data file which is being merged. NRMOLD

i.e. the SUMMARY data file which is being merged. NRMOLD is the sum of the CNORM(I,J) values in the merging region based on only the old data which has been previously merged. Figure F.1 illustrates the data regions in (E,q) space used in the merging procedure.

The merged coincidence count is equal to the total coincidence count times a scaling factor, $R \geq 1$. The merged coincidence counts are scaled so that counts at different (E,q) points sampled for varying lengths of time can be compared directly. The total coincidence count and scaling factor are used to calculate new, merged coincidence counts and the error associated with those counts. The program EQPLOT uses the following algorithm to calculate a value for the merged data at each (E,q) point, MERG(I,J):

$$\mathrm{MERG}(I,J) = \begin{cases} \left[\frac{1}{\mathrm{NRMOLD}/R}\right] \cdot \mathrm{COIN}_A(I,J) & ; \text{ only old data} \\ \left[\frac{1}{\mathrm{NRMNEW}}\right] \cdot \mathrm{COIN}_B(I,J) & ; \text{ only new data} \\ \left[\frac{1}{\mathrm{NRMOLD}/R + \mathrm{NRMNEW}}\right] \cdot \left[\mathrm{COIN}_A(I,J) + \mathrm{COIN}_B(I,J)\right] & ; \text{ both old and new data} \\ 0 & ; \text{ no data} \end{cases} \qquad \text{(F.1)}$$

1) At (E,q) points where there is only old data (unshaded part of Region A in Figure F.1) the merged value is equal to the total coincidence count of the old data, $\mathrm{COIN}_A(I,J)$, times a weighting factor. The weighting

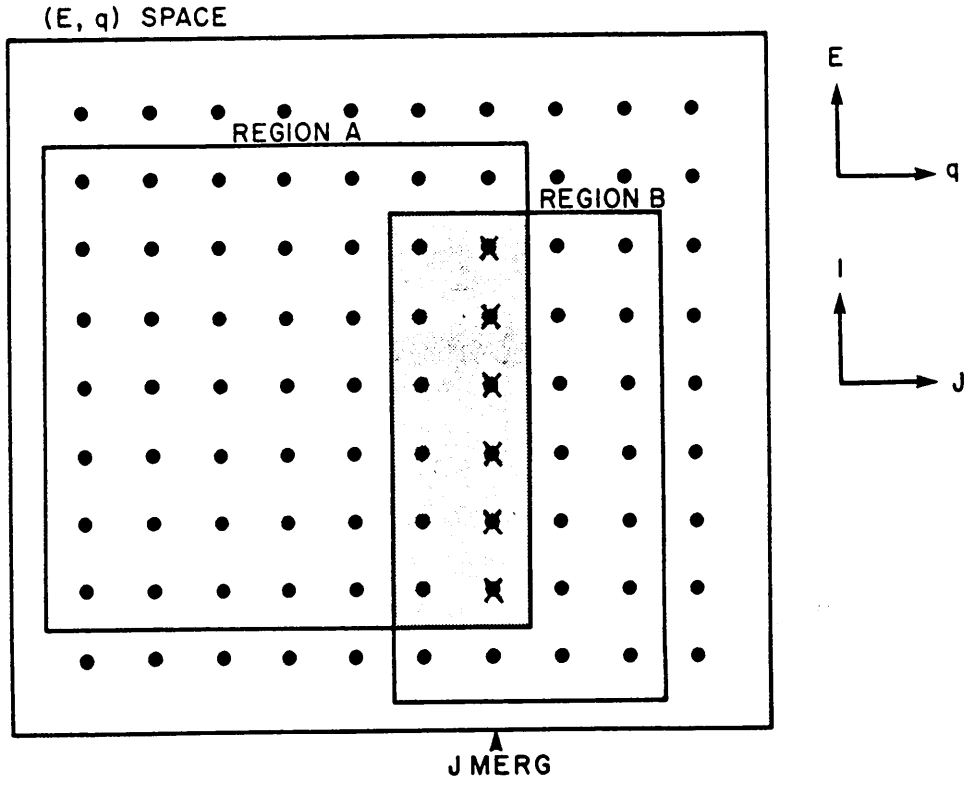

Figure F.1: Diagram of data regions in (E,q) space used in the merging procedure.

This is a diagram of the (E,q) data regions used in merging a new SUMMARY data file (Region B) with other data that has already been merged into the (E,q) array (Region A). The overlap region where there is both old and new data is shown shaded. The merging column is indicated and the (E,q) points in the merging region are denoted by x.

factor equals the inverse of NRMOLD divided by R.

2) At (E,**q**) points where there is only new data (unshaded part of Region B in Figure F.1) the merged value is equal to the coincidence count of the new data, $COIN_B(I,J)$, times a weighting factor. The weighting factor equals the inverse of NRMNEW.

3) At (E,**q**) points where there are both old and new data (shaded overlap region in Figure F.1) the merged value is equal to the sum of the old and new coincidence counts times a weighting factor. The weighting factor equals the inverse of the sum of NRMOLD divided by R plus NRNEW.

4) At (E,**q**) points where there is no data (outside Region A union Region B in Figure F.1) the merged value is equal to zero.

The scaling factor R is equal to the ratio of the normalized data CNORM(I,J) to the total number of counts $COIN_A(I,J)$. If, by chance, $COIN_A(I,J)$ equals zero, R is calculated using the sums of CNORM and $COIN_A$ over all energies for their momentum. In the unlikely event that this sum of $COIN_A$ is zero, R is arbitrarily set to one.

Finally, the merged counts are normalized such that the total coincidence rate over all(E,**q**) space sums to unity. It is this merged, normalized coincidence rate array, CNORM(I,J), that is used for all further data

analysis.

The standard deviations for the raw (e,2e) data, i.e. the coincidence-plus-background, the background, and the two scalar counts for each (E,**q**) point from each SUMMARY file, are the square root of the counts. This follows from the assumption that these counts follow a Poisson distribution. The relative error in the raw data is the reciprocal of the square root of the counts.

The error for the individual coincidence count for each (E,**q**) point from each SUMMARY file is equal to the error of the raw coincidence-plus-background count plus the error in the raw background count divided by r added in quadrature,

$$\Delta(\text{Coin}) = \left\{ \left[\Delta(\text{Coin-plus-Back}) \right]^2 + \left[\Delta(\text{Back})/r \right]^2 \right\}^{1/2} \qquad \text{(F.2)}$$

where r is the ratio of the coincidence-plus-background time window to the background time window (see Section V). The error in the total coincidence counts at each (E,**q**) point is the sum of the errors of the coincidence count for each SUMMARY file added in quadrature. Thus, the standard deviation in the total coincidence count is given by

$$\sigma_{CTOT} = \left\{ \sum_{n=1}^{N} \left[\left| (\text{Coin-plus-back})_n \right| + \frac{1}{r^2} \cdot \left| (\text{Back})_n \right| \right] \right\}^{1/2} \qquad \text{(F.3)}$$

where the sums are over N SUMMARY files.

If we assume that R is exact and that the error in NRMOLD and NRMNEW are small compared with the errors in the total coincidence counts at each (E,**q**) point (i.e., there are a large number of points in the merging column summed to obtain NRMOLD and NRMNEW), the relative error in the merged, normalized array is equal to the relative error in the total coincidence count. The relative error of the merged, normalized coincidence rate, CNORM, is

$$\frac{\Delta(\text{CNORM})}{\text{CNORM}} = \frac{\left\{ \sum_{n=1}^{N} \left[|(\text{Coin-plus-back})_n| + \frac{1}{r^2} \cdot |(\text{Back})_n| \right] \right\}^{1/2}}{\sum_{n=1}^{N} \left[(\text{Coin-plus-Back})_n - \frac{1}{r} \cdot (\text{Back})_n \right]} \qquad \text{(F.4)}$$

If there is a relative systematic error in the measured count rates Δ_s, then the error in CNORM is

$$\Delta\text{CNORM} = \left\{ \sum_{n=1}^{N} \left[\left(\frac{1}{|(\text{Coin-plus-back})_n|} + \Delta_s^2 \right) (\text{Coin-plus-Back})_n^2 \right] + \frac{1}{r^2} \left[\left(\frac{1}{|(\text{Back})_n|} + \Delta_s^2 \right) (\text{Back})_n^2 \right] \right\}^{1/2} \qquad \text{(F.5)}$$

The errors in the total background count and scalar counts are equal to the square root of the total counts.

2. Deconvolution techniques

The problem of deconvoluting the instrumental broadening and multiple scattering from the measured (e,2e) data was formally solved in Section II.B4. However, the

problem of how best to carry out the numerical inversion of Equation II.54 was left to this appendix. Many possible approaches exist.

One approach is the Fourier transform method. Taking the Fourier transform of equation II.52 it follows from the convolution theorem that

$$\mathbf{A}(t,x) = \mathscr{A}(t,x) \cdot \mathscr{T}(t,x)\ (2\pi)^2 \qquad \text{(F.6)}$$

where $\mathbf{A}$ and $\mathscr{A}$ are the Fourier transforms of $\mathbf{R}$ and $\mathscr{R}$, respectively. In theory, this can be immediately inverted to find $\mathscr{A}$; the inverse Fourier transform of $\mathscr{A}$ is $\mathscr{R}$, which is the function sought. In reality the problem is not this simple for several reasons [31]:

1) Including random noise errors in the measurements, described by $\mathbf{N}(E_0,\mathbf{k}_0)$, requires that Equation II.54 must be rewritten as

$$\mathbf{R}(E_0,\mathbf{k}_0) = \mathscr{R} \otimes \mathscr{S} + \mathbf{N}(E_0,\mathbf{k}_0) \qquad \text{(F.7)}$$

Since $\mathbf{N}$ is not known, one must solve the now approximate Equation II.54, neglecting the random noise. This problem can be alleviated somewhat by using smoothing procedures to improve the quality of the measured cross section, $\mathbf{R}$. In practice, this smoothing can be accomplished by clipping the high-frequency components of the function $\mathbf{A}$ before taking the inverse Fourier transform to find $\mathbf{R}$; this results in $\mathbf{R}$ being evaluated at wider intervals in

energy-momentum space.

2) Deconvolution does not yield a unique solution, since any function $M(E_0,\mathbf{k}_0)$, whose convolution with the smearing function is either exactly or approximately zero, can be added to $\mathcal{R}$ without greatly affecting its convolution with $\mathcal{S}$. Random high-frequency noise [87], for example, satisfies the condition on M. Again, clipping the high-frequency components of A can help alleviate this problem.

3) In general, we do not take data over all dimensions of energy-momentum space. This does not present a serious problem as long as $\mathcal{R}$ does not vary appreciably in these unmeasured dimensions over the width of the smearing function, or simply that the experimental resolution is sufficient to see the important features in R. In essence, this results formally in approximating the dependence of $\mathcal{R}$ on these unmeasured dimensions by a delta function when performing the Fourier transform to calculate $\mathcal{A}$; this results in a factor of $\frac{1}{\sqrt{2\pi}}$ in $\mathcal{A}$ for each such dimension. This is of course an approximation, and does introduce unknown errors into the calculation.

4) The measured data does not extend over an infinite range of energy or momentum. Formally, $\mathcal{R}$ is equivalent to convoluting a hypothetical function extending the

measured data to infinity $\mathcal{R}_\infty$ with two rectangular functions limiting the range of $\mathcal{R}_\infty$

$$\mathcal{R} \sim \mathcal{R}_\infty \otimes \text{rect}\ (\epsilon_{min},\epsilon_{max}) \otimes \text{rect}\ (q_{min},q_{max}) \qquad \text{(F.8)}$$

Then the Fourier transform of $\mathcal{R}$ is

$$\mathcal{A} \sim \mathcal{A}_\infty \cdot \text{sinc}(t) \cdot \text{sinc}\ (x) \qquad \text{(F.9)}$$

that is the Fourier transform of the extended data broadened by two sine functions.

As the range of data is extended, the "width" of the sinc functions decrease, however so does the spacing of the points in Fourier space. Beyond the nth point away from a given point in Fourier space, the sinc function associated with the given point is nearly zero. By considering only every nth point of $\mathcal{A}$, the broadening is minimized. If **A** is then calculated using only every nth point of $\mathcal{A}$, then **R** will extend over one nth of the range of $\mathcal{R}$. However, if $\mathcal{R}$ is artificially extended in energy and momentum space to a function $\mathcal{R}_{ext}$ which is n times as wide as $\mathcal{R}$, $\mathcal{A}$ is calculated from R_{eff}, and **A** is then calculated at every nth point, then the Fourier transform of **A**, **R**, will extend over the full range of measured data.

It is relatively straightforward to extend the measured data. Beyond a certain point in momentum space

the (e,2e) form factor goes monotonically and quickly to zero. Beyond the measured data, $\mathfrak{R}$ can be extended smoothly to zero by splicing an error function to the last measured momentum data point. Likewise, above the Fermi energy the count rate fall to zero and an error function can be spliced to the last measured energy data point [180]. At high binding energy the ideal $\mathfrak{R}$ should fall to zero, however the count rate is held at an approximately constant level rate by multiple scattering for at least the width of the first plasmon peak beyond the last true (e,2e) band. An error function of the width of the plasmon peak width is a reasonable approximation to the extension of $\mathfrak{R}$ in this direction.

This technique is crude and has the potential for disastrous results. It introduces unknown errors into the value of $\mathbb{R}$ and can diverge unpredictably by amplifying noise in the data. However, it is numerically simple to perform. It has been used with good results on a-C data as described in reference 144.

Another, more conservative, deconvolution technique is the van Cittert iterative method [169]. We have made use of the variation of this method described by Wertheim which incorporates a smoothing of the data into the iterative process [181]. Application of this method to (e,2e) spectroscopy is described in Reference 90 where examples of

its application are shown. This technique has the same pitfalls as noted for the Fourier transform method and also has a problem with divergence of solution and introduces unknown errors into the value of **R** This is the deconvolution method used for the data described in Section XIII.

Another method of deconvolution, a hybrid Fourier Transform technique has been developed by Rick Jones and is in the process of being implemented. This technique offers the potential to keep track of the errors introduced by the deconvolution.

APPENDIX G: DATA COLLECTION PROCEDURES

Careful planning and the proper order of data collection greatly facilitates the execution of an experiment. The following section provides a suggested order of collecting the necessary data. This includes a logical sequence for determining the parameters listed in Tables VIII.1 and VIII.2. First, however, it is important to know what range of parameters is acceptable by researching the literature. Useful studies include the band structure, density of states, electron momentum density, angle resolved PES spectra, plasmon energies, and mean free paths.

Once the spectrometer is tuned in the elastic mode on the sample, a series of measurement should be taken to characterize the sample and tune conditions. The tune conditions should be recorded. The Fluke probe calibration should be checked and the probe carefully monitored throughout the experiment. The sample thickness can be measured with ESWEEP using the (e,e') arm. The sample orientation and the momentum calibration factor and offset are determined from QSWEEP data from the (e,e') arm. ESWEEP data extending beyond at least the first two plasmon

peaks and on both sides of the zero loss peak should be taken for both (e,2e) arms. This data provides information on the target thickness, the energy resolution and the Wien filter offset voltages. QSWEEP data should be taken over the full range of momenta for a number of fixed binding energies for both (e,2e) arms. This data determines the extent of the systematic error in the count rates as a function of momentum.

The spectrometer should next be tuned to the inelastic mode. The existence of coincidence counts should be established first. This is done by taking data at only a few points over a range of binding energies at zero momentum. Once this is confirmed a finer energy grid of data at q = 0 can be used to determine an approximate Fermi level. Next a set of data at several widely spaced momenta should be taken to determine the momentum offset and the extent of the data in momentum-space. A final scan at the true momentum zero over a wide range of energy is used to better define E_F and to establish the lower limit of data. These measurements define a region of interest in (E,q) space. It extends in energy from approximately one plasmon energy above the Fermi level to about one and a half times the plasmon energy below the bottom of the valence band. In the momentum direction, it extends approximately one FWHM of the momentum resolution beyond

where the cross section falls to zero.

It is best to first take a set of coarse data over this entire region of interest. This confirms the extent of the region of interest and provides a framework for merging the finer data. The finer grid data should be taken in sets that take approximately 3-6 hours to sample once. It is crucial that all (E,q) points in the region of interest be sampled and that each scan overlap the initial course grid at at least one momentum value which can be used to merge the data. The final (e,2e) data set should repeat the first coarse data set to provide a check for sample degradation and systematic errors. Finally, ESWEEP and QSWEEP data should be repeated.

Preparation of Thin Graphite Samples

I. Extracting Graphite from surrounding rock

A. Choose large, flat crystals with little twinning.

B. Remove excess rock with pliers or a hammer and chisel.

C. Dissolve the remaining rock in concentrated hydrofloric acid in a wax-lined glass beaker.

D. Rinse the crystals in distilled water.

II. "Standard Scotch-tape method" of cleaving

A. Choose a large crystal ($\lesssim$ 3 cm^2 surface area) with a smooth surface. If necessary, the crystal can be cleaved with a razor blade. Do not try to polish the crystal.

B. Mount the crystal on a piece of cellophane tape with the smooth surface towards the adhesive. Note that cheap cellophane tape (as opposed to Scotch-brand tape) must be used, since it only has toluene soluble adhesive.

C. Cleave with another piece of tape. The freshly cleaved surfaces facing up are the best surfaces to continue working with.

D. The goal is to continue cleaving the sample with successive applications of tape until you get a large ($\sim$ 1 mm^2) uniform area that you can see through. Holding the tape up to a light or over a light table is a good way to see the thin spots.

E. Patience is the most important ingredient. Alternating directions in which the graphite is peeled improves the chances for thin samples. The tape can be applied lightly to remove small graphite flakes and to smooth the crystal surface.

III. Removing the tape.

A. Once you have a thinned sample, place it adhesive face down on a microscope slide. Remove the excess tape and graphite with a razor blade. A rectangular piece of tape twice the size of the thin area should be left. This facilitates removal of the sample from the microscope slide and subsequent handling. In this state, the sample can be more closely examined or stored with less likelihood of damage.

B. Fill a glass petri dish with approximately 1 cm of toluene. Remove the sample from the microscope slide and place it tape face down in the petri dish. Cover the dish and wait until the adhesive dissolves, typically 4-6 hours. It is best to have only one sample in a dish because the mounting process will tend to break other samples in the dish.

IV. Mounting the sample

A. This is the most delicate operation; do it carefully. Using tweezers, gently lower a sample holder into the toluene. Raise the sample by holding the tape and turn it over onto the sample holder, taking care not to break the surface. If you are lucky, the sample will be properly mounted and the tape can be lifted off.

B. If the sample stays on the tape slowly raise the tape out of the liquid allowing surface tension to separate the film. Move the holder under the target and align the hole with the thin spot. Raise the holder straight out of the dish. It is best to use two pairs of tweezers.

C. Once the sample has been removed from the liquid it must be dried. It is best to place the holder on clean absorbent paper at an angle with one edge resting on a microscope slide. The hole should be positioned so that it is not in contact with the paper or slide.

D. After the sample has dried, it should be placed on a slide or in a container. Air currents caused by movement can break the sample.

The vita has been removed from the scanned document